Inverting domes for needle-less powder injection

Davide De Focatiis

Michaelmas Term 2003

Abstract

A thesis submitted for the degree of Doctor of Philosophy at the University of Oxford.

Davide De Focatiis **Lincoln College** **Michaelmas Term 2003**

Inverting domes for needle-less powder injection

This thesis is concerned with a gas-powdered needle-less injection device where drug particles situated on the underside of an inverting dome are accelerated due to the inversion of the dome when a pressure shock wave reaches it. The objective of the thesis is to understand the process of dome inversion, and to increase the peak velocity of the powder leaving the dome from around $240m/s$ in the past to beyond $300m/s$.

A number of experiments are performed to investigate the behaviour of the thermoplastic elastomer Hytrel from which domes are made, and find its mechanical response to be mildly strain-rate dependant, affected by thermal history, and anisotropic when injection-moulded. Two methods are used to investigate the failure of the material. The geometry, quasi-static and dynamic response, and biaxial burst strength of inverting domes is then explored using a range of techniques. Finite element modelling is used to find the trajectory and velocity of particles leaving the dome. The difference between nominal and actual domes has been examined, together with the sensitivity to various manufacturing imperfections. The effect of heat and pressure treatments on the inversion velocity of domes is considered. A dome with an optimised geometry is proposed that inverts at $299.8m/s$.

Additionally, a new manufacturing technique, compression moulding, is used to produce domes from Hytrel sheet material. A two-stage biaxial stretching process is used to produce orientation in the sheets. Domes stamped from this sheet invert at between 350 and $425m/s$.

to my parents

Table of Contents

List of Figures

List of Tables

Acknowledgements

I would like to acknowledge the help of a number of people during the course of this research. Firstly my thanks go to my DPhil supervisor, Dr. Zhong You, whose insight into this project provided me with a large number of ideas and avenues to explore. His support has been invaluable, and I wish to express my gratitude for the encouragement, guidance and the freedom given to me to follow my instincts, even if they often led me to dead ends. A significant debt of gratitude is also owed to Prof. Brian Bellhouse, co-founder of PowderJect, whose faith and determination in this project even when confronted with disappointing results has been unfailing. His convictions on the virtues of the inverting dome device have provided the persuasion needed to carry out a long-haul research project within the environment of a fast-moving company.

I am indebted to a very large number of people for discussions, assistance, ideas and support during the course of the thesis. The members of the Medical Engineering unit, the Civil Engineering group, the Solid Mechanics group and all of the technical and support staff of the Engineering Department have provided the productive and interesting environment within which this work was produced. Special thanks go to Richard Koltermann, John Greenford, Roger Lewis and Gerald Walker for manufacturing and assisting with the large number of domes, devices and test equipment that has been used within the research. Financial support has been kindly provided through a CASE studentship by the EPSRC and PowderJect Pharmaceuticals.

On a personal note, I owe my gratitude to all of the friends I have made in Oxford University for providing a stimulating, supportive and entertaining environment throughout. I especially wish to thank my girlfriend Anne-Christine for her energetic enthusiasm, unfailing support and stern belief in my ability to carry this project through. Her capacity to turn a disappointment around and recharge my batteries has been unique.

Finally I wish to thank my family for being there when it mattered. The intriguing discussions in mathematics and science, and ever-present assistance provided by my mother throughout my education have been a wonderful gift, and came in addition to being generally a great mum. The example set by my father has led me to tackle each obstacle with determination and perseverance, and eventually to become and engineer and appreciate its exciting rewards. I dedicate this thesis to my parents.

Chapter 1

Introduction

1.1 Background

A novel approach to injection pioneered by PowderJect Pharmaceuticals is to accelerate powdered drug particles to sufficient velocities such that they are able to penetrate and come to rest within the skin [4, 50–52]. This is done by using compressed gas to accelerate either the particles themselves, or a suitable carrier that stops before reaching the skin. This approach to injection is needle-free and pain-free, and additionally removes the risk of contamination since it is only the drug itself that comes into contact with and penetrates the skin.

Development of needle-free injection devices began in the 1990s at Oxford University's Medical Engineering Unit. A range of devices have been produced, including a shock-tube device that entrains drug powders held between bursting membranes in supersonic gas flow [30, 47]; a similar device utilising the Venturi effect to introduce the particles in the supersonic flow [13]; and a device that makes use of a solid projectile to accelerate the powders [31, 37, 60]. The shock-tube devices have been successful in clinical trials for dermal applications [38], while the projectile device is considered too dangerous for clinical use.

An alternative to the shock tube devices uses a dome-shaped elastic membrane to

carry the drug powder. During injection the membrane is hit by an oncoming shock-wave and rapidly inverts by deforming in such a way as to flip inside-out, its convex side becoming concave and vice versa. During this process, the membrane accelerates the powder to velocities sufficient to penetrate the skin. This device is known as the *inverting dome device* /indexdevice!inverting dome. It is intended for applications where the release of gas during injection would not be permissible, such as oral and catheter injections.

This thesis seeks to develop an understanding of the inverting dome within this device with the aim of optimising the design of the dome to achieve higher particle velocities.

1.2 The inverting dome device

The inverting dome device is a self-contained mechanism whose function is to accelerate drug powders to velocities suitable for tissue penetration. The key components of the device are illustrated in Fig. 1.1.

Prior to injection the device is assembled with a new bursting membrane (D) and the gas reservoir (A) is filled to a specified pressure with helium gas (B). A new dome (G) is loaded with drug powder and fixed to the device. The button cylinder, normally of volume $5ml$, and containing high pressure helium gas at 25bar, is pressed in order to release the gas into the rupture chamber (C). Once the pressure in the chamber reaches the bursting pressure of the diaphragm (D), the diaphragm bursts, generating a shock wave. The shock wave forms as it travels along the shock tube (E) and impinges on the convex surface of the dome (G), causing it to invert and accelerate. The particles on the underside of the dome (H) are accelerated with the dome, and since they are loosely attached they continue with the same velocity even after the dome has started to slow

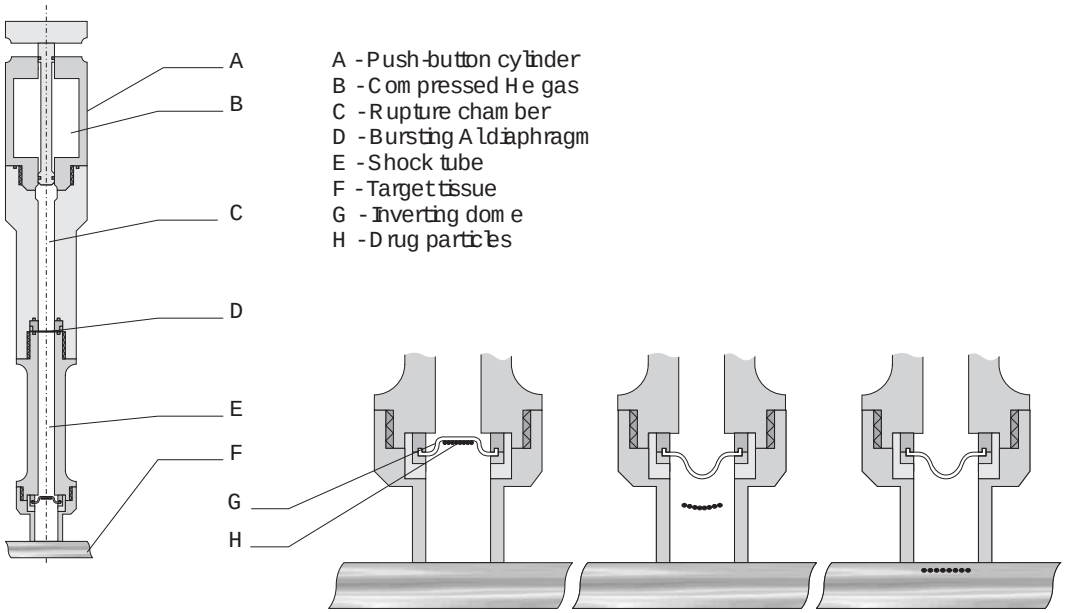

Fig. 1.1: The inverting dome device, and the sequence of events that take place during injection.

down. The particles travel through the air and penetrate the tissue (F), as shown in Fig. 1.1.

There are a number of advantages in the use of inverting dome devices. Firstly, the noise generated by the device is very limited since the device is approximately self-contained. Secondly, there is no uncomfortable release of gas as with the shock-tube and Venturi devices. Thirdly, the device lends itself well to catheter applications since, provided that the catheter length and shape does not significantly reduce the shock wave strength, the dome may be placed at the end of the catheter, and used to achieve injection within the body. Also, the device may be shaped with curved shock tubes for potential applications in dentistry. Laboratory versions of a straight device and two devices with bent shock tubes similar to those used in Duckworth *et al*'s 1998 clinical trial [15] are shown in Fig. 1.2. The speed induced on the drug powder by inverting dome devices is not significantly affected by the size and density of the powder, provided that the total mass of the powder is significantly less than the mass of the dome.

Fig. 1.2: Laboratory versions of the inverting dome devices, shown straight and with bent and kinked shock tubes. Devices similar to these were used in the 1998 clinical trial [15].

Prior to the author's research on these devices, the main limitation with the devices had been in the inversion velocities of the domes, and hence the final powder velocity. Early dome device powder velocities typically did not reach $150 m/s$ [40]. Later, when injection-moulded Desmopan and Hytrel domes were introduced to replace thermo-formed polyurethane and fabric domes, the particle velocities were increased to $220 m/s$ [12]. This limitation, together with the potential of a bent device or a catheter, suggested that inverting dome devices would be best suited for mucosal delivery and catheter delivery, where the target tissue is softer and presents less of a barrier to the oncoming drug powder. Even with these relatively low powder velocities, the early devices were the subject of a successful clinical trial administering local anaesthetic to the oral mucosa [15] and were deemed worthy of further research, primarily aimed at increasing the dome and powder velocity in order to enable injection to a greater variety of target tissues.

1.3 Scope and aims

The inverting dome device offers some considerable advantages over the other devices; prior to this research its main limitation has been in the limited drug powder velocities that can be obtained [12]. In addition, the behaviour of the inverting dome and the properties endowed upon it by the material it is made of were poorly understood. The dome had been considered as a freely moving surface by Nabulsi [40] who found relatively poor agreement between the predicted and the observed behaviour in injection-moulded domes. Early tests caused domes to burst, and the conditions for this failure had not been explored [40].

This thesis aims to develop an understanding of the mechanism of inversion in the dome, and its effect on drug particle velocity. This will be done by means of an extensive experimental programme looking at the behaviour of the dome itself, coupled with experiments aimed at understanding and enhancing the properties of the material. Computational modelling will be used where possible to assist the investigation into both the quasi-static and dynamic behaviour of the dome. Once a sufficient understanding of the current inverting dome is reached, methods for producing powder velocities in excess of $300m/s$ will be proposed. The manufacturing procedure, the shape and other characteristics of the inverting dome will be put under scrutiny for possible improvements.

1.4 Outline

This thesis consists of 8 chapters. Chapter 2 presents a review of the available literature relevant to the thesis. Previous work on both the gas dynamics within the inverting dome device and on the early designs of the inverting dome itself is reported. Previous

research on the structure and properties of the thermoplastic elastomer Hytrel with which domes used in this thesis are made is then summarised.

Chapter 3 is concerned with a number of experiments that have been performed in order to obtain additional information on the structure and properties of Hytrel. The effects of processing, thermal history, process-induced orientation, strain rate and cyclic loading are investigated by means of a number of controlled experiments. Two methods are then presented to obtain information about the failure of the material.

Chapter 4 reports a number of experimental techniques used in the investigation of the behaviour of the inverting domes. The geometry of manufactured domes is examined using a microtome slicing technique. The pressure near to the dome's surface is recorded during injection. The non-linear quasi-static response of the dome to an applied pressure is investigated, and the high-speed behaviour during injection is recorded using high-speed imaging. A particle velocimetry method for obtaining the velocity of drug powder during injection is presented. The failure of domes under quasi-static and dynamic conditions is also discussed.

Chapter 5 makes use of the finite element method to investigate inverting domes. A general method for meshing dome shapes is given, and suitable input and boundary conditions are stated. The quasi-static snap-through behaviour is then analysed using stabilised and post-buckling static calculations. The dynamic behaviour is then addressed, and results are used to project the paths taken by drug particles once they leave the dome. A simple dynamic mechanical model of dome inversion that makes use of a mass, a non-linear spring and a time-varying input force to predict the peak dome velocity is also presented. Manufacturing imperfections and their effect on dome inversion velocity are also addressed.

Chapter 6 investigates two methods by which the performance of injection-moulded

inverting domes may be improved. The first technique consists of a combined heat and pressure treatment that induced small amounts of permanent deformation to the domes. The second method involves altering the basic geometry of the domes. A combination of the two methods is also discussed.

Chapter 7 proposes a different method of producing inverting domes from Hytrel: compression-forming. Domes are produced from compression-moulded sheet and pre-stretched sheet using a set of moulds that permanently deform the sheet material into a dome shape. The mechanical properties of pre-stretched sheet are investigated in the context of changes to the microstructure of the material. Domes produced with this method are tested using particle velocimetry and quasi-static burst strength tests.

Chapter 8 presents the conclusions and some recommendations for further work.

Chapter 2

Literature review

This chapter consists of a summary and review of the available literature that is of interest for this thesis. Section 2.1 outlines the gas dynamics that take place on release of the helium gas within an inverting dome device. The need to introduce a small vent hole within the device is also addressed.

Section 2.2 reports the developments that have taken place on the inverting dome itself, presenting the dome with which this research has begun. The way in which the dome is clamped to the device is presented, and will be improved upon in Chapter 4. Dome behaviour is responsible for the trajectory and penetration of particles, and previous research that addressed these issues is reported.

Section 2.3 investigates the behaviour of the thermoplastic elastomer Hytrel, with which domes are currently manufactured, starting from the chemistry and physics of its components, and how production methods and subsequent treatment can alter the polymer's microstructure. The chemical structure and thermal properties will be investigated. The important temperature transitions are then identified and related to the physical molecular structures they originate from. Assembling together the work of a number of authors, a picture of the morphology of Hytrel is constructed that will be invaluable in understanding the mechanics of the deformation of the material. Material

failure is also addressed.

2.1 Gas dynamics in the inverting dome device

Since the performance of most of the PowderJect devices is driven almost exclusively by the gas dynamics , a considerable fraction of the early work of Oxford University's Medical Engineering Unit has been centered around this area. The gas dynamics of the inverting dome device have been the subject of previous investigations [12, 40], and a brief treatment will be given here.

The inverting dome device is made up of a gas reservoir connected to a rupture chamber. The gas reservoir is a button cylinder of approximately $5ml$ internal volume containing high pressure helium gas at $25bar$. The gas is released from the button cylinder by pressing the actuator button on the cylinder. The gas then expands to fill the rupture chamber, of internal volume $1.84ml$. Situated at the end of the rupture chamber is a cassette containing a diaphragm designed to burst at a predetermined pressure. Typically this diaphragm is $30\mu m$ thick annealed aluminium, which bursts at approximately $15.4bar$ [12]. The gas expansion into the rupture chamber is able to generate pressures of approximately $18.5bar$, comfortably above the pressure needed to burst the membrane. Once the membrane bursts, a compressive shock wave propagates further down the device along the shock tube , typically $60mm$ in length and $6mm$ in diameter. This shock wave is reflected against the dome, and travels back up the shock tube. This reflection is associated with a substantial increase in pressure in the vicinity of the dome. Also travelling down the shock wave, at a slower velocity, is the contact surface between the helium/air mixture in the rupture chamber and the air in the shock tube. At the same time as the shock wave leaves the diaphragm, an expansion wave is also generated and travels backwards along the rupture chamber. This expansion wave

is reflected at the button cylinder and travels forward again down the rupture chamber and shock tube. The shock waves and their reflections are shown in the diagram in Fig. 2.1.

The theory behind the propagation and interaction of the shock waves has been researched previously for general shock tubes [19] and in the context of the inverting dome device [5, 12, 40] and is beyond the scope of this thesis. The main findings relevant to this work were concerned with the lengths of the rupture chamber and the shock tube. The rupture chamber needs to be long in order to delay the arrival of the reflected expansion wave since the interaction between this reflected expansion and the pressure in the shock tube this will reduce the pressure in the vicinity of the dome. The dome requires a finite time to invert, and therefore it is necessary to maintain the pressure in the vicinity high during this time. It was found that for the rupture chamber a length

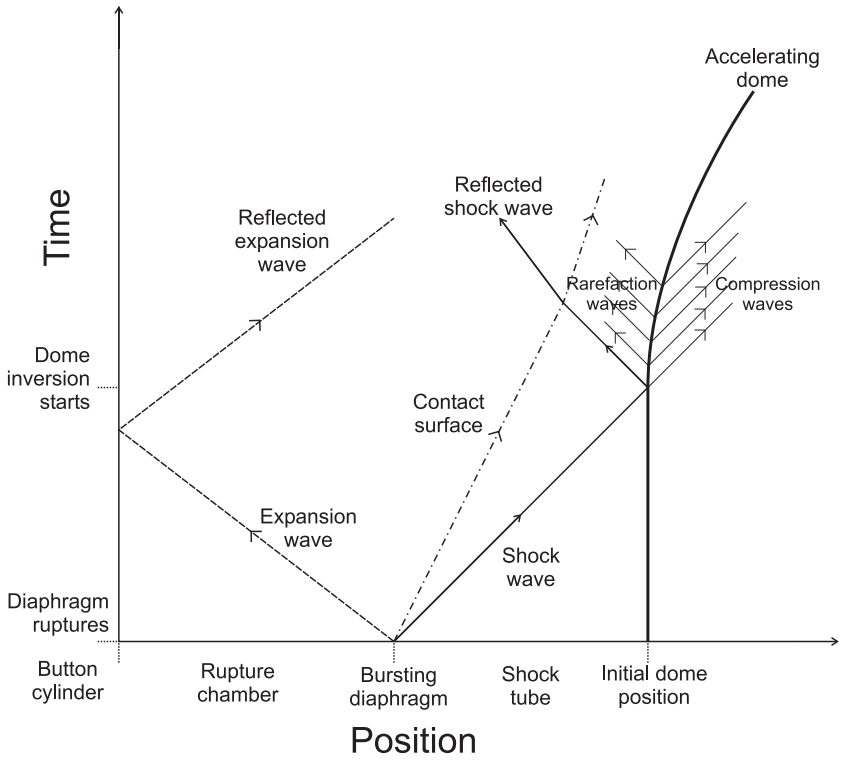

Fig. 2.1: Shock waves generated at the bursting of the diaphragm within the inverting dome device. Adapted from [40].

of $65mm$ was satisfactory for this purpose [12]. Furthermore, the shock tube needs to be long in order to allow a normal shock wave to form. The minimum theoretical recommended length is of the order of 5-6 tube diameters, and a minimum of $60mm$, or 10 tube lengths, was found to be satisfactory for this purpose [12].

Costigan *et al* [12] also reported tests using air and carbon dioxide as driver gases at pressures of $28bar$, although average measured particle peak velocities with these driver gases were low, $118m/s$ and $97m/s$ respectively. Using helium at the same pressure results in average particle velocities of $241m/s$. The authors investigated different diaphragm thicknesses and materials, and found that the peak shock wave pressure is affected by the rupture pressure of the diaphragm. In addition, the rupture pressure of the aluminium membrane varies with fill pressure, probably as a result of strain rate effects.

2.1.1 Venting the shock tube

Initial tests with injection-moulded inverting domes failed because of the rupture of the dome itself. Although the dome successfully inverted and accelerated the powdered drugs, it subsequently inflated too far and was not able to withstand the pressure. Nabulsi [40] found that the earlier fabric reinforced domes were inverting in under $50\mu s$ but the bursting in the injection-moulded domes occurred in $30ms$. This suggested that the domes were bursting as a result of the pressure some considerable time after the inversion, and Costigan [12] suggested that providing a small outlet for the gas at some distance away from the dome but still within the shock tube might solve the problem. Costigan designed a $1mm$ diameter vent hole in the shock tube $15mm$ from the bursting diaphragm. He reported that this allows a controlled decay in pressure and minimises the possibility of dome rupture. Although the vent hole has some effect on the pressures,

this becomes significant only after the dome has inverted.

Clearly introducing a hole in the device means that the device is effectively open to the outside, and hence noisier. However, the reduced size of the vent-hole and the position of the hole away from the dome means that a small silencing sleeve can easily reduce the sound intensity to appropriate levels. Fig. 2.2 shows a device with and without the attached silencer. Costigan reported a small decrease in powder velocity with the silencer attached, and a considerable improvement in the sound levels.

The vent hole has therefore become an integral part of the design. The device used in tests in this thesis has an unsilenced vent hole, and the noise produced even without a silencing sleeve is not uncomfortable.

2.2 The inverting dome

2.2.1 Early development of the inverting dome

Bellhouse *et al* [3] conceived the idea of an inverting dome to inject particles in 1997. In their patent they described the inverting dome as "an eversible dome-shaped membrane" or as "a bistable membrane that is moveable between an initial, inverted position and

Fig. 2.2: Laboratory versions of the inverting dome device, with and without a silencer.

a dynamic, everted position". The diagram of the inverting dome from the 1997 patent is shown in Fig. 2.3.

The 1997 patent indicated polyurethanes, silicone rubber or polyester as suitable candidates materials. Nabulsi *et al* [40] describe a thermo-formed composite dome made of a polyurethane film and a fabric sheet, as well as an early injection-moulded Desmopan dome, but do not give the precise geometry of the domes. They cite a *travel distance*, given as $3.4mm$ for the fabric reinforced version and $4mm$ for the injection-moulded version, and this is understood to mean the distance between the apex of the dome at the two bistable positions.

Costigan *et al* [12] explain that the inverting dome needs to be light and flexible in order to invert rapidly, and resistant to rupture. A number of domes were designed for these tests with virtually identical cross-sections , one of which is shown in Fig. 2.4. The differences in the designs consisted in the size and number of small fibres injection-moulded on the concave face of the dome in order to help to retain drug particles of different sizes.

Using these latest dome designs Costigan was able to successfully accelerate powders

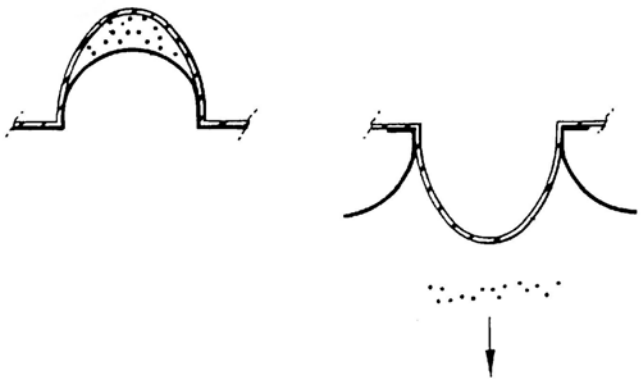

Fig. 2.3: The inverting dome diagrams, reproduced and adapted from the 1997 patent [3].

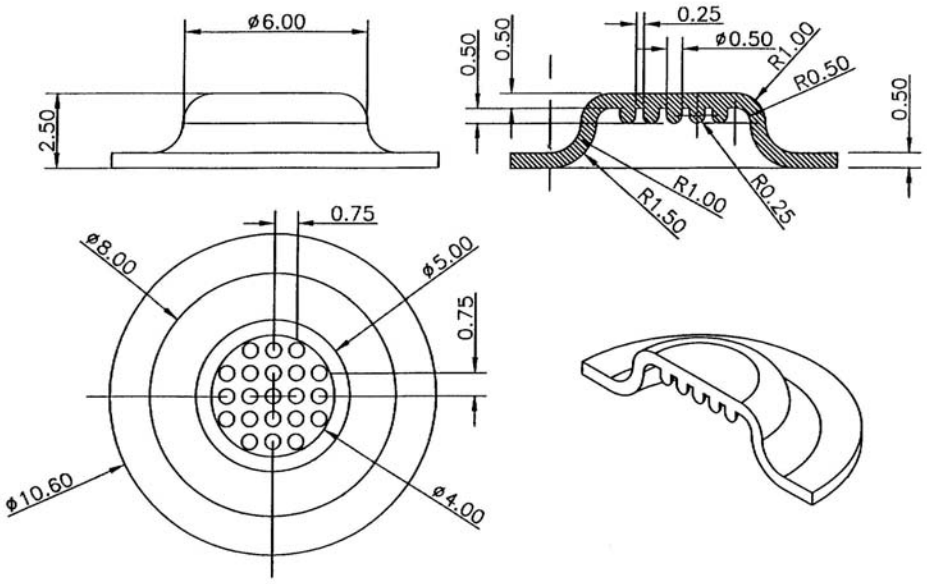

Fig. 2.4: Design of the inverting dome used in the 2000 trials [12]. A number of fibres are injection-moulded on the dome for drug retention.

to velocities of approximately $220 - 240 m/s$ without dome failure. Similar devices were successfully used in a clinical trial [15].

2.2.2 Retention of the dome

Costigan *et al* [12] reported that older domes had been clamped with a ring of $6mm$ inner diameter through which the dome inverted. They found that this exit diameter was too narrow to allow uninhibited inversion, and increased the diameter of the clamping ring to $8mm$. This wider opening was favoured since it is allowing faster and uninhibited dome inversion.

A closer look at the clamping arrangement reveals that due to manufacturing issues the outer clamp ring's 8mm hole has a manufacturing round edge with a radius of approximately $0.5mm$. This was introduced to prevent the sharp edge of the clamping ring cutting through the dome as it inverts. A diagram of the clamping arrangement is

shown in Fig. 2.5.

Costigan also reported that domes were accelerating powders to different speeds depending on whether they were *as received* or *degreased*. *As received* domes were averaging $226m/s$ and *degreased* domes $245m/s$. He suggested that a reason for this difference might be that the degreasing was contributing to clamping the edges of the domes more efficiently, or perhaps that the drying that followed degreasing was altering the material properties. In addition to this, domes were occasionally slipping out of the clamping arrangement during firing, a problem likely to have been introduced by the widening of the exit ring.

2.2.3 Drugs and targets

Particle density and size is not an issue with the inverting dome devices provided that the particle's travel distance between the dome and the target tissue is small, and that the mass of particles is much less than the mass of the dome. Laboratory tests performed with drug particles as large as $500\mu m$ have achieved successful injection although particle sizes in excess of $100 - 200\mu m$ tend to cause excessive dermal response. The density

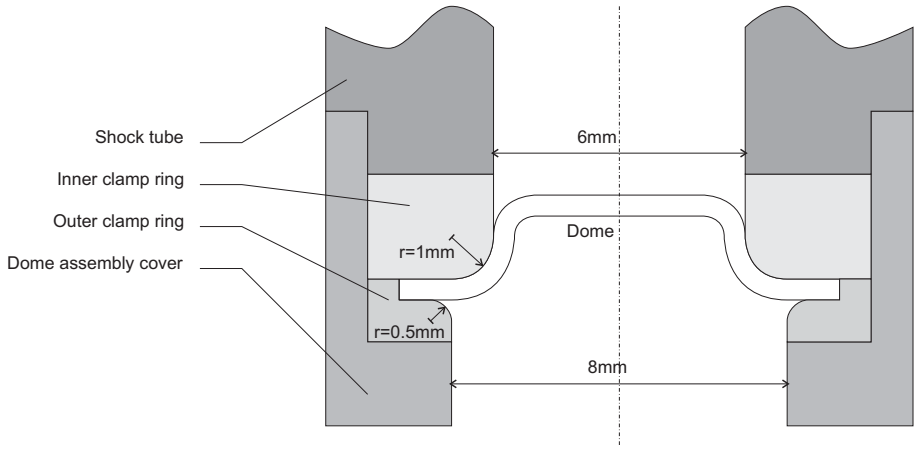

Fig. 2.5: The clamping arrangement and the manufacturing radius on the outer clamp ring.

of pharmaceutical drugs is typically in the range of $1000 - 1600kg/m^3$ [60] but due to the porosity of particles and the addition of lower density excipients, powdered particle density varies between $600kg/m^3$ and $1300kg/m^3$ [37].

For the purpose of intracellular delivery, genetic material is precipitated onto inert gold particles of diameter $1 - 3\mu m$. This technique has been successfully used in pre-clinical immunization of mice for influenza and hepatitis b viruses [11]. These particles are generally too small and dense to be injected using shock-tube and Venturi devices, and as such are ideal candidates for the inverting dome device. Within this thesis, most of the testing of the inverting dome devices has been done with mannitol powder, a readily available sugar of diameter range $38 - 53\mu m$ and density that closely resembles typical pharmaceuticals.

Clinical powder injection using the inverting dome device has concentrated on the buccal (mouth) mucosa as a target. Considerable research has already been undertaken on the mucosa as a target to powder injection methods [37]. The buccal mucosa presents a much deeper target to powder injection than skin, and this is desirable due to injection devices generally having a range of particle velocities, and hence penetration depths. Also, it is a softer target than skin, and as such lower velocities are required of particles for equivalent penetration depths.

2.2.4 Particle trajectory and penetration

Mitchell [37] has investigated particle penetration using a projectile device , and has shown that penetration is dependant upon the component of the velocity that is perpendicular to the target surface. Hence particles impacting at an angle to the vertical will embed less deep than particles impacting perpendicular to the target.

This aspect has been briefly investigated in the context of the inverting dome device

by Costigan *et al* [12] using a dome with drug-retaining fibres and larger than usual particles, $400\mu m$ in diameter. They found that the velocity of particles drops from a maximum for particles placed at the centre of the dome to lower values as particles are placed further outwards. Fig. 2.6 shows the velocity measurements of Costigan *et al* as well as an agar gel target in which the particles embedded during the test. From the agar target it can also be seen that the tracks left by the particles whilst travelling through the gel give clues as to the paths the particles took to get there. The paths of particles on the outside of the target are at an angle to the vertical, suggesting that the particles were travelling with a component of radial velocity, and that the direction of travel was not vertical.

The eventual outcome of a powder injection using the inverting dome device is to achieve particle penetration. The area of microparticle penetration has been at the core of a number of extensive studies [31, 37, 38, 60]. The question of which particle parameters affect particle penetration has been debated at great length, and the generally

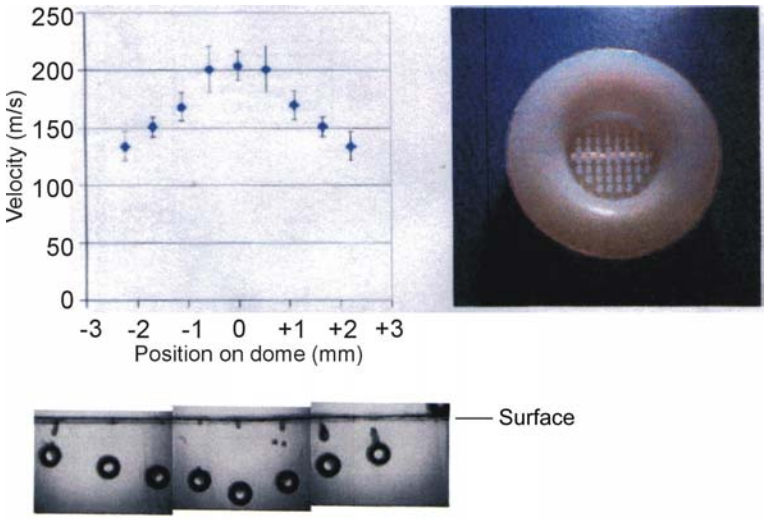

Fig. 2.6: Effect of particle position on the dome on velocity and penetration of $400\mu m$ particles. The penetration of the particles in the agar gel target is also shown. Reproduced with permission and adapted from [12].

agreed view is that the product of particle density ρ_p, particle radius r_p, and vertical component of particle velocity $V_p(z)$ is proportional to particle penetration. This proportionality has been shown both theoretically and experimentally by Mitchell [37].

The velocity given to particles fired by the inverting dome is not sensitive to particle size [12]. The particles are accelerated mechanically, and there is very little deceleration of particles as they travel through the air between the dome and the target, since the air is at atmospheric pressure and the travel distance is kept short. This is not the case with shock-tube and Venturi devices, whose performance is closely linked to particle size. In these devices the particles are accelerated and decelerated by the gas flow and the drag effect in the impingement region has a significant negative effect on particle impact velocities.

In addition, the particles make up only a small fraction of the mass of the dome. Typically a payload of particles of $0.25mg$ is used, with a dome weighing approximately $60mg$. Although the effective mass of the moving dome is smaller than the overall mass, provided that the mass of the payload is much smaller than the effective mass of the dome, the velocity of the particles can be considered independent of particle size and density.

The penetration of the particles will therefore be proportional to three independent parameters: particle radius, density, and vertical velocity component. Since the particle radius and density depend on the specifications of the particles, only the vertical velocity component is dependant upon the performance of the dome. The vertical component of velocity, and its distribution across a dome diameter, is the main criterion in evaluating the particle penetration performance of the inverting dome.

Mitchell [37] discussed the possibility of ricochet during particle impact using $48\mu m$ polystyrene particles. These particles are model particles, but are representative of the

sorts of drug powders that might be used in an inverting dome. He found that particles would embed in a model target if their vertical component of velocity exceeded $160m/s$, with no penetration occuring even for vertical impact at velocities less than $160m/s$. This lower-bound of $160m/s$ on the vertical component of velocity is specific to $48\mu m$ polystyrene particles in agar gel.

2.2.5 Dome failure

Clearly another criterion for dome performance is that it should fulfil its requirement of resisting the incoming pressure without burst during use. The dome is stretched as a result of its inertial movement as well as the deformation that comes from its inversion. A successful dome will not burst during or shortly after injection.

This aspect of dome performance has not been thoroughly investigated; Costigan [12] reported that the combination of $25bar$, $5ml$ helium in the button cylinder and $30\mu m$ aluminium membrane did not cause domes to burst, and that increasing the pressure in the button cylinder to $30bar$ caused virtually all of the domes to burst, but no effort was made to understand why this was the case.

2.3 The thermoplastic elastomer Hytrel

The first inverting domes were compression-formed from polyurethane sheet and a layer of fabric. Subsequent domes were injection-moulded from Desmopan, a commercial elastomer. Currently, domes are injection-moulded from Hytrel, another commercial elastomer. Apart from the fabric sheet, all the other aforementioned materials are thermoplastic elastomers, a relatively recent development in polymer technology. This section seeks to give the reader an introduction into thermoplastic elastomers and will review the available literature on Hytrel.

2.3.1 Introduction to thermoplastic elastomers

Elastomers are natural or man-made polymers with mechanical properties similar to those of natural rubber. Elastomers such as vulcanised rubber are able to withstand enormous deformations and recover completely their original shape with very little degradation or damage. However, due to the permanent covalent cross-linking, the polymers are difficult to recycle, and relatively expensive to manufacture [2, 53].

Thermoplastics are linear, or close-to linear long-chain polymers that are not cross-linked. At room temperature the secondary bonds hold the molecules together, and as the temperature is raised these bonds break down and allow the polymer to flow. Thermoplastics are enormously appealing as polymers because of the ease with which they can be manufactured, by extrusion, injection-moulding, vacuum and blow forming, and compression-moulding. In addition, they are easy to recycle since they can be melted down and reformed with minimal degradation [2, 53].

Thermoplastic elastomers are a recent development in polymer technology that attempts to capture the mechanical properties of elastomers and the manufacturing appeal of thermoplastics. Although they can often stretch to ultimate strains comparable with rubbers, they do not fully recover the strains because of the non-permanent nature of their cross-links. In a thermoplastic elastomer, the cross-links are not covalent bonds, but bonds that can be broken and reformed by heating and cooling the polymer. This can take place when regions of the polymer crystallize and tie together, or when polar ionic groups cluster away from the non-polar backbone chain, or by other mechanisms.

One family of these polymers is that of the *block copolymer elastomers*. Within this family are the segmented polyether-ester block copolymers. This type of polymers, invented by Witsiepe in the 1970s [59], is marketed under the trade name of Hytrel

by DuPont, and of Arnitel by Akso. A block copolymer is a polymer made up of long chains of two or more different monomers. The monomers are first polymerised into blocks of monomer, repeating as many times as necessary. These blocks of monomers are subsequently polymerised, or grafted to other blocks of different monomers, making a block copolymer. A diagram showing this procedure schematically is shown in Fig. 2.7.

In Hytrel , the blocks are made up of a polytetramethylene ether glycol terephthalate soft segment and a polybutylene terephthalate hard segment [10, 22]. A segment is defined as soft if it is above its glass transition temperature at room temperature, and hard if it is below. The glass transition temperature is the temperature at which, on heating, the properties of the polymer change from being more like a glass to more like a rubber. The modulus of the polymer typically drops by 3 orders of magnitude across this transition [36].

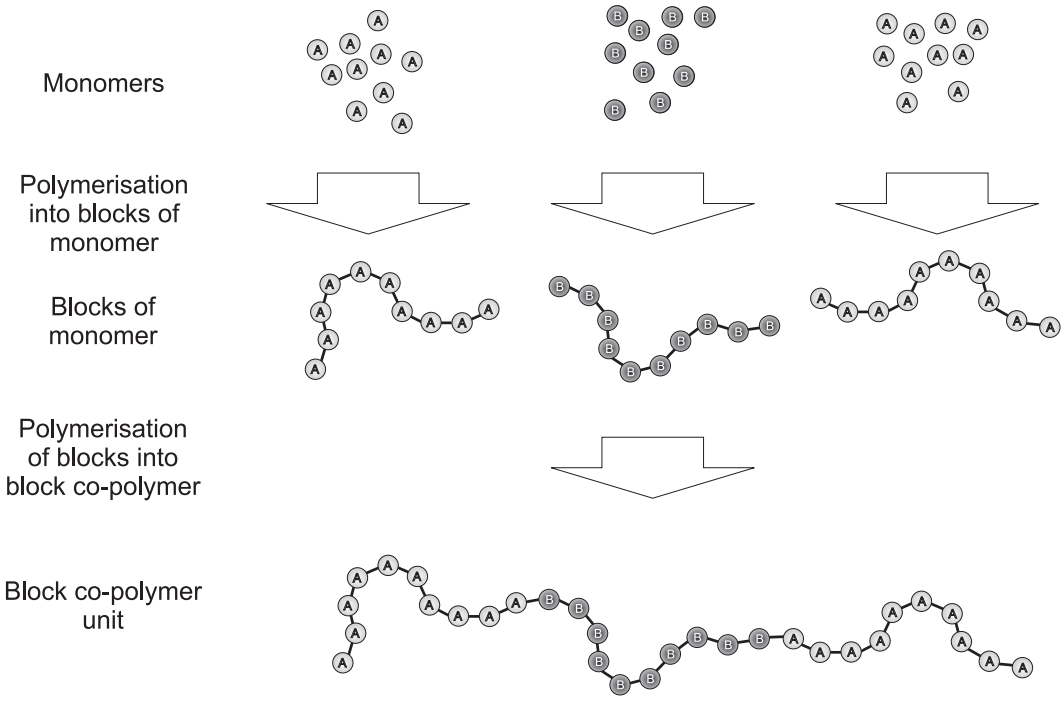

Fig. 2.7: Schematic representation of the formation of a block copolymer made up of monomers Ⓐ and Ⓑ .

The different types of polymer in a copolymer do not like to mix well, and have a tendency to phase-segregate on cooling [10]. At room temperature, the hard segments from different copolymer units form crystalline areas, while the soft segments are amorphous, and provide rubbery links across the different crystalline hard segments. Hence, the crystal units act as non-permanent cross-links and the soft segments give the polymer its flexibility. Because the ends of the soft segments are embedded in the hard segment's crystalline areas, the polymer is able to recover a substantial amount of deformation, as with a rubber. Differently to a rubber, however, the hard segment crystals can be broken down by heating the polymer to its melting point. Whilst molten it can be shaped differently, and once cooled, new hard segment crystals will form again. By varying the relative proportions of soft and hard segments, polymers with different properties and applications can be produced. A diagram of the morphology of such a copolymer at room temperature is shown in Fig. 2.8.

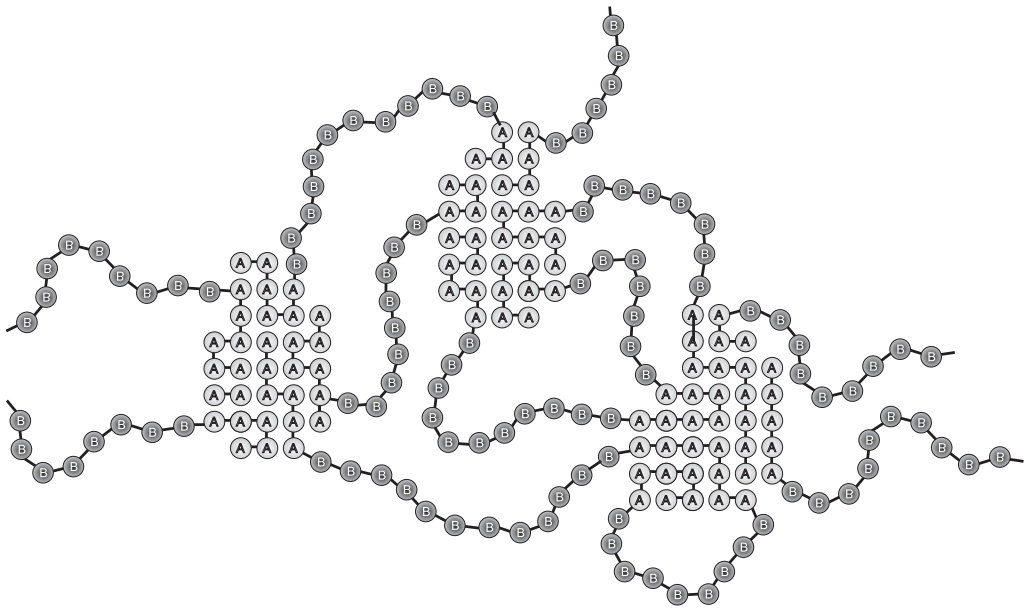

Fig. 2.8: Schematic representation of the morphology of a block copolymer such as Hytrel with crystalline hard segments Ⓐ and amorphous soft segments Ⓑ .

2.3.2 Chemical structure and composition

The generic chemical structure of a molecule of Hytrel is shown in Fig. 2.9. The soft segment that gives elastomeric character to the polymer is a poly(tetramethyleneoxy ether glycol) terephthalate, PTMEG-T, and the hard segment that forms the thermally reversible cross-links is a poly(tetramethyleneoxy) terephthalate, PTMT. The soft segment consists of oligobutylene glycol ether with typically 12 to 16 butylene ether monomer units, shown as m in Fig. 2.9. This corresponds to a molecular segment weight of about $1000 - 1400 gmol^{-1}$. The hard segment consists of oligobutylene terephthalate units corresponding to a molecular segment weight of about $250 gmol^{-1}$.

The soft and hard segments are linked together by ester groups. The soft segment is usually present with a single monomer unit, and has an average polymerisation ranging from 1 to 1.1 units, shown as n in Fig. 2.9. The hard segment is usually polymerised

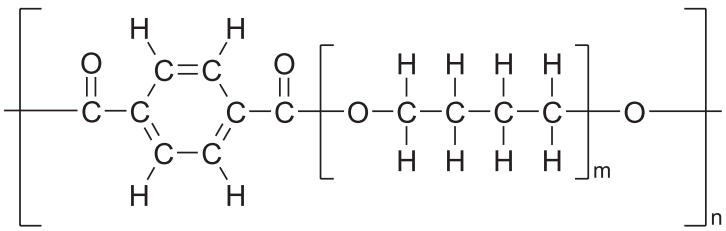

Soft segment, PTMEG-T, m=12-16, n=1-1.1

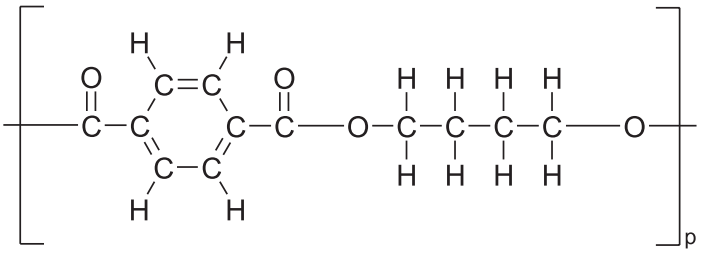

Hard segment, PTMT, p=7-10

Fig. 2.9: Chemical structure of the segments making up Hytrel, with typical polymerisation values.

to 7-10 monomer units on average, shown as p in Fig. 2.9. This makes the segment molecular weight of the hard segment about $1700 - 2500 gmol^{-1}$. The topological ratio of hard to soft segments is typically around 8 to 1 [26].

Varying the number of butylene ether monomers in the soft segment, and the overall ratio of soft to hard segments allows the production of thermoplastic polyesters with different mechanical properties. A thorough account of the details involved in the time-temperature-pressure arrangements of the chemical manufacture of the component parts is given in the first Hytrel patent [59] and by Hoeschele *et al* [24, 25] and Cella [10].

Hytrel 4068 is the polymer currently used in dome manufacture, and is part of the high-performance grades of Hytrel, with a hardness of 40D and a flexural modulus between 55-67MPa [18]. Two similar products are also offered by DuPont: Hytrel 4056, with the same hardness and modulus as Hytrel 4068, but with slightly lower melting temperature, and Hytrel 4078, also with a hardness of 40D. These grades are mentioned here because virtually all of the references have made use of grades 4056 and 4078. Grade 4068 is a more recent addition to the range. Nevertheless, the properties of the three grades are expected to be broadly similar. Where possible, properties will be given for all of these grades for comparison with the literature. Also, properties of the homopolymers PTMT, the hard segment, and PTMEG-T, the soft segment, will be given as comparison of the specific properties of the Hytrel grades where they are available.

The exact make-up of Hytrel 4068 is not known, but is expected to be similar to the 4056 grade, which has 44% hard segment by weight and an average degree of polymerisation of the hard segment of 6 [48].

2.3.3 Thermal properties

A number of methods have been adopted to investigate the thermal properties of Hytrel and several temperatures have been identified that are important in describing the microstructure, important changes in mechanical behaviour, and in prescribing any thermal treatments. The properties from the literature are summarised in Table 2.1 for the grades 4056, 4068 and 4078, and where possible for the homopolymers.

Starting with the lowest temperature of interest, the glass transition temperature T_g^{soft} refers to the temperature at which the soft segments of the polymer change from a glassy state to a rubbery state. The soft segment of the polymer is amorphous, and the stiffness of this segment changes rapidly, typically by 3 orders of magnitude across a small temperature range surrounding T_g^{soft}. Below this temperature the copolymer is brittle, and does not behave as an elastomer. This temperature has been identified in different Hytrel grades by dynamic mechanical measurements of modulus and associated loss factor by a number of authors [22, 27, 42, 54].

Table 2.1: Important temperatures for PTMT, Hytrel 4078, 4068 and 4056, and PTMEG-T. Data from [17, 18, 27, 28, 33, 48].

Polymer	T_g^{soft} ($^\circ C$)	T_c^{hard} ($^\circ C$)	T_g^{hard} ($^\circ C$)	T_V ($^\circ C$)	T_m ($^\circ C$)
PTMT (hard segment)	—	—	40	—	221
Hytrel 4078	-37.5	120	—	—	170
Hytrel 4068	-51	112	—	134	193
Hytrel 4056 (44% hard)	-32	70	80	—	173
PTMEG-T (soft segment)	-84	—	—	—	38

The hard segment of the molecule is mostly crystalline, with the exact degree of crystallinity depending strongly on the thermal history of the sample. The next temperature range of interest is the crystallisation temperature, T_c^{hard}, of the hard segments. Crystallisation is a process driven by kinetics, and as such it is strongly dependant both on the driving force and on the mobility of the molecules. The driving force controls crystal nucleation and is proportional to the supercooling temperature, which is the difference between the melting temperature of the crystals and the temperature at which crystallisation is being measured. The mobility of the molecules is the ability that the molecules have to rearrange themselves in order to crystallise, and controls the growth of crystal structures, and increases with temperature. Hence, it is difficult to speak of a precise crystallisation temperature when the circumstances are not isothermal. The temperature given in the DuPont literature [17] refers to the temperature at which the rate of crystallisation is a maximum under specific circumstances.

Richeson and Spruiell [48] have investigated the kinetics of crystallisation of Hytrel 4056 in some detail by analysing quenched amorphous samples by differential scanning calorimetry (DSC) measurements. They have found that although crystallisation in the reheated quenched samples begins as low as $-12°C$, the rate of crystallisation in general is very slow. The crystallisation half-times at supercooling temperatures of $-58°C$ ($58°C$ below the melting point) are of about 4 minutes. Richeson and Spruiell have shown that crystallisation in Hytrel 4056 can and does occur at temperatures even well below room temperature, although very slowly.

The hard blocks in the polymer also have a glass-transition temperature, T_g^{hard}. This temperature only affects the non-crystallised components of PTMT since they are amorphous. Experimentally it is easier to identify T_g^{hard} in samples with a high degree of crystallinity because at temperatures near T_g^{hard} the crystallisation rate is high, and

its effect often swamps the effect of the glass transition temperature. The extent of the effect of T_g^{hard} on the copolymer is thus related to the degree of crystallinity of the hard phase, and hence to the thermal history of the polymer as a whole. Hourston and Hughes [27] have looked for this temperature in Hytrel 4056 from DSC measurements made on as-supplied samples and on samples precipitated from a methylene chloride solution, centrifuged, vacuum-dried and subsequently annealed for 2 hours at $150°C$. They were not able to identify the glass-transition temperature from DSC on samples heated above the melting temperature and quenched in liquid nitrogen, and on samples annealed at $100°C$ since the crystallinity was too low and samples were crystallising during the experiment. They did identify the glass-transition temperature on the other samples, and their value is close to the glass-transition temperature of the pure hard segment homopolymer [34].

In a follow-up paper, Hourston and Hughes [28] point out that in their dynamic mechanical analysis there is a slight shoulder in the damping curve at around $80°C$ that probably arises as a direct result of the glass transition of the hard blocks . This shoulder is not noticeable on quenched samples since it is swamped by the endotherm due to the crystallisation of the hard segment during the experiment. At this temperature there is clear evidence of crystallisation, as shown by Richeson [48].

Non-isothermal crystallisation rate was also investigated by Richeson and Spruiell [48] at different cooling rates for Hytrel 4056. They give results in terms of a crystallisation temperature which varies from around $70°C$ at $10°C/min$ to around $20°C$ at $100°C/min$. It is interesting to note that the crystallisation temperature for cooling rates typical of injection-moulding is probably below room temperature. This would indicate that in injection-moulded samples, crystallisation occurs some time after moulding, and that the expected nucleation rate is high although the kinetics will inevitably be slow.

A temperature given in the DuPont literature [16] is the Vicat softening temperature, T_V. This is generally related to the viscosity of the samples, and can be understood as the temperature above which the material becomes too soft to be of use as a solid.

The melting temperature of the polymer, T_m, has also been found from DSC measurements by a number of authors [10, 27, 33, 48]. In practice polymers such as Hytrel do not have a sharp melting point, but rather a gradual increase in the melt flow rate, or a decrease in viscosity. What is meant here by the melting temperature is the endotherm seen in DSC. The region around the melting temperature corresponds to the breaking down of the hard segment crystals. The viscosity at this temperature is still high due to the relatively long molecules, and processing is generally done at temperatures of $20 - 30°C$ above this temperature [17]. Hourston and Hughes [27] have reported that a lowered melting temperature is found after annealing of samples due to some thermal degradation . In addition they discovered a small temperature endotherm at around $112°C$ in Hytrel 4056 in all their samples and suggest that this could be the melting of the small, imperfect crystal structures that link the hard segment spherulites.

Of interest is also Pesetskii *et al*'s [46] thermomechanical analysis of various grades of Hytrel as well as of the homopolymers. Measuring a combined response to load and thermal expansion over a wide temperature range they were able to identify T_g and T_m for both homopolymers within a copolymer. They postulate that the homopolymers take on three different structures at low, intermediate and high temperatures. For instance, in a 50% PTMT by weight copolymer they identify T_g^{soft} as $-67°C$ for an average molecular weight component of $\overline{M}_W = 4200$, the soft segment, and T_g^{hard} as $116°C$ for a component of $\overline{M}_W = 83700$, the hard segment crystals. They also found an additional T_g of an intermediate structure at $51°C$ for a component of $\overline{M}_W = 9160$, although it is not clear what this intermediate structure corresponds to. Their T_g values

do not agree precisely with other literature, mainly due to scatter in their temperature readings.

The glass transition temperature of the soft segment and the Vicat softening point generally form lower and upper bounds to the useful operating ranges of the polymer as an elastomer.

T_g^{soft} of the Hytrel grades is higher than that of the soft homopolymer. Shen *et al* [54] propose two explanations for this increase. One is the reduced mobility of the PTMEG-T chains, since they are effectively anchored at the crystal domains, and require greater energy for equivalent Brownian motions in the copolymer. Another suggestion is the possibility of some hard segments being present in the soft domains exhibiting an anti-plasticisation effect.

T_g^{hard} of the Hytrel grades is higher than that of the homopolymer, and this is thought to be due to the shorter, less mobile segments of hard PTMT in Hytrel as compared to the homopolymer.

2.3.4 Thermal degradation

The monomer components of Hytrel are polymerised by dehydration synthesis, or condensation, a reaction where the byproduct of polymerisation is water. An example of the polymerisation of polyether glycol is shown in Fig. 2.10. Most of the polymerisation reactions involved in the assembly of the component parts of the polymer use this form of reaction [10]. This is a reversible reaction, and the polymer, like all polyesters, is hygroscopic, or water-seeking, becoming more and more so at higher temperatures. Some hydrolytic degradation, or reverse polymerisation, can be expected after prolonged periods in the presence of moisture, such as might be found in air. This hydrolysis would have a negative effect on the mechanical properties of the bulk polymer, since it would

effectively break up different parts of the molecules.

The polymer's resistance to thermal degradation is particularly important during processing, where the temperature is high. In injection-moulding, the times for which the polymer is exposed to high temperatures are relatively short, usually only a few seconds. When the polymer is manufactured from compression-moulding , however, the exposure times are longer. Degradation can occur because of the presence of water in the polymer, and also from moisture in the atmosphere, and will result in the polymer breaking up into smaller molecular chains and becoming less viscous. The graph in Fig. 2.11 provided by DuPont [17] shows the recommended processing times at different temperatures as a function of the melt flow rate.

Injection-moulding of specimens normally takes place at $225°C$ and takes $10 - 15$ seconds per sample. There is no degradation expected during injection-moulding. Compression-forming is a slower procedure, and care has to be taken to avoid thermal degradation, especially where samples are cooled slowly. A temperature of $230°C$ and a time at the highest temperature of 10 minutes should be safely away from the degradation zone, even allowing for warm-up and cool down times.

If the polymer is not dried prior to processing, hydrolytic degradation will occur. Although this may not appear as visible defects, the mechanical properties will be affected. The polymer is also likely to be more brittle, especially at low temperatures [17].

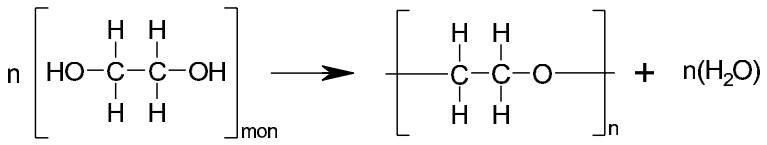

Fig. 2.10: Polymerisation reaction of polyether glycol, releasing water as a byproduct. This reaction is reversible given favourable conditions such as heat and the presence of moisture.

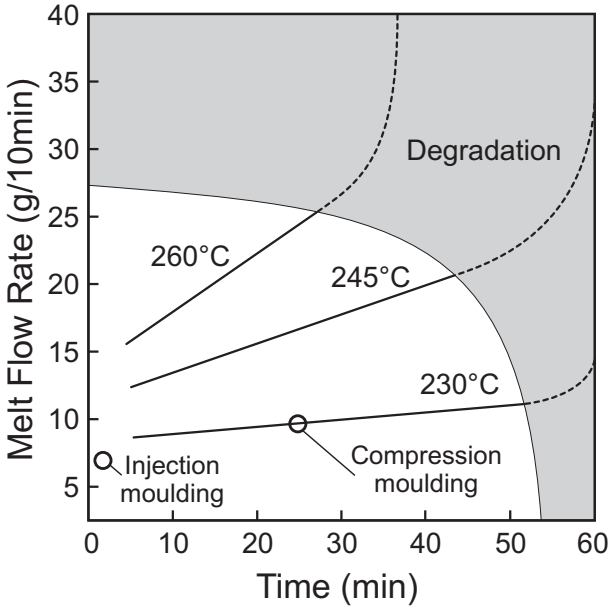

Fig. 2.11: Degradation of Hytrel during processing at different temperatures. Reproduced and adapted from [17].

2.3.5 Structure and phase segregation

Whilst other types of thermoplastic elastomers have been the subject of many studies, the polyester thermoplastic elastomers have not been investigated in the same detail on the nature of the phase segregation, /indexphase segregation the interactions between soft and hard segments, and the composition of domain boundaries. The first to investigate the microstructure of Hytrel using transmission electron microscopy has been Cella [9, 10]. Cella found from solvent cast films that the polymer exhibits a two-phase structure of continuous and interpenetrating crystalline and amorphous domains. He reports that the crystalline domains are lamellar in shape and approximately $100\mathring{A}$ in thickness and several thousand angströms in length, and that these crystalline lamellae are interconnected by short lengths of tie molecules. He also investigated compression-moulded specimens from replica electron micrographs, and reports that the crystallites are smaller, only $25 - 30\mathring{A}$ in width, with a similar morphology.

Zhu *et al* [62] reported that in isothermal crystallisation spherulitic structures were produced at low supercooling temperatures. Increasing the supercooling dramatically increased the nucleation rate. Samples produced by quenching in liquid nitrogen were clear, due to the lack of crystal structures. Subsequent annealing did not change the optical characteristics, indicating that the crystal structures formed were smaller than the wavelength of visible light, and hence that the nucleation density was extremely high. Zhu and Wegner [63] pointed out that the morphology of quenched samples was of a continuous network of lamellae rather than the spherulites observed in slow cooled samples.

Briber and Thomas [7] found using wide angle X-ray scattering (WAXS) and electron diffraction (ED) that the crystal structures are relatively pure and that some short hard segments are being rejected to the surfaces of these structures and into the soft segment matrix. They pointed out that the short hard segments can crystallise both at the edges of the crystals and within the soft amorphous matrix, although this can take several weeks to happen at room temperature.

Examination of a stretched polymer close to breaking point by Cella [10] revealed that the crystalline matrix becomes disrupted and both the crystal PTMT domains and the amorphous PTMEG-T domains become highly oriented in the draw direction. Cella states that orientation increases with elongation up to about 300% strain, beyond which little change in orientation takes place. The stretching of spherulitic structures into ellipsoids was also reported by Shen *et al* [54], who additionally state that no voids were found in the microstructure. Shen *et al* investigated the effect of thermal history on the microstructure, and showed that after annealing the features became more difficult to discern due to increases in the crystallinity and in the lamellar thicknesses. In addition, they observed that in a sample remelted and quenched all spherulitic structure was

destroyed.

Cella [9] also observed that T_g^{soft} increases with increasing percentage of hard segments in various Hytrel grades. He concludes from this that T_g^{soft} is increasing as a result of the non-complete phase segregation , and the presence of molecularly dispersed hard segments within the soft segment domains. He saw no crystallisation of the hard segments within the soft domains and states that these segments are probably too short to crystallise, due to the high viscosity and the possible chain entanglement.

Jelinski *et al* [29] have performed carbon-13 nuclear magnetic resonance (NMR) studies on four grades of Hytrel in order to characterize the molecular motions at the domain boundaries. They confirmed the finding of phase segregation in the polymer, and stated that there is negligible mixing of phases at the domain boundaries.

2.3.6 A model of the Hytrel microstructure

Cella first proposed a model for the unoriented structure of Hytrel as being made up of interconnected crystal regions, with soft segments spanning across the regions, and the occasional hard segment within the soft segment domains [9]. A schematic representation of the structure of Hytrel is presented in Fig. 2.12, based on Cella's original concept with some additions from the more recent literature. Shown on the diagram are the hard segment crystal domains Ⓐ that are interconnected Ⓔ. The amorphous regions Ⓑ are made up mostly of soft segments that span across different crystal domains Ⓒ, but also of trapped uncrystallised hard segments Ⓓ. Some short hard segments are uncrystallised on the border of the crystal domains Ⓕ, although these may also crystallise over time in the right conditions.

Slow-cooled Hytrel exhibits larger PTMT spherulitic crystal structures, linked together by shorter crystal lamellae, and surrounded by amorphous PTMEG-T regions.

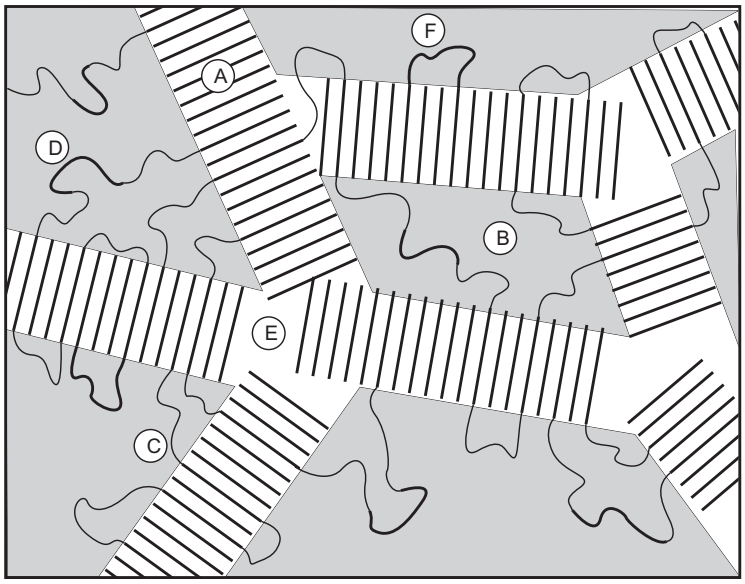

Fig. 2.12: Schematic representation of the microstructure of Hytrel.

Fast-cooled Hytrel has large numbers of small interconnected crystal lamellae with interdispersed amorphous regions. The overall crystallinity will depend on the overall thermal history. This model of the Hytrel microstructure is fundamental in understanding the different stages involved in the mechanical deformation of the material.

2.3.7 Mechanical properties

Limited data is available in the literature on the mechanical properties of the polymer, especially when considering the effects of thermal history and process-induced orientation. The DuPont documentation [16] gives stress-strain data for grade 4056 at different temperatures performed according to ASTM D 638 standards. No such stress-strain data is available for grade 4068 from which the inverting domes are made. Stress-strain tests have also been performed by Cella [10], by Henderson at low strains [22], and by Nishi *et al* [42] on various other grades of Hytrel. Nishi *et al* observed a small difference in the mechanical behaviour at high strains at different strain rates. Measurements of

stress-strain behaviour in highly oriented Hytrel filaments have been made by Richeson and Spruiell [48].

Data is also available from DuPont for the dynamic elastic modulus measured at low strain at different temperatures, again only for grade 4056. Dynamic elastic modulus measurements have also been made by Hourston and Hughes [27], Shen *et al* [54] and Nishi *et al* [41, 42] on various other Hytrel grades. A summary of the available data on the various relevant Hytrel grades is given in Table 2.2.

Cella [10] first qualitatively explained the stress-strain behaviour in terms of the microstructure of the material. The stress-strain response identified by Cella in a grade of Hytrel with a greater proportion of hard segment component than in Hytrel 4068 is shown in Fig. 2.13. The initial part of the deformation, region I, is characterised by a linear and quasi-linear response, due to the reversible deformation of the continuous crystalline matrix. This is what gives Hytrel a much higher elastic modulus, A on Fig. 2.13, than conventional elastomers. At these low strains the strain is largely recoverable, even though the response is dominated by the deformation of the hard segments and not the soft elastomeric segments. At larger strains, region II, the material's crystal matrix is irreversibly disrupted. The crystallites are orienting and strains in this region

Table 2.2: Mechanical properties of various Hytrel grades [16, 18].

Polymer	Elastic modulus at $23°C$	Tensile stress at break	Tensile strain at break	Density kgm^{-3}
Hytrel 4078	—	—	—	—
Hytrel 4068	55MPa	27.6MPa	600%	1110
Hytrel 4056	62MPa	28MPa	550%	1170

result in varying amounts of permanent deformation. The yield stress is marked as B on Fig. 2.13. At very large strains, region III, the polymer's behaviour resembles that of a cross-linked elastomer, with the increase in tangent modulus being due to the stretching of the elastomeric matrix. Eventually the soft elastomeric matrix fails and results in tensile break.

Cella found that increasing the proportion of hard segment in the polymer increased both the yield stress and the modulus. Since both the modulus and the yield stress are measures of deformation of the crystal structure, this behaviour is expected.

Cella observed morphological changes in samples that were loaded, unloaded and reloaded. The disruption to the crystal matrix is irreversible, and upon reloading the material exhibits stress-softening to the point at which it had been previously loaded. Loading then proceeds along the original stress-strain curve of a virgin sample.

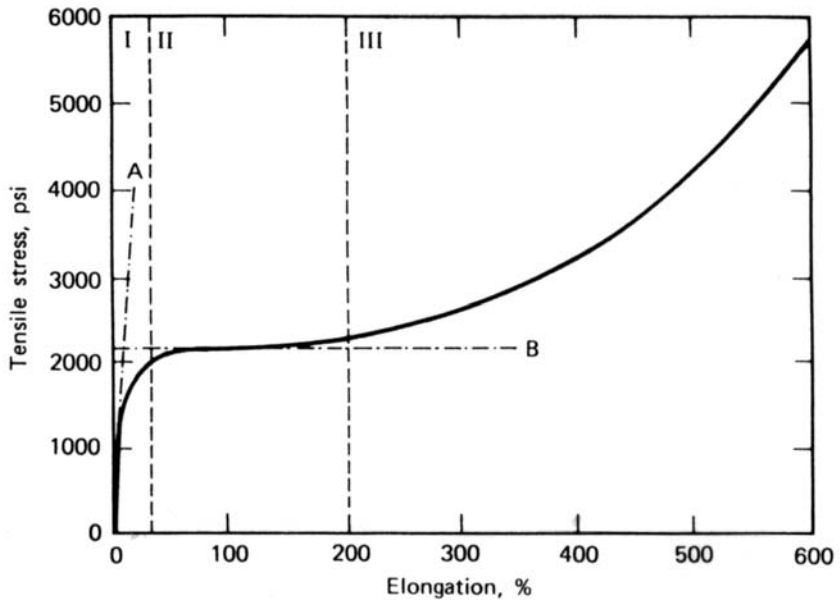

Fig. 2.13: Stress-strain response identified by Cella in a grade of Hytrel with 58% hard segment by weight [10].

2.3.8 Dynamic mechanical properties

The dynamic mechanical properties of various grades of Hytrel have been investigated by a number of authors at low strains using torsion pendulums [22, 27, 28, 42, 54]. Dynamic modulus and loss factor data is available for a variety of Hytrel grades including grade 4056 from DuPont [16], but not for grade 4068.

Empirical evidence has shown that in mainly glassy polymers it is possible to achieve a time-temperature superposition of the dynamic properties around the glass-transition temperature. Williams, Landel and Ferry [61] proposed that a shift in temperature could be related to a change in the behaviour at a different frequency, and that this temperature shift a_T would be given by

$$\log a_T = \log(\frac{\omega_s}{\omega}) \tag{2.1}$$

where ω_s is the frequency of testing of the dynamical data and ω is the frequency of interest. The time-temperature shift relies on linear viscoelasticity and in semicrystalline polymers this is a poor assumption. In addition, at room temperature Hytrel is not particularly close to either the glass-transition temperatures of its polymer components. Hence it is difficult to apply (2.1) to the torsion pendulum data available for Hytrel.

The dynamic modulus and loss factor measurements of Hourston and Hughes have relevance to the microstructure of Hytrel [28]. These authors measured the loss factor over a range of temperatures for Hytrel 4056 samples that had been quenched, and on samples that had been annealed, and found that the annealed samples showed a decrease in the loss factor, or poorer damping characteristics. This indicates that there is increased crystallinity of the hard segments on annealing.

2.3.9 Material failure

The failure of Hytrel has been investigated little in the literature. Cella [9, 10] explained that failure at ultimate tensile strains is due to the failure of the soft matrix. Nishi *et al* [41, 42] investigated the impact strength of blends of Hytrel and PVC, but do not comment on the impact strength of Hytrel alone.

Richeson and Spruiell [48] investigated highly oriented, drawn Hytrel 4056 filaments and observed elongations to break of $700 - 950\%$, around 1.5 times higher than the DuPont literature values for Hytrel 4056 of 550% [16]. The literature values for Hytrel 4068 have been given in Table 2.2.

DuPont literature is also available on the fatigue failure and resistance to flex cut growth that is more generally useful with standard Hytrel components; typical cycles are of the order of millions and failure is not observed at all in standard tests on Hytrel 4068 [16]. With the inverting dome, there is currently no intention to re-use the domes and it is the failure upon first use that is of concern. Thomas *et al* [56] measured the tear strength in Hytrel 4056 using a standard unnotched 90° test piece, and found that ductile failure occurs with a tear strength of about $100kJ/m^2$.

2.4 Summary

This chapter has presented the available literature on the inverting dome device and on the thermoplastic elastomer with which domes are made. The gas dynamics of the device have been reproduced using an x-t diagram, and the important shock waves identified in Section 2.1. A vent-hole has been introduced into the device in order to allow the gas to escape after actuation.

The development of the inverting dome has been presented, and the specifications of the currently used dome have been given in Section 2.2. There are indications that

the way in which the dome is currently clamped to the device is in need of improvement since dome slip increases uncertainty about the way in which it inverts, and makes obtaining repeatable experiments more difficult. Previous work on the trajectory of particles accelerated by a dome has been reviewed, and issues concerning the relationship between particle penetration and dome behaviour have been addressed in Section 2.2.4. The vertical component of velocity that a dome passes on to particles will ultimately influence the depth of penetration for a particular size and density of particles.

Section 2.3 has reviewed a large body of work on the thermoplastic elastomer Hytrel. Analysis of the chemistry, physics, structure and morphology of Hytrel has enabled an understanding of the effects of thermal history on the microstructure and the mechanical properties of the material. The crystal structure of the material is affected by the thermal history. Quenched samples that are allowed to crystallise have finer, smaller crystals than slow-cooled samples, where the crystal spherulites are larger and better defined. This information is useful in understanding how the properties of the polymer can be best obtained using, for instance, heat-treatments and pre-deformation. The relationship between mechanical properties and physical structure has been investigated using a range of literature. Available information on dynamic properties and material failure has also been reported.

Chapter 3

Material properties of Hytrel 4068

The previous chapter has reviewed a number of properties of the family of Hytrel polymers. This chapter will present a number of experimental techniques to investigate the material properties specific to Hytrel 4068. The preparation of samples is reported, and suitable bounds for isothermal and adiabatic experiments are obtained. Injection-moulded and compression-moulded samples are used in a variety of mechanical tests to investigate the stress-strain relationships, the effects of strain rate, of process-induced molecular orientation, of temperature, of thermal history, and of cyclic and load-unload-reload conditions.

The failure of the material will be investigated through trouser tear tests and burst tests.

3.1 Preparation for material testing

Injection-moulding has been used as the primary industrial production method for dome manufacturing. Compression-moulding, a variant of melt casting with added pressure is explored as an alternative. Two different microstructures are expected from injection-moulding and compression-moulding due to the dramatically different temperature histories experienced by the material, as reported in Section 2.3.5.

In order to reduce the risks of hydrolytic degradation at high temperatures and mois-

ture levels, the polymer is dried prior to any processing. Hytrel 4068 has an equilibrium moisture level after 24 hours of 0.7%. Recommended drying times are 2-3 hours in a dehumidified hopper drier, or 4-6 hours in an air-circulating oven in dry conditions. The drying temperature used is $110°C$. It is recommended to reduce the moisture content to below 0.1% before processing [17].

A dehumidified hopper drier was not available in Oxford at the time of this research, and pellets have been dried in a conventional air-circulating `LTE` oven and `Eurotherm` controller set to $110°C$. The drying time used is a minimum of 5 hours.

3.1.1 Injection-moulding

Injection-moulding of test samples and inverting domes has been performed using a `Butler 12/90V` injection moulder. It is a small machine by industrial standards, and due to the limited pressure available only relatively small components can be produced with this machine. The material is fed into the hopper, and the feed temperature is set at $198°C$. The temperature of the injection moulding tip is set at $225°C$. It was found that with these temperature settings it was possible to injection mould products to a reasonably good standard. Increasing the temperature further was causing flow of molten polymer out of the moulds, and reducing the temperature was causing poor quality areas in products. The mould itself is not heated, although it does warm slightly during use.

Samples and domes are produced in small batches, and usually the first 50 items are discarded due to poor quality. This lead-up time has the effect of gently heating the mould, although the temperature of the mould does not exceeds $40°C$ even at the end of an injection moulding run. Items can be produced at a rate of about 1 every 10-15 seconds using this moulder. At this rate and temperature it has been shown in

from Fig. 2.11 that there is no risk of material degradation coming from the moulding procedure. The cooling rate of injection-moulded samples is estimated to be of the order of $100°C/s$.

It is noted that injection-moulded products have a high degree of transparency immediately after moulding, but that they become opaque white after a few minutes at room temperature. This confirms the findings that the fast cooling rate of the injection-moulding does not allow for significant crystallisation during moulding, and that this occurs subsequently, at room temperature, over relatively long time scales.

3.1.2 Compression-moulding

In order to produce large and isotropic samples, not affected by the orientation that may be induced by the viscous flow in injection-moulding, sheets of Hytrel 4068 were manufactured by a compression-forming technique. A series of moulds are manufactured from stainless steel, shown in Fig. 3.1. The moulds are comprised of upper and lower square plates, typically $2mm$ in thickness and $200mm \times 200mm$ long sides, and a picture-frame mould of the required thickness and outer side $200mm$ and an inner cut-out square of side $150mm$. Prior to moulding, the steel parts are cleaned with acetone and sprayed with a PTFE dry spray lubricant to aid release after moulding.

The mould is filled with an amount of Hytrel pellets corresponding to the required volume. In order to allow for some material flushing out of the mould, an additional 10% of material by weight is added. The pellets are distributed evenly in the square, leaving a $5mm$ gap around the edges of the mould to prevent material flushing out of the mould too early.

The filled mould is then placed between the platens of a `Moore` hydraulic press with a capacity of 50 tons. The press platens can be heated by means of in-built heating

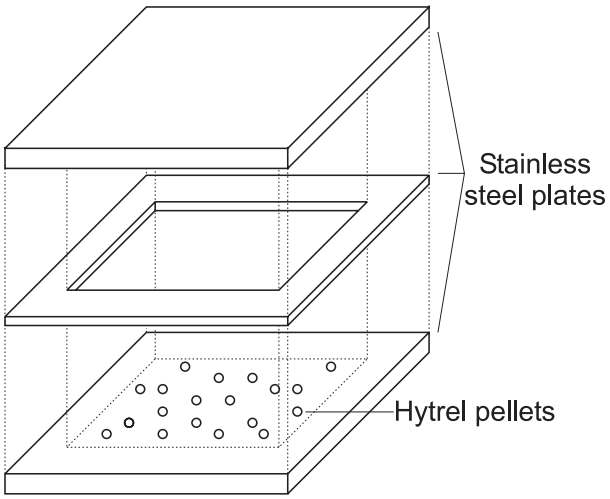

Fig. 3.1: Compression-moulding picture-frame arrangement used to produce Hytrel sheet material.

elements and can also be cooled using compressed air and water flowing in appropriate channels. The press is pre-heated to $230°C$. The mould takes approximately 10-15 minutes to reach the moulding temperature. A force of 2 tons is then applied on the mould, and cycled on and off 5 times to try to dislodge any air bubbles that might be present. The force is increased in steps of 2 tons through to 10 tons with 5 cycles of the pressure on and off at each step. The force is then left on 10 tons. The cycling procedure takes approximately 10 minutes, and is reasonably effective at removing air bubbles in the sheet material. The mould is then cooled using air and water. The cooling rate has been varied to attempt to capture differences in the material properties due to different cooling rates. The standard cooling procedure used for most samples is the application of air for approximately 1 minute, and of water for the remaining 10-15 minutes required to cool the platens to room temperature. The mould can be safely removed once the temperature has dropped below $60°C$, typically after 10 minutes. In this case, the cooling rate is estimated to be approximately $0.3°C/s$.

The mould is opened after cooling, and the sheet material can be peeled off the

stainless steel plates. This procedure is not always straightforward, with Hytrel sticking to the plates even with the application of the PTFE release agent.

Material is produced in three additional ways in order to vary the microstructure of the sample. This is achieved by altering the thermal history in the sample after pressing. *Quenched* sheets are produced by placing the mould in cold water straight from the press at $230°C$, although the sheet quality is reduced due to the lack of pressure on cooling. Here the cooling rate is estimated to be in the range of $10-50°C/s$, and should be closer to injection-moulded products in terms of the microstructure determined by the cooling rate. *Slow-cooled* sheets are produced by programming a cooling ramp on the press plates with a cooling rate of $0.02°C/s$. Sheet produced by this method have a darker colouring, possibly due to some material degradation taking place. *Annealed* sheets are produced using the standard cooling procedure, but with subsequent annealing at $110°C$ for 24 hours. Compression-moulded products are always opaque white, indicating that large crystallites have formed during moulding.

3.1.3 Test conditions

The tensile and compressive tests are performed on an `Instron 4204` test machine with an environmental chamber. The test machine allows a variable cross-head speed from $0.05mm/min$ to $500mm/min$. For practical reasons testing needs to be as fast as possible, but in order to achieve a good quality isothermal test, there will be an upper limit on the allowable test speed. A thorough account of the issues involved in testing elastomeric materials is given by Buckley [8], and his method is used here to evaluate suitable testing conditions.

In order to ensure that any stress measurements are uniform during testing, inertial forces must not be present, and the material must be in mechanical equilibrium. Buckley

proposes that at least 10 wave reflections should be allowed for to achieve equilibrium [8]. The longitudinal stress wave velocity in a solid, v_{stress} is given by

$$v_{stress} = \sqrt{E/\rho} \tag{3.1}$$

where E is the modulus of elasticity and ρ is the density. Using nominal values of $E = 55MPa$ and $\rho = 1110kgm^{-3}$ [18], the stress wave velocity is approximately $220ms^{-1}$. Hourston and Hughes [28] measured the sonic velocity in quenched Hytrel 4056 as $220ms^{-1}$ and in annealed Hytrel 4056 as $240ms^{-1}$, indicating either a change in modulus, in density, or in both. Assuming a specimen gauge length of approximately $30mm$, the time taken for 10 wave reflections along the specimens is approximately $t^{10}_{wave} = 1ms$. If we aim for a strain resolution of the order of 1% and maximum strains ϵ_{max} of approximately 500%, the smallest measurable strain increment is $\epsilon_{inc} = 0.05$. Since there must be at least t^{10}_{wave} time elapsing between each measurement, test strain rates $\dot{\epsilon}$ must be

$$\dot{\epsilon} < \frac{\epsilon_{inc}}{t^{10}_{wave}} = \frac{0.05}{0.001} = 50s^{-1} \tag{3.2}$$

In order to ensure isothermal testing conditions, and assuming that temperature equilibrium has been ensured prior to the start of any test, there must be sufficient time for the specimen to dissipate any heat that is generated during the test. The generated heat must diffuse through the specimen by conduction, and away from the specimen by convection. Dissipation of heat by radiation is usually small and is neglected here. Assuming a specimen of thickness d, width w and length l, the rate of heat loss is $\dot{Q}$ is given by

$$\dot{Q} = -\rho C \dot{T} dwl \tag{3.3}$$

where C is the specific heat capacity and $\dot{T}$ is the rate of temperature change. $\dot{Q}$ must be equal to the heat flow through the specimen. The shortest distance the heat must flow through is $d/2$, or half the thickness. Assuming a constant temperature gradient, conduction through each half of the specimen is governed by

$$\dot{Q}_{half} = \frac{\lambda wl}{\frac{d}{2}}(T - T_e) \tag{3.4}$$

where λ is the thermal conductivity, T is the temperature variable and T_e is the temperature of the environment. Taking only half of the specimen and rearranging (3.3) and (3.4) gives the linear first order differential equation

$$\dot{T}\left(\frac{\rho C d^2}{4\lambda}\right) + T = T_e \tag{3.5}$$

with characteristic time constant τ_{cond} equal to

$$\tau_{cond} = \frac{\rho C d^2}{4\lambda} \tag{3.6}$$

The time constant is indicative of the time taken for a transient process to decay to about 37% of its initial value. Although equation 3.5 uses a simplification of the real temperature distribution, it is dimensionally correct and sufficient for yielding an approximate value of the time constant.

The DuPont literature gives values for $\lambda = 0.190 W m^{-1} K^{-1}$ at room temperature and $C = 1.75 kJ kg^{-1} K^{-1}$ at $20°C$ [16]. Specimen thickness is typically of $d = 1mm$, and thus the time constant τ_{cond} is approximately 25 seconds.

The same heat must also be dissipated away from the specimen by convection. Using Newton's law of cooling, the rate of heat lost by natural convection through the two large faces of the specimen (defined by w and l) is

$$\dot{Q} = 2wlh(T - T_e) \tag{3.7}$$

where h is the heat transfer coefficient, in units of $Wm^{-2}K^{-1}$, usually found by experiment. Using (3.4) and (3.7) and rearranging we obtain

$$\dot{T}\left(\frac{\rho C d}{2h}\right) + T = T_e \tag{3.8}$$

with characteristic time constant τ_{conv} equal to

$$\tau_{conv} = \frac{\rho C d}{2h} \tag{3.9}$$

A typical value of h is $10Wm^{-2}K^{-1}$ [8]. The time constant is thus approximately 100 seconds. Hence it is the convection that is the slower of the two processes, and the most critical as far as achieving isothermal testing conditions is concerned.

During testing it must be ensured that the heat produced by the deformation of the specimen, $\dot{Q}_s$, is limited to an amount that can be diffused by convection,

$$\dot{Q}_s < \frac{c\Delta T_{tol}\rho wld}{\tau_{conv}} \tag{3.10}$$

where the temperature tolerance allowed in tests is ΔT_{tol}. The maximum energy given to the specimen during a test by the test machine is

$$\dot{Q}_s = \sigma_n \dot{\epsilon} wld \tag{3.11}$$

where σ_n is the nominal stress and $\dot{\epsilon}$ is the strain rate. Hence, for an isothermal test the strain rate must be

$$\dot{\epsilon} < \frac{\rho C \Delta T_{tol}}{\sigma_n \tau_{conv}} \tag{3.12}$$

The nominal stress in Hytrel 4068 tests can reach $25MPa$ and for a temperature tolerance of $\pm 2°C$ the strain rate must be $\dot{\epsilon} < 1.5 \times 10^{-3} s^{-1}$. This calculation is conservative since it does not account for the large increase in the surfaces due to stretching that are present in elastomers, and in practice it is likely that slightly faster strain rates can be used for testing while still keeping the specimen under isothermal conditions. This will be verified by temperature measurements on samples during tests at different strain rates in Section 3.3.4.

In order to achieve adiabatic conditions, the test time t_{test} must be much less than τ_{cond}, the faster of the two processes. For typical tests to 500% strain, the strain rate must therefore be $\dot{\epsilon} \gg 0.2 s^{-1}$. Stress-strain data in the adiabatic range could be obtained using high-speed testing machines or with a split Hopkinson bar technique. The strain rates experienced by the inverting dome during inversion are expected to be in the adiabatic range. The range of acceptable test conditions is shown in Fig. 3.2.

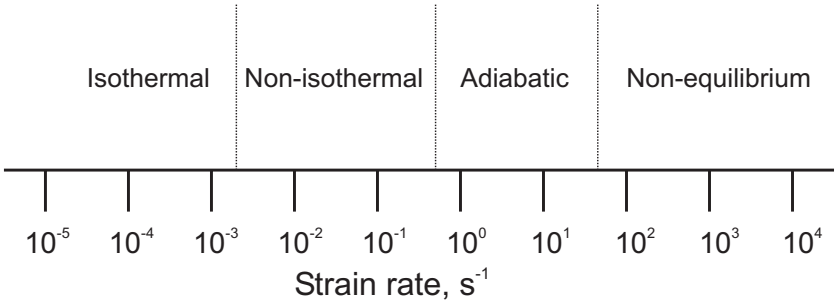

Fig. 3.2: The strain rate space for the testing of Hytrel, and the conditions of specimens being tested at these rates.

3.2 Injection-moulded samples

A range of samples have been produced for tensile and compressive testing using the `Butler 12/90V` injection moulder. These samples are produced in a similar way to the injection-moulded inverting domes, and as such are expected to have a similar thermal history. Dog-bone specimens with a long, straight section, and thin disc specimens are produced. Comparison of these two specimens is likely to yield clues as to whether the processing induces anisotropy in the material, and how significant we can expect the anisotropy to be in the inverting domes. Button specimens are produced for compression-moulding.

One drawback of using injection-moulded samples for testing is that the maximum sample size is limited by the injection-moulder's pressure, and since only small samples can be produced, it is difficult to use standard test fittings and extensometers in testing.

3.2.1 Dog-bone samples

A dog-bone specimen mould has been designed to produce tensile specimens for testing. The specimen is smaller than typical test specimens due to the limitations in product size of the injection moulder. The specifications of the specimen are shown in Fig. 3.3. The moulding gate is situated off one of the grip regions, in the direction of the straight test piece.

The specimens are tested in tension on an `Instron 4204` with custom-made grips. A pin is placed through the grips and through the holes in the specimen to identify any slip out of the grips. Unfortunately the reduced size of the specimens has not permitted the fitting of a strain-measuring gauge on the actual samples, and as such only the grip displacement is available for processing. The force and displacement at the grips are recorded.

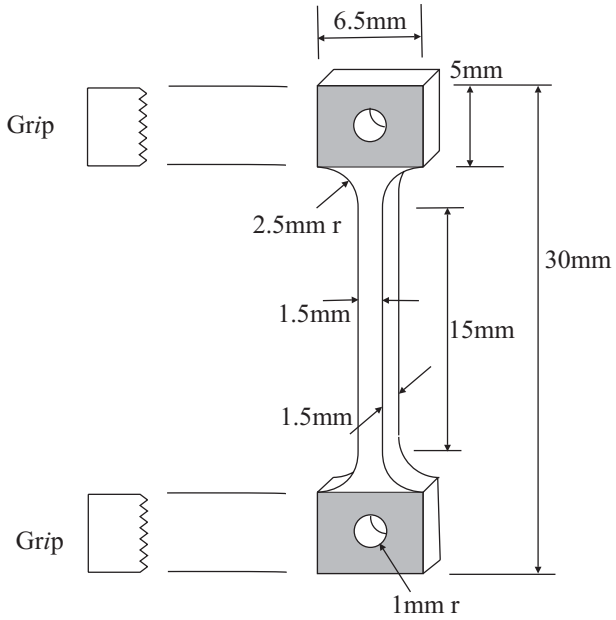

Fig. 3.3: Specifications of the dog-bone shaped tensile test specimen, injection-moulded.

The specimens are tested with a cross-head speed of $50mm/min$ which corresponds to a nominal strain rate of $0.042s^{-1}$ for a grip separation of $20mm$. Although this strain rate appears too fast for isothermal conditions, the tests of Section 3.3.4 indicate that this rate is likely to be within acceptable bounds. A total of 10 samples are tested at room temperature, measured on the day of testing to be $22°C$. Micrometer measurements of the width of the central portion, and the thickness throughout, are made for each specimen.

Due to the unavailability of extensometer strain data and the non-linear stress-strain curve, as well as the non-uniform sample cross-section, a procedure is developed for reconstructing the stress-strain data. The procedure assumes the stress-strain data to be piecewise linear between recorded data points, and integrates over the sample for each data point to find the strain. Details of the procedure are given in Appendix A. The reconstructed stress-strain data for the 10 samples is shown in Fig. 3.4. The data is considered valid only to 400% strain due to the difficulties encountered with the small

gripping area and slip at the custom-made grips. Beyond 600% the slip is visible in some curves as excess apparent strain.

The data shows a good level of consistency in the early part of the curve, up to $100 - 200\%$. The small discrepancy is likely to be due to non-uniform samples where the thickness and width measurements are not representative of the entire sample.

Some of the specimens failed around 650% by tearing at the grips. This is not considered as the ultimate tensile strain , as the failure was induced by the geometry of the gripping area, and did not occur in the thin part of the specimen being tested. Other specimens did not fail at the grips, but in the uniform section at beyond 800% strain. Fig. 3.5 shows the original specimen, and two specimens after testing, one of which is torn at the hole in the grip region.

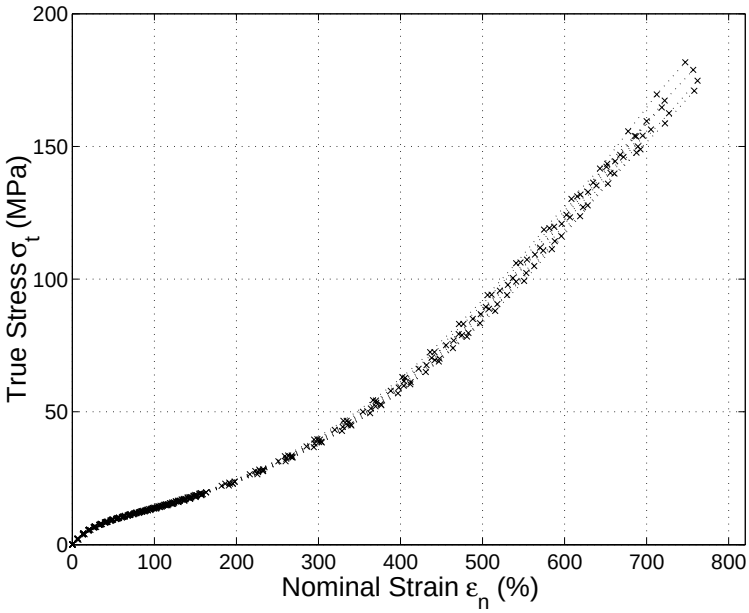

Fig. 3.4: Stress-strain data obtained from the injection-moulded dog-bone samples, reconstructed using the method described in Appendix A.

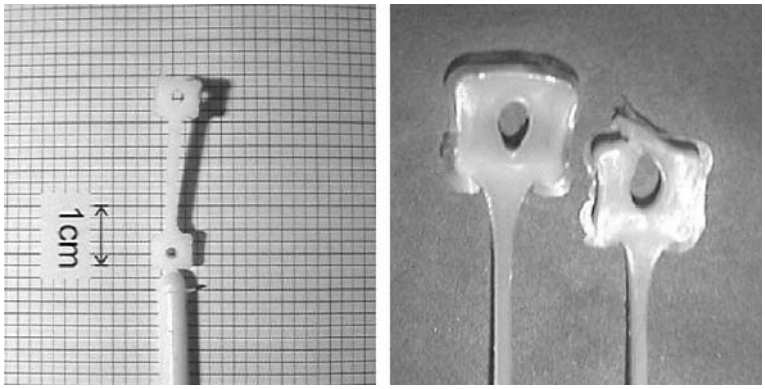

Fig. 3.5: An injection-moulded dog-bone specimen used in tensile testing, and the ends of two tested specimens, one of which is torn at the hole.

3.2.2 Disc samples

A mould is produced to injection-mould thin circular discs in order to investigate the anisotropy induced into the material by the process of injection moulding. The specimens are injection-moulded from the edge of the disc, and subsequently cut in three different orientations. The specifications of the disc mould and the sample after cutting are shown in Fig. 3.6.

An attempt has been made at moulding specimens for testing in smaller thicknesses, in order to simulate the dome's dimensions and nominal thickness of 0.5mm. However, due to the size and shape of the specimen required for testing and the limits posed by the

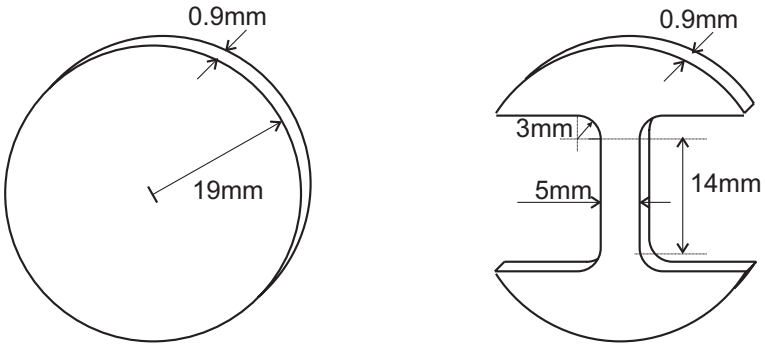

Fig. 3.6: Specifications of the injection-moulded disc, and the sample after cutting with the help of a metal template.

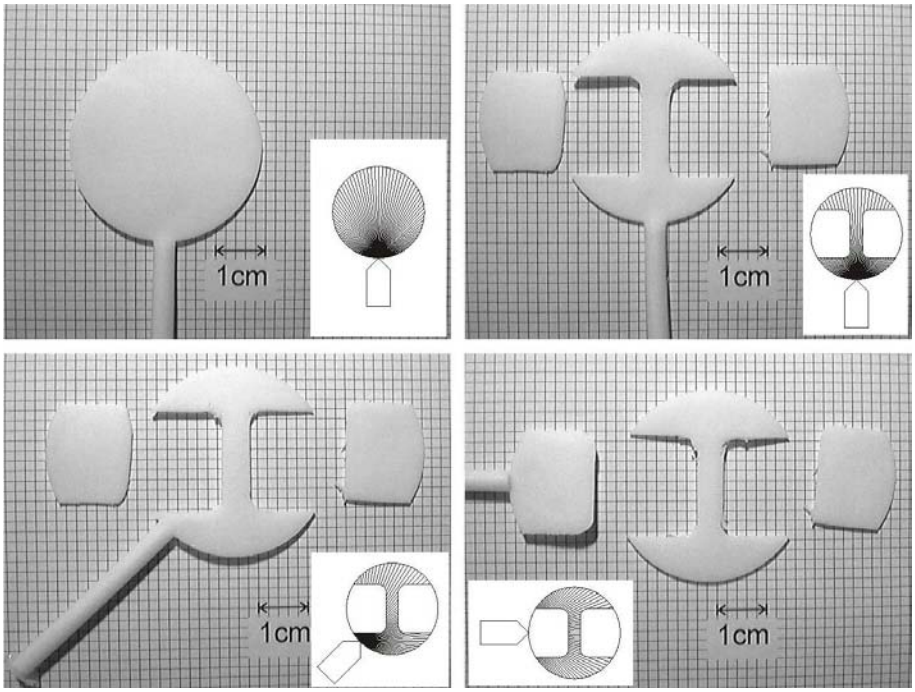

Fig. 3.7: The injection-moulded disc specimen, and the cut specimens, showing the three orientations, shown with a representation of the sort of material orientation that may be present in samples cut in different orientations to the injection-moulding direction.

small injection-moulder, thinner specimens did not manage to fill the mould completely and thicker moulds have had to be used. The 0.9mm thick specimens that managed to consistently fill the mould are cut into the typical testing dog-bone shape shown in Fig. 3.7. The flow pattern of the melt into the mould is a complex matter, and it is likely to be sensitive to small changes in thickness in the mould. In order to depict the effect of process-induced material orientation that may be present, the specimens are shown in sketches with the alignment of the material shown as radial lines emitted from the injection-moulding gate in Fig. 3.7.

The specimens are tested in a similar manner to the dog-bone specimens of the previous section, through to 800% strain. The temperature on the day of testing was $23°C$. Standard pneumatic grips are used to hold the specimen, but no extensometer has been used due to the small size. 6 specimens are tested for each of the orientations.

The cross-head speed is set at $5mm/min$ corresponding to a nominal strain rate of $0.0042s^{-1}$ which is expected to give isothermal conditions. The force and displacement at the grips are recorded.

As before, micrometer measurements are made to record the actual thickness of the specimens, although due to the flexibility of the thin sheets, no reliable measurement was possible of the width of the specimens. The width is assumed to be $5mm$, and the tapers are assumed to be as shown in Fig. 3.6. The same technique as in Section 3.2.1 is used to obtain the stress-strain curves from the grip displacement.

The stress-strain data for the three orientations is shown in Fig. 3.8. It shows a reasonable level of consistency, although there is some overlap in the curves from different specimen orientations. This is expected due to the complex nature of the injection-moulding. Overall only a small difference between the orientations is present up to $100-150\%$ strain. At larger strains the difference in stress at a given strain is more significant, with stress measurements ranging from $80MPa$ to $110MPa$ at 600% strain.

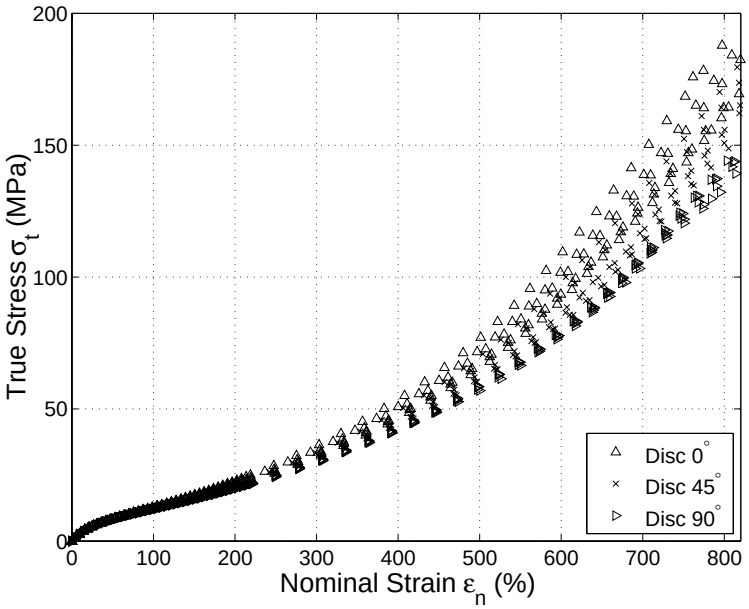

Fig. 3.8: Stress-strain data for the samples cut from discs at three different orientations.

The samples cut along the injection-moulding axis appear to be stiffer and to stiffen faster than the samples cut perpendicular to the axis. This magnitude of difference in behaviour can be expected in different parts of the inverting dome, although the actual distribution is likely to be more complex due to the dome's 3-dimensional geometry. A larger gripping area is present on these samples and no slip was detected.

3.2.3 Compression button samples

A mould is designed to produce button specimens by injection-moulding for compressive testing. The specimens are cylindrical, $6mm$ in diameter, and $6mm$ in thickness, and the injection-moulding gate is placed midway along the side of the specimen. The specimen is shown in Fig. 3.9(a). The specimens are tested in groups of 7, in the configuration shown in Fig. 3.9(b), compressed by two custom-made greased brass plates. This method of testing is far from ideal, but has had to be employed in order to reduce the effect of the compression plates not being perfectly parallel. The temperature on the day of testing was $19°C$.

Three batches of 7 specimens are tested, the first batch at a crosshead speed of

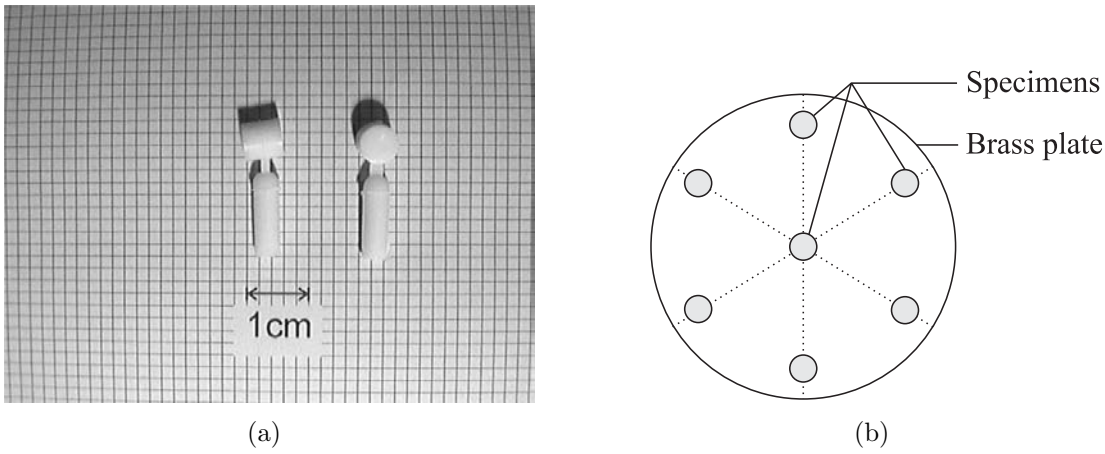

(a) (b)

Fig. 3.9: Button specimens used in compression testing (a) and the loading arrangement (b).

1mm/min, the second at 10mm/min and the third at 100mm/min; these test speeds correspond to nominal strain rates of $0.014s^{-1}$, $0.14s^{-1}$ and $1.4s^{-1}$ respectively.

The testing machine takes a short time to accelerate to the test speed, and this is most noticeable at higher crosshead speeds. The specimens are tested through to 65% compressive strain. Although the plates are greased before each test, there is some evidence of *barrelling*. The effect is due to the friction between the specimen and the plates, and results in a more complex stress state than the uniaxial compression desired. The barrelling effect is visibly noticeable above 30% compressive strain.

In this data set the displacement of the anvil plates corresponds to the displacement of the sample directly, and the nominal strain can be evaluated simply by dividing the displacement by the samples' length. The stress-strain data for the three test speeds is shown in Fig. 3.10.

The three tests show little difference in the behaviour across this range of strain rates until about 10% compressive strain. The fastest strain rate shows a slightly stiffer

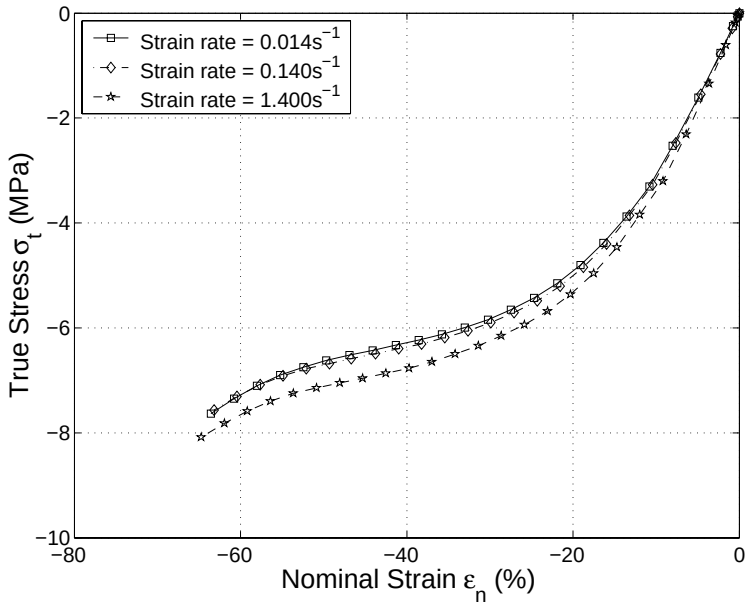

Fig. 3.10: Stress-strain data from the button compression specimens, shown at three test speeds.

behaviour than the slower rates. The difference is not large, even at higher strains. It is noted that anisotropy is expected in the specimens, but its effect is difficult to quantify.

3.2.4 Comparison of data from injection-moulded samples

Fig. 3.11 shows the stress-strain data obtained from the dog-bone specimens, the disc specimens, and the button compression specimens all on the same set of axes. The extent of the anisotropy can be seen in the range of stress-strain data from the dog-bone and disc specimens at a given strain.

There is relatively little change in the stress in the samples tested across the range from -10% to 150% strain. This is the expected range of deformation of the inverting dome, and it is reassuring to see that any anisotropy from injection-moulding is unlikely to play a significant role in injection-moulded domes. Unfortunately it is not possible to compare samples from this data at a fixed strain rate.

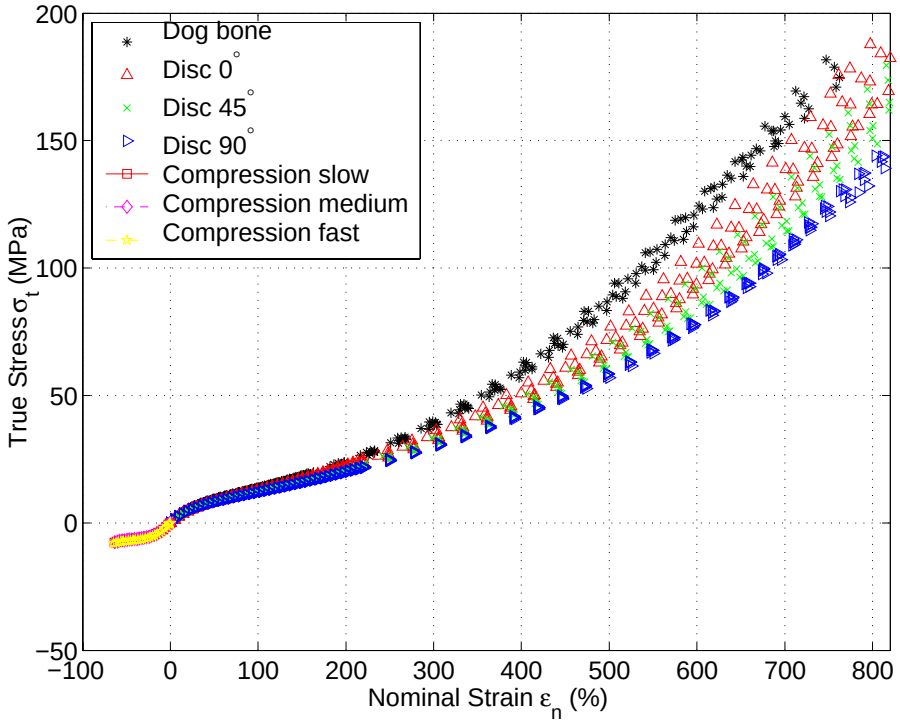

Fig. 3.11: Stress-strain data from three injection-moulded test conditions.

3.2.5 Flow pattern in injection-moulded discs

In order to investigate the flow pattern of material in the injection-moulded discs, and to attempt to understand the process-induced orientation that may be present in the discs, a number of discs are viewed under polarised light. The discs are placed behind a screen with a hole slightly smaller than the discs themselves and a linear polariser is held between a light source and the disc. In order to increase the transparency of the discs they are held in liquid nitrogen between injection-moulding and imaging. Five such images are shown in Fig. 3.12.

There is evidence of a non-uniform flow pattern in the discs that is probably due to small changes in thickness through the discs, and although the pattern is similar in the discs there are small differences across the range. A single disc is viewed using an optical microscope and a linear polariser, and the most evident features of the flow are reproduced in Fig. 3.13.

Near the centre of the disc there appears to be process-induced orientation due to shearing of the viscous melt, and this takes an anticlockwise curved path. Near the edges of the disc there is significant evidence of orientation, although the effects at the edges are less relevant in the mechanical tests since these tests are only concerned with the central portion of the disc.

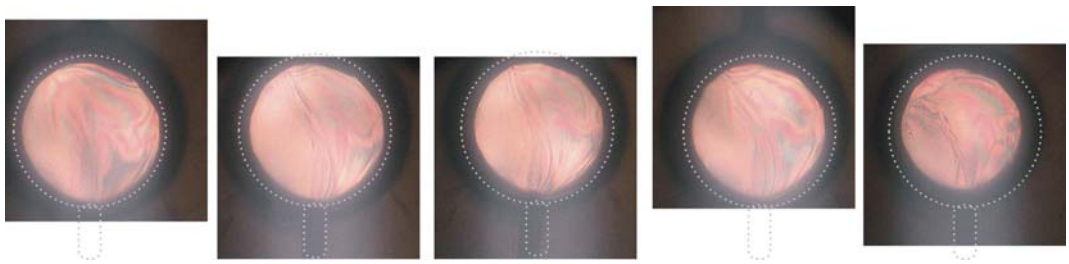

Fig. 3.12: Five injection-moulded discs viewed through polarised light. The dimensions of the disc and the position of the injection-moulding gate is shown with a dotted line.

Fig. 3.13: Series of polarised images from a single injection-moulded disc viewed under an optical microscope.

3.3 Compression moulded samples

Samples produced with the injection moulder have shown a small amount of process-induced anisotropy, and it is useful to test isotropic samples for comparison. In addition, the cooling rate seen by samples in the injection-moulder is fast, and observations on the effect of cooling rate can give additional insight into the microstructure of the material. For these reasons, a number of test samples are cut from compression-moulded sheet material produced with the technique described in Section 3.1.2 in order to achieve samples that are as close as possible to being isotropic. The specimens are cut using a custom-made jig holding two single-bevelled blades parallel to each other and a fixed distance

apart. The samples are taken from material nominally $0.5mm$ thick, manufactured using the standard cooling rate described in Section 3.1.2 corresponding to approximately $0.3°C/s$ and are cut to a nominal width of $5mm$ and a length of $75mm$. Since these samples are larger, an `Instron` elastomer extensometer can be used for direct strain measurements in room temperature tests.

Prior to testing, micrometer measurements are made of the sample thickness, and samples are weighed on a balance accurate to $\pm 1\mu g$. The mass is used to obtain a value for the sample width, which is difficult to measure directly due to the flexibility of the samples.

3.3.1 Ambient temperature load-unload tests at different strain rates

Samples are tested using the `Instron 4204` at room temperature, measured as $21°C$ on the day of testing. Cross-head speeds of $0.5mm/min$, $5mm/min$, $50mm/min$ and $500mm/min$, corresponding to strain rates of $0.00017s^{-1}$, $0.0017s^{-1}$, $0.017s^{-1}$ and $0.17s^{-1}$ respectively, are used. Samples are loaded and unloaded to maximum strains of 25%, 50%, 100%, 200%, 400% and 600%. A gauge length of $50mm$ is used, and the elastomer extensometer is set to measure strain in the central $25mm$ of the sample. The elastomer extensometer is a counterbalanced travelling extensometer able to cope with the large deformations present in materials such as Hytrel. The samples are unloaded in order to measure the residual strain due to permanent deformation, as well as to help in the understanding of the mechanism of deformation of the material.

The true stress - nominal strain curves obtained are shown in Fig. 3.14. There is an anomalous curve on the $0.00017s^{-1}$ graph, loaded to 400% strain, possibly due to a trapped air bubble in the specimen that was not spotted. Apart from this anomaly,

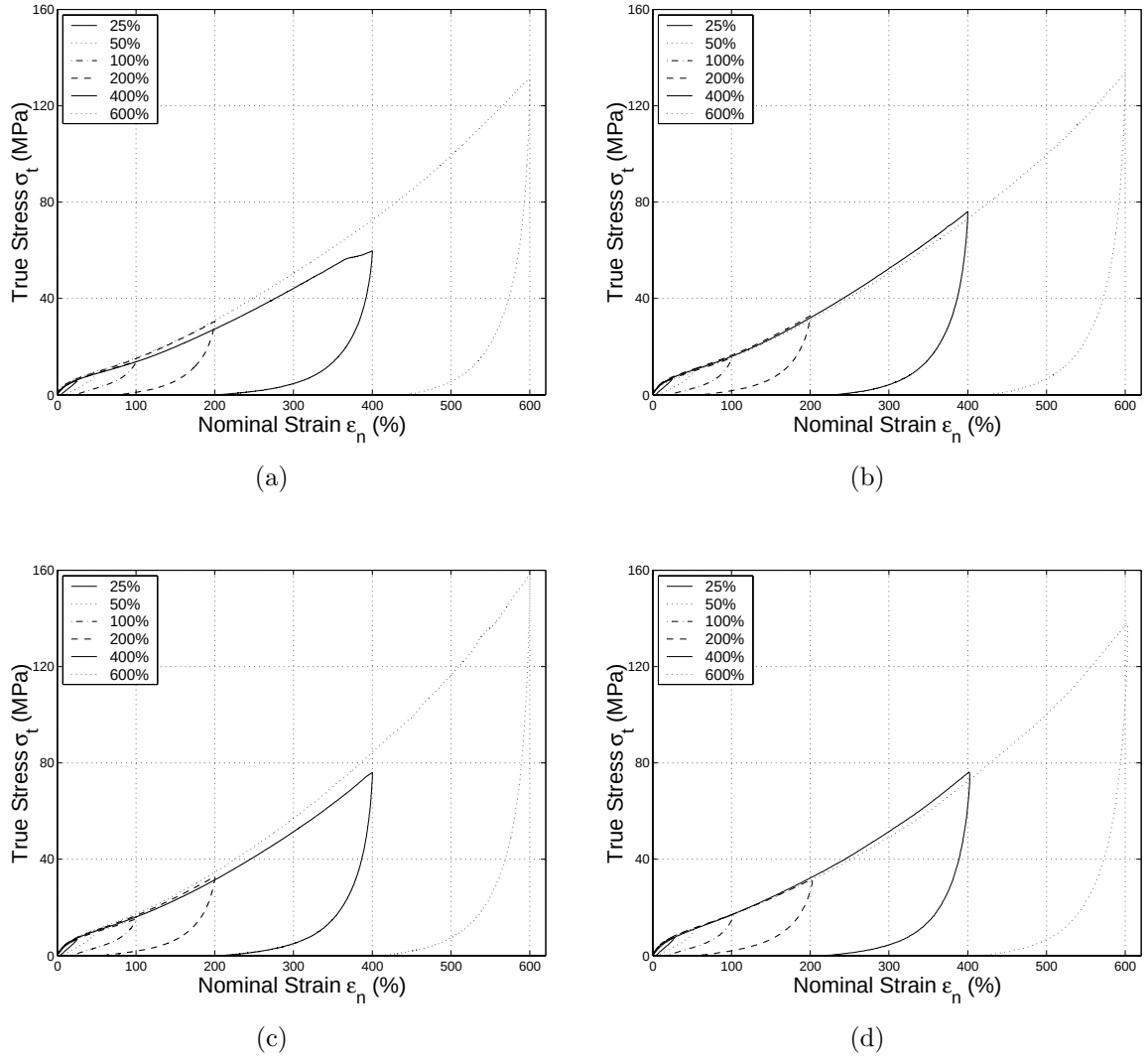

Fig. 3.14: Loading and unloading stress-strain curves from isotropic samples at strain rates of (a) $0.00017s^{-1}$, (b) $0.0017s^{-1}$, (c) $0.017s^{-1}$, and (d) and $0.17s^{-1}$.

the curves show a reasonably good level of consistency in the regions of loading where they overlap. The difference in behaviour is expected to be largely due to non-uniform specimen dimensions.

3.3.2 Tests on materials with different thermal histories

A second series of tests are performed on Hytrel 4068 compression-moulded sheets with different thermal histories , produced as described in Section 3.1.2. A quenched sheet, with an approximate cooling rate of $10-50°C/s$, a standard sheet, with a cooling rate of

approximately $0.3°C/s$, an annealed sheet produced from a standard sheet and annealed at $110°C$ for 24 hours, and a slow-cooled sheet with a cooling rate of $0.02°C/s$ are used in the tests [1].

The samples are tested at room temperature, measured as $20°C$ on the day of testing. A cross-head speed of $50mm/min$ is used, corresponding to a nominal strain rate of $0.017s^{-1}$. The samples are loaded and unloaded to 400% strain. An elastomer extensometer is used for strain measurement.

The stress-strain data is shown in Fig. 3.15. The three repeats from each sheet show a very good level of repeatability, and a distinct difference in behaviour can be seen between the different thermal histories. One of the annealed sampled fractured mid-way through the test by tearing at the grips.

The quenched samples are the least stiff of the samples, followed by the standard sheet, the annealed sheet, and the slow-cooled sheet. This is thought to be an effect of the degree of crystallinity in the hard phase. The slow-cooled sample is likely to have a higher

[1] This series of tests is performed in collaboration with Michael Blundred of the Oxford University Engineering Department.

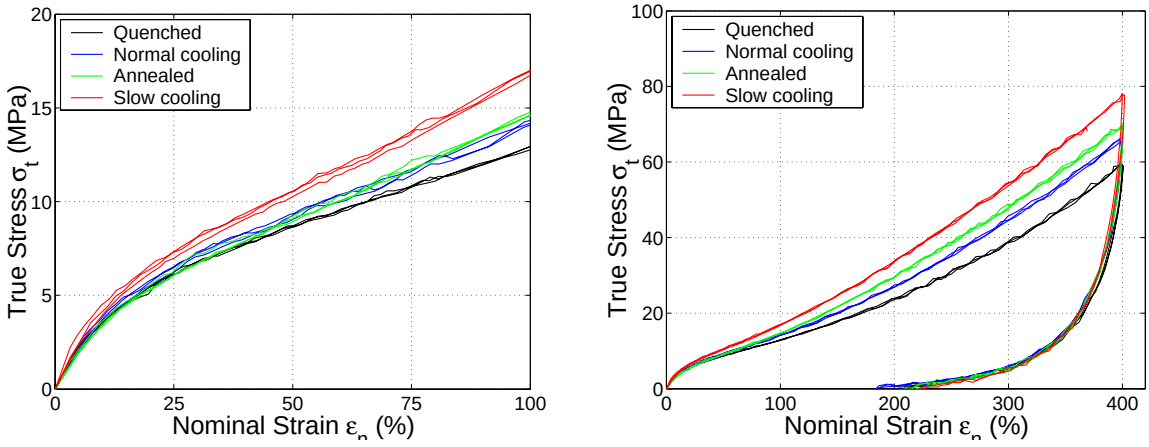

(a) (b)

Fig. 3.15: Stress-strain curves from isotropic samples with different thermal histories tested to a maximum strain of (a) 100% and (b) 400%.

degree of crystallinity as well as larger and stiffer crystal spherulites. The annealed sample is annealed at a temperature likely to be near the crystallisation temperature of the hard phase and is expected to have increased crystallisation. The standard sample is cooled relatively slowly compared with injection-moulded samples, and is still expected to have large spherulitic structures, although smaller than in the slow-cooled sample. The quenched sample has a cooling rate that is closer to that of injection-moulded samples, and is more likely to have a large number of small interconnected crystal structures, as well as a lower overall degree of crystallinity.

Additionally it can be seen that while the quenched sample is less stiff to begin with, it appears to strain harden as further strain is applied. This can be seen by the increase in the gradient at higher strains. This increase in the gradient is less significant in the other samples. This could be a result of strain-induced crystallisation. The level of crystallisation in the sample may be lower to begin with compared with the other samples, and as plastic strain is induced, molecules are given the energy needed to rearrange. Some crystallisation could take place during the test due to the change in geometry and the plastic deformation. In the other samples, the initial crystallisation is greater, and could even be dropping as a result of the plastic deformation.

We know that there is extensive plastic deformation since the samples only recover to approximately 200% strain. In unloading, all of the samples are very similar, with no obvious differences being visible in the data.

3.3.3 Tests over a wide temperature range

In order to shed light on the mechanical behaviour of Hytrel, a series of tests are performed on samples cut from isotropic compression-moulded sheet, as in the previous section, at a range of temperatures from $20°C$ through to $160°C$. Samples are tested us-

ing the `Instron 4204` test machine fitted with an environmental chamber [2]. The strain measurements are made using a non-contact video extensometer that tracks the movement of two horizontal lines drawn across the specimen, drawn approximately $10mm$ apart in the centre of the specimens. The specimens are tested at a cross-head speed of $50mm/min$ with a gauge length of $50mm$, corresponding to a strain rate of $0.017s^{-1}$, to a maximum strain of 400%.

The stress-strain data for these tests is shown in Fig. 3.16. The curve at $120°C$ does not have a complete data set because the video extensometer lost track of the lines. The data sets fluctuate more than the data obtained with the elastomer extensometer due to the video extensometer's recording of the strain - the lines drawn on the specimen become faint wide bands at larger strains, and become difficult to follow. In addition, the environmental chamber fan causes some flutter in the specimen, especially at low strains, which renders recording more difficult.

A plot of the true stress against temperature at different stretch levels is shown in

[2]This series of tests is performed in collaboration with Michael Blundred of the Oxford University Engineering Department.

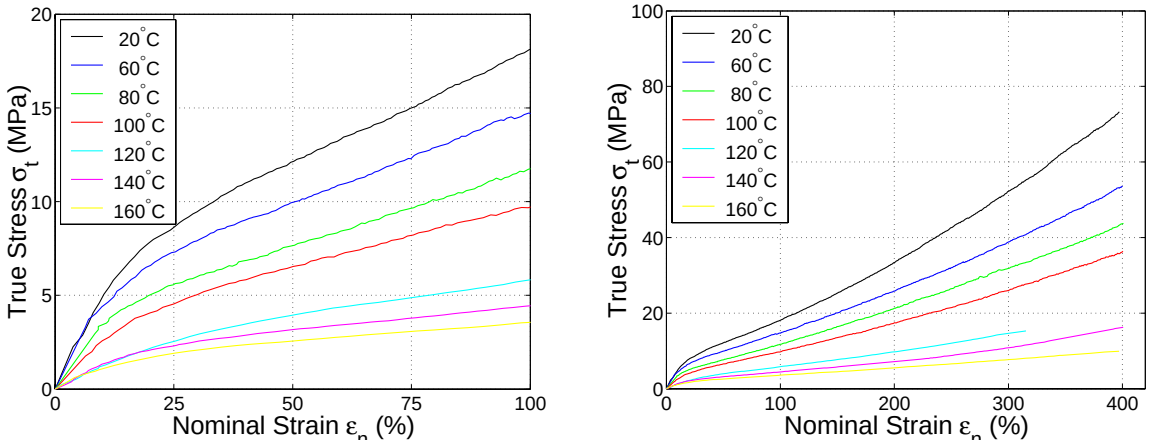

(a) (b)

Fig. 3.16: Stress-strain curves from isotropic samples at temperatures from $20°C$ to $160°C$ to a maximum strain of (a) 100% and (b) 400%.

Fig. 3.17. Here it is possible to see a noticeable drop in stress levels between $100°C$ and $120°C$ likely to be due to the effect of the glass-transition temperature of the hard blocks occurring across this temperature range. T_g^{hard} for Hytrel 4056 has been located at around $80°C$ by Hourston and Hughes [27].

3.3.4 Temperature-monitored tests

A small number of tests are performed in order to check the assumptions of isothermal conditions made in Section 3.1.3, and to investigate the thermal behaviour under stress of Hytrel 4068 [3]. Samples are cut from isotropic compression-moulded sheet as in the previous sections, and a fast response thermocouple is inserted in a small cut made in a direction parallel to the test direction in the centre of the sample. The temperature is monitored using data logging equipment. Ambient temperature measured on the day

[3]This series of tests is performed in collaboration with Michael Blundred of the Oxford University Engineering Department.

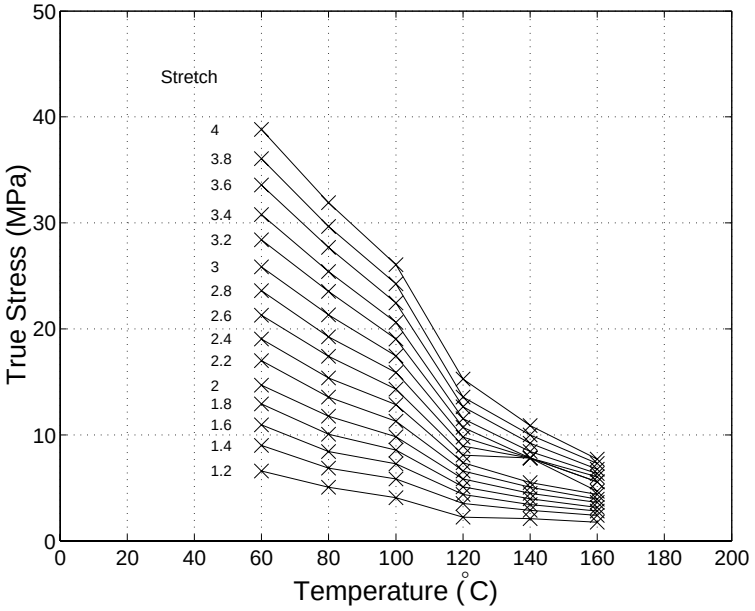

Fig. 3.17: True stress as a function of temperature at a range of stretches, showing a shoulder in the data that indicates the presence of the glass-transition of the hard blocks somewhere between $100°C$ and $120°C$.

was $21°C$. Three tests are performed at strain rates of $\dot{\epsilon} = 0.002^{-1}, 0.02^{-1}$ and $0.2s^{-1}$. The temperature-time and stress-time relationships are shown in Fig. 3.18.

It is clear from this data that stress-strain tests performed at speeds of up to $0.02s^{-1}$ can be considered isothermal to within $\pm 2°C$. This is a faster strain rate than that evaluated in Section 3.1.3. The increased strain rate is possible due to the conservative assumptions made in Section 3.1.3; for instance, the convection equation area increases due to the strain applied, and this is not accounted for in the planning equations. The fastest strain rate is clearly not isothermal to within $\pm 2°C$.

An additional test is performed at the fastest strain rate loading a sample and unloading it after the temperature has settled again. The temperature-time and stress-

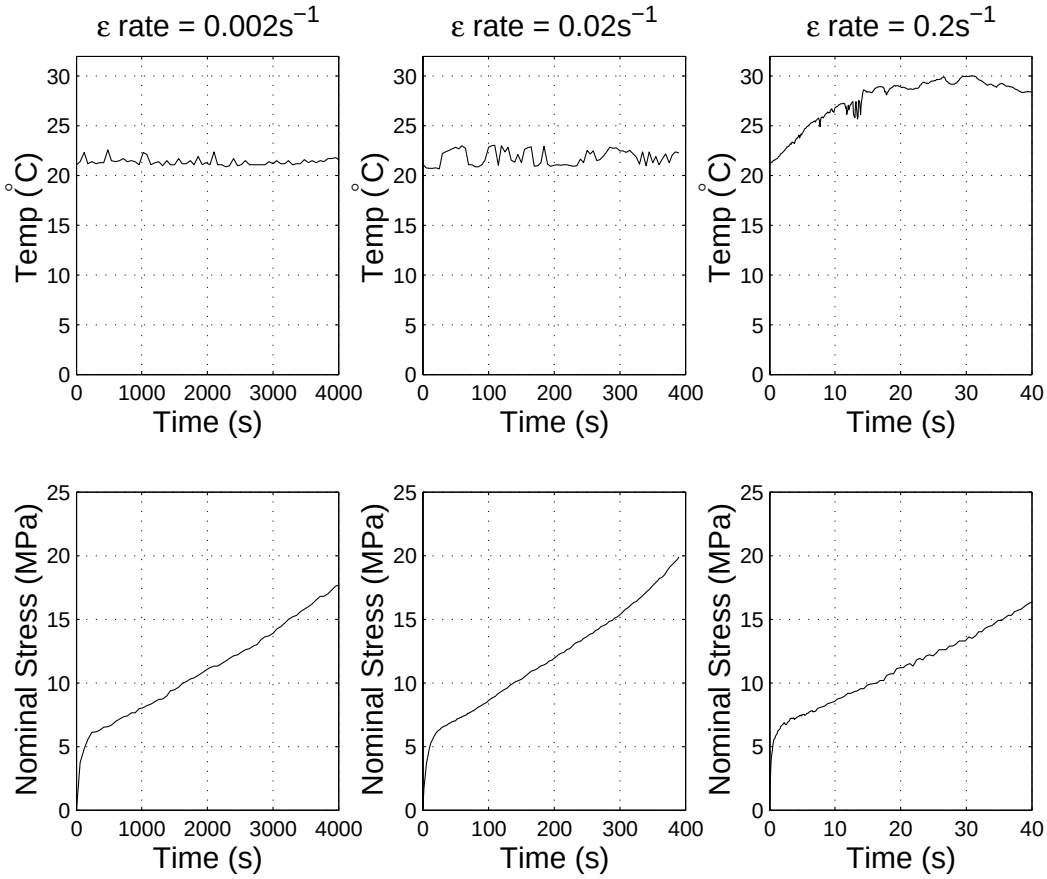

Fig. 3.18: Temperature-time and stress-time measurements made on samples stretched at rates of $\dot{\epsilon} = 0.002^{-1}, 0.02^{-1}$ and $0.2s^{-1}$.

time relationship is shown in Fig. 3.19.

The sample warms up by approximately $4°C$ on loading, and cools by approximately $2°C$ on unloading. This is typical of rubber elastomers; since the stretching process is isentropic , the thermal entropy must increase as a result of the decrease in the conformational entropy of the stretched chains. The sample is allowed to cool to room temperature during the experiment between loading and unloading, so when the sample is unloaded its thermal entropy decreases to counter the increase in conformational entropy, and its temperature drops below room temperature.

3.3.5 Cyclic and reloading tests

A small number of tests have been performed in order to investigate the effects of cyclic loading and of load-unload-reload situations. It is noted that Cella [10] has already pointed out that the material exhibits strain-softening upon reloading for a grade of Hytrel with greater hard segment content. A test is performed on a sample cut from

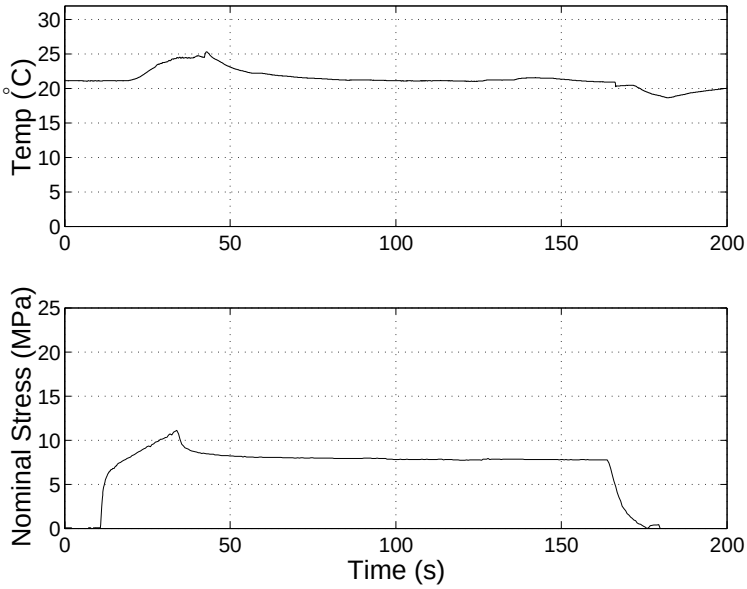

Fig. 3.19: Temperature-time and stress-time measurements made on a sample loaded and unloaded at a rate of $\dot{\epsilon} = 0.2s^{-1}$.

compression-moulded sheet cycling the load between N and $15N$ a number of times. A second test is performed taking the strain to 50% and back to 25%, then to 100% and back to 50%, then to 200% and back to 100%, then to 400% and back to zero load, and then to about 450% when failure occurred at the grips. The strain is monitored with an elastomer extensometer, and the strain rate used is $0.002s^{-1}$. The nominal stress - strain relationship for the two tests are shown in Fig. 3.20.

The cyclic loading test, Fig. 3.20(a), indicates that when primary loading occurs in virgin material, the sample is permanently deformed, and the crystal structure is affected. On the second and subsequent loadings, however, very little happens to the sample, and it is able to load, unload and reload on virtually the same path. There is a small amount of hysteresis, indicating that there is evidence of viscoelasticity dissipating some of the energy.

The load-unload-reload to higher strains test, Fig. 3.20(b), verifies Cella's original observation that the sample strain-softens, and once it is past the strain to which it was loaded to originally, the first load-unload-reload cycle appears to have no effect.

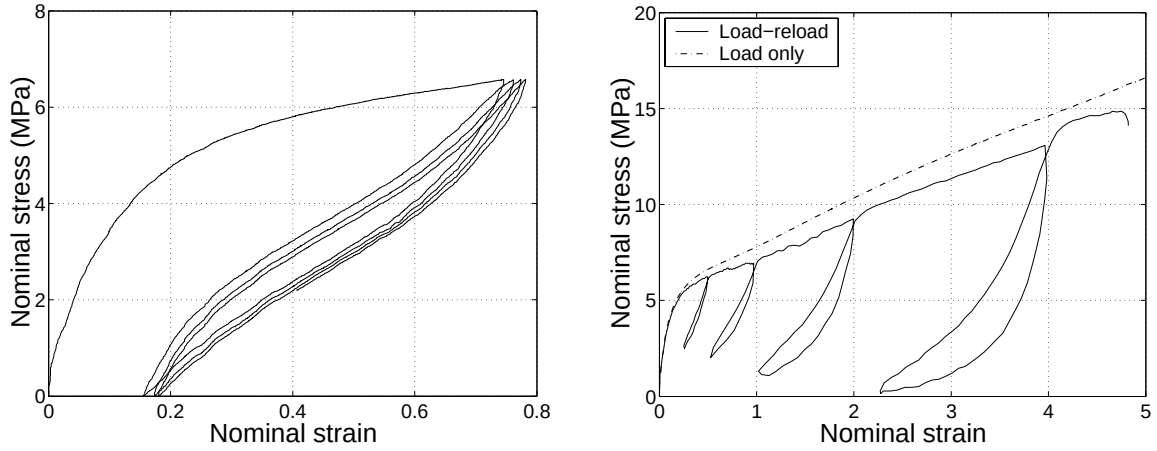

(a) (b)

Fig. 3.20: The effect of (a) cyclic loading and (b) reloading on samples at a stain rate of $\dot{\epsilon} = 0.002s^{-1}$.

The sample approximately rejoins the original stress strain curve produced by a virgin sample to within an acceptable error. There is a small recovery period in which the rejoining curve bends over to rejoin the original and does so in a gradual manner, in a way similar to carbon-black filled rubbers. This stress-softening effect is known as the Mullins effect [39].

In practice, it appears that the behaviour of the material can be approximately described in terms of the peak strain to which it has been previously loaded to, which is related to the damage incurred in its crystal structure.

3.3.6 The effect of strain rate

In order to observe the effect of the strain rate on the material, some of the data from Section 3.3.1 is reproduced in Fig. 3.21.

Although there is some experimental scatter, it is possible to see the limited effect of strain rate. Fig. 3.21(a) shows that as the strain rate is increased the response of the samples becomes stiffer, with the fastest strain rate corresponding to the curve with the highest stress levels at equivalent strains. There is a small but noticeable increase

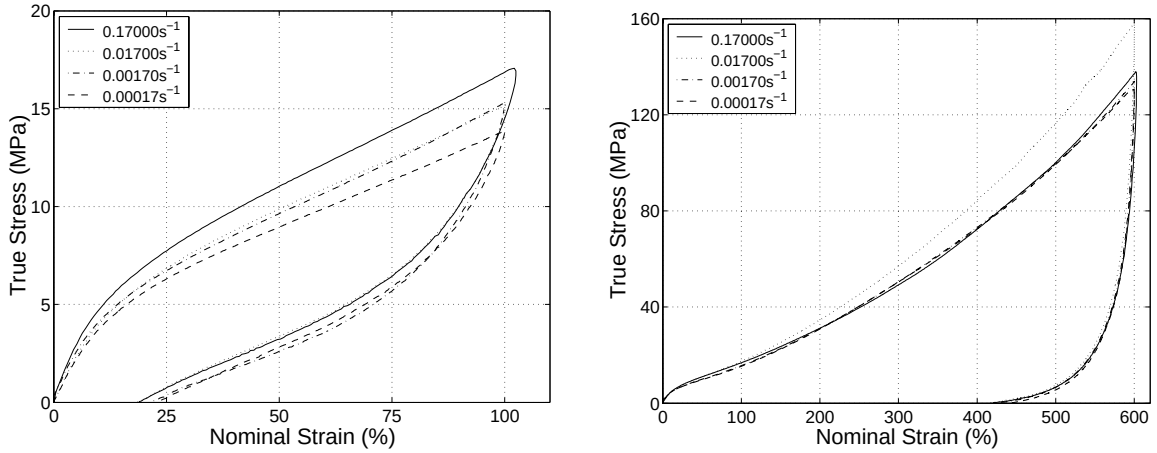

(a) (b)

Fig. 3.21: Loading and unloading stress-strain curves from isotropic samples to maximum strains of (a) 100% and (b) 600% (b) showing the effect of strain rate.

in the initial elastic modulus with strain rate. Fig. 3.21(b) shows tests to a greater maximum strain of 600%, and here the fastest strain rate, $0.17s^{-1}$, gives the highest stresses only to $50-60\%$ strain, dropping down to lower stresses afterwards. This is very likely to be due to the adiabatic heating effect of testing at a speed beyond what can be considered isothermal. The strain rate $0.017s^{-1}$ appears to give the highest stresses at higher strains since it remains at a lower temperature during testing. As has been shown in Section 3.3.4 at test speeds greater than $0.02s^{-1}$ the test can no longer be considered isothermal to $\pm 2°C$, and this is confirmed by these stress-strain curves.

Overall, the material does not show a very large strain rate dependance. The tests have covered 4 orders of magnitude of strain rate, and although a small amount of strain rate dependance has been observed, it does not appear to be highly significant. At dramatically different strain rates, however, this small effect may become more significant.

3.3.7 Residual strain

The residual strain after unloading can also be obtained from the same set of tests. It is shown both as a residual strain and as a percentage of the maximum strain in Fig. 3.22.

The residual strain shown is the point at which the test first measures zero load on unloading. Generally polyether ester elastomers are expected to fully recover only from strains of between $7-25\%$, depending on the specific grade [26]. Apart from an anomalous point at $\dot{\epsilon} = 0.17s^{-1}$ and $\epsilon_{max} = 400\%$, Fig. 3.22(b) shows that the percentage of residual strain exhibits a small decrease with increasing strain rate. This effect could be explained by considering that the flow in the material is mildly viscoelastic, and hence time-dependant.

The stress in the material at large strains can be thought of as being separated into

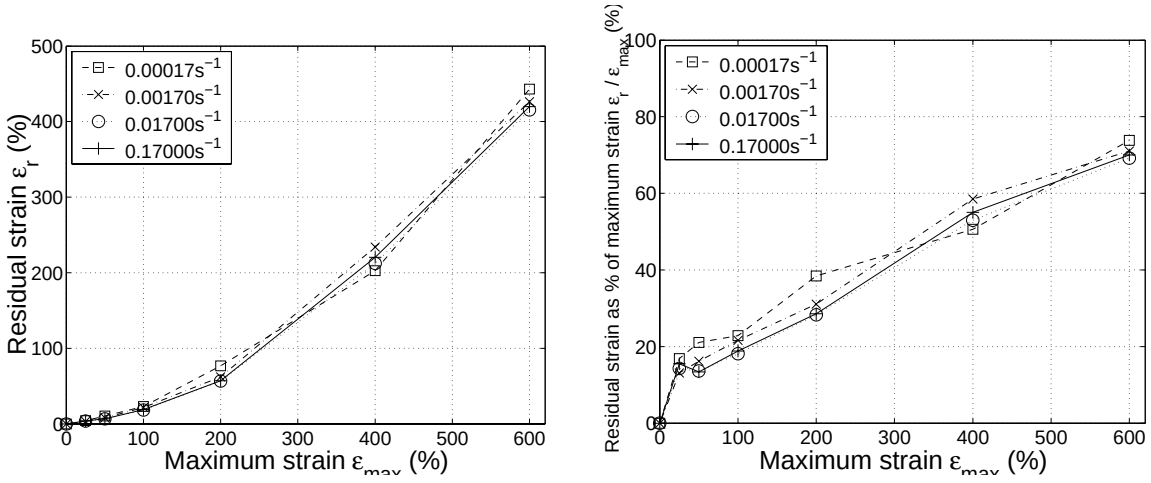

(a) (b)

Fig. 3.22: Residual strain after loading and unloading, (a) as a strain, and (b) as a percentage of the maximum strain at a range of strain rates.

two components - one is the stress of a rubbery nature, due to the rearrangement and straightening of the long-chain soft polymer matrix, and hence mostly recoverable; the other is a viscous flow, a time-dependant 'dashpot' due to the permanent deformation of the crystalline structure. In practice, however, the crystal structures will also contribute to the recoverable stress. If more time under stress is given to the material, more permanent deformation will take place. This effect does not appear to be very marked in this grade of Hytrel. It is very likely that this effect would be enhanced at higher temperatures, where it is easier for the crystal structure to deform. It is also possible that some further recovery may take place some time after the tests, but this effect was not investigated.

3.3.8 Yield and Eyring flow

In ductile polymers in which macroscopic drawing is more pronounced, such as polyethylene, the yield stress σ_y is defined as the point in the (nominal) stress - strain curve where the stress is a maximum. In less ductile polymers such as Hytrel there is no maximum,

and hence no obvious yield stress. In the true stress, σ_t - extension ratio, λ curve, the slope changes to a lower value at yield, and the yield stress is arbitrarily taken to be the stress at the knee [36]. The extension ratio, or stretch λ , is simply the current length over the original length, and is related to the nominal strain by $\lambda = \epsilon_n + 1$. The yield point is obtained by fitting straight lines to the surrounding parts of the curve, as shown in the example in Fig. 3.23. This procedure is carried out for all of the tests of Sections 3.3.1 and 3.3.3.

The well known flow model proposed by Eyring [36, 61] aims to correlate the effects of strain rate and temperature on the flow stress in polymers. From a molecular perspective, in order to flow a molecule segment must pass over an energy barrier, and this energy barrier is affected by both temperature and shear stress.

According to Eyring, the strain rate at yield $\dot{\epsilon_y}$ is given by

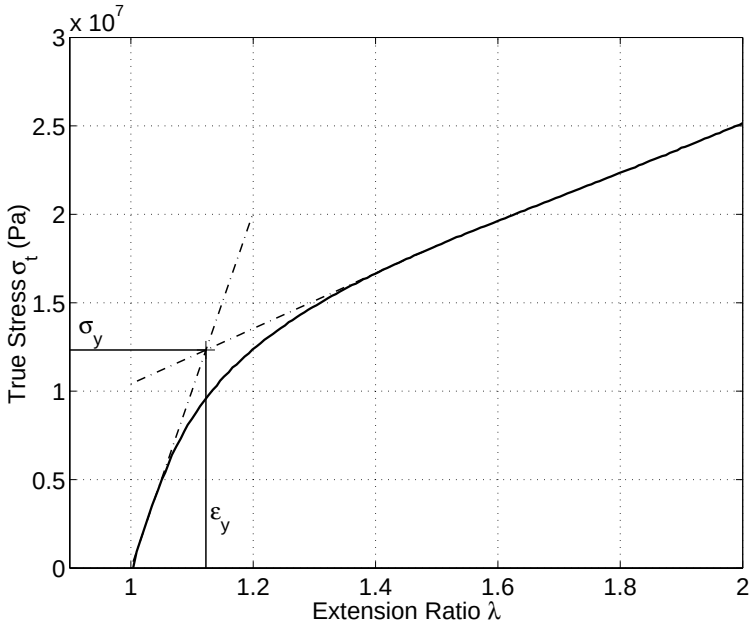

Fig. 3.23: Procedure used to establish the yield stress σ_y for Hytrel.

$$\dot{\epsilon_y} = \dot{\epsilon_0} \exp\left[-\frac{\Delta H}{RT}\right] \exp\left[\frac{\sigma_y V^*}{2RT}\right] \tag{3.13}$$

where $\dot{\epsilon_0}$ is a constant, ΔH is the enthalpy required for a mole of molecule segments to pass over the energy barrier, R is the gas constant, T is the absolute temperature, and V^* is known as the activation volume, or the product of the area over which the stress acts and the distance moved by the molecule segment. Conveniently rearranging (3.13),

$$\left(\frac{\sigma_y}{T}\right) = \left(\frac{2}{V^*}\right)\left[\left(\frac{\Delta H}{T}\right) + 2.303R \log\left(\frac{\dot{\epsilon_y}}{\dot{\epsilon_0}}\right)\right] \tag{3.14}$$

it is possible to plot $\left(\frac{\sigma_y}{T}\right)$ against $\log \dot{\epsilon_y}$ in an *Eyring plot* in order to find the material constants. The Eyring plot for the strain rate tests of Section 3.3.1 and the environmental chamber tests at different temperatures of Section 3.3.3 is shown in Fig. 3.24.

Linear regression is used to obtain the gradient from the room-temperature data. The points obtained at the highest strain rate are ignored since they can no longer be

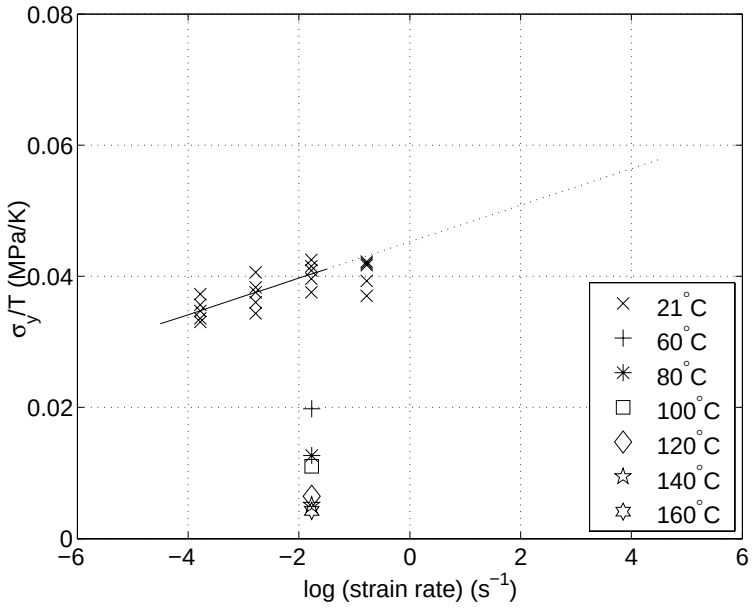

Fig. 3.24: Eyring plot from the isotropic stress-strain data. The higher strain rate tests show evidence of adiabatic heating, and as such are ignored from the linear regression at room temperature.

considered to be isothermal. As expected, these points show a decrease in the yield stress due to the higher temperature reached by the polymer during testing. The line is extrapolated to include high strain rates that might be present in the inverting dome. These values of σ_y/T assume isothermal conditions, and would need to be corrected for any adiabatic heating that will be present at these high strain rates. The activation volume is obtained from the gradient as $V^* = 0.0137m^3/mol$ and relates to a mole of polymer segments.

The activation enthalpy, ΔH, is obtained from the separation of the data at different temperatures. Using the single measurement at $60°C$ and the linear regression at room temperature we obtain $\Delta H = 35.5kJ/mol$. This value is relatively high compared to typical chemical reactions, but this is mainly due to the fact that it refers to a mole of the large number of polymer segments defined by V^*.

Linearity of the Eyring plots across a range of strain rates at fixed temperatures can only be assumed provided that there is a unique flow mechanism governing the yielding. We know from literature on thermal analysis [27, 28, 46, 48] that there are a likely to be a number of mechanisms in a copolymer such as Hytrel, but in a temperature range sufficiently removed from the glass transition temperature of the soft and the hard blocks, it is fair to assume that a single mechanism will be significant.

Assuming that the Eyring equation can be considered valid over a larger strain rate space, it is possible to estimate values of the yield stress at the very high strain rates involved with the inverting dome, and with additional temperature data adiabatic heating can be accounted for.

3.3.9 Adiabatic heating

An upper limit on the heat generated during a stress-strain test can be obtained by calculating the work input done by the movement of the crosshead of the test machine during the test. The energy input to the material, or strain energy W_λ, expressed as energy per unit volume at a given stretch λ, can be found from

$$W_\lambda = \int_0^\lambda \sigma(\lambda) d\lambda \tag{3.15}$$

The data from Section 3.3 at a strain rate of $0.0017 s^{-1}$ is used for the calculation. The energy is shown in Fig. 3.25 as a function of stress and of strain.

In order to calculate the heat rise that this energy would be equivalent to, we need to divide the energy per unit volume by the specific heat capacity, C, and the density ρ. The calculation is performed with C at $20°C$, and is shown as a function of stress and strain in Fig. 3.26. Also shown is the temperature rise assuming that at any particular strain, some of the energy is stored as linear elastic strain energy, and that this energy

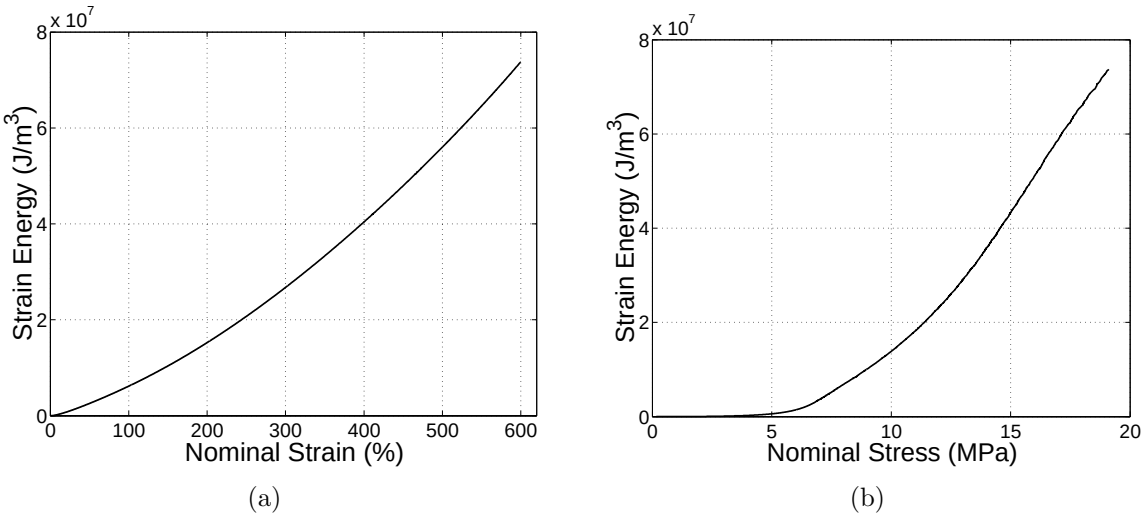

(a) (b)

Fig. 3.25: Strain energy function per unit volume, evaluated from the area under the stress-strain curve, as a function of (a) strain and (b) stress.

would not be given out as heat, but stored as elastic potential energy. A modulus of $55MPa$ is assumed for the linear elastic part. Although it has been shown that the material is able to unload to greater strains due to its rubbery network, that part of the unloading would result in a temperature drop, as has been demonstrated on Fig. 3.19.

In the tests performed in Section 3.3 at the fastest available strain rate of $0.17s^{-1}$ a temperature rise of approximately $4°C$ is recorded at a stress of $11MPa$, and this compares to a predicted value of $9°C$ for a fully adiabatic expected temperature rise. We know from Section 3.1.3 that this strain rate is lower than that predicted for fully adiabatic conditions, even though the test was only performed to a maximum strain of 200%. It is likely that to achieve fully adiabatic conditions much faster speeds than those used so far must be employed, but these are currently impossible on the available test machine.

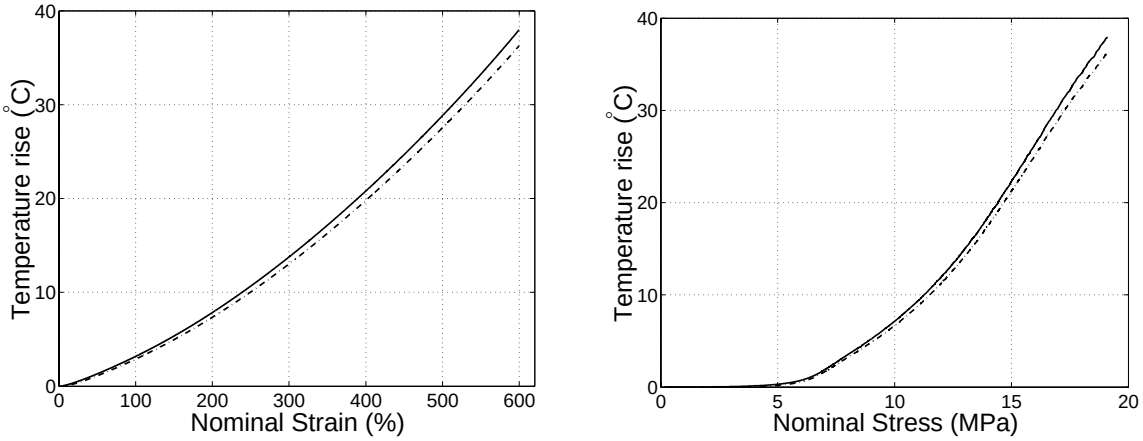

(a) (b)

Fig. 3.26: Temperature rise expected under adiabatic conditions (solid line) and with the linear-elastic energy part removed (dot-dash) as a function of (a) strain and (b) stress.

3.3.10 Comparison of injection and compression moulded data

Fig. 3.27 shows a full set of injection-moulded and compression-moulded tests with strain rates ranging between $0.0042s^{-1}$ and $0.017s^{-1}$. Here it is possible to observe the combined effect of process-induced molecular orientation and thermal history , having shown that the strain rate effect is relatively small across this range. There are small differences in small strain modulus mainly in the injection-moulded samples tested at different orientations to the spur. Significant differences in stress at a given strain begin at around 50% strain. The compression-moulded quenched samples are closest in response to the injection-moulded samples, indicating that a fast cooling rate has been achieved, but perhaps that it is not as fast as in injection-moulding. At a strain of 100% the stress varies from approximately $12MPa$ to $16MPa$ in the full range of samples. At a strain of 400% there is a significant difference in the stress experienced by the different samples, $77MPa$ in the slow-cooled samples and $43MPa$ in the injection-moulded discs at 90° to the injection axis.

This data indicates that the effects of thermal history and of process-induced molecular orientation are both significant at higher strains, but that at low strains the behaviour is less dependant upon thermal history and orientation. These effects are much more significant than the effect of strain rate over the observed range.

3.4 Material failure

In injection-moulded samples tested in Section 3.2, strains of up to 800% are reached with stresses seldom exceeding $22MPa$, less than the $27.6MPa$ stress to break given by DuPont [16]. In the compression-moulded tests it is likely that the stresses would reach $27MPa$ if the tests had continued beyond 600% strain. No full assessment of strain to break is performed in this thesis since it is thought that the mechanism of failure in a

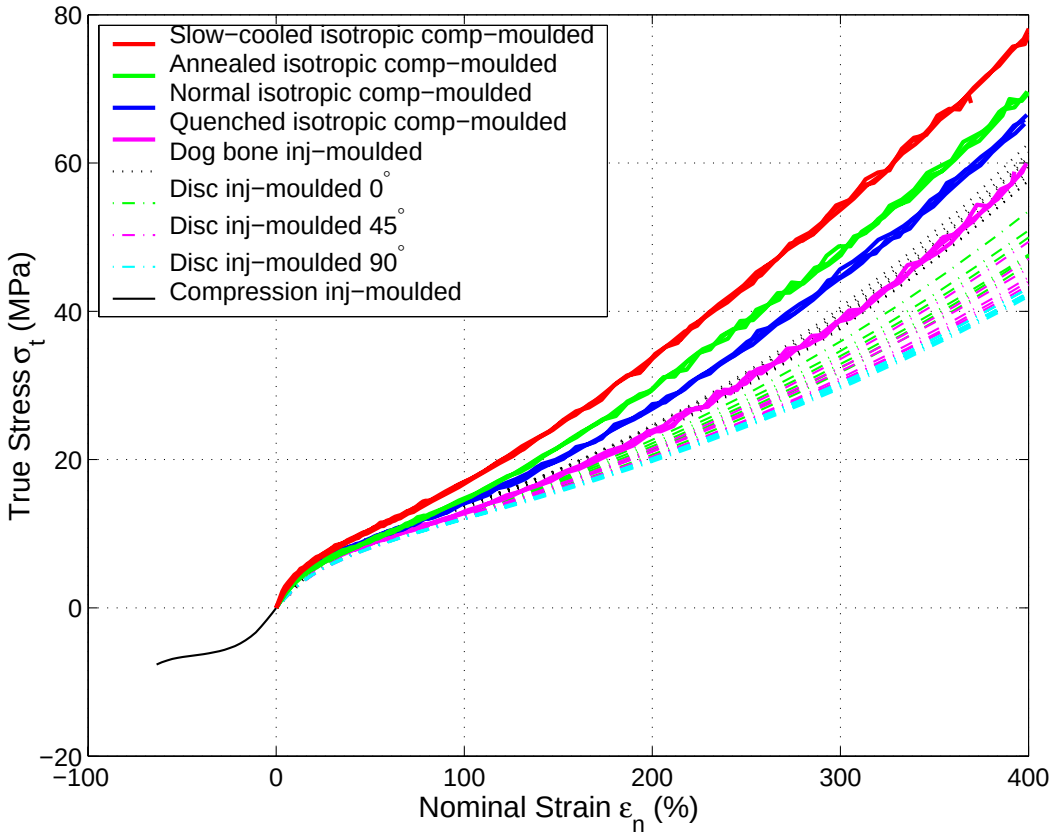

Fig. 3.27: Stress-strain data from injection-moulded and compression-moulded samples with different thermal histories.

uniaxial elongation test to break would be substantially different to the mechanism of failure in a dome.

Two approaches are attempted here. The first is the tear test approach, with the most successful being the well-known trouser test that aims to quantify the fracture energy release rate in a controlled manner. The second approach looks at bursting of discs under equibiaxial stress, a mode of failure virtually identical to that of the inverting dome.

3.4.1 Tear tests

Some attempts have been made by the present author to test samples with centre cracks and edge cracks, but due to the excellent tear resistance of Hytrel these tests

resembled uniaxial stress-strain curves with the cracks having no discernable effect upon the specimen other than to reduce its cross-section. A test that has been successfully used on rubbers is the trouser tear test [49]. The trouser test takes its name from the trouser-like shape of the specimen used, typically a long, thin rectangle with a long cut along its length. The specimen is shown schematically in Fig. 3.28.

Here we wish to obtain a relationship between the work done by the pulling force and the energy dissipated by the formation of new surface. We follow a method similar to that used by Anderton and Treloar [1]. The specimen is divided into three areas, an unstrained area (I), a region in inhomogeneous strain (II), and two leg regions under approximately uniform strain (III). If we define as dl a small increment in the displacement of the grips holding the trousers, and as dc a small increment in the length of the tear, the work done by the force F in moving a distance dl has to be equal to the energy dissipated in order to create new surface plus the change in elastic strain energy dW. Hence we can write

$$Fdl = 2\gamma tdc + dW \tag{3.16}$$

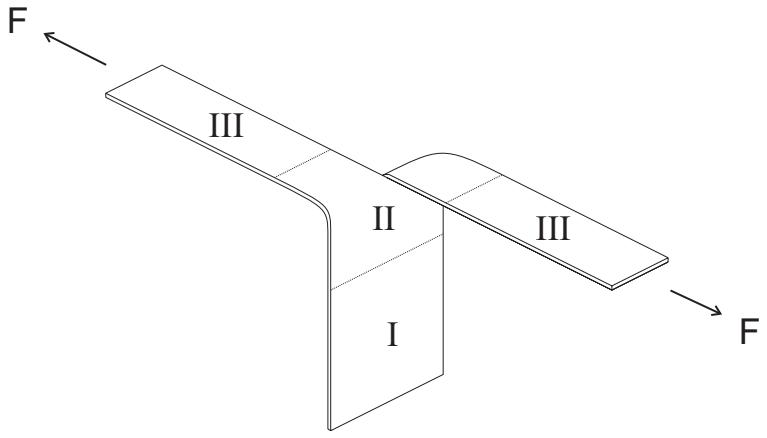

Fig. 3.28: Specimen used in the trouser tear test.

where t is the thickness of the sheet, and γ is the surface free energy, or the energy required to form new surface, per unit surface area. $2\gamma = G_C$, which is more commonly known as the critical strain energy release rate, and is the energy required to open a crack per unit area (since a crack forms two new surfaces), and both are in units of J/m^2. Now it can be assumed that a crack growth of dc results in a volume of material $A_0 dc$ being transferred from region I to region II, and the same from region II to region III, where A_0 is the cross-sectional area of the material in the unstrained configuration. Hence, the volume of material in the inhomogeneous region II stays constant. The change in elastic strain energy dW will thus be the energy required to strain the additional material, and is given by

$$dW = W_\lambda A_0 dc \tag{3.17}$$

where W_λ is the stored energy per unit volume at a stretch of λ. The distance moved by the force $dl = 2\lambda dc$ due to conservation of volume. Hence we can rewrite (3.16) as

$$\gamma = \frac{\lambda F}{t} - \frac{W_\lambda A_0}{2t} \tag{3.18}$$

and we can find γ in terms of the tearing force F, the stretch in the legs λ, and the strain energy function W_λ.

If the strain was fully elastic and recoverable, W_λ would simply be the integral of the stress-strain curve as a function of stretch. We have shown in Section 3.3.7 that the strain is not fully recoverable for strains beyond 20%. The problem with non-recoverable strain is that we do not know which part of the work is going to forming the new surface and which to permanently deform the inhomogeneous region II. If this strain were recoverable, then this would not be an issue, even for a non-linear elastic

material such as rubber.

One way to avoid this problem is to use a very wide specimen in which the stretch in the legs remains close to 1. For stretches close to 1, the term $\frac{W_\lambda A_0}{2t}$ in (3.18) is negligible when compared to the term $\frac{\lambda f}{t}$, and $\gamma \approx \frac{F}{t}$. This results in negligible strains being present in the inhomogeneous region II, and all of the work going to form new surface (providing that the bending of the legs is not an issue). It was not possible to achieve this with Hytrel because of the difficulties in producing large good-quality sheets without bubbles, and difficulties associated with gripping very large sheets in the `Instron` test machine.

A number of attempts are made at achieving tearing at constant force, using a cross-head speed of $50mm/min$. The strain in one of the legs is monitored using an elastomer extensometer. This is not ideal since it prevents some rotation of the leg, and since the strain is not constant across the width of the leg. One of the more successful tests is shown in Fig. 3.29. The sample is approximately $0.5mm$ in thickness, $100mm$ in length and $50mm$ in width. The cut is produced with a sharp razor blade, and is initially $30mm$ long, and $15mm$ are used in the grips. Numerous problems have been encountered, such as the tear proceeding to the side of the sample rather than along the length, or the load continuing to rise throughout the test. Greensmith and Thomas [20] showed that the results are not highly sensitive to the tear direction.

Fig. 3.29: Typical trouser tear test sequence.

Little consistency was observed in the various force-displacement curves, with many samples failing before reaching a steady force. Data from one of the more successful tests is shown in Fig. 3.30. Here the mean force during tear at constant force is approximately $115N$.

The strain measurements indicate a stretch in the legs of approximately 2, although it was difficult to achieve consistency also with the strain measurements. The value of W_λ (the integral of the stress-strain curve) at $\lambda = 2$ for compression-moulded sheet is approximately $6MJ/m^3$. Using these values, and assuming the strain to be fully recoverable, we obtain a critical strain energy release rate G_C of about $6 \times 10^5 J/m^2$. This value compares reasonably well to the value of $10^5 J/m^2$ obtained by Thomas [56] for Hytrel 4056 since G_C values are usually expressed as orders of magnitude. A typical value for a rubber is $10^3 - 10^4 J/m^2$ [1] and Hytrel is advertised as having a much better tear resistance than rubbers [18]. However, little confidence is placed on the precision of this value of G_C since there are problems in applying the theory correctly at these strains

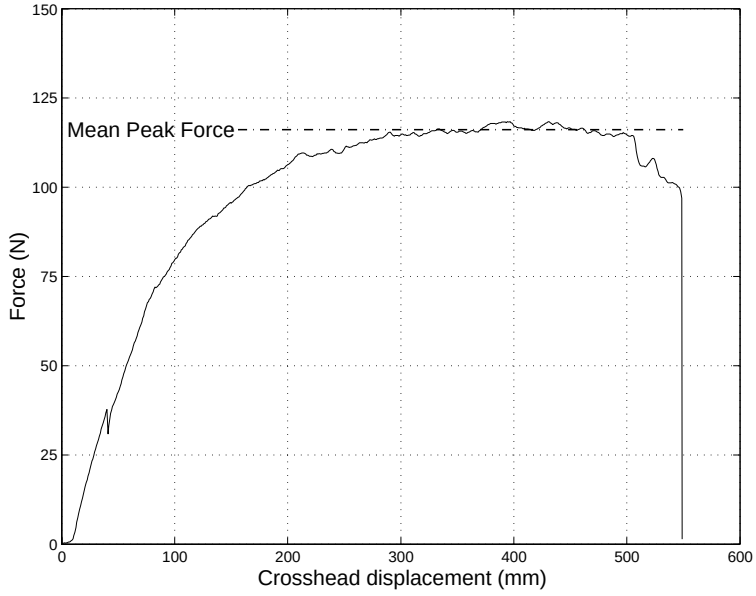

Fig. 3.30: Force-time data generated by a successful trouser test.

for an inelastic material, as well as the difficulty in achieving good quality and repeatable experimental data. Tsunoda and coauthors [58] pointed out that G_C is affected by the tear rate, and this is partly derived from the dependance of G on W_λ in (3.18), although this effect is thought to be small in Hytrel 4068.

The sample after tearing shows a highly deformed and thinned-out region next to the tear, indicating that significant strain has occurred prior to failure next to the crack tip. One such sample is shown in Fig. 3.31. The magnitude of the strain energy release rate is determined by the work done at the crack tip as the crack propagates, and has been shown by Thomas [55] to be given by

$$G = W_t d \tag{3.19}$$

where d is the crack tip diameter, and W_t is the strain energy density at break in the crack tip region. Accurate measurement of this region during tear could be an alternative way in which to obtain a value of G, although this has not been attempted.

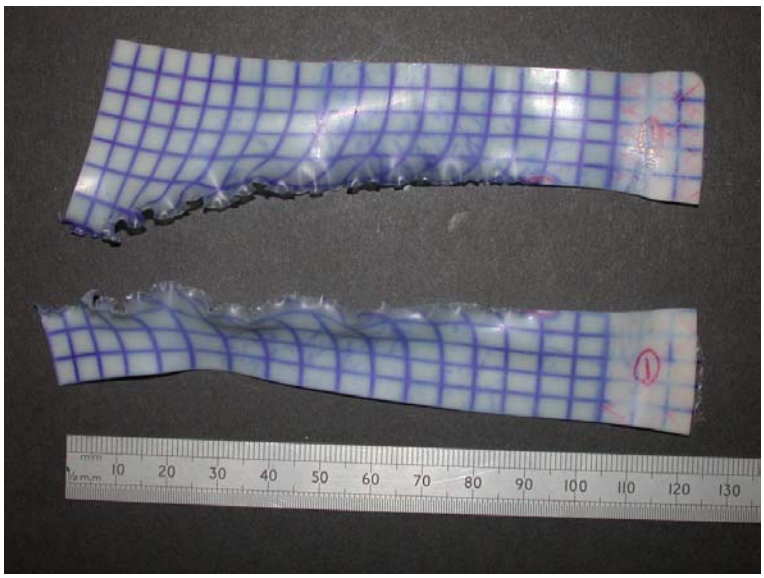

Fig. 3.31: Specimen used in the trouser tear test. There is a highly deformed and wrinkled region next to the tear where large strains have occurred.

3.4.2 Burst tests

Although the trouser tear tests are able to give an indication of the magnitude of the strain energy release rate, the mode of failure observed and expected in the inverting domes is a biaxial burst rather than a tear. No such tests have been reported in the literature. A number of burst tests are performed on discs produced from both injection-moulded and compression-moulded material by clamping the discs along the circumference and inflating to rupture with the aid of compressed gas. The discs are stamped out of Hytrel sheet with the aid of a punch, and are clamped at a radius of $4.25mm$, with the same clamping arrangements as are used for inverting domes [4]. Samples are marked with a grid in order to measure the stress and strain at rupture. The pressure is applied at a rate of approximately $1bar/s$. The entire procedure is monitored using a video camera, and the burst pressure is measured to within $\pm 1bar$ using an analogue pressure gauge. Thickness measurements of samples before testing are recorded using a micrometer. Two typical sequences of inflation to burst are shown in Fig. 3.32.

It is clear from the images that the burst failure is localised, typically producing a hole $1mm$ in diameter, possibly due to a local inflation instability [21]. The centre of the disc is under a state of equibiaxial stress, and the burst test can essentially be interpreted as an equibiaxial test. Since we expect the apex to be deformed in an approximately spherical manner, the stress at burst, σ_b, can be obtained from

$$\sigma_b = \frac{p_b r}{2t} \tag{3.20}$$

where p_b is the pressure at burst, r is the radius of curvature at the centre at burst, and t is the thickness at burst. The radius of curvature is obtained from side-view

[4] Details of improved clamping arrangements are given in Section 4.3.2

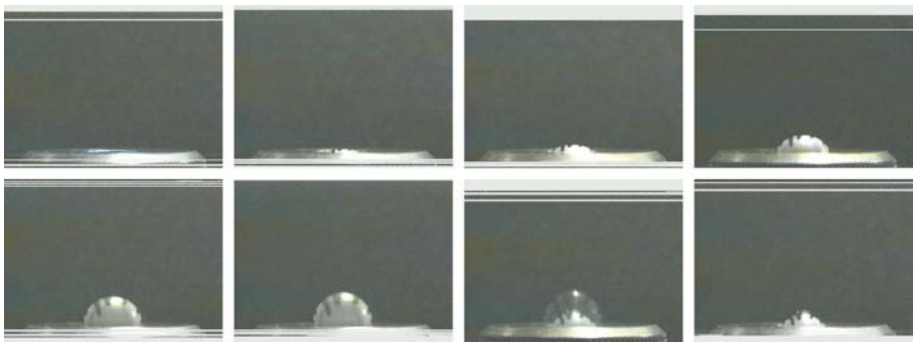

(a)

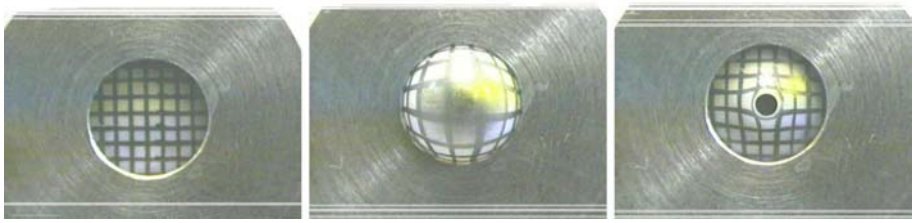

(b)

Fig. 3.32: Inflation to burst tests on $0.5mm$ thick discs, viewed (a) from the side, and (b) from above.

photographs by recording the position of the apex, and of two points close to the apex on either side. It is then found from simple geometry since three points define a circle. Measurements of the points on the circle are taken $1-2mm$ away from the apex. A compromise between measuring as close to the apex as possible, and obtaining sufficient resolution in the measurements on the digital images has to be reached.

The burst strain, ϵ_b, is evaluated from the separation of the markers on the scale drawn on the disc, and is used to evaluate the thickness at burst assuming equibiaxial strain and incompressibility. The thickness at burst is given by

$$t = \frac{t_0}{(1+\epsilon_b)^2} \tag{3.21}$$

The Poisson's ratio of the material at small strains has been measured by DuPont as 0.45 [16]. This is sufficiently close to 0.5 for incompressibility to be assumed. Some

care has to be taken in using (3.20) since it assumes that the wall thickness is thin relative to the curvature. For thick-walled vessels there is a third stress component in the thickness direction that is no longer negligible. The validity of the equation for a thickness of $0.5mm$ in typical samples is checked by testing material over a range of thicknesses from $0.138mm$ through to $0.532mm$ and observing if there is any significant variation in the burst stress at the larger thicknesses. The burst stress as a function of thickness for standard compression-moulded sheet is shown in Fig. 3.33.

At lower thicknesses the burst pressure is very low, and hence the measurement accuracy is particularly poor. To within measurement error, the burst stress does not appear to be affected by the thickness of the sheet. Burst tests are performed on compression-moulded sheet with standard, annealed, slow-cooled, and quenched heat treatments, and on injection-moulded discs. The results are presented in Table 3.1.

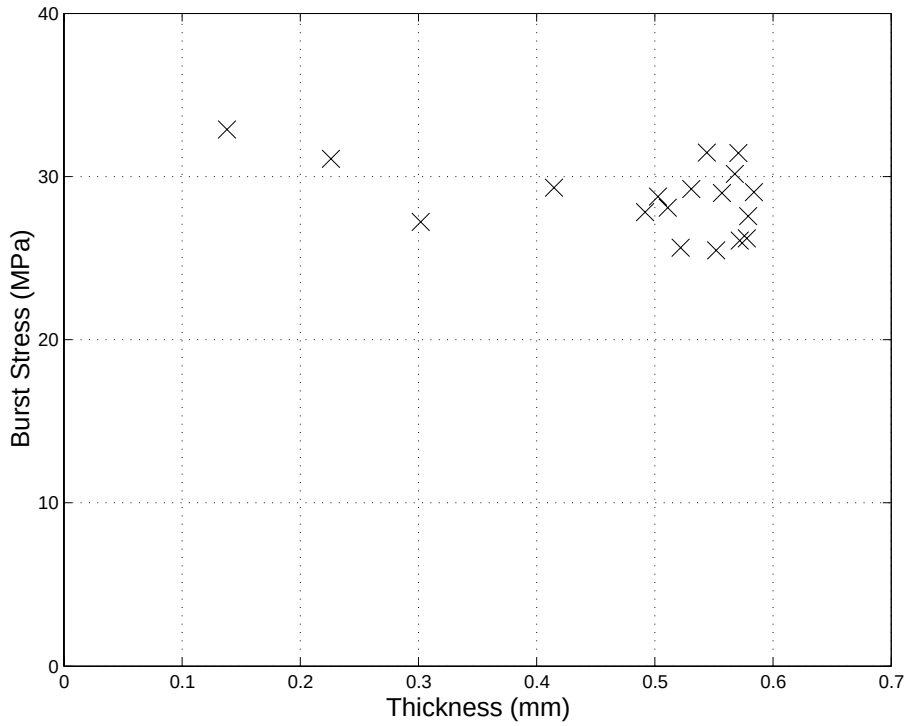

Fig. 3.33: Burst stress in standard compression-moulded sheet as a function of sheet thickness.

Table 3.1: Burst stresses under pressure for Hytrel 4068 sheets with a range of thermal histories. The number of samples tested in each condition is shown as n.

Sheet material	Mean Burst Stress (MPa)	Standard Deviation (MPa)
Compression moulded		
Slow cooled ($n = 8$)	30.7	1.7
Annealed ($n = 10$)	28.5	1.2
Standard ($n = 18$)	28.7	2.1
Quenched ($n = 4$)	26.7	1.7
Injection-moulded (n=4)	24.6	1.4

The mean radius of curvature at burst measured across the full range of experiments is $r = 3.76 \pm 0.26mm$ and does not appear to vary with microstructure. The strain at burst was measured only on a smaller sample of tests as $\epsilon_b \simeq 135\%$ and also appears to be independent of microstructure.

Although the experiment is performed with limited measurement accuracy, especially in the pressure measurement which is measured to $\pm 1bar$, there does appear to be a noticeable effect of thermal history on the burst stress going beyond the measurement error. The slow cooled sheet produced the strongest material, and the quenched sheet is closer to the injection-moulded sheet and is weaker. It is likely that the increased crystallisation in the slow-cooled sheet produces a microstructure that is harder to break. This is a little unexpected since it was previously thought that the ultimate stress in the material was governed by the elastic soft segment failure alone. This test indicates that the crystal matrix could be manipulated to produce a stronger sheet, perhaps by orientation of the spherulites, and that it plays a part in the ultimate strength of the

copolymer. The value of burst stress obtained from these experiments corresponds to a true stress to break in an equibiaxial test.

3.5 Summary and conclusions

Sections 3.1, 3.2 and 3.3 have described a large number of mechanical tests performed on Hytrel 4068. Samples tested have come from a range of production methods, some of which exhibited the effects of process-induced molecular orientation, and with a range of thermal histories, and have been compared to each other. Many of the features predicted from the morphology have been identified. Tests have been performed in tension and compression, at different strain rates, over a range of temperatures, and with cyclic and repeated loading. The effect of strain rate has been observed, and does not appear to be highly significant over the 4 measured decades in strain rate. The effect of thermal history on the mechanical properties becomes significant beyond 50% strain, and there is a pronounced difference between injection-moulded and compression-moulded samples. The effect of process-induced molecular orientation has been qualitatively observed in injection-moulded discs tested in a range of directions, and in dog-bone shaped injection-moulded samples.

The Eyring model is used to correlate the effects of temperature and strain rate on the yield stress of the material. The glass-transition temperature of the hard blocks has been identified as being between $100 - 120°C$.

Section 3.4 has described two methods implemented to investigate the failure properties of the material. Trouser testing has given a strain energy release rate G of about $6 \times 10^5 J/m^2$, which is high, and fits well with experiments on similar polymers. Burst testing, a failure mode closer to that experienced by the inverting dome, measures the stress at failure under an equibiaxial stress state, and has shown that the failure stress is

not independent of thermal history, with slow-cooled samples failing at $30.7 \pm 1.7MPa$ and injection-moulded samples at $24.6 \pm 1.4MPa$. This is an unexpected find, and indicates that the hard segment of the polymer is playing a role in the ultimate strength. Also, this find suggests that it may be possible to strengthen the material by altering the thermal history as well as the microstructure. It was previously thought [10] that the ultimate stress in the material was governed solely by failure in the soft, amorphous phase.

Chapter 4

Experimental methods for the analysis of inverting domes

This chapter describes a number of experimental techniques that are used in the process of investigating the behaviour of inverting domes. Section 4.1 discusses manufacturing imperfections in injection-moulded domes. A slicing technique is developed to measure the thickness of the dome, which will be used later in reconstructing the geometry of real domes for finite element analysis. The pressure near to the dome's surface is measured using high speed pressure transducers in Section 4.2. This data will be used both as an input to dynamic finite element modelling and to the simple mechanical model presented in Chapter 5. Section 4.3 monitors the quasi-static response of the dome to pressure. The response is highly non-linear, and is tracked using imaging techniques. In Section 4.4, the high-speed behaviour of domes during injection is investigated using high-speed imaging equipment. The position of the apex of the dome is measured at different time intervals and yield useful velocity information. The position and velocity of a drug particle cloud is measured in Section 4.5. This is done by measuring the time taken for the particle cloud to obscure two light beams a short distance away from the dome. This technique is coupled to the high-speed imaging to investigate the time at which the particles leave the dome. Analysis of the bursting of domes under quasi-static pressure

is performed in Section 4.6, in a manner similar to the experiments on Hytrel sheet burst of Section 3.4.2. The rate of decay of pressure in the device through the vent hole is investigated in Section 4.7, to ensure that after inversion the pressure is always lower than the burst pressure of the domes.

Many of the experimental techniques presented in this chapter will be used to compare to finite element modelling data in Chapter 5, and will be applied to observe the effects of a number of dome modifications in Chapters 6 and 7.

4.1 Dome manufacturing

For consistency, the inverting domes used in virtually all of the experiments are manufactured from the same mould. A *plain* mould is used, without the holes producing drug-retaining fibres. The manufacture of the moulds is performed in-house at the Medical Engineering Unit workshops at Oxford University. Where possible the moulds are checked for key dimensions and appear to fit to the specifications to within tolerances of about $\pm 1\%$, but the most important dimensions of the moulds are difficult to check since they can only be verified from within the moulds once the upper and lower moulds are closed together, as in any injection-moulding.

4.1.1 Microtome slicing of inverting domes

A microtome slicer is used to cut thin sections of domes at various orientations to the injection-moulding spur in order to investigate the accuracy of the manufacturing process. Because the polymer is deformed as a result of the slicing, a set of plastic dome-retaining half-moulds are manufactured to restrain this movement, and soapy water is used to aid movement of the stainless steel blade of the micrometer across the dome. Additionally, a suitable cutting angle has to be found. The cutting is more successful

when the blade is moving both in the cutting direction and in a perpendicular direction to the cutting direction, in a manner similar to a meat slicer. A slice thickness of $500\mu m$ is found to be most successful; thinner slices were difficult to produce due to the flexibility of the polymer.

A total of 24 domes have been sliced, 6 in each of the four directions, at 0°, 45°, 90° and 135° to the axis, measured anticlockwise on the convex face of the dome, as shown in Fig. 4.1. The slices are cut as close as possible to the centre of the dome. The slices are then placed between microscope slides and a series of images are taken. The images are then assembled together to reconstruct the cross-section of the dome. Typically 10 microscope images are required for the reconstruction of a single cross-section.

Measurements of the thickness are made at key positions along a cross-section, at the beginning, middle and end of the straight and curved sections, as shown in Fig. 4.2. The measurements are calibrated with a graticule measurement. The measurement accuracy is $\pm 3\mu m$. The mean and standard deviation of the measurements are shown in Table 4.1.

Although the sample size for each measurement is only 6, the measurements show a good degree of consistency, with relatively small standard deviation values, typically less

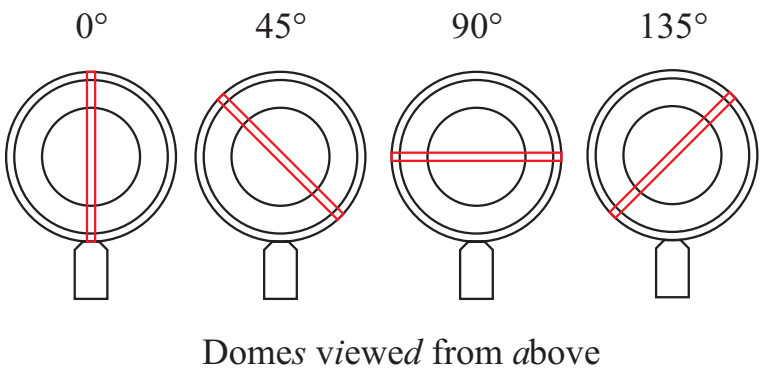

Fig. 4.1: Projection of the domes showing the location of the microtome slices taken on the plain batch of inverting domes.

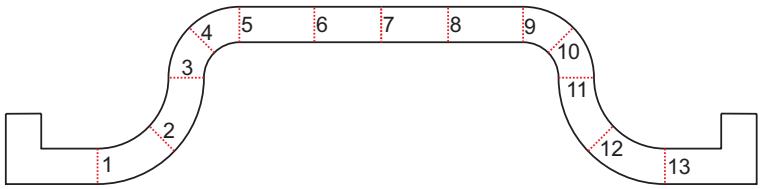

Fig. 4.2: Approximate positions of the thickness measurements.

than 5% of the mean measurements. Nominally the dome is $0.5mm$ thick throughout, but *actual* domes appear to be thicker, with some parts exceeding $0.7mm$.

For comparison, a small number of domes remaining from Costigan's study [12] have also been sliced, but it was not possible to perform the same full set of measurements due to the lack of domes available. Two reconstructed images from typical slices along the axis are shown in Fig. 4.3.

It is evident even from simple observation of the images that, ignoring the fibres, the

Table 4.1: Mean (M) and standard deviation (SD) measurements of thickness of the domes in four cut directions.

Pos	0° M	0° SD	45° M	45° SD	90° M	90° SD	135° M	135° SD
1	586	17	556	20	563	10	567	26
2	671	22	693	8	688	29	647	26
3	640	15	625	11	645	39	596	41
4	721	20	656	17	663	32	632	25
5	744	12	665	21	659	13	669	21
6	690	12	628	10	626	13	627	13
7	689	27	619	13	624	20	627	10
8	668	17	619	13	635	15	618	15
9	703	11	652	19	673	9	672	15
10	627	26	589	21	637	47	654	33
11	558	29	514	7	572	56	602	32
12	667	26	582	13	631	55	658	25
13	628	31	554	9	577	24	576	15

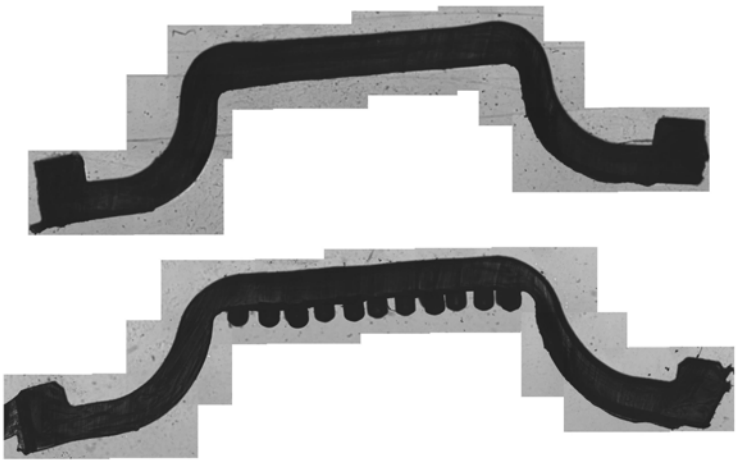

Fig. 4.3: Two reconstructed images of dome slices from a plain new batch (above) and an old batch with drug-retaining fibres (below).

new batch (plain) is substantially thicker than the old batch (with fibres). In addition, the old batch has a particularly thin region near the upper right corner, measuring only $0.35mm$. It is important to bear these differences in mind when observing particle velocity measurements of domes from different batches. A number of domes have been first tested in injection and subsequently sliced. No discernable permanent deformation in the thickness of the domes has been detected as a result of testing.

4.2 Pressure measurements near the dome's surface

Ultimately it is the pressure at the surface of the dome inside the shock tube that influences the inversion process. Experimentally it is not feasible to place a sensor on the dome to measure this pressure without adversely affecting its performance. Instead, we measure the pressure at a fixed point on the shock tube wall as near as possible to the dome. Although the pressure history during inversion at this point will not be identical to the pressure history at the fixed point on the shock tube wall, the two are not expected to vary significantly [40].

An inverting dome device is instrumented with a `Kulite XCQ-080` pressure trans-

ducer, flush mounted on the shock tube wall at a distance of $5mm$ from the flat face of the dome, and attached to a triggering data-logging oscilloscope. $5mm$ is the closest distance to the dome that the current device manufacturing will allow. The experimental set-up is shown in Fig. 4.4.

The device is then fired and the pressure at the transducer is recorded on a digitizing oscilloscope with a frequency of $10MHz$, giving a time resolution of $\pm 0.1\mu s$. The pressure resolution is $\pm 0.3bar$. The start of the recording is triggered approximately $100\mu s$ before a pressure rise at the transducer. This procedure is repeated 10 times with identical device parameters. Zero time is determined as the time at which the shock wave reaches the dome. This is calculated from the distance of the pressure transducer to the surface of the dome and the speed of the incoming shock wave, which was reported as $800m/s$ [12]. Hence a time of $6.25\mu s$ is subtracted from the total time elapsed from the trigger at the pressure transducer, $5mm$ away from the surface of the dome. One such recording is shown in Fig. 4.5(a). The pressure is shown as relative to atmospheric pressure.

Salient points are numbered on the figure. Point 1 is the first pressure rise, due to the arrival of the shock wave . Point 2 is the effect of the reflected shock wave and is the

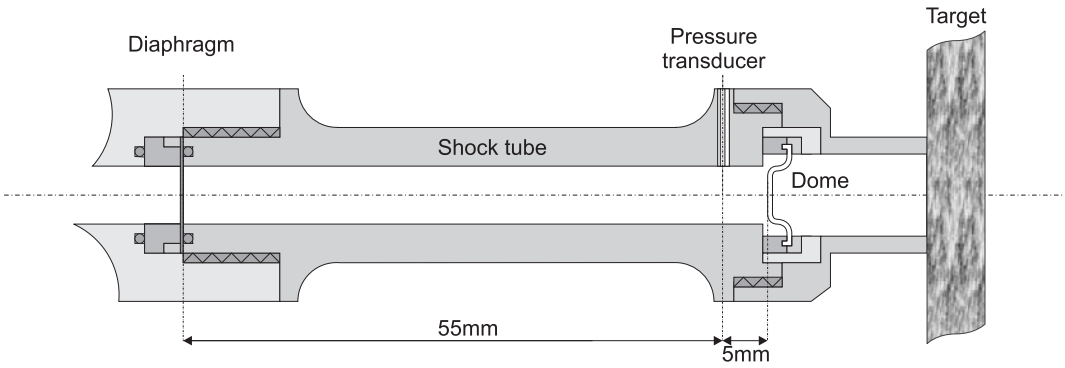

Fig. 4.4: Position of the pressure transducer within the injection device.

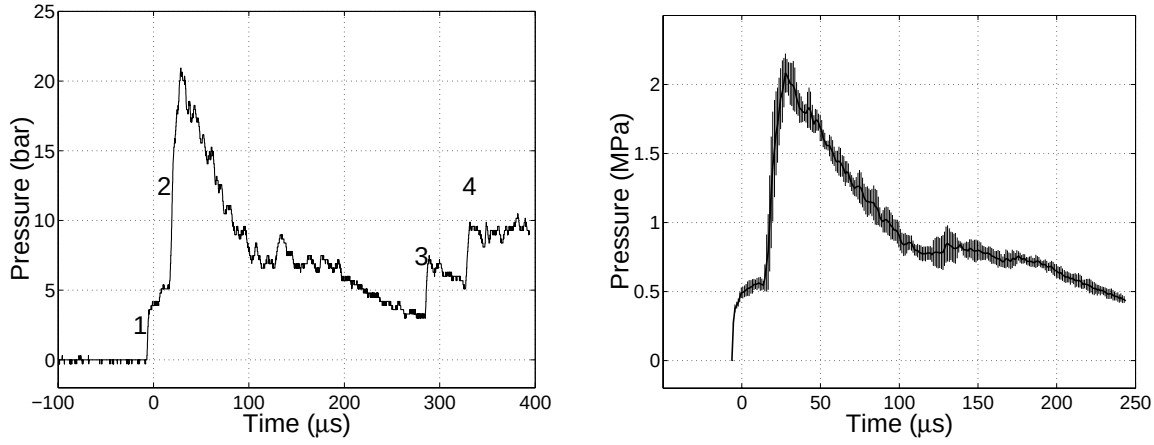

(a) (b)

Fig. 4.5: Pressure history recorded at 5mm from the dome's surface, (a) a single recording $0 - 400\mu s$; and (b) mean and standard deviations from 10 tests sampled at 1MHz $0 - 250\mu s$.

most significant pressure rise. There is a time lag between these pressure rises due to the fact that the transducer is a short distance away from the dome, and the shock wave has to travel to the dome and back. The dome itself is unlikely to see any significant time lag between these pressure rises. Points 3 and 4 correspond to various reflected shocks arriving.

The same experiment is repeated 10 times and the repeats exhibit a good level of consistency. In addition, the experiments fit in well with the theoretical calculations of salient pressure points, in which the peak after point 1 was calculated as 5.9 bar and the peak after point 2 as 20.4 bar [12]. The mean and standard deviations are shown in Fig. 4.5(b), and will be used as input to the dynamic finite element modelling and to the simple mechanical model in Chapter 5.

4.3 Quasi-static dome response

The response of the inverting dome under quasi-static pressure is investigated in this section. The objective of the measurement of the quasi-static response is to offer a

benchmark set of tests with which to compare and calibrate the finite element modelling of Chapter 5, as well as to help in the characterisation of the behaviour of the domes.

4.3.1 Dome inflation

This experiment is performed to observe the dome's response to an inflating pressure. A simple clamping unit is manufactured to retain the dome and to allow maximum visibility during measurements [1]. The pressure applied to the dome is recorded using an analogue pressure gauge accurate to $\pm 0.5 bar$ and the displacement of the dome is recorded using digital images with a `Philips` digital camera and a suitable calibration grid. The images are taken at right angles to the dome's axis of symmetry, as shown in Fig. 4.6. A typical set of images from an inflation experiment is shown in Fig. 4.7.

Only the displacement of the apex of the dome is measured and the resolution is $\pm 0.05 mm$, from the digital image resolution of approximately $30 pixels/mm$. There appears to be a small amount of movement in the clamping arrangement during the

[1] At the time of performing these experiments, the dome retaining lip described in Section 4.3.2 had not been designed yet, and as such these domes are retained in a less efficient manner than the later domes.

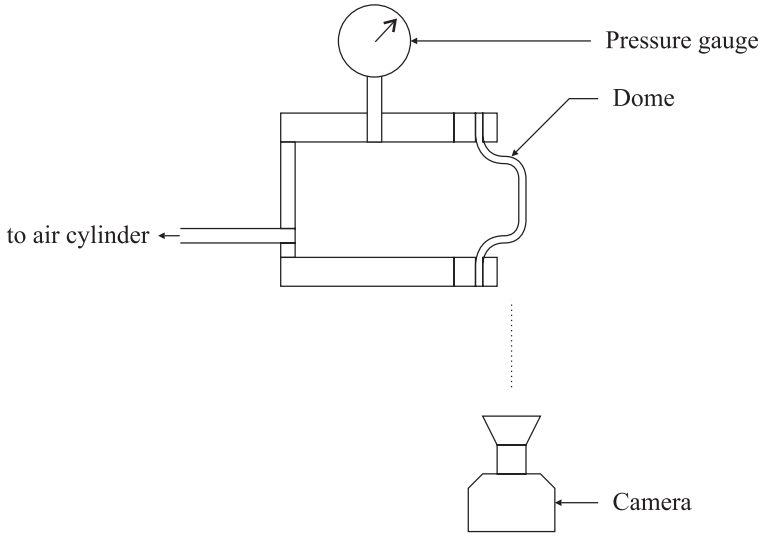

Fig. 4.6: Apparatus used to inflate domes, and to record the digital images.

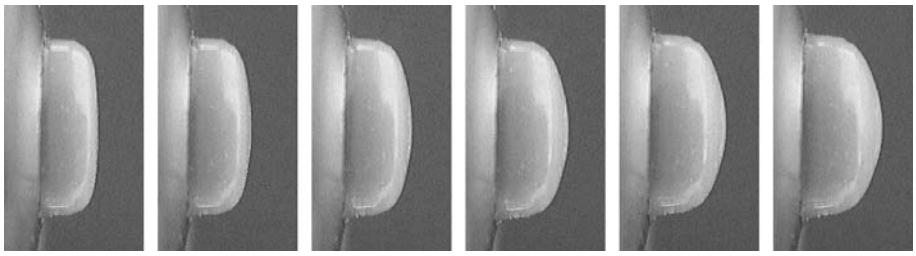

Fig. 4.7: Images from a typical dome inflation experiment, shown at $0bar$, $2bar$, $4bar$, $6bar$, $8bar$ and $10bar$ in loading only.

first inflation, and in order to minimise this effect domes are inflated through to $10bar$ and back to $0bar$ before being inflated in steps of $2bar$ through to $10bar$ and back in steps of $2bar$ through to $0bar$. The domes are then inflated to $10bar$ and back to $0bar$ once again for verification. The pressure is applied manually through an air cylinder valve at a rate of approximately $0.5bar/s$.

A total of 6 domes are inflated and deflated using this procedure, and the results are summarised in Table 4.2. Zero displacement is recorded as the displacement after the initial inflation to $10bar$ and subsequent deflation to $0bar$. Although there is definite evidence of hysteresis in the loading and unloading process, the domes do return to their approximate original position to within the bounds of the measurement accuracy. The hysteresis in the inflation and deflation is expected due to the hysteresis observed in the material cyclic loading curves of Section 3.3.5.

The pressure is considered to be negative since the dome is traditionally inverted due to positive pressure and for consistency with the next section. The data after the first loading cycle is shown in Fig. 4.8. It is noted that the initial loading and unloading process to reduce clamping movement may induce small permanent deformation in the domes, but this is small compared to the clamping movement.

Table 4.2: Mean and standard deviation (SD) of recorded dome apex displacements at a range of pressures. The displacement measurements are zeroed after the first inflation and deflation.

Pressure (bar)	Mean Displacement (mm)	SD Displacement (mm)
0	-0.31	0.15
10	1.37	0.14
0	0.00	0.00
2	0.28	0.08
4	0.63	0.12
6	0.93	0.11
8	1.17	0.11
10	1.39	0.13
8	1.24	0.13
6	1.08	0.14
4	0.84	0.10
2	0.50	0.10
0	0.06	0.03
10	1.41	0.13
0	0.07	0.10

4.3.2 Improvements to the clamping arrangements

Two improvements to the initial clamping arrangements are introduced here to remove the uncertainty of the clamping movement highlighted in 4.3.1. Firstly, a $0.5mm$ lip is added to injection-moulded domes, shown in Fig. 4.9(a). Secondly, if the lip cannot be produced (as will be the case for the domes produced by compression-forming, see Chapter 7), the ring surfaces are roughened by introducing small notches that help to retain the domes, shown in Fig. 4.9(b). Both clamping arrangements are satisfactory and no further dome slip was observed, reducing uncertainty in their behaviour.

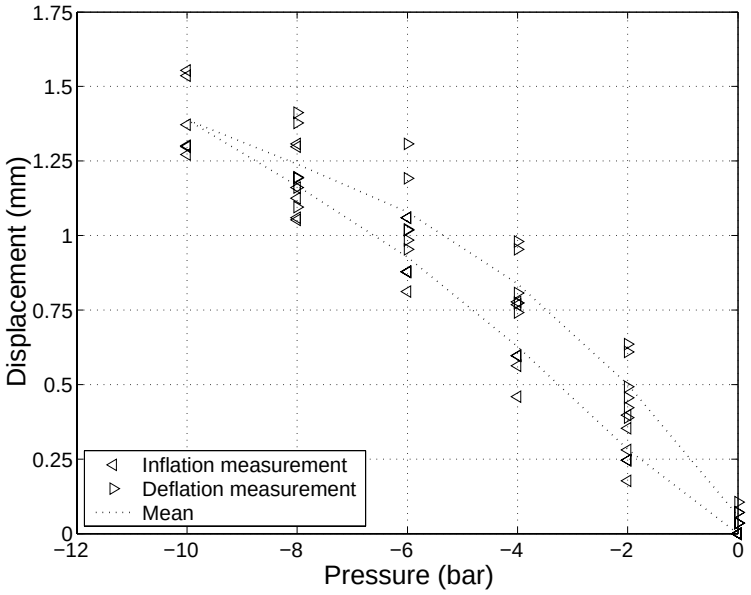

Fig. 4.8: Dome apex displacement vs. pressure in loading and unloading.

4.3.3 Dome inversion

Two possibilities exist in the mounting and subsequent firing of the domes: the convex face facing the shock tube and the concave face outwards, and the reverse, or convex face outwards and concave face in the shock tube. These configurations are termed *inversion* and *eversion* respectively. In the *eversion* procedure there is an extra step, after loading

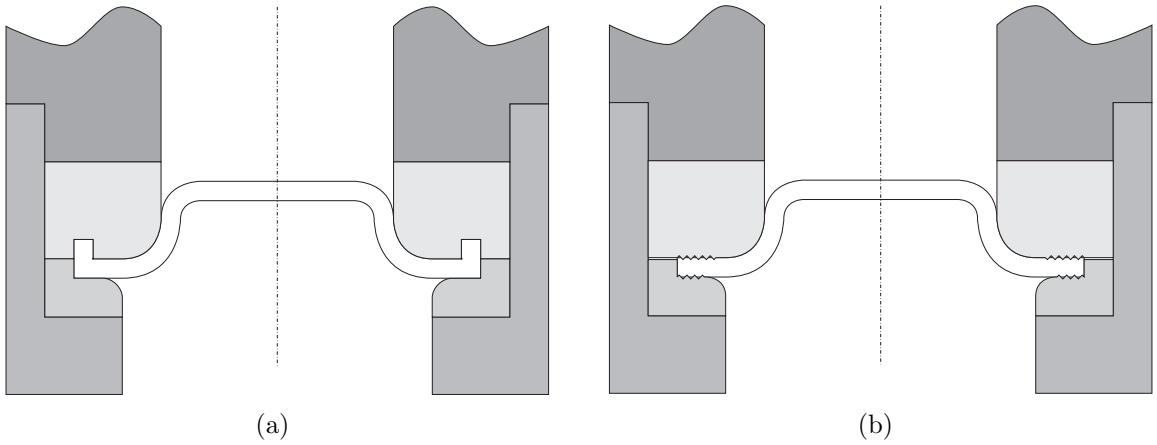

Fig. 4.9: Two proposed improvements to the clamping arrangements: (a) an injection-moulded lip and groove, and (b) a series of notches.

and before firing, that requires the dome to be manually inverted into its second stable configuration, performed with the help of a plunger. The two configurations are shown in the diagrams in Fig. 4.10.

In order to view the dome during the full quasi-static inversion process, clamping units are manufactured in clear perspex with identical dimensions to those of conventional devices, but with a flat outer surface to aid the imaging procedure. Two clamping units as shown in Fig. 4.9(a) are designed, one for *inversion*, and one for the reverse mounting, *eversion*. Due to the curvature of the inner part of the perspex shock tube the images produced cannot be directly compared to dome deformations, although the displacement of the apex of the dome will be unaffected by the refraction. A calibration tool with a millimetric scale is manufactured to fit in the shock tube, and is used to measure the apex displacements from the digital images. The experimental set-up is shown in Fig. 4.11.

The pressure is applied manually through an air cylinder at a rate of approximately $0.5bar/s$, and is measured on an analogue pressure gauge to within $\pm 2.5psi$, which is approximately $\pm 0.2bar$. The pressure is applied through to approximately $12bar$ and back to $0bar$. At around $3bar$ of pressure, the dome becomes unstable and either inverts

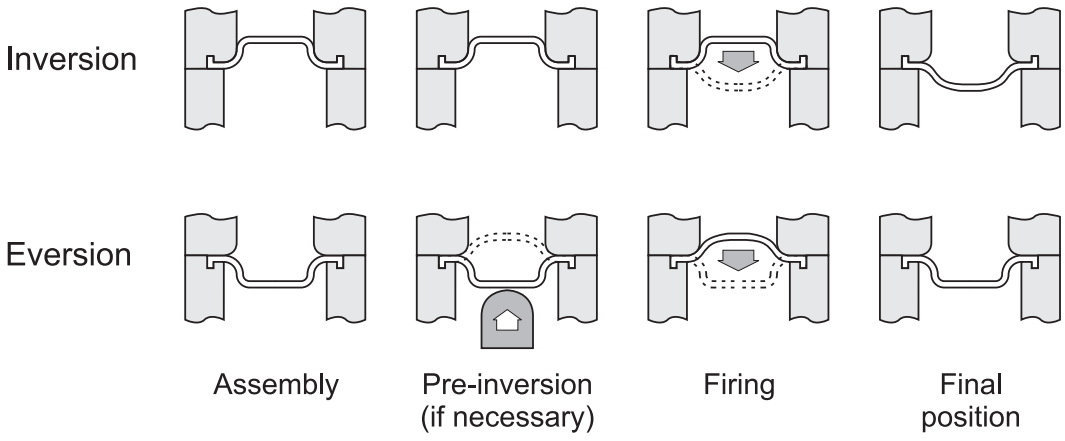

Fig. 4.10: Firing configurations: *inversion*, and the reverse *eversion*.

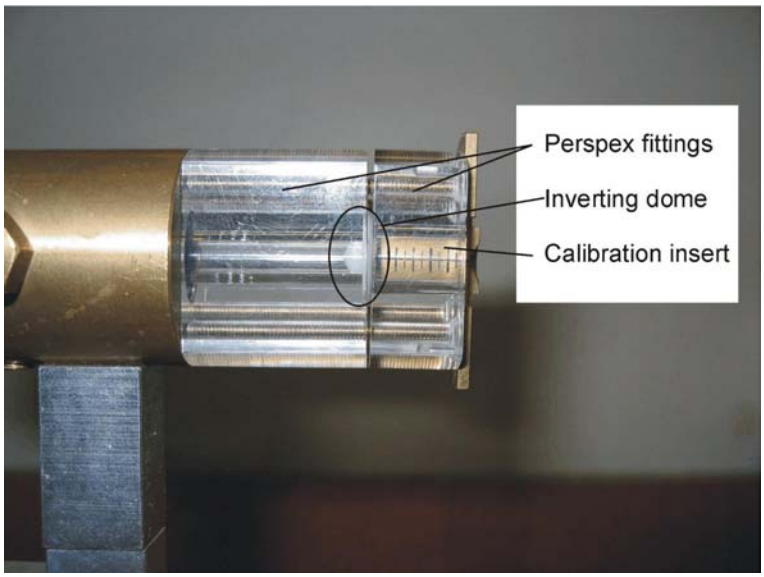

Fig. 4.11: Perspex end fittings and calibration insert used to observe dome response.

or everts, depending on the configuration. Three domes are used in the *inversion* procedure and three in the *eversion* procedure. Typical quasi-static *inversion* and *eversion* experiments are shown in Fig. 4.12. It can be seen from the set of images that the bulk of the displacement occurs rapidly over a very small pressure range. Typically the dome becomes unstable either as the pressure is being raised, or even during steady pressure, and snaps through.

The measured apex displacements are shown as a function of pressure in Fig. 4.13. During dome *inversion*, the apex of the dome is obscured by the dome itself until the snap through, and hence cannot be measured. During *eversion* this is not a problem as the dome becomes unstable before it obscures the apex. The recorded displacements of the apex correspond to the displacement of the apex of the dome on the surface that is convex in the unstrained configuration. The measurement error is $\pm 0.05mm$. In the positions where only the bottom surface is visible, the measurements are corrected by the thickness of the dome. It is assumed that the variation in thickness is small compared to the overall displacement, and that the original thickness can be used for

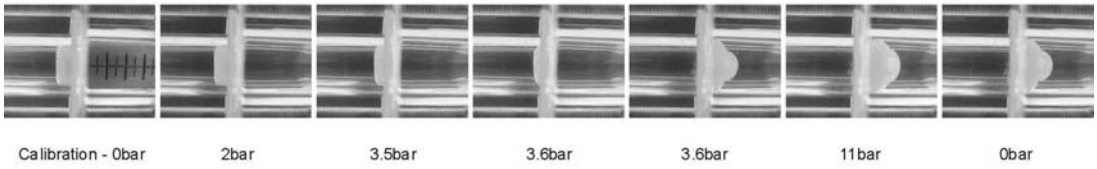

(a)

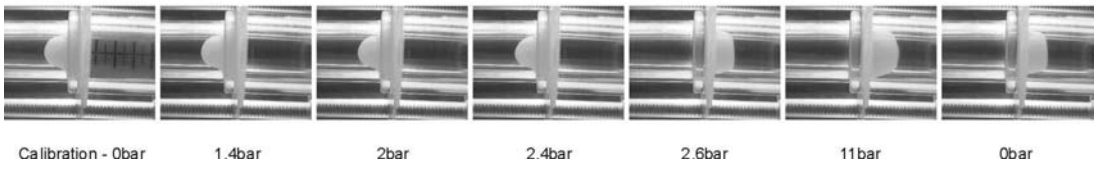

(b)

Fig. 4.12: Typical quasi-static (a) *inversion* and (b) *eversion* experiments.

this correction.

A number of useful measurements can be made from this data, including the dome travel, defined as the distance travelled by the apex between the two stable positions (at zero pressure), and the *inversion* and *eversion* pressures. This data is given in Table 4.3.

The dome travel measurement is only measured on domes that are stretched through to $12bar$ pressure, and there may be residual strain in the dome after the application of this pressure. The value is greater than the $4mm$ measured by Nabulsi [40], and

Table 4.3: Dome travel and inversion pressures for the standard injection-moulded dome.

Dome travel	$5.5mm$
Inversion pressure	$3.45 \pm 0.17bar$
Eversion pressure	$-2.38 \pm 0.21bar$

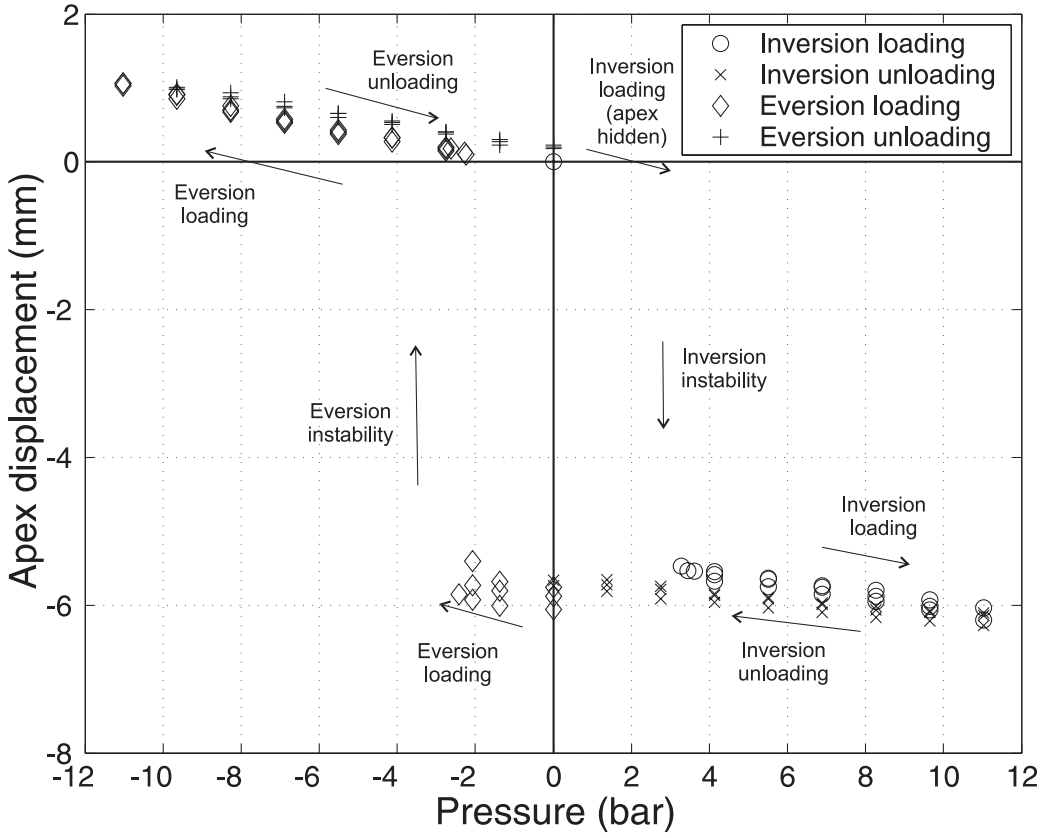

Fig. 4.13: *Inversion* and *eversion* displacements of the apex of the dome as a function of pressure. The apex of the top surface of the dome is shown.

this is due to the change in the clamping conditions as pointed out by Costigan [12]. The measurements of *inversion* and *eversion* pressures are consistent with the expected measurement error. In general there is a good level of consistency shown by the repeated experiments.

The inversion of the dome does not always occur in an axisymmetric manner under quasi-static conditions. The inversion will occur along a path of minimum energy, and due to non-uniform thickness in the dome, this path may not be the axisymmetric one. Fig. 4.14 shows a sequence of images recorded over approximately three seconds that have captured an asymmetric *inversion*.

In most domes the inversion is not perfectly axisymmetric, but the deviation from

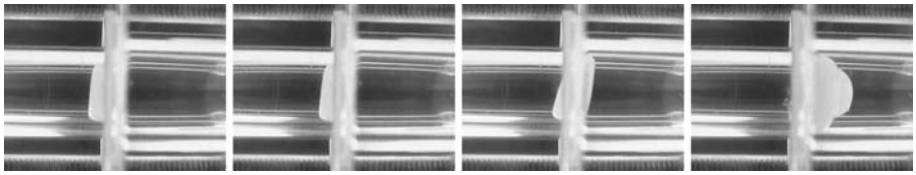

Fig. 4.14: Images of a quasi-static asymmetric *inversion*, captured over approximately three seconds.

symmetry is small. Cases such as that of Fig. 4.14 are not treated due to the complexity of the data. Under high speed it is unlikely that the dome would invert along such an asymmetric path since the rotational kinetic energy that would be required is likely to make it unfavorable.

4.4 High-speed imaging

In order to gain information about the movement of the dome during injection, a `PCO FlashCam` high-speed black and white digital camera is used in conjunction with a high-power flash unit to image the dome in the timescales occurring whilst firing. A bellows extension is used to allow the camera to focus and magnify the domes sufficiently. The camera is placed at right angles to the axis of symmetry of the dome. It is used at the minimum exposure time of $1\mu s$ with an interval of $10\mu s$ between frames, and a resolution of approximately 70pixels/mm. Dome displacement can be measured with a resolution of $\pm 0.02mm$.

A device is instrumented with a `Kulite XCQ-080` pressure transducer, flush mounted on the shock tube wall at a distance of $40mm$ from the flat face of the dome, and attached to a triggering data-logging oscilloscope, in a manner similar to that of Section 4.2. A variable delay trigger unit is designed to trigger the camera at different times after the arrival of this first trigger, and to trigger the flash unit. This enables images to be recorded at different points in the inversion. The setup used in these experiments is

shown in Fig. 4.15.

A calibration image is recorded prior to each high-speed image using the calibration insert described in Section 4.3.3. The aperture settings and distance and angle of the flashlight are adjusted regularly, and the camera is focused on the calibration insert, which is at the same distance to the camera as the axis of the dome.

Zero time is determined as the time at which the shock wave reaches the dome, as in Section 4.2, and a time of $50\mu s$ is subtracted from the total time elapsed from the first trigger at the pressure transducer, $40mm$ away from the surface of the dome. The time of individual images is determined as occurring half-way into each $1\mu s$ exposure. Typically there is a $1\mu s$ exposure every $10\mu s$, 5 exposures on each image. This places the images at $0.5\mu s$, $10.5\mu s$, $20.5\mu s$, $30.5\mu s$ and $40.5\mu s$ after the main delay. Delays between exposures of less than $9\mu s$ cause the frames on the images to be difficult to distinguish. Negative times refer to the time before the principal shock wave has reached

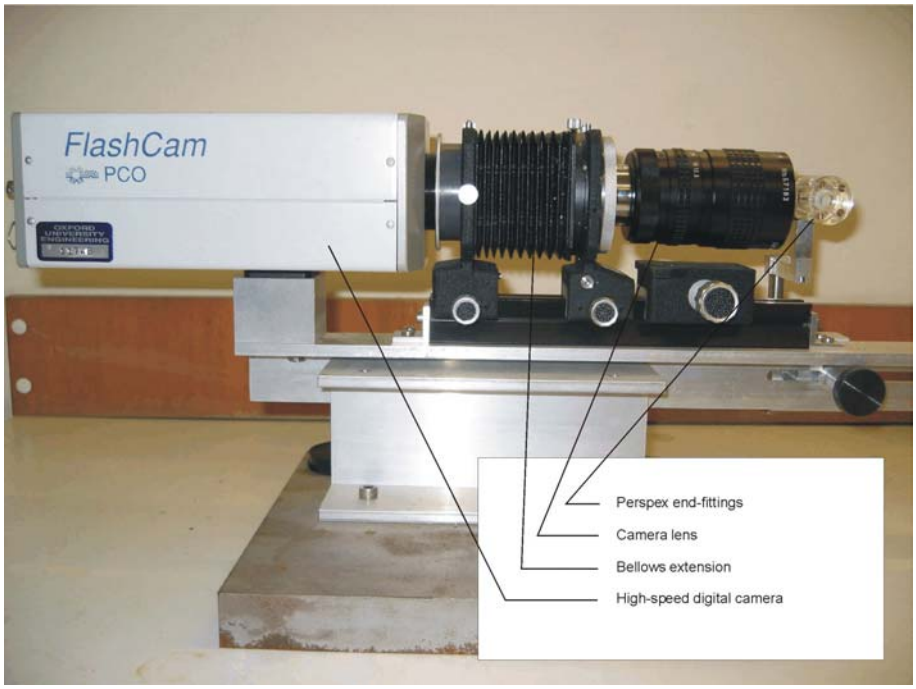

Fig. 4.15: Experimental setup used for the high-speed imaging of the inverting dome. Cables have been removed for clarity.

the dome, where there should be no movement in the dome.

For each high-speed multi-exposure image, a new dome is fitted. The device parameters are standard, with a $5ml$, $25bar$ helium button cylinder and a $30\mu m$ aluminium bursting membrane, a $65mm$ rupture chamber and a $60mm$ shock tube, all $6mm$ in diameter. The domes used are from the plain batch described in Section 4.1.

Unfortunately the apex of the dome is obstructed by other parts of the dome during the early part of the inversion process, and as such its displacement cannot be recorded in every image. Once the apex becomes visible below the dome, it is assumed that the thickness of the dome is $0.5mm$ for the purpose of recording the displacement of the top surface apex.

It can be seen from the sequence of typical high-speed camera images shown in Fig.

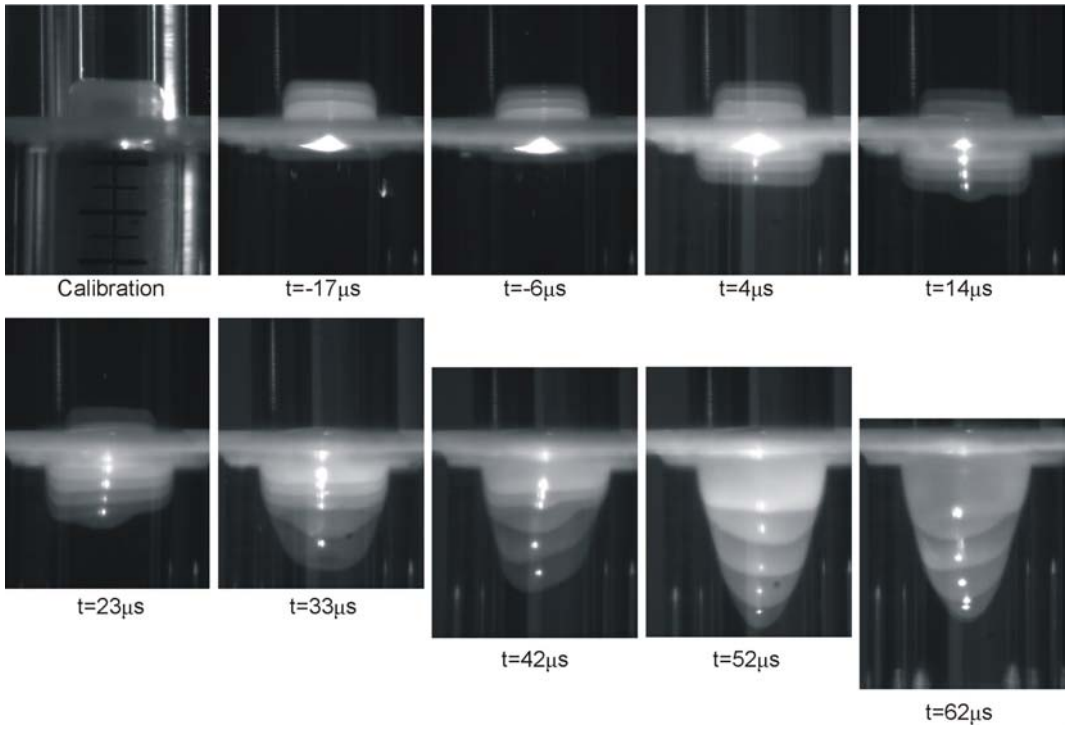

Fig. 4.16: A set of images from the high-speed camera. The time at the beginning of each exposure is marked on each image. There are 5 frames at $1\mu s$ exposure every $10\mu s$ on each image, with the first frame starting at the marked time.

4.16 that the inversion process is not perfectly axisymmetric . This is attributed mainly to the uneven thickness of real domes measured in Section 4.1.1. The measurement of the apex displacement is taken at the point of maximum deflection of the dome, even if this point is a short way off the axis of symmetry. Attempts at marking the apex of the dome prior to firing have not been successful due to the limited available lighting.

A sequence of high-speed images is taken for the dome during *inversion* , and a second sequence during *eversion* . The apex displacement data can be processed to give a mean velocity across the time between frames each time two successive frames are visible. The velocity is taken to occur at an average time between the two recordings, which is $10\mu s$, a relatively long period in comparison with the full event. The velocity is taken to be negative in the downwards vertical direction. The displacement and corresponding mean velocity measurements against time are given in Fig. 4.17.

The inversion data is limited by the fact that the apex is hidden for much of the event. Nevertheless, there appears to be a good level of consistency in the separate events with the apex displacement measurements. Table 4.4 summarises the main features of both the *inversion* and *eversion*.

Table 4.4: Maximum recorded displacements and velocities, and associated times, during high-speed *inversion* and *eversion*.

	Inversion	Eversion
Maximum displacement	9.02mm	10.05mm
Time of max displacement	$92.5\mu s$	$120.5\mu s$
Maximum recorded velocity	138.2m/s	162.4m/s
Time of max velocity	$68.5\mu s$	$85.5\mu s$

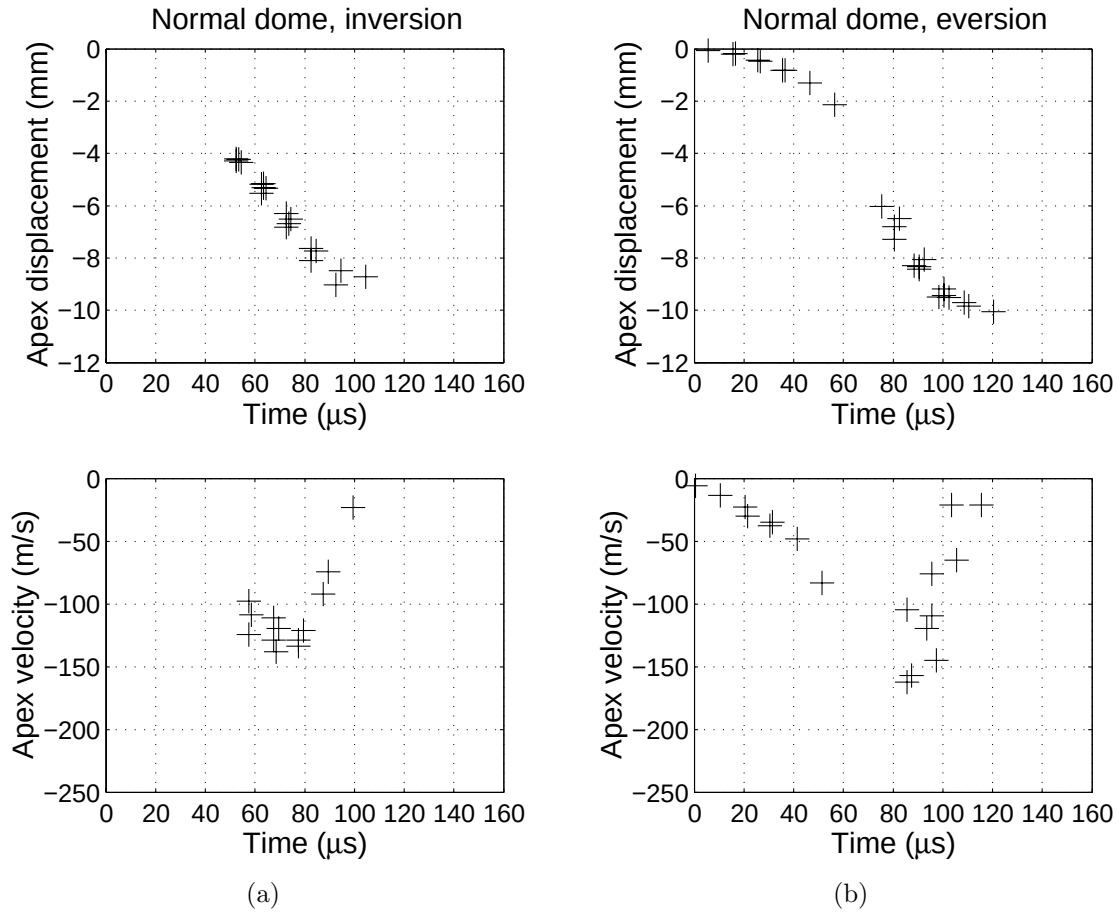

(a) (b)

Fig. 4.17: Apex displacement (above) and velocity (below) recorded from the high-speed images for domes in (a) *inversion* and (b) *eversion*.

The imaging is difficult to pursue once the dome slows down and reverses direction as it is difficult to distinguish between the superimposed frames on a single image. Nevertheless, the last velocity measurements in both cases are of the order of $20m/s$ and hence it appears that the dome velocity is about to change sign. The *eversion* produces a greater maximum displacement, as well as a higher maximum recorded velocity. This is expected due to the additional elastic strain energy that is released during *eversion*.

The recorded velocities in this batch of domes for *inversion* are low compared to Costigan's equivalent recorded velocities, but the batch of domes used has been found to be thicker, and in addition, this method is not guaranteed to capture the peak velocity.

In particular, velocity measurements taken are $10\mu s$ time averages, which are likely to be some way below the peak velocity.

A measure of the total inversion time, defined as the time between the arrival of the shock wave and the peak displacement, is given in Table 4.4. These times are long compared to Nabulsi's [40] measured inversion time measurements in fabric-reinforced domes. The reason for this is that Nabulsi is measuring the time taken for the domes to travel a shorter distance than is used here.

The high-speed imaging method requires a complicated and time-consuming procedure before successful results can be obtained. Because the curved shape of the perspex shock tube causes optical distortion, it is not feasible to record full dome displacements. Additionally, the method is not considered optimal for the measurement of the peak velocity since it can only provide time-average velocities over relatively long times compared with the total inversion times. An alternative method for indirect measurement of dome velocity will be presented in the next section.

4.5 Particle velocimetry

In this section, the velocity of the particle cloud a short way off the dome is found by measuring the time taken for the cloud to cross two light beams. This information can be used to infer the peak velocity of the dome.

4.5.1 Experimental method

A shock tube instrumented with two pairs of LEDs and photodiodes which create light beams that are interrupted by the passing particle cloud. The device is shown in Fig. 4.18 [2].

[2]The experimental set-up has been designed by George Costigan.

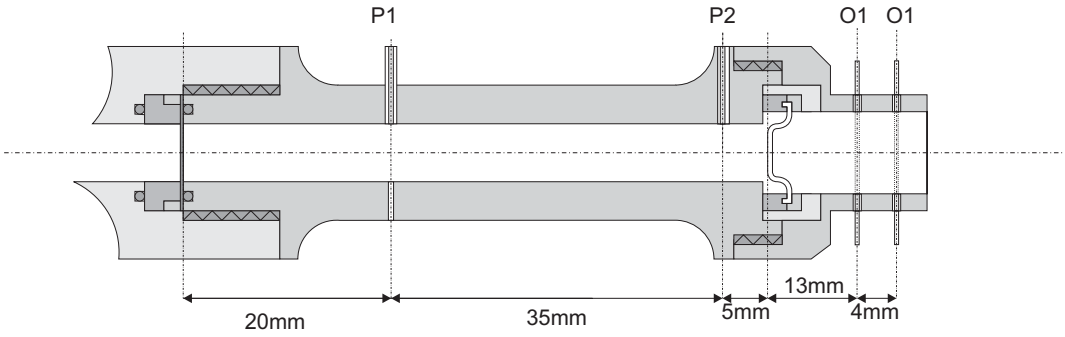

Fig. 4.18: Device for measuring particle cloud velocities. P1 and P2 are pressure transducers and O1 and O2 are light beams between LEDs and photodiodes.

The centres of the light paths are at a distance of $13mm$ (O1) and $17mm$ (O2) from the head of the uninverted dome. The light is carried to and from the device by fibre optic cables generating a light beam approximately $0.5mm$ in diameter. The signal from the photodiodes is amplified and recorded on a triggering data-logging oscilloscope. In addition, two `Kulite XCQ-080` pressure transducers are flush mounted on the shock tube wall at a distance of $5mm$ and $40mm$ from the flat face of the dome. The pressure is also recorded on the oscilloscope. The pressure rise in P1 is used to trigger the recording event.

A small amount of $38 - 53\mu m$ diameter mannitol powder is carefully distributed on the dome prior to actuation. The mass of applied powder is approximately $0.25mg$. A typical set of recorded voltages for a dome in *inversion* is shown in Fig. 4.19. Time t_0 is defined as the time at which the shock wave reaches the dome, similarly to the high-speed imaging experiment of Section 4.4.

As the particle cloud leaves the dome, it obscures the light path O1 at time t_1 and light path O2 at time t_2 creating a rise in the recorded voltages. The exact obscuration time is defined as the time at which the rate of change of voltage is a maximum. Assuming that the particle cloud travels at constant speed, the velocity of the powder v_p

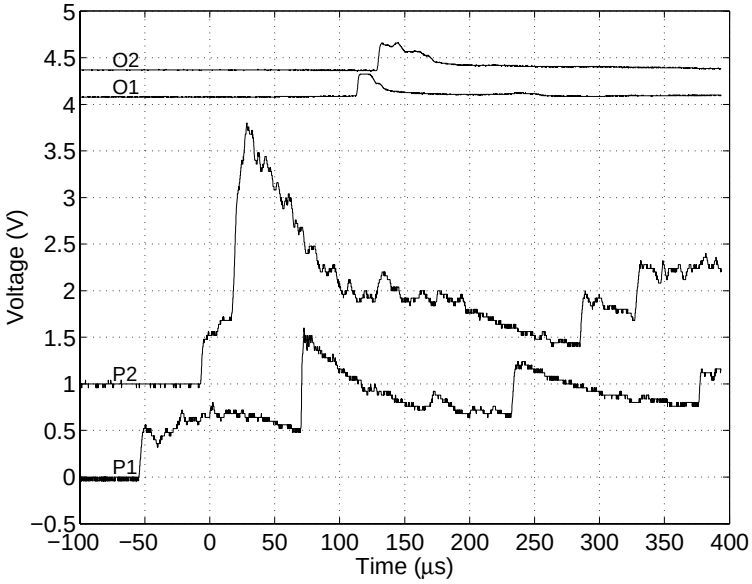

Fig. 4.19: Typical set of recorded voltages showing light beam obscuration and pressure variations.

can be evaluated from the time taken to travel between O1 and O2 from

$$v_p = \frac{d}{t_2 - t_1} \tag{4.1}$$

where $d = 4mm$. The measurement resolution in time is $\pm 0.05\mu s$ and the position of the light beams is accurate to $\pm 0.01mm$, giving a measurement uncertainty in the velocity of less than $1m/s$. The width of the light beam is $0.5mm$, and therefore a finite amount of powder must cross the beam in order to generate an obscuration signal.

4.5.2 Results

Particle velocity measurements and times at a position of $13mm$ from the head of the dome, corresponding to $12.5mm$ of actual travel (since the particles start $0.5mm$ below the top surface of the dome due to dome thickness) are recorded for domes in high-speed *inversion* and *eversion*. A second series of experiments is performed on a device without a bursting membrane where the pressure is applied slowly, and the domes invert under

quasi-static conditions. The results are shown in Table 4.5. These experiments will be coupled to the dome deformation measurements made in Section 4.4 in order to identify the time the particles detached from the dome.

There is evidence of scatter in the data that is greater than that expected from the measurement error. The domes in high-speed *eversion* produce faster powder velocities and appear to reach the first measurement point O1 sooner than in *inversion*. The shortened arrival time in *eversion* is consistent with what is expected from the faster powder velocities. The measured velocities are $20 - 40m/s$ higher than those recorded using the high-speed imaging equipment. This is probably due to the high-speed imaging measurement being a time average over $10\mu s$.

Under quasi-static conditions the domes in *inversion* move very slowly, failing to raise a well-defined powder. The *eversion* is better, reaching average velocities of $27.4m/s$,

Table 4.5: Particle velocity measurements and time at $12.5mm$ travel, the position of the first light beam, for high-speed and quasi-static *inversion* and *eversion*. The number of domes tested for each condition is shown as n.

Condition	Mean particle velocity (m/s)	SD particle velocity (m/s)	Mean time at $12.5mm$ (μs)	SD time at $12.5mm$ (μs)
High-speed				
Inversion (n=12)	162.2	5.2	117.8	5.1
Eversion (n=13)	206.9	9.6	108.9	3.2
Quasi-static				
Inversion (n=5)	2.8	0.8	-	-
Eversion (n=5)	27.4	4.9	-	-

but is still slow compared to the high-speed shock-wave application. This indicates that during the high-speed event it is the continuous application of pressure that generates the bulk of the dome acceleration, and not the snap-through effect. The snap-through buckling of the domes may contribute to faster inversions, but it appears from this data that the effect is small.

4.5.3 Discussion

It is important to note that the experimental measurements rely upon a number of assumptions if they are to give information about the peak *dome* velocity:

- The fastest velocity achieved by the dome occurs at the apex.
- The inversion of the dome is axisymmetric.
- The powder leaves the dome at the time of fastest velocity.
- The obscuration time refers to the obscuration of the centre of the light beam.

Let us now discuss the validity of these assumptions. It is intuitive to assume that the fastest velocity will occur at the apex of the dome, since it is the point of the dome that has the greatest freedom of movement. Although no experimental measurements have been made to confirm this, dynamic finite element modelling to be reported in Chapter 5 will show that this is the case in domes with a nominal geometry.

We have observed from high-speed imaging that the inversion of domes is not always perfectly axisymmetric . This may result in the peak velocity occurring off-centre, and missing the light beam all together. The measurement would then refer to a slower portion of the particle cloud. In addition, if the powder crossing the light beam is not travelling along the axis, and has a radial component of velocity, only the axial component will be measured by this technique.

The coupling of this experiment with measured deformations from the high-speed imaging will be able to identify the approximate time at which the particles are released from the dome. Results to be presented in Section 5.3.6 will addressed the problems of the powder leaving the dome too early and not being given the maximum possible velocity due to early deceleration of the dome using FE analysis data.

The obscuration is a relatively rapid event, with the voltage signal varying from a minimum value (unobscured) to a maximum value (obscured) in $2 - 3\mu s$. The actual magnitude of the voltage increase due to the obscuration is not constant across all tests due to its sensitivity to the alignment of the fibre optic endings, in addition to variations in the amount and distribution of powder on the dome. Therefore the peak in the rate of change of voltage is used to determine a consistent obscuration time. Using a simplistic approach where the particle cloud is a flat solid body, the greatest rate of change of obscuration will occur when the solid body is traversing the centre of the light beam. Hence, although the light beam itself is $0.5mm$ in diameter, the time measurement is intended to refer to the moment at which the centre of the light beam is obscured.

4.5.4 Combining dome and particle paths

Fig. 4.20 reproduces the diagrams shown in Figure 4.17 based on measurements made from the high-speed imaging and the data from the particle velocimetry experiments.

Here zero displacement refers to the initial position of the particles on the underside of the dome. The position of the light beams O1 and O2 are at $12.5mm$ and $16.5mm$, and the region of particle measurement is shown with a solid line in the displacement diagrams. The velocities are then obtained using (4.1), and are shown as solid lines in the velocity diagrams. Extrapolation of the particle position and velocity outside the range O1 to O2 is shown as a dotted line.

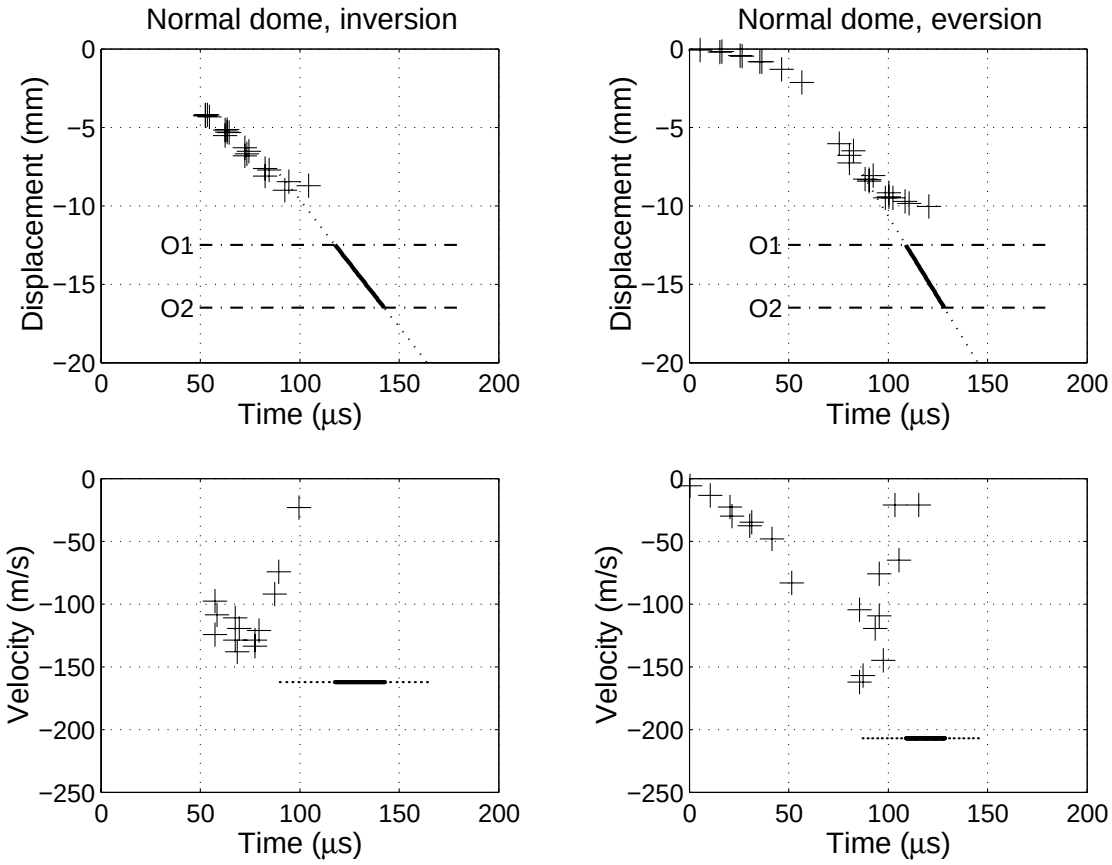

(a) (b)

Fig. 4.20: Displacement and velocity of the apex of the dome (cross marks) and the particle cloud (solid line) in high-speed *inversion* and *eversion*. Extrapolation of the particle cloud position is also shown (dotted line).

In the dome *inversion* experiment the linear extrapolation of the particle path crosses the dome position at a time of approximately $95\mu s$. This is the time at which the particles appear to leave the surface of the dome. Hence the fastest velocity appears to be achieved at the very end of the inversion. In dome *eversion* , the particles appear to leave the dome earlier in time, between 60 and $80\mu s$. The two experiments complement each other well, and have given some indication as to when the fastest portion of the particle cloud detaches from the dome.

4.5.5 Comparison with old dome batches

The same particle velocimetry technique has been used by Costigan [12] to measure particle cloud velocities. Costigan measured particle velocities of between $220 - 240 m/s$ on a different batch of domes with the same nominal geometry. A small number of unused domes from Costigan's batch have been tested using particle velocimetry in *inversion* only, and subsequently sliced and measured using the microtome method described in Section 4.1.1. Due to the limited number of domes available from this batch, domes are sliced along the injection-moulding axis only. A set of domes from the new plain batch is tested and subsequently sliced along the axis for comparison. The measured particle velocities against mean measured thickness for each dome are shown in Fig. 4.21.

Although the number of tests is limited, the effect of the mean thickness parameter can be observed. Domes from the thinner batch produced velocities in excess of $200 m/s$,

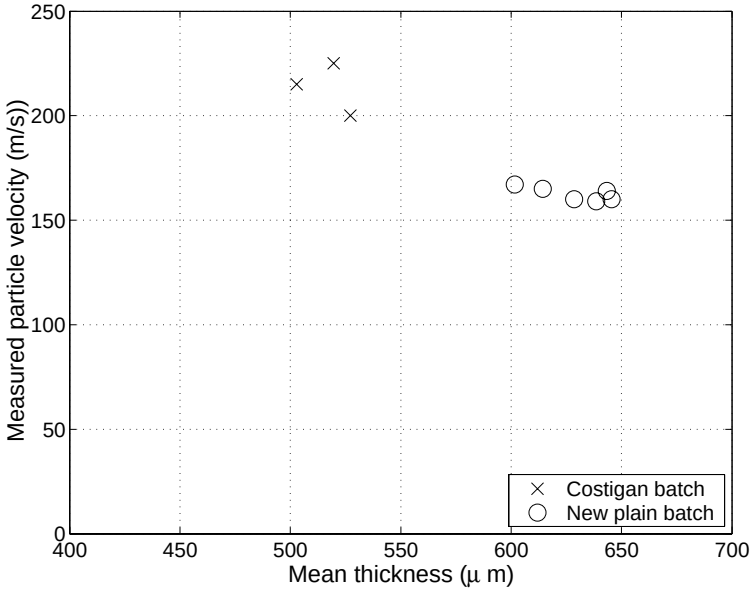

Fig. 4.21: The measured particle velocity shown for domes where the mean thickness along the injection-moulding axis has been measured.

close to the velocities measured by Costigan [12]. Domes from the new plain batch are thicker, and produce velocities of around $160m/s$. Clearly the mean thickness parameter is not sufficient to fully describe the effect of inversion on a 3-dimensional dome. This investigation will be pursued with the use of finite element modelling in Chapter 5.

4.6 Quasi-static dome burst

A number of quasi-static burst tests have been performed using identical equipment to that used in the disc burst tests of Section 3.4.2, but using inverting domes instead of plain discs. Domes are mounted in both directions, with the convex face in the shock tube as is done in *inversion*, and with the concave face in as is done in *eversion*. Hence, domes burst in *inversion* have to snap through prior to burst, and domes burst in *eversion* are pre-inverted prior to the application of pressure using a plunger, as explained in Section 4.3.3, and snap through as the pressure is applied. The measurement accuracy of the pressure is $\pm 1bar$.

The burst pressure is compared to the expected burst pressure using an injection-moulded disc of equivalent thickness evaluated from the data obtained in Section 3.4.2. The results are shown in Table 4.6.

The burst pressure measured in the domes both in *inversion* and *eversion* is a little below the equivalent for an injection-moulded disc. The small difference, which is within the measurement accuracy, is likely to be due to the added deformation that dome *inversion* applies on the domes. It is noted that while most of the domes failed near the apex, some failed between the apex and the side wall region, in an area where the injection-moulding produced a weakening effect. The small differences in burst pressure indicate that the defects in the moulding are not highly significant effects when it comes to quasi-static dome burst. The stress state of the apex of the domes at burst will be

Table 4.6: Mean and standard deviation (SD) in dome burst pressure in quasi-static *inversion* and *eversion*, and the equivalent expected burst pressure for injection-moulded sheet.

Condition	Mean burst pressure (bar)	SD burst pressure (bar)
Dome *inversion* (n=8)	14.5	0.5
Dome *eversion* (n=8)	14.9	0.4
Equivalent injection-moulded disc, mean thickness = $640\mu m$	15.6	

investigated using finite element modelling in Section 5.2.2.

4.7 Dynamic dome burst

The experiments of Section 4.6 indicate that the quasi-static burst pressure of inverting domes is significantly lower than the peak pressure reached in the early part of the inversion. The peak pressure is typically around $21bar$, and this occurs around $25\mu s$ after the shock wave reaches the dome. At this instant in time, the dome has just begun the inversion, and has not had sufficient time to stretch and burst. The pressure history of a number of points in the device is observed for approximately $4ms$ in Fig. 4.22.

It is clear that there is an initial part of the pressure which is dominated by the arrival of the shock wave , followed by a period dominated by oscillatory transients due to the shock reflections, settling to an exponential decay in the mean pressure in the longer term. Although the peak pressure due to the shock wave is higher than the static burst pressure of the domes, it is present only for a very short time, early on during

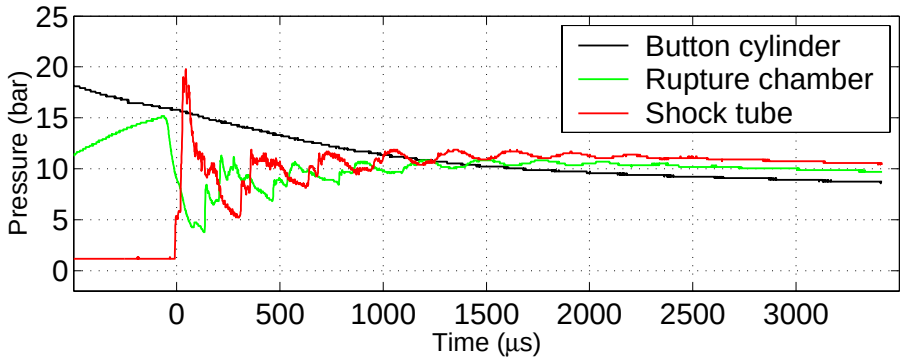

Fig. 4.22: Pressure history recorded for $4ms$ at the button cylinder, rupture chamber and shock tube.

the inversion at around $t = 30\mu s$. At this time the apex of the dome has moved less than $4mm$ and is not fully inflated. Immediately after the shock wave there is a drop in pressure, and from this time through to around $1ms$ the pressure at the dome is lower than the button cylinder pressure, and is dominated by shock wave reflections. At around $1ms$ the pressure at the dome is close to the pressure elsewhere in the device, and is subject to a gradual decay that is controlled by the size and shape of the vent hole described in Section 2.1.1.

If we can ensure that the pressure at the dome is less than the static dome burst pressure *after* the inversion has taken place, and that the decay in pressure ensures that the pressure continues to drop after that, then burst will not occur. An approximate analysis is performed next assuming that there is an instantaneous adiabatic mixing of the helium and the air, and that the mixture subsequently leaves the device through the vent-hole. The precise pressure characteristics including shock-wave reflections are complex, and would best be tackled with computational fluid mechanics methods.

We wish to find the pressure of the air-helium mixture after the adiabatic mixing and after all transients have disappeared. For this calculation we assume that no gas is allowed to escape through the vent hole. We use the adiabatic pressure - volume

relationship [14]

$$pV^{\gamma} = constant \tag{4.2}$$

for the helium (He) in the button cylinder, the air in the rupture chamber (Air R) and the air in the shock tube (Air S), as shown schematically in Fig. 4.23. For each component we have

:

$$p_{He}V_{He}^{\gamma_{He}} = C_1 \qquad p_{atm}V_{AirR}^{\gamma_{Air}} = C_2 \qquad p_{atm}V_{AirS}^{\gamma_{Air}} = C_3 \tag{4.3}$$

where p_{He} is the pressure in the button cylinder, p_{atm} is atmospheric pressure, $V_{He}, V_{AirR}, V_{AirS}$ is the volume of the button cylinder, rupture chamber and shock tube respectively, $\gamma = \frac{\tilde{c}_p}{\tilde{c}_v}$, the ratio of specific heat capacities at constant pressure $\tilde{c}_p$ and constant volume $\tilde{c}_V$, both of which are gas constants, and C_1, C_2, C_3 are constants. Using $V_{He} = 5.00 \times 10^{-6}m^3$, $V_{AirR} = 1.84 \times 10^{-6}m^3$, $V_{AirS} = 1.69 \times 10^{-6}m^3$, $\gamma_{He} = 1.63$, $\gamma_{Air} = 1.4$ and $p_{He} = 25 \times 10^5 Pa$ we can evaluate the constants as

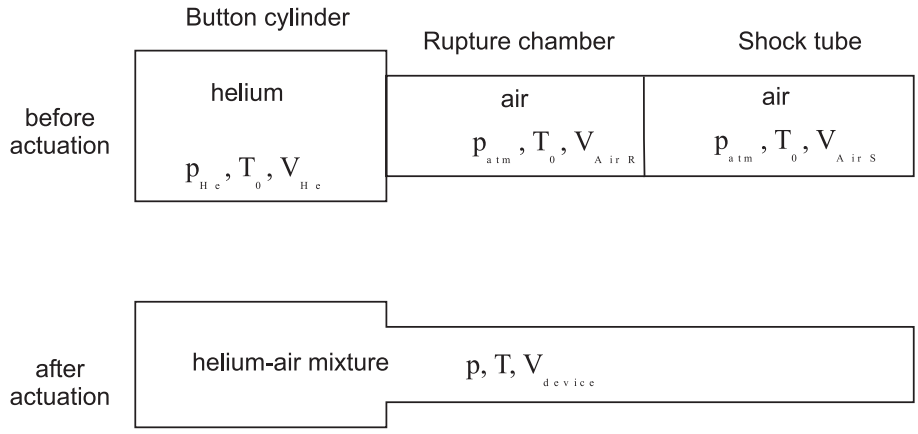

Fig. 4.23: Adiabatic mixing of the helium and air in the device.

$$C_1 = 5.718 \times 10^{-3} J \qquad C_2 = 0.935 \times 10^{-3} J \qquad C_3 = 0.830 \times 10^{-3} J \tag{4.4}$$

The pressure of the mixture p can be found from the sum of the individual contributions of the three components after expansion,

$$p = \frac{C_1}{V_{device}^{\gamma_{He}}} + \frac{C_2 + C_3}{V_{device}^{\gamma_{Air}}} = 10.69 \times 10^5 Pa \tag{4.5}$$

where $V_{device} = 8.53 \times 10^{-6} m^3$ is the total volume of the device. The temperature after a fully adiabatic expansion can be found from the ideal gas equation

$$T = \frac{pV_{device}}{nR} \tag{4.6}$$

where n is the total number of moles of gas and R is the gas constant. The number of moles of gas can be found from the initial conditions

$$n_{He} = \frac{p_{He} V_{He}}{RT_0} \qquad n_{Air} = \frac{p_{atm}(V_{AirR} + V_{AirS})}{RT_0} \tag{4.7}$$

where T_0 is the initial temperature. Using $T_0 = 293K$ we find the temperature after expansion as $T = 208K$. If the temperature were to rise back to atmospheric, the pressure p_{Tatm} would reach

$$p_{Tatm} = \frac{nRT_0}{V_{device}} = 14.04 \times 10^5 Pa \tag{4.8}$$

Assuming a full thermal recovery, the pressure becomes close to the burst pressure of the domes, measured as 14.5bar in inversion. In practice the effect of the vent hole dominates the mixing, and we can see from Fig. 4.22 that after the transients have attenuated, at around $1.5ms$, the average pressure in the device is around 11bar, close

to the value predicted from equation 4.5, and that the pressure continues to drop after that, even though the temperature may be slowly rising back.

In order to estimate the speed of decay in pressure within the device through the vent hole, we consider only the effect of the helium and use the derivation of Douglas *et al* [14] for the maximum mass flow rate of gas from a reservoir through an orifice producing choked flow, given as

$$\dot{m} = \frac{C_d A_{vent} p}{\sqrt{T_0}} \sqrt{\left[\frac{\gamma W_{He}}{R} \left(\frac{2}{\gamma + 1} \right)^{\frac{\gamma+1}{\gamma-1}} \right]} \tag{4.9}$$

where C_d is a discharge coefficient between 0 and 1 depending on specific conditions of flow such as friction and reservoir shape, A_{vent} is the cross-sectional area of the vent hole, $\gamma = \frac{\tilde{c}_p}{\tilde{c}_v}$, the ratio of specific heat capacities of helium at constant pressure $\tilde{c}_p$ and constant volume $\tilde{c}_V$ which are gas constants, and W_{He} is the molecular weight of helium. The reason why there is no outlet pressure dependance on the mass flow rate is that any effect of the outlet pressure could only propagate through the vent hole at the velocity of sound. Since the velocity of the gas in the vent hole is sonic, the nozzle is choked and no effect is felt. The flow becomes unchoked only once the pressure in the device has dropped significantly, and then different equations will apply [14]. Pressure is related to mass through the ideal gas equation, which can be differentiated with respect to time to give

$$\dot{p} V_0 = \frac{\dot{m} R T_0}{W_{He}} \tag{4.10}$$

and assembling (4.9) and (4.10) producing the linear first order differential equation in pressure

$$\dot{p}\tau_{discharge} + p = 0 \tag{4.11}$$

with time constant

$$\tau_{discharge} = \frac{V_0}{C_d A_{vent}} \sqrt{\left[\frac{RW_{He}}{T_0}\left(\frac{\gamma+1}{2}\right)^{\frac{\gamma+1}{\gamma-1}}\right]} \tag{4.12}$$

Using $V_0 = 8.53 \times 10^{-}6m^3$, $\gamma = 1.63$, $A_{vent} = 7.85 \times 10^{-7}$, $W_{He} = 4 \times 10^{-3}kg/mol$ and $C_d = 1$, the time constant is $\tau_{discharge} = 0.0193s$. Although this time constant is relatively large, the pressure at the dome continues to be well below the burst pressure throughout.

In practice, Fig. 4.22 shows that the behaviour is more complex. The effect of shock wave reflections is visible until around $2.5ms$, and the initial decay in pressure is faster than predicted by the theory since initially the pressure at the vent hole is higher than the average pressure in the device. This ensures that the pressure at the dome never exceeds the burst pressure after the initial shock wave has passed.

Equation (4.12) shows that the time constant is inversely proportional to the area of the vent-hole. Hence, increasing the size of the vent hole can reduce the time taken for the pressure to drop. However, if the vent-hole is made too large, it will adversely affect the magnitude of the primary shock wave. If the vent-hole was removed, the pressure in the device after the expansion and after the temperature returns to atmospheric would be very close to the average burst pressure of the domes. The vent hole is therefore considered important in ensuring that domes do not burst during use of the device.

4.8 Summary and conclusions

This chapter has investigated the behaviour of the inverting dome using a range of complementary experimental techniques. Section 4.1 has shown that *actual* injection-

moulded domes exhibit geometrical differences from their nominal specifications, and that these differences can be significant. Using a microtome slicer and subsequent optical microscopy, the thickness of a batch of inverting domes has been investigated, and although domes are nominally $0.5mm$ thick throughout, the measurements have recorded thicknesses ranging from $0.5mm$ to $0.75mm$. Domes from a previous study have also been observed, and recorded thicknesses ranged from $0.37mm$ to $0.72mm$. Due to these substantial differences from specifications, it is important to record dome geometry in order to compare different batches.

The pressure during injection at a distance of $5mm$ from the top surface of the dome has been measured by repeat tests in Section 4.2. The salient points on the pressure-time function compare well to Costigan's [12] theoretical values. This data will be used in the simple mechanical model and as an input to dynamic finite element modelling in the next chapter.

The highly non-linear response of the dome to an applied pressure has been investigated under quasi-static conditions in Section 4.3. A small amount of hysteresis has been observed, and is explained by the cyclic tests performed on Hytrel specimens in Section 3.3.5. The pressure at which the dome becomes unstable and snaps through has been recorded both for *inversion* and *eversion*. Under quasi-static conditions the inversion is not always axisymmetric.

The displacement of the dome under high-speed injection is observed in Section 4.4 using high-speed imaging equipment. A number of recordings of the position of the apex of the dome have been made, and an estimate of the peak velocity during injection in both *inversion* and *eversion* has been obtained.

The velocity of the drug particle cloud is recorded using a light-obscuration technique in Section 4.5. The particle cloud velocities recorded are faster than the maximum peak

velocity recorded for the dome during high-speed imaging, due to differences in the measurement technique. A reconstruction of the position and velocity of the apex of the dome and the powder has been performed, and indicates that particles leave the dome at approximately $95\mu s$ in *inversion* and $80\mu s$ in *eversion*. Eversion has produced mean powder velocities of $206.9m/s$ and *inversion* of $162.2m/s$. Although the *inversion* velocity is slower than that recorded by Costigan [12] on a thinner batch of domes, when the data is shown as a function of mean dome thickness there appears to be correlation between the thickness and the velocity that explains this discrepancy.

An analysis of the quasi-static burst pressure of domes performed in Section 4.6 has shown that the domes burst at a pressure very close to that of an injection-moulded disc of equivalent thickness. Pressure measurements in Section 4.7 have shown that a vent-hole of $1mm$ diameter is suitable for reducing the pressure in the device sufficiently fast to prevent dome burst.

The techniques developed in this chapter will prove useful in verifying the quality of the finite element modelling of Chapter 5. They will also be used to investigate experimentally a number of modifications and improvements to domes in chapters 6 and 7.

Chapter 5

Numerical modelling

The previous chapters have provided the tools needed to set up a finite element model of inverting domes. Real domes have a different geometry from the specifications, and this will be an important aspect to be considered. Section 5.1 will identify the parameters needed for any FE simulation of an inverting dome, from the material model through to the meshing, geometry and input and boundary conditions. A mesh representing the *actual* domes measured through the microtome slicing technique of Section 4.1.1 will be constructed.

The quasi-static behaviour of domes will be used as a benchmark experiment to ascertain the level of mesh refinement required, and the post-buckling behaviour will be investigated. Using the 3-d reconstruction of *actual* domes, a number of dynamic analyses will be run to optimise the level of material damping required for the high strain rate behaviour of the domes. The model will then be used to investigate both *inversion* and *eversion* in domes of nominal specifications. The data from the FE simulations will then be used to follow the paths of model particles on the dome's surface as they are accelerated and leave the dome.

A simple dynamic mechanical model will be presented in Section 5.4 that uses a number of results from static and frequency FE simulations to model dome inversion

as the movement of a point mass on a non-linear spring in response to a time-varying force.

Section 5.5 will then use FE analysis to look at the effect of a number of model manufacturing imperfections that may come as a result of poor injection moulding conditions, such as misalignment of the moulding plates.

5.1 Simulation parameters

5.1.1 Material properties

The mechanical response of Hytrel to stress has been shown in Chapter 3 to be highly non-linear, mildly time-dependant, affected by molecular orientation and thermal history, and exhibiting a complex load-unload-reload cycle. A material model that is compatible with finite element formulations that encompasses all of these effects is not readily available, and a hyperelastic model is chosen instead. Hyperelasticity defines the response by means of a strain energy function that depends on the deformation, and is a reliable way to handle the large displacements that are expected in dome deformation. One of the principal drawbacks of the hyperelastic model is that it assumes that all of the strain is fully recoverable, and we know that this is not the case with Hytrel. The strain recovers fully at low strains of below 25%, but at higher strains the residual strain on unloading rises to a significant proportion of the load strain, as discussed in Section 3.3.7. However, provided that in the inverting dome there is no significant loading and unloading, especially at high strains, the model ought to be satisfactory.

There are a number of approaches to the form of the strain energy function [57], and the Ogden form [43] is selected for its good compromise between stability and an accurate fit to the data with appropriate parameters. The form of the Ogden strain energy function U for use with `ABAQUS` [23] is

$$U = \sum_{i=1}^{n} \frac{2\mu_i}{\alpha_i^2}(\lambda_1^{\alpha_i} + \lambda_2^{\alpha_i} + \lambda_3^{\alpha_i} - 3) + \sum_{i=1}^{n} \frac{1}{D_i}(J^{el} - 1)^{2i} \tag{5.1}$$

where n is the order of the Ogden function, μ_i and α_i and D_i are material parameters to be fitted to the data, λ_i are the principal stretches and J^{el} is the elastic part of the volume ratio. Assuming that there is no expansion/contraction due to temperature, J^{el} is simply given by

$$J^{el} = \lambda_1 \lambda_2 \lambda_3 \tag{5.2}$$

but when thermal expansion is significant, it must be accounted for as given in [23].

Commonly in static analyses involving elastomers, the polymers are assumed to be incompressible, and hence the second summation of (5.1) disappears. This can be justified for Hytrel since the bulk modulus is several orders of magnitude greater than the shear modulus, and Poisson's ratio is 0.45 [16], and additionally the inversion of the dome does not put the material under a particularly hydrostatically constrained loading. In dynamic analyses incompressibility cannot be imposed for reasons of numerical stability, and a compromise is reached between a high value of Poisson's ratio and the speed and accuracy of the solution.

Hence an Ogden formulation of order n has $3n$ adjustable parameters if it is compressible, and $2n$ if it is not. The true stress t_j in a given principal direction j is then found by differentiation of U with respect to the stretch in that direction, from

$$t_j = \lambda_j \frac{\partial U}{\partial \lambda_j} \qquad (j = 1, 2, 3) \tag{5.3}$$

There is no simple solution to the problem of dealing with the anisotropy that results from injection-moulding. A material model dealing with the anisotropy would need to be

coupled to flow simulations in order to obtain the orientation distribution in the inverting dome. This would be a lengthy procedure, and there are likely to be variations across an injection-moulding batch as the mould warms up. In addition, we have observed that the flow is sensitive to small changes in mould thickness. The basic Ogden formulation does not cater for anisotropy. Later formulations are able to deal with some symmetric forms of anisotropy [44] but these are currently not implemented in `ABAQUS`. Hence, we will assume that the material is isotropic, and that it behaves in a manner most similar to the tests on the injection-moulded discs cut at 45° to the injection-moulding axis to account for an *average* orientation.

The `ABAQUS` software performs a non-linear optimisation for the parameters of the Ogden model to a given set of stress-strain tests. A more complex model is computationally more demanding, and hence the simplest model with a reasonable fit is chosen. After considerable experimentation with the parameter n and the range of input data on which to perform the optimisation, the value of $n = 2$ and input data in tension only from 0 to 200% strain is used. A 1-element model is used to verify the quality of the fit, and to observe the limitations of the model. Fig. 5.1 compares the stress-strain obtained in uniaxial deformation for an Ogden form of order $n = 2$ to the experimental data from Section 3.2.2. Although the optimisation is performed on the tensile data alone, compressive data from Section 3.2.3 at a similar strain rate is also shown for comparison. The use of combined tension and compression data in the optimisation produced a much poorer fit to the data in tension and little improvement in compression.

The model shows a good fit to the data in tension through to 100% strain, and a reasonable fit through to 200% strain. In compression, the model follows the experimental data only to about -10% strain. Thereafter the model produces a much stiffer material than has been observed in the experiments. The deformation of the inverting

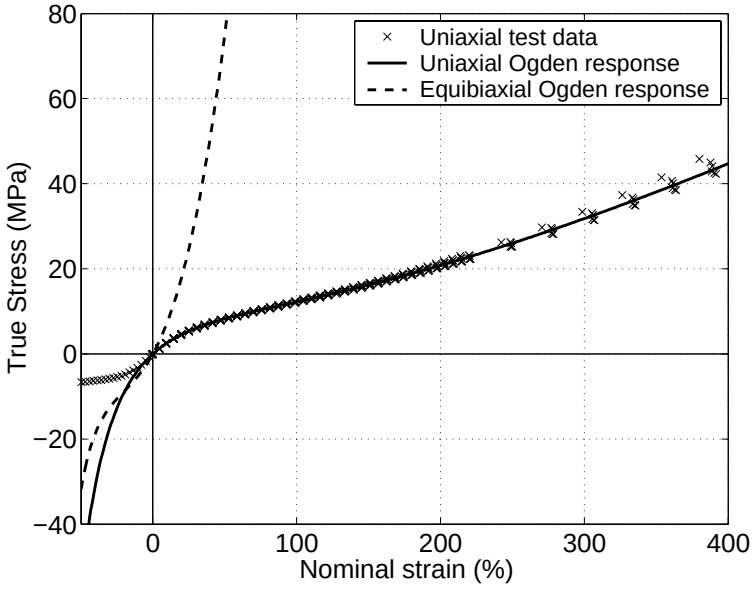

Fig. 5.1: Uniaxial and equibiaxial stress-strain behaviour of Hytrel for an Ogden strain energy functions of order $n = 2$. Tensile and compressive experimental data is also shown.

dome is not expected to exceed the range -10% to 100% strain, and hence this model is considered appropriate. The Ogden parameters for this model are given in Table 5.1.

The model is based on data at relatively low strain rates, and is more appropriate for use with quasi-static deformations. No suitable data for Hytrel 4068 at very high strain rates is available, and hence the low strain rate data is currently the closest estimate. At the high strain rates involved in the high-speed inversion the model is likely to be too flexible, as has been observed in the tests over a range of strain rates of Section 3.3.1.

Table 5.1: Parameters from the Ogden model of order $n = 2$, optimised on the injection-moulded disc data.

i	μ_i	α_i	D_i
1	-0.169×10^8	0.024	0.979×10^{-8}
2	0.271×10^8	-1.816	0

The Ogden model allows the computation of the mechanical response to complex 3-dimensional strain states. Other than the behaviour of the dome itself, no specific experiments have been performed to explore strain states more complex than simple uniaxial. Therefore it is difficult to judge directly whether the Ogden model provides a good representation of the response in complex strain states. There are a number of parameters that can be extracted from an Ogden model for direct comparison with the literature [16], such as the shear modulus μ_0, and the bulk modulus K_0, given by

$$\mu_0 = \sum_{i=1} n\mu_i \qquad\qquad K_0 = 2/D_1 \tag{5.4}$$

and the shear modulus from the Ogden model of $37.3MPa$ is very close to that of Hytrel 4068 ($37.8MPa$) while the bulk modulus of $200MPa$ is slightly higher ($183.3MPa$).

Another means of comparison with a more complex stress state can be achieved from the biaxial burst tests of Section 3.4.2. There it has been shown that injection-moulded material fails under an equibiaxial stress state of $24.6 \pm 1.4MPa$ and has been measured to be under equibiaxial strain of approximately 135%. The Ogden model predicts only 25% strain at this equibiaxial stress. The Ogden model predicts a larger equibiaxial stress at a given strain compared with the single experimental value. During inversion the dome deformation is mainly a bending problem, and the inability to accurately model equibiaxial stress states is unlikely to be of concern. The material model would be inappropriate to model significant inflation, such as may occur after the inversion is complete.

The Ogden model has been calibrated for smaller deformations than those that occur at material failure, as well as from a different strain state, but nevertheless the biaxial behaviour can be compared to the failure stress and strain. In equibiaxial tension the strain corresponding to around $25MPa$ from the Ogden model is around 125% strain,

a little lower than was found at material failure from the burst tests. The Ogden model behaviour for equibiaxial stress is shown in Fig. 5.1.

The extent of the permanent deformation in the material at more complex strain states has not been investigated experimentally. The hyperelastic model assumes that all deformation is fully recoverable, and that the sample unloads along the same stress-strain curve as it loads on. Although experiments have shown this not to be true, during dome deformation there is only limited and localised unloading and reloading, and hence this is a reasonable approximation to make.

5.1.2 Dome geometry meshing

The nominal geometry of the inverting dome has been presented in Section 2.2.1. In order to provide a flexible approach to meshing that is adaptable to a range of inverting domes with similar geometries, meshing code is written in `Matlab` [35]. The geometry is defined by straight and curved segments and is subsequently subdivided into a number of elements along the length and thickness, as shown in Fig. 5.2.

Starting with the production of an axisymmetric mesh for simplicity, only the cross-section needs to be defined. It is preferable to achieve elements with aspect ratios, or the ratio of the length of the sides close to 1; hence, in order to obtain approximately square elements, the ratio of elements along the cross-section to elements across the thickness

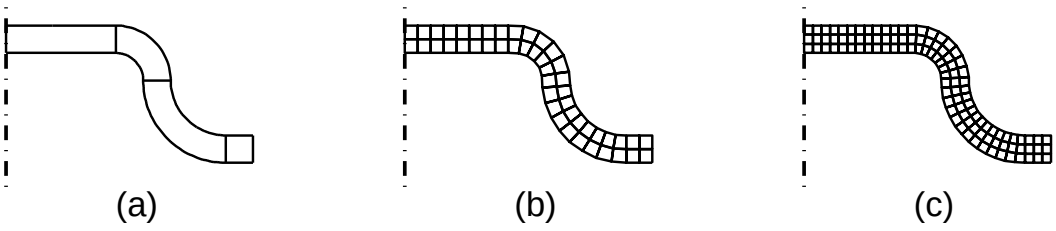

Fig. 5.2: Construction of the inverting dome mesh. (a) The geometry is defined by straight or curved segments; two meshes containing (b) 24×2 and (c) 36×3.

is fixed at 12 to 1. The elements produced along the curved paths will not be exactly square, but as long as the radius of curvature is much larger than the element size, the element aspect ratio will be close to 1. Two such meshes are shown in Fig. 5.2(b) and 5.2(c), with 24×2 and 36×3 elements. An additional boundary condition of vertical movement only at the axis of symmetry needs to be set on axisymmetric meshes.

The elements used in axisymmetric meshes are 4-noded quadrilaterals with axisymmetric deformation. The use of axisymmetric analyses is much more efficient than that of the equivalent 3-dimensional analyses as the number of elements is substantially reduced, and the number of degrees of freedom is also reduced. In theory, the inversion of a perfect dome is a process with axisymmetric input and boundary conditions taking place in an axisymmetric environment. In practice, however, even though the input and environment are axisymmetric, the inversion of the dome may not be. In Section 4.3.3 the quasi-static inversion of domes was observed not to be axi-symmetric, and some of the high-speed images in Section 4.4 also indicated asymmetry. The most likely reason behind the asymmetry is probably the *actual* dome itself, which is not perfectly symmetric, as was shown in the cross-sections of Section 4.1.1. Hence, there is a need for 3-dimensional analyses to verify when axisymmetric analyses can be considered valid, and to observe the extent of asymmetry in real domes.

Once a cross-section is defined by means of the segment-based code, the dome is composed of two surfaces of revolution, one on the top and one on the bottom. A common approach for meshing discs is to subdivide the disc into 4 quarters, and to triangulate each quarter by dividing the straight sides and the curved side into subdivisions. A triangulated quarter is shown in Fig. 5.3(a). Although the dome is not a flat disc, the shape is topologically identical, and geometrically not very different from one. Four quarters can easily be meshed together to form a disc, as shown in Fig. 5.3(b).

The side of the quarter in the actual dome follows a curved path, and subdivisions are taken along this path. The curved path produces some distortion in the triangles, but the aspect ratio remains close to 1. The aspect ratio also moves away from 1 towards the corners of the quarters, but again this is not very significant. In 3 dimensions this triangulation produces 6-noded triangular prismatic solid elements. The dome is also subdivided in the thickness direction, simply by dividing up the triangular prisms, in a manner equivalent to the axisymmetric case, in order to keep the aspect ratio of the prisms close to 1. Fig. 5.4 shows a simple 12×1 mesh, and a more useful and complex 24×2 mesh.

Table 5.2 shows the number of nodes and elements produced by a range of axisymmetric and 3-d meshes.

5.1.3 Meshing the geometry of real domes

Section 4.1.1 has revealed using microtome slices of inverting domes that real domes are sometimes significantly different from the specifications. A number of measurements of dome thickness have been made at several key points on the dome shown previously in

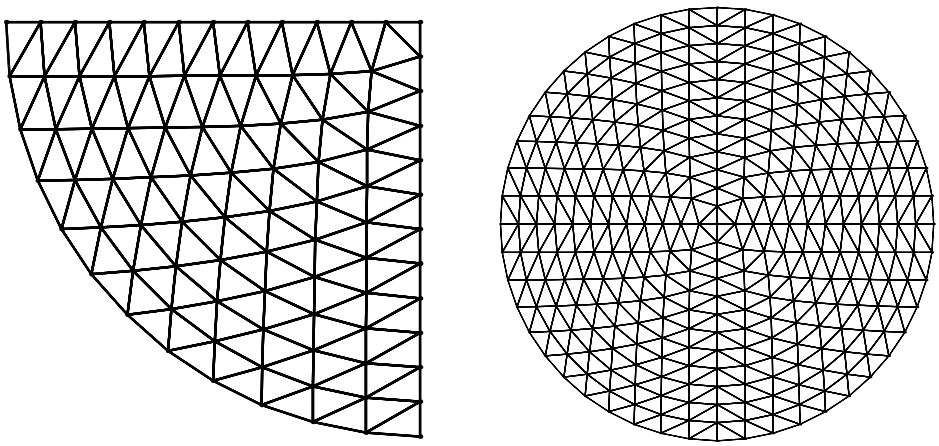

(a) (b)

Fig. 5.3: The construction of a triangulated disc for the meshing of the inverting dome. (a) A disc quarter is shown triangulated; (b) four quarters are meshed together.

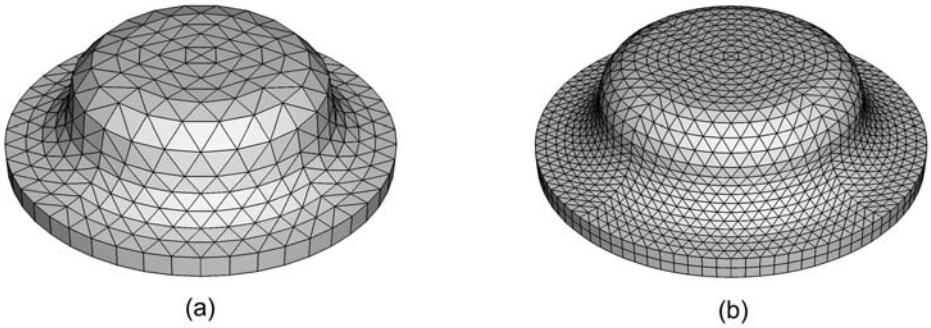

Fig. 5.4: Construction of a 3-dimensional mesh for the inverting dome. (a) a 12×1 mesh; (b) a finer 24×2 mesh (b).

Fig. 4.2. Although only thickness measurements are available, and not a full 3-d map, it is likely that the thickness will be the most significant factor in determining dome behaviour.

With the aim to enable a finite element mesh to capture the real geometry of the manufactured domes as much as possible, linear interpolation is used between the mean measurements of Table 4.1 to generate a more complete set of thickness data throughout the dome. It will be assumed that the overall shape of the dome remains as prescribed

Table 5.2: Number of nodes and elements in a range of inverting dome meshes.

	Mesh	Nodes	Elements
Axisymmetric	12×1	26	12
	24×2	75	48
	36×3	148	108
	48×4	245	192
Full 3-d	12×1	728	576
	24×2	4608	3900
	36×3	15552	11248
	48×4	36864	24500

by the design, shown in Fig. 2.4, and that the thickness variation is evenly distributed between the inner and outer surfaces of the dome. In addition, thickness measurements will also be linearly interpolated along circular arcs between measurements for points that are between different slices. The mean thickness at each point of the *actual* dome is shown in the four slices superimposed on the design thickness in Fig. 5.5.

A mesh is produced that accounts for these variations in thickness of the *actual domes* from the measurements made. It is assumed that the basic shape remains the same, and the start and end thicknesses of the segments that make up the dome are determined from the measurements. The thickness of points that lie between these measurement points is found from linear interpolation between the points. The refinement of this mesh is variable, as with the nominal specifications mesh.

The use of the *actual dome* mesh helps to observe the effects of such large manufacturing imperfections, and assists in explaining why finite element calculations using a mesh with nominal specifications may differ from the experimental data obtained on imperfect moulded domes.

5.1.4 Input and boundary conditions

The pressure is applied normal to the top surface of the elements on the top layer of the dome. In quasi-static analyses, the pressure is applied as required, and in dynamic

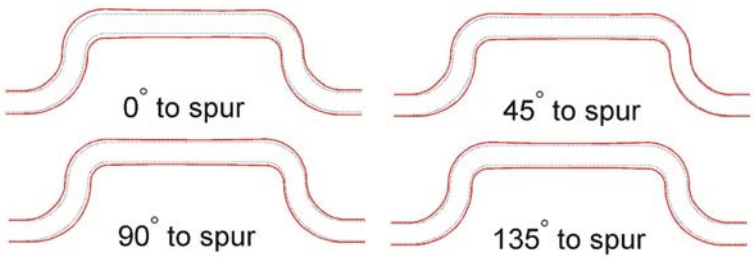

Fig. 5.5: Reconstruction of dome slices from the measurements at the four orientations, superimposed on the design thicknesss.

analyses the pressure applied is the mean measured pressure from Section 4.2. Some dynamic analyses are also run with the mean pressure plus and minus one standard deviation to observe the effects of fluctuations in pressure on the velocity of the dome.

The dome is restrained from movement by the clamping arrangements shown in Section 4.3.2. Effectively, material is restrained beyond a radius of $4.5mm$, although the actual mechanism by which this occurs is through the friction generated by the pressure in the clamps on the surfaces in contact with the clamps, as well as the effects of the retaining lip (if it is present). In the finite element procedures, it is assumed that the nodes at a distance of $4.5mm$ are fixed. It is likely that experimentally there will be some deformation close to the clamps that will result in material being drawn out of the clamps due to the applied stress.

In addition, there is the effect of the small manufacturing radius in the bottom clamp creating a contact surface with the dome as it inverts. The effect of the radius will be analysed in Section 5.3.4.

5.2 Quasi-static behaviour

The experiments of dome inflation of Section 4.3.1 offer a simple and stable deformation that can be used to assess the convergence of the finite element modelling with respect to mesh refinement, and a simple comparison to assess the quality of the analysis. In this section a large displacement static finite element analysis is used first to obtain the response of the dome to an inflating pressure and calibrate the refinement.

Subsequently, analyses are performed to observe the deformation of the inverting dome during quasi-static *inversion* and *eversion*. The dome is highly non-linear in response, and Section 4.3 has observed that the dome becomes unstable and snap-through occurs at specific pressures. In order to deal with the buckling phenomenon,

two types of analyses are employed: a RIKS post-buckling analysis is used to trace the post-buckling behaviour, and a numerically stabilised analysis is used to follow the snap-through as it takes place in the dome. In the parts of the paths where the dome is stable and does not buckle, standard static analyses are used.

5.2.1 Dome inflation

For the purpose of understanding what level of mesh refinement is necessary to achieve convergence, a range of nominal dome meshes are used in a simple static analysis inflating the dome at pressures from $0bar$ to $10bar$. The apex displacement is reported in Table 5.3 for a number of meshes. Convergence is defined in terms of the ratio of the change in displacement between progressively refined meshing to the total displacement. The axisymmetric meshes achieve convergence in apex displacement much faster than the 3-dimensional meshes, and a 24×2 mesh is sufficient for 1% convergence for this deformation. More complex deformation might require a finer mesh to converge, and where possible a 36×3 mesh is used. In the 3-dimensional case, although being much more computationally demanding, convergence is slower, and there is still a difference of 2.5% between the 36×3 mesh and the 48×4 mesh. Due to the much larger computational requirements in dealing with 3-d meshes, 36×3 3-d analyses are used sparingly, only in cases where the dome is not axisymmetric, and much of the work is done with 24×2 meshes. Also shown is the apex displacement from a full 3-d reconstructed dome using the method described in Section 5.1.3. There is a significant difference in apex displacement between this mesh and the equivalent full 3-d for the *actual dome*, due to the increased thickness of the dome.

Table 5.3: Apex displacement for a 10*bar* pressure, for a range of nominal and *actual* dome meshes.

Mesh		Displacement at 10*bar* (mm)
Axisymmetric	12×1	1.456
	24×2	1.409
	36×3	1.404
	48×4	1.404
Full 3-d	12×1	1.026
	24×2	1.220
	36×3	1.299
	48×4	1.334
Full 3-d *actual dome*	36×3	1.001

5.2.2 Dome inversion

The quasi-static inversion of the domes is modelled using 36×3 axisymmetric nominal dome meshes in a series of analyses to trace the buckling and post-buckling behaviour. The RIKS analysis [23] is employed to trace the deformation in the unstable part of the dome's response. The analysis is also performed using numerical stabilisation to compare directly to the experimental data of Section 4.3. Both analyses are computationally demanding, and it has not been possible to use the 3-d *actual dome* mesh here.

The vertical displacement of the apex of the dome vs. the applied pressure is shown in Fig. 5.6. The experimental data from Section 4.3 is also given for comparison, although it is expected to be a little different due to the known manufacturing differences between nominal and real domes. The FE *inversion* and *eversion* buckling pressures are $2.86bar$ and $-2.68bar$ respectively, and compare reasonably well to the mean measured experimental buckling pressures of $3.45bar$ and $-2.38bar$ respectively. The experimental

data at large negative displacement is a little greater than the calculation predicts. This is probably due to the dome edge not being perfectly clamped, and sliding a little out of the ring clamps.

The stabilised and post-buckling calculation performed in Section 5.6 can be used to construct a pressure-volume relationship for the inverting dome. The nodal displacements from the calculation are exported and used to calculate the volume swept by the dome at a specific pressure, both in the stabilised and in the unstable post-buckling part of the curves. The pressure-volume relationship is shown in Fig. 5.7.

There is a loop in the force-displacement graph for the apex of the dome (Figure 5.6) and in the pressure-volume relationship (Figure 5.7). The loops can be interpreted

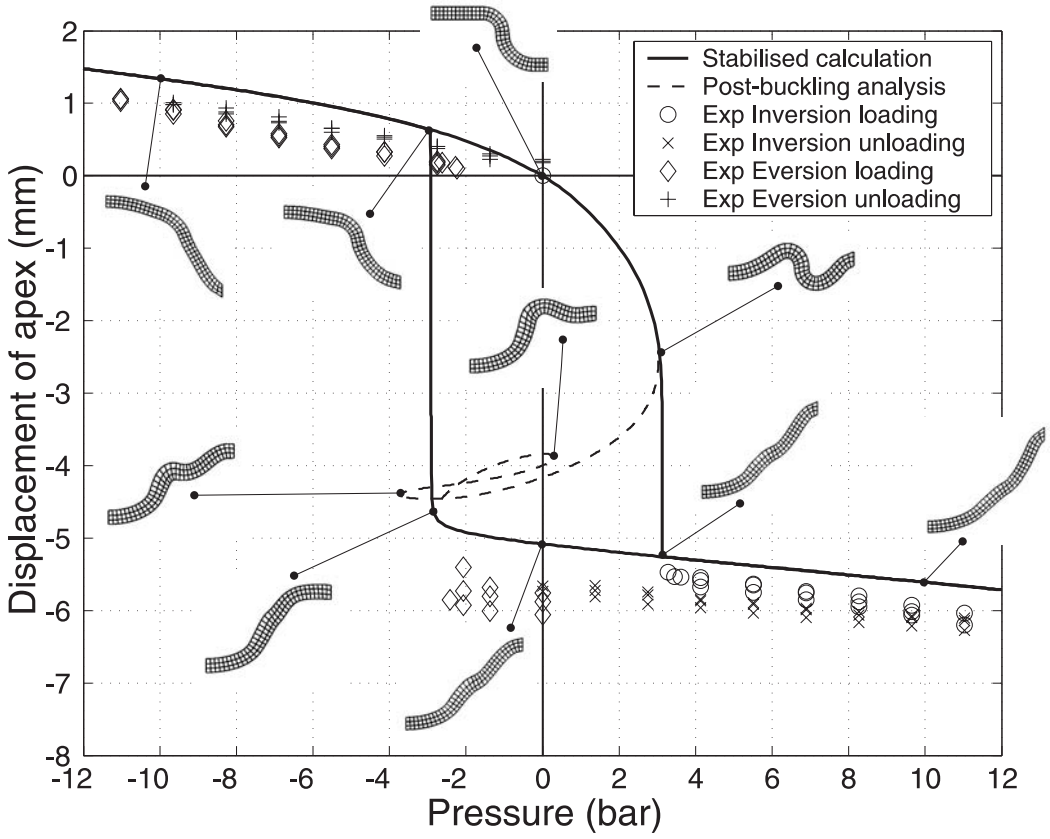

Fig. 5.6: Vertical displacement of the apex of the dome vs. the applied pressure during quasi-static *inversion* and *eversion*, showing stabilised and post-buckling behaviour. Experimental data from Section 4.3 is also shown.

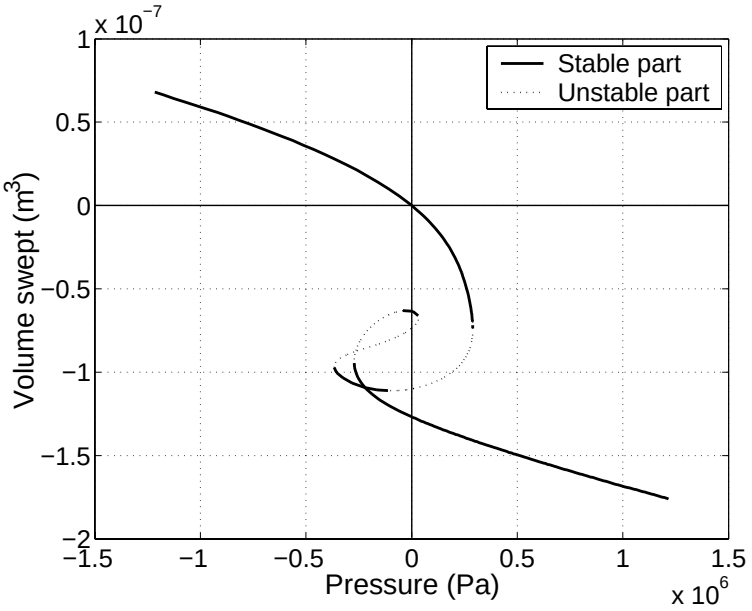

Fig. 5.7: Pressure - volume swept relationship during stable and unstable post-buckling inversion of the dome. Zero volume is set at zero pressure. The numerically stabilised parts are not shown for clarity.

in terms of the stability of the dome at any particular position. Taking the pressure-volume relationship as an example that is easiest to interpret physically, the dome is stable if the gradient of the pressure-volume graph is negative, because the volume swept has been determined as being negative when the dome travels vertically down, and the pressure is positive when this happens. For this to happen we need the dome to provide a resisting pressure to an applied volume, just like with a spring. We can see that in the parts of the graph where the dome is obviously stable, the gradient is negative. As the dome starts to invert, the gradient becomes infinite and eventually positive in the unstable post-buckling part. As the loops form there are small sections in the post-buckling behaviour which indicate that there are small islands of stability within the big unstable loop, shown in Figure 5.7.

The loop in the force-displacement graph effectively means that the relationship is not monotonic with respect to displacement. It is easier to understand this in terms of

the pressure-volume relationship, where there can be different ways in which the dome can arrive at a specific swept volume since the dome is a 3-dimensional object that can deform in a variety of modes.

Using the same sort of analysis at a higher pressure, it is possible to observe the stress at a pressure which causes burst in the domes. The 36×3 *actual dome* mesh is inflated to a pressure of $-14.9bar$ as measured in dome *eversion* (during *eversion* the dome bursts as if it was simply inflated). The stress at the apex is essentially equibiaxial, and the principal stresses in the plane of the dome are approximately $15MPa$. This compares poorly to a measured in-plane stress at burst in injection-moulded discs of $24.6MPa$ from Section 3.4.2. The discrepancy is due to the material model being calibrated on uniaxial test data and not providing such a good representation of equibiaxial stress states.

The analysis is resumed after dome *inversion* using a standard static analysis, and the pressure is raised to $+14.4bar$, the measured burst pressure for quasi-static dome *inversion*. Here the stress at the apex is again essentially equibiaxial, and the principal stresses are approximately $10.5MPa$. This compares poorly to a measured stress of $24.6MPa$ in injection-moulded discs from Section 3.4.2 for the same reasons as in the *eversion* burst.

5.3 Dynamic behaviour

5.3.1 Frequency analysis

The natural frequencies and modes of vibration of an inverting dome are found using an FE frequency analysis. A range of mesh refinements is used to ensure appropriate convergence. A 36×3 3-d mesh is used for the data that follows. The most important motion as far as achieving particle acceleration is concerned is vertical motion. The fun-

damental mode of vibration of the dome exhibits mainly vertical motion, at a frequency of 5234.5Hz.

5.3.2 Rayleigh damping optimisation

The strain rate experiments of Section 3.3.6 have given indications that the material's constitutive behaviour is mildly strain-rate dependant. The highest strain rate observed in the tests is about $0.2s^{-1}$, whilst the highest strain rate expected during the high-speed inversion of the dome is $10^4 - 10^5 s^{-1}$. Hence it is possible that the constitutive response during high speed inversion will be significantly different to that of the slow tensile tests. In order to account for this difference in behaviour, an amount of strain-rate proportional damping will be introduced into the dynamic FE calculations. Rayleigh damping is available with `ABAQUS`, in which an additional damping stress σ_d is defined as

$$\sigma_d = \beta_R D^{el} \dot{\epsilon} \tag{5.5}$$

where β_R is the Rayleigh stiffness-proportional damping constant, D^{el} is the material's undeformed elastic stiffness, and $\dot{\epsilon}$ is the strain rate. This damping stress is added to the stress due to the hyperelastic constitutive response from (5.3). Hence the response essentially corresponds to a Voigt viscoelastic model since a part of the stress seen by the response of the material is proportional to the strain rate. `ABAQUS` does not include the damping stress in the stress outputs.

β_R introduces viscous material damping simulating the sliding, stretching and re-arrangement of the polymer's crystal matrix. It is related to the fraction of critical damping ξ_i of the ith mode of vibration as

$$\xi_i = \frac{\beta_R \omega_i}{2} \tag{5.6}$$

where ω_i is the natural frequency of the ith mode of vibration. This type of damping tends to reduce the effect of the highest modes of vibration. The highest modes refer to the deformation of a single element, and are non-physical. The value of β_R cannot be derived from basic theory, and is found from optimisation involving the comparison of experimental data to dynamic simulations over a range of values of β_R. The main difficulty with a direct comparison of FE displacements and experimental data is that the pressure time-history applied to the FEM is not identical to the pressure history on the moving dome. Additionally it has been measured a short distance away from the dome, see Section 4.2. The optimal value of β_R is therefore found by comparing the peak velocity (of the apex) recorded in the FE analyses to the average peak powder velocity recorded from particle velocimetry experiments of Section 4.5.

The FE simulations are performed using a 3-dimensional *actual* dome mesh reconstructed from the microtome thickness measurements of the same domes, using full 3-d 24×2 mesh simulations. The computation time is additionally increased by the addition of damping [23]. The peak velocity recorded over a range of percentages of critical damping factors is shown in Fig. 5.8.

Linear interpolation is used on the logarithmic damping in order to obtain the value of damping corresponding to a peak velocity of $162.2 m/s$, as obtained from particle velocimetry. The fraction of critical damping matching this velocity is around 7% and the Rayleigh damping factor is $\beta_R = 3.9138 \times 10^{-6} s$. These values will be used in all further dynamic analyses.

The timescale of β_R is small compared with the duration of the inversion event, approximately $100 \mu s$. This level of damping removes non-physical vibrations of single

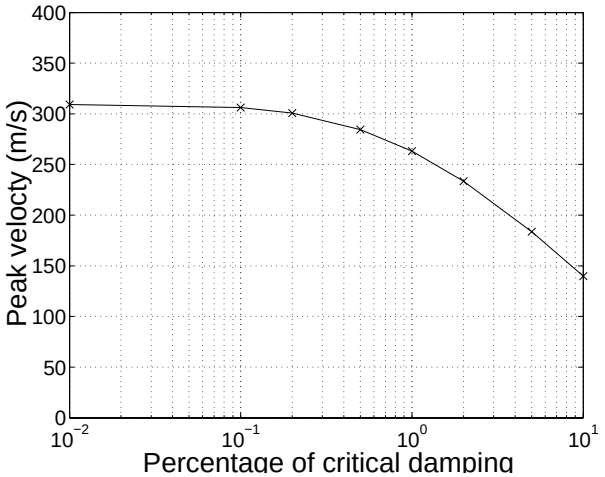

Fig. 5.8: Peak velocity for a range of damping factors in full 3-dimensional *actual* dome FE analyses.

elements from the finite element simulations.

5.3.3 Nominal and actual domes

The optimisation has provided a damping value that is now used in both the 3D reconstructed *actual dome* mesh and in a more refined axisymmetric nominal dome mesh in order to compare the difference between the real domes with manufacturing imperfections and the domes specified in Fig. 2.4. The peak vertical component of velocity reached by a number of points on the dome and the time at which the peak occurs is shown for both the reconstructed and the nominal dome geometry in Fig. 5.9. Calculations are also performed with the pressure history plus and minus one standard deviation.

There is a substantial difference in peak velocity throughout the dome between the nominal domes and the 3-d reconstructed mesh. The nominal dome reaches around $250m/s$ at the apex, and the peak velocity never drops below $175m/s$ in points between the apex and a $2mm$ radius. The reconstructed, thicker domes have a peak velocity of around $160m/s$ at the apex and a lowest velocity at $2mm$ radius of around $115m/s$.

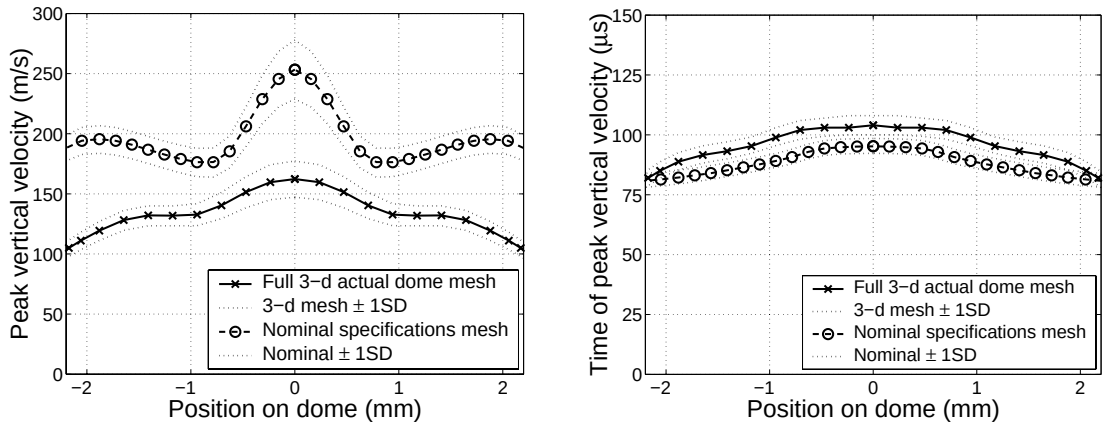

(a) (b)

Fig. 5.9: (a) Peak vertical velocity in *inversion* of 3-d *actual dome* meshes and in nominal specifications meshes, and (b) the time at which the peak velocity occurs.

The time at which the peak velocity occurs is similar in the two dome meshes. The edge of the region containing the powder reaches the peak first, at $\sim 80\mu s$ in both cases. The apex reaches peak velocity at around $95\mu s$ in the nominal domes and around $105\mu s$ in the reconstructed domes. Manufacturing precision is therefore very important when it comes to achieving fast *inversion* velocities. The effect of a number of model manufacturing imperfections will be examined in Section 5.5. A sequence of images of a nominal dome in *inversion* at $10\mu s$ intervals is shown in Fig. 5.10.

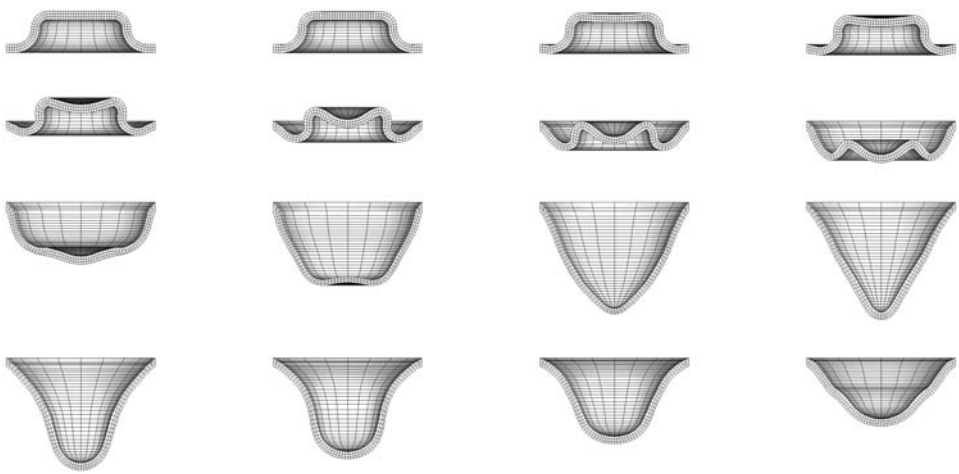

Fig. 5.10: Images of dome *inversion* at $10\mu s$ intervals from axisymmetric analysis.

5.3.4 Contact on inversion

The clamping arrangement can result in a possible contact between the dome and the lower part of the clamp on inversion, as explained in Section 4.3.2. To ascertain the significance of this contact, an analysis with a contact surface between the dome and the clamp edge is performed on a dome with nominal geometry. The peak velocity of a number of points, and the time at which the velocity occurs is shown in Fig. 5.11.

It becomes clear that the contact surface reduces the peak velocity by around 20% at the apex, although this reduction becomes smaller, being almost negligible at a radius of $2mm$. There is virtually no change in the time at which the peak velocities are reached. It is interesting that the contact surface has the effect of lowering the peak velocity at the apex but not the peak velocity at the edges. The overall effect is to narrow the peak velocity distribution across the dome. This effect is desirable since it would ensure that particle penetration becomes more uniform across the particle footprint, although it does produce lower apex velocities.

Introducing a contact surface lengthens the time required for each analysis consider-

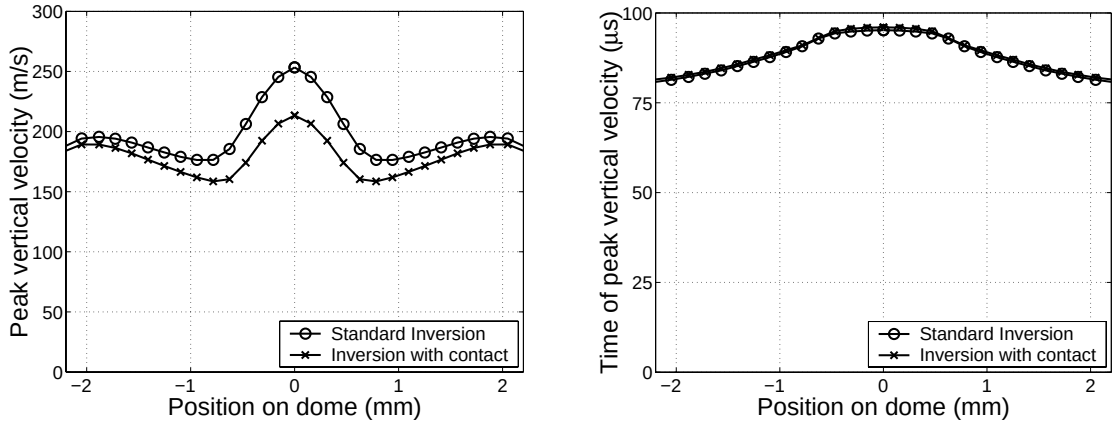

(a) (b)

Fig. 5.11: (a) Peak vertical velocity during *inversion* with and without the contact surface below the dome, and (b) the time at which the peak velocity occurs.

ably. Hence the contact surface will not be included in all subsequent analyses, although its effect is not negligible and should be considered for a final design.

A sequence of images of a nominal dome in *inversion* with contact at $10\mu s$ intervals is shown in Fig. 5.12. The $0.5mm$ radius contact surface can be seen in the images.

5.3.5 Eversion

The quasi-static post-buckling analysis provides the shape and stress-state of a dome that is pre-inverted and in its second stable configuration. This data is used as the input for a dynamic *eversion* analysis. The peak vertical component of velocity reached by a number of points on a nominal dome geometry in *eversion* and the time at which the peak occurs is shown in Fig. 5.13.

The FE analysis indicates much faster particle velocities for dome *eversion*, reaching $450m/s$ at the apex and dropping steadily to $200m/s$ at around $1.6mm$ radius. These velocities are significantly larger than the experimental values since a dome with nominal geometry is used for the analysis. Although the velocities are high, the distribution is less uniform than in *inversion*. The time at which the peak velocity is reached is similar to

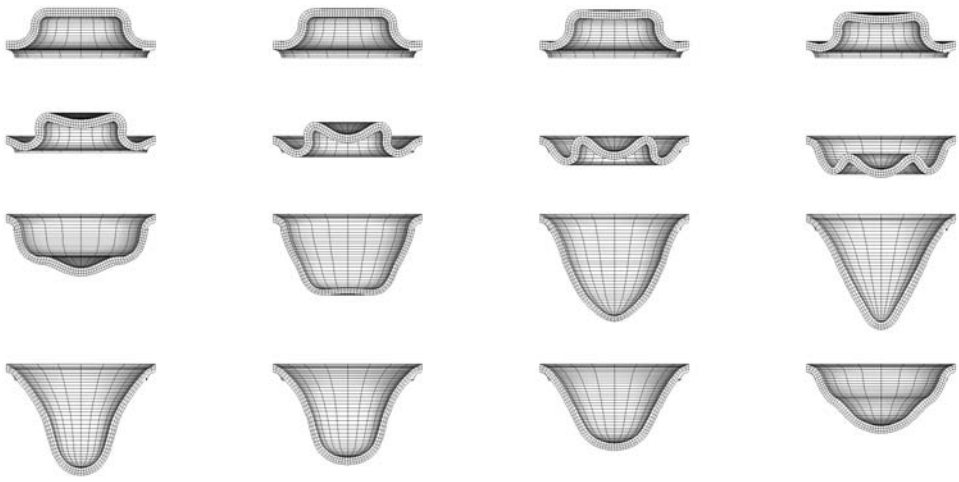

Fig. 5.12: Images of dome *inversion* with contact at $10\mu s$ intervals from axisymmetric analysis. The 0.5mm radius contact surface is also shown.

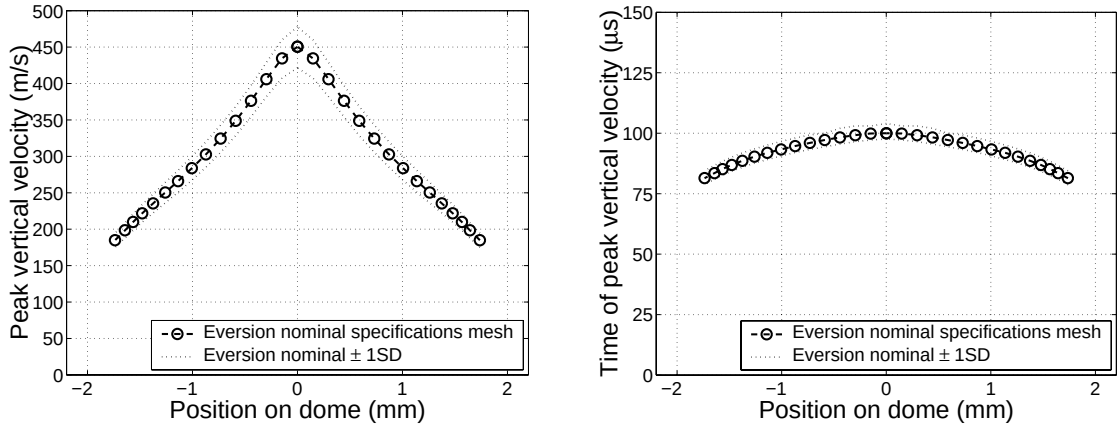

(a) (b)

Fig. 5.13: (a) Peak vertical velocity during *eversion* in a nominal geometry dome, and (b) the time at which the peak velocity occurs.

that of domes in *inversion* and is approximately the same as was found experimentally.

A sequence of images of a nominal dome in *eversion* at $10\mu s$ intervals is shown in Fig. 5.14. The same simulation for domes with a reconstructed geometry has not been carried out.

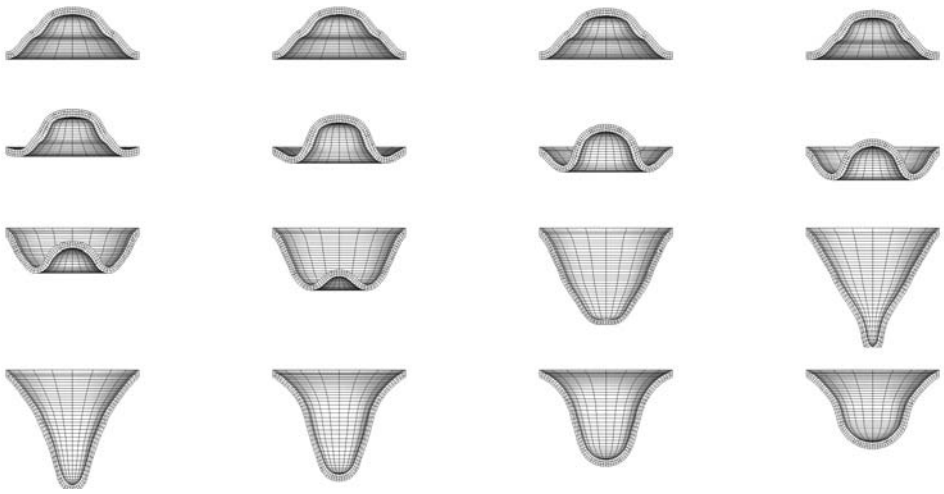

Fig. 5.14: Images of dome *eversion* at $10\mu s$ intervals from axisymmetric analysis.

5.3.6 Particle detachment considerations

Currently particles are placed on the outer surface of an inverting dome either with the aid of drug retaining fibres, as shown in Fig. 2.4, or as a coating in the case of very small gold particles. When fibres are employed, the drug powder is lightly placed in the gaps between the fibres. When the dome begins to invert, the powder is no longer constrained by the fibres and is effectively unattached to the surface of the dome. In the case of gold particles, which are usually painted on the dome in a solution, there is likely to be a small adhesion force that needs to be overcome before the particles detach themselves from the surface.

Assuming that any adhesion force present is small enough to be ignored, particles will be accelerated by the dome's surface and will leave the surface when the dome starts to decelerate. We define the vertical z axis of symmetry as the direction in which the dome inverts, with particles travelling in the negative z direction, or vertically down. If the dome experiences a simple increase and subsequent decrease in speed, the particles will leave the dome at the start of the deceleration and progress towards the target unaffected by the dome's movement. For this to take place, the dome's acceleration must be negative (down) to start with, then positive (up) until well after the dome has stretched to its maximum displacement. However, the mechanism can be more complex if the dome's acceleration changes sign more than once during the dome's travel between its starting and fully stretched position. If this takes place, the particles are likely to leave the dome when the acceleration *first* changes sign. What subsequently happens depends on the details of the dome's and the particle's motions. If the dome has sufficient acceleration, it will catch up with the particles and accelerate them further. If it doesn't, it may reach a faster peak velocity without giving the particles this peak velocity.

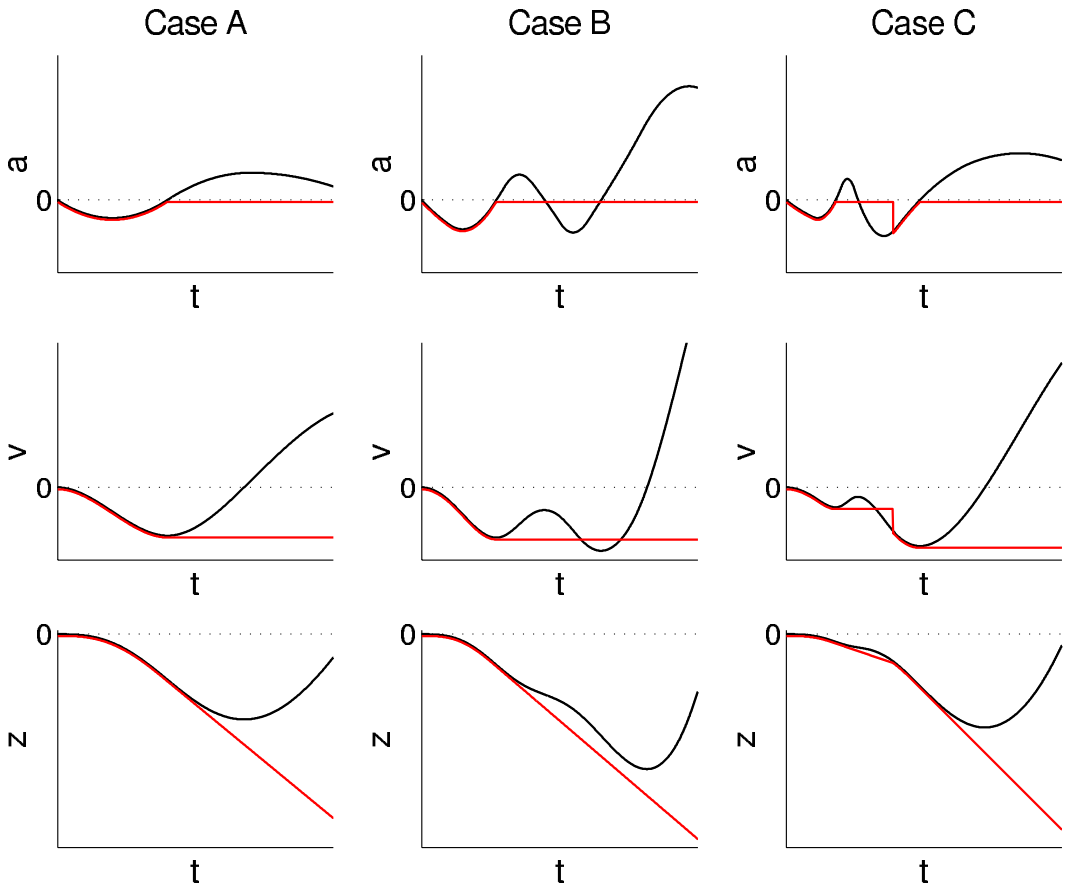

Fig. 5.15: Hypothetical acceleration a, velocity v and displacement z of an inverting dome and a particle. The dome is shown in black and the particle shown in red. Case A is a simple acceleration and detachment; case B shows how a dome can reach a faster velocity than the particle without giving this peak velocity to the particle; case C shows an example of the dome releasing the particle and catching up with it, accelerating it further.

Fig. 5.15 shows acceleration, velocity and displacement as functions of time during inversion in three hypothetical situations. Dome parameters are shown in black and particle parameters in red. Case A, on the left, represents an inverting dome that accelerates and decelerates in a simple manner. The acceleration changes sign a single time, and the particles leave the dome as soon as the dome starts to decelerate, and carry on with the same velocity as the maximum velocity of the dome.

Case B, in the middle, shows a situation where the dome's acceleration is more complex. Here the dome accelerates and decelerates a number of times prior to complete

inversion; in this case the particles leave the dome the first time it decelerates, and carry on with that local peak velocity. The dome subsequently reaches a higher velocity, but is not able to give this velocity to the particles, and as such they do not travel with the peak velocity reached by the dome. This situation is wasteful and should be avoided.

Case C, on the right, shows a similar situation to case B, but in this case the particles leave the dome at the first deceleration and are subsequently 'caught up' by the accelerating dome. The particles would then reattach to the dome and be accelerated further. They would eventually leave with the dome's peak velocity. In practice, this situation is also undesirable as the particles could be damaged by the dome and as there will be some energy loss associated with the subsequent impact between dome and particles.

In practice the dome is not a point with acceleration, velocity and displacement, but a moving surface where each point experiences a different acceleration, velocity and displacement. The analysis shown in Fig. 5.15 is performed for individual particles regularly spaced every $0.23mm$ across a dome diameter. In order to establish when the particles leave the dome, the vertical component of displacement is used. If the particles leave the dome and the vertical component of the dome catches up with them, they are assumed to re-attach at the place where they left. The nominal dome FE analysis is used for the displacement data. Fig. 5.16 shows acceleration, velocity and displacement components for the dome at 15 equally-spaced points along its underside between the apex and $2mm$ radius. The circles indicate the points at which the particles are finally detached from the dome, assuming detachment whenever the vertical velocity drops, and the acceleration changes sign, and reattachment when the vertical dome displacement exceeds the particle displacement. Fig. 5.17 shows the same components for the particles.

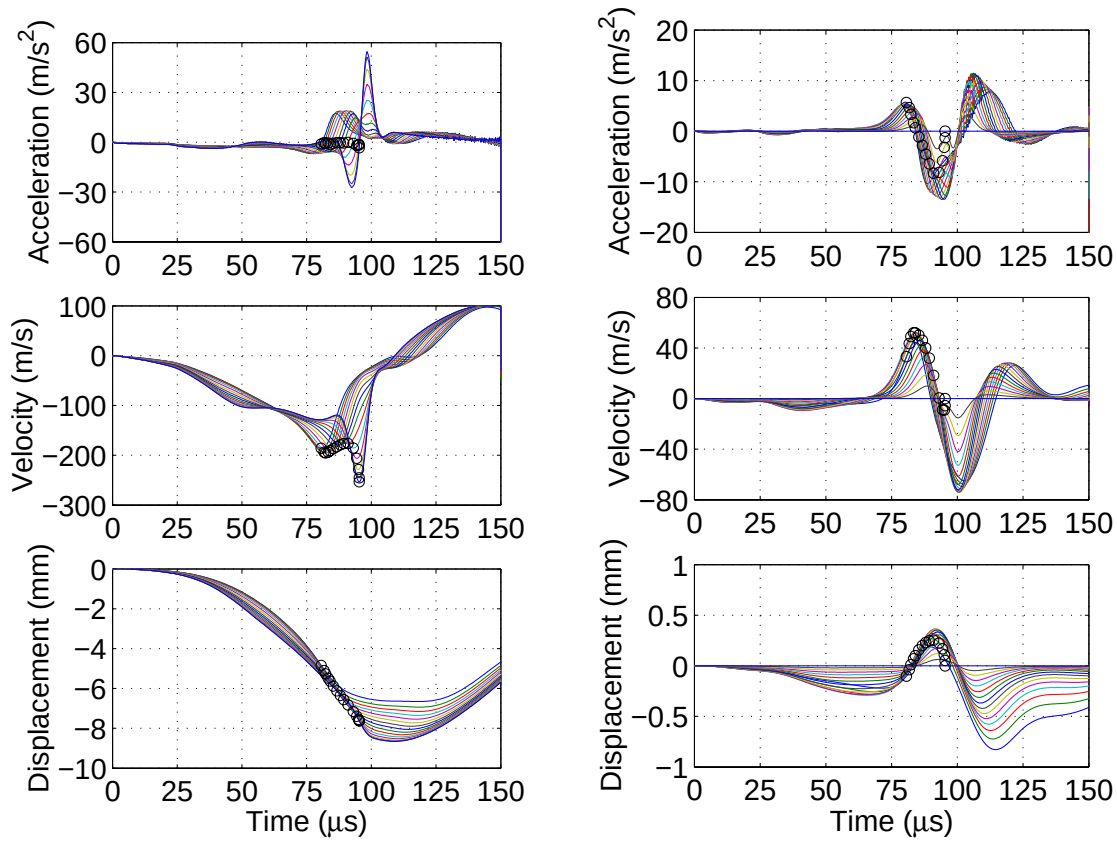

Fig. 5.16: Acceleration, velocity and displacement of 15 points on the underside of a dome in the (a) vertical and (b) horizontal direction. The position of particle detachments are shown as circles.

For this particular dome, detachment , reattachment and subsequent detachment (as in case C, Fig. 5.15) occurs for points at radius $0 - 0.5mm$. All other points leave the dome with a single detachment (as in case A, Fig. 5.15). All of the particles finally leave the dome with the corresponding peak velocity point on the dome on which they were located. Since the horizontal displacement of points near the apex is not large, the assumption that particles reattach at the same point is considered to be valid.

When detachment and reattachment occurs, particles could be damaged and the contact will result in energy loss. This condition is not desirable as far as the inversion is concerned. However, it is also possible that if the deceleration of the dome is

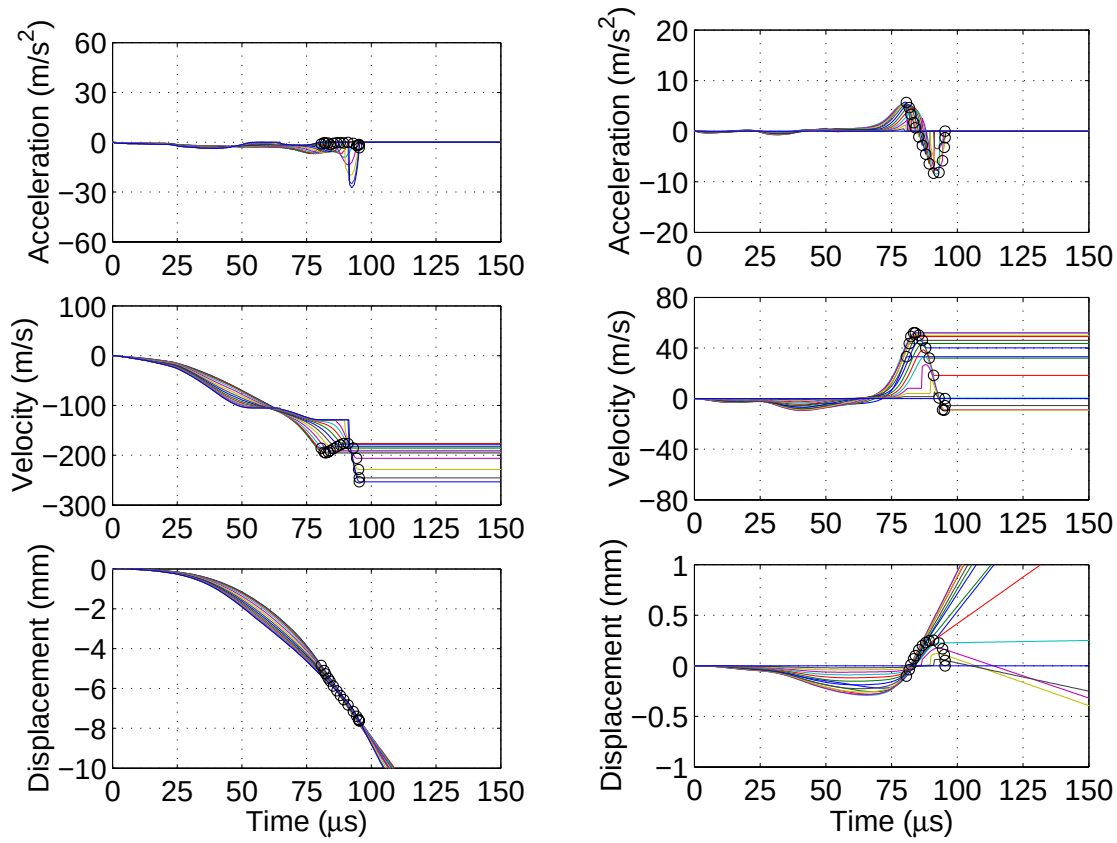

Fig. 5.17: Acceleration, velocity and displacement of 15 particles on a dome in the (a) vertical and (b) horizontal direction. The position of particle detachments are shown as circles.

not significant, the particles may not detach. They may only detach when the dome deceleration is sufficiently large.

For this particular inverting dome, it appears that the velocity of the particles can simply be found from the peak velocity of points on the dome. This simplifies the analysis required to find particle velocities. This condition may no longer be true if the dome configuration is significantly altered. Another important issue that needs to be addressed is the understanding of how the velocity of individual particles leaving the dome eventually affects the positional distribution of the drug powder on its surface. Fig. 5.17(b) has shown that particles leave the dome with a component of velocity in

the horizontal direction, following the horizontal velocity of the dome at the time of particle release. Hence the particles will spread out before embedding in the target.

Fig. 5.18(a) shows the particles during the dome inversion and after they leave the dome using the data from Fig. 5.16. A similar analysis is performed for a dome in *eversion*, and the particle profile is shown in Fig. 5.18(b). The possible collisions of particles are not considered in this analysis.

This analysis can be used to help identify the best target distance for a particular dome. If some particles have a radial component of velocity, they travel towards or away from the axis of symmetry as they approach the target. This can be used as a

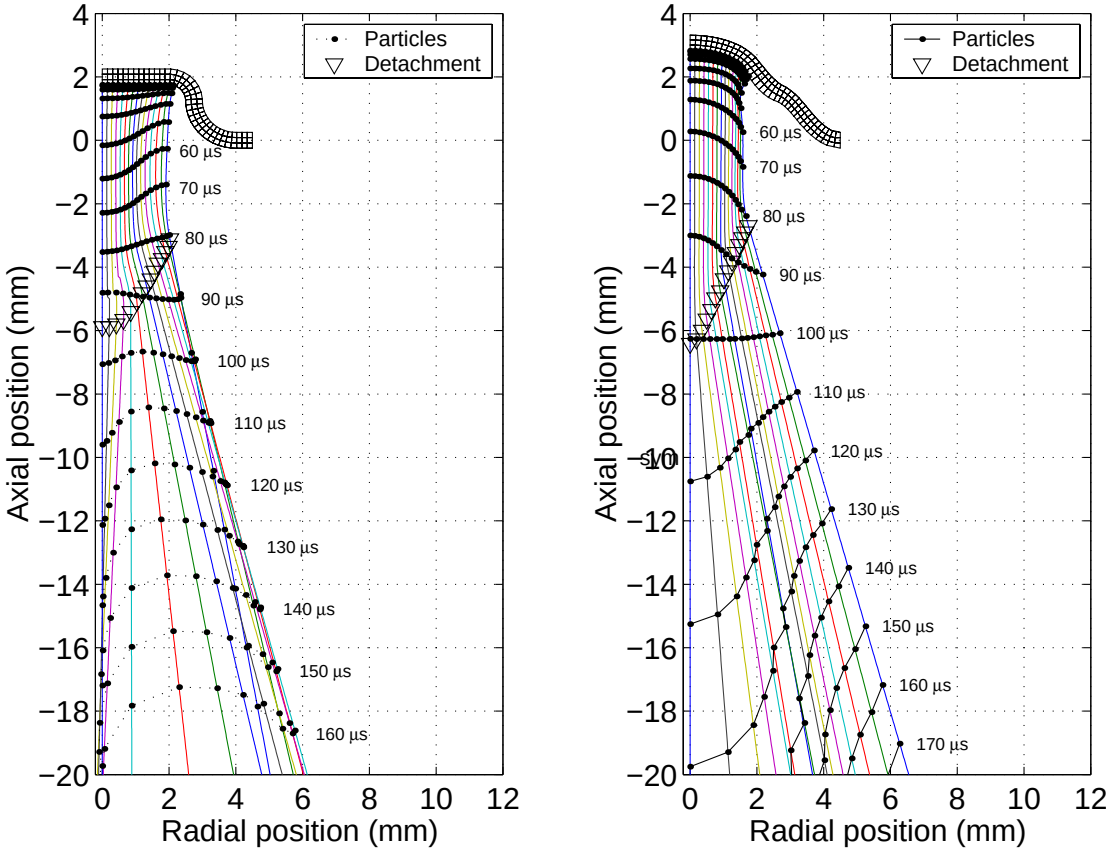

(a) (b)

Fig. 5.18: The position of particles whilst on the dome and after they leave the dome in (a) *inversion* and (b) *eversion*, shown at $10\mu s$ intervals.

method of producing a target with a larger diameter, and reducing the density of powder injected per unit area, and does not necessarily need to be a negative side-effect. For this current dome it appears that in *inversion* particles will be more concentrated near the apex and near the edge, and that there will be a region of lower particle density in between. This is a result of the horizontal component of velocity at particle detachment. In *eversion*, the centre of the target will have a lower particle density, increasing and then remaining approximately constant moving away from the apex. The overall target footprint is slightly larger in eversion, reaching $6.5mm$ radius at a distance of $20mm$, compared with $6mm$ in *inversion*.

5.3.7 Energy considerations

The inverting dome is an energy transfer device between the energy of the gas jet and the kinetic energy of the particles. A small fraction of the energy may be lost due to sound, contact, collisions and permanent deformation, while the rest is split into the strain energy and the kinetic energy of the dome. To increase particle velocities the strain energy should be as low as possible at the point of release. We consider two cases in which this can be achieved. The first case is where the dome acts as a travelling membrane with little stiffness involved in the travel. Here the strain energy of the dome increases to a small value as it starts to invert, and remains approximately constant during inversion. Eventually it will rise as the dome stretches out to its point of maximum displacement, but this will take place only after the particles have been released. As the strain energy rises, the kinetic energy drops. The particles would be released at the peak in kinetic energy.

The second case is where the dome acts as a stiff, bistable diaphragm, and during inversion its strain energy rises to a high value before dropping to the second stable

configuration. Here the kinetic energy would be low to begin with since energy is going into straining the dome. As the dome travels past its point of stability, it would spring towards its other stable configuration, and in doing this, the strain energy would drop. The kinetic energy will rise sharply as a result of the snap-through. Eventually, the strain energy would rise again and the kinetic energy would drop as the dome is stretched further. Again the particles would be released at the peak in kinetic energy.

The energy output from the FE analyses on nominal domes in *inversion* and *eversion* is shown in Fig. 5.19. The input energy shown is the work done by the pressure. Although the strain energy at $t = 0$ in *eversion* is not zero since the dome is in a state of self-stress, it has been normalised to zero for the purpose of this figure. The time window in which particles leave the dome is also shown.

In both *inversion* and *eversion* the dome appears to behave more like a travelling membrane, i.e. the first case. Although the total kinetic energy is a maximum at or near the start of particle release, it has dropped substantially by the time the last particles leave the dome. The kinetic energy of each individual particle will still be at a maximum at the time of release. The particles leave the dome at a time just before the input energy reaches its maximum.

5.4 A simple dynamic model of dome inversion

This section will make use of a number of the results developed in the previous sections to construct a simple dynamic mechanical model of dome inversion. Numerical integration of the equations of motion is carried out to calculate displacement, velocity and acceleration as functions of time for domes modelled as point masses in *inversion* and *eversion*.

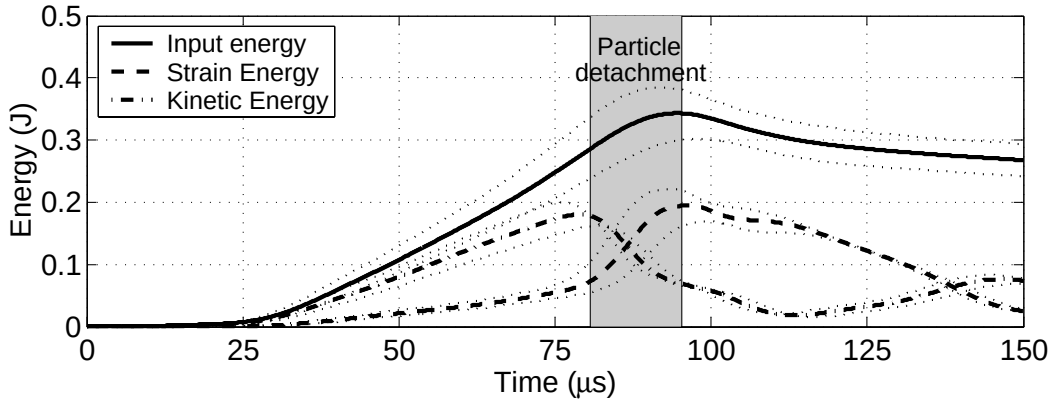

(a)

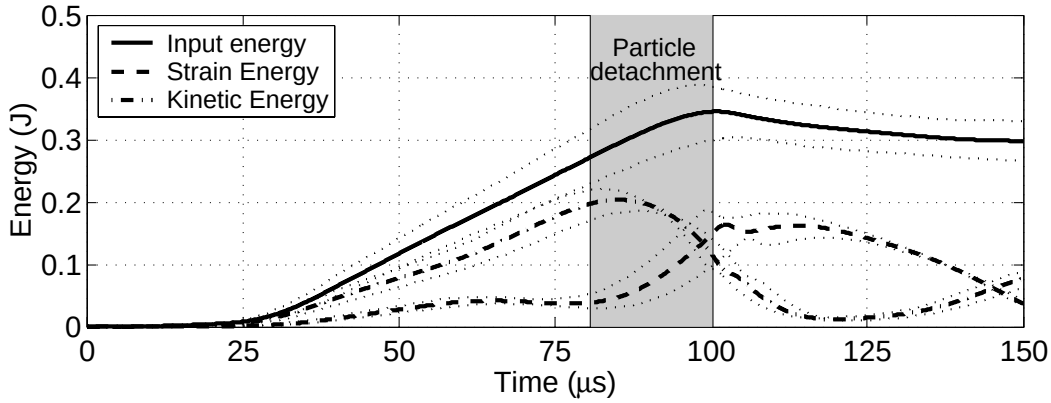

(b)

Fig. 5.19: The input, strain and kinetic energy during (a) *inversion* and (b) *eversion*.

5.4.1 Introduction

In its simplest form, the dome is a moving carrier that accelerates the particles on its surface. It deforms while travelling in a mostly vertical direction, and during its travel it is subjected to internal forces resulting from its complex deformation. Hence it can be treated as a point mass that moves in a vertical direction as a result of a time-varying input force, and whose motion is resisted by a highly non-linear spring, as shown in Fig. 5.20.

The time-varying input force due to the pressure $F_P(t)$ will be found from the measured pressure histories near the dome's surface made in Section 4.2. The effective mass

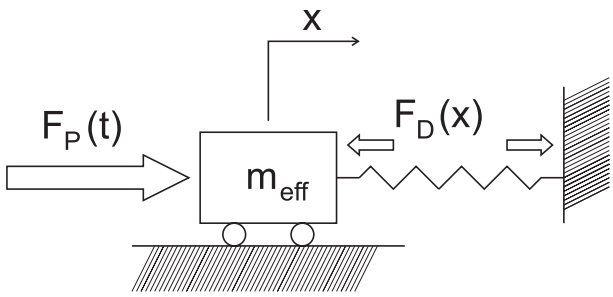

Fig. 5.20: Simple dynamic model used to analyse the behaviour of the inverting dome. A time-varying force, $F(t)$ acts upon a mass, m_{eff} connected to a non-linear spring.

of this model, m_{eff}, will be taken from dynamic FE frequency analysis. The non-linear stiffness of the spring representing the deforming dome will be obtained from quasi-static post-buckling calculations of the stability curves in Section 5.2.2 as a function of the displacement u in the form $F_D(u)$.

5.4.2 Numerical integration of the equations of motion

The discrete numerical integration of the equations of motion will be done using a simple trapezium rule method. Time is discretized in units of Δt. We start the iteration at $t = 0$ with $u(0) = v(0) = 0$. A forward integration is performed to obtain a first guess of the values of $v^*(t + \Delta t)$ and $u^*(t + \Delta t)$ in order to be able to calculate a value of the dome spring force at $t + \Delta t$ from

$$\begin{aligned} v^*(t + \Delta t) &= a(t)\Delta t \\ u^*(t + \Delta t) &= v(t)\Delta t \end{aligned} \tag{5.7}$$

We can then evaluate a better estimate of $F(t + \Delta t)$ from

$$F(t + \Delta t) = F_P(t + \Delta t) + F_D(u^*(t + \Delta t)) \tag{5.8}$$

where the value of F_D at $u^*(t + \Delta t)$ is found from a linear interpolation on the discrete $F_D(u)$ data. We can then proceed to integrate using the trapezium rule for $v(t + \Delta t)$ and $u(t + \Delta t)$, given by

$$\begin{aligned} v(t + \Delta t) &= v(t) + \frac{1}{2}(a(t) + a(t + \Delta t))\Delta t \\ u(t + \Delta t) &= u(t) + \frac{1}{2}(v(t) + v(t + \Delta t))\Delta t \end{aligned} \tag{5.9}$$

and provided the value of Δt is kept reasonably small, the iteration should provide an adequately accurate reconstruction of the displacement and velocity data as functions of time.

5.4.3 Model parameters

The input parameters to the simple mechanical model consist of the effective mass m_{eff}, the time-varying input force due to the pressure $F_P(t)$, and the displacement-dependant force from the dome's deformation $F_D(u)$. The effective mass is obtained from a FE frequency analysis. The dome deformation force is obtained from the stability analysis of Section 5.2.2, and the shock wave input force is then obtained from the recorded pressure measurements of Section 4.2.

Section 5.3.1 has reported that the fundamental mode of vibration of the dome exhibits mainly vertical motion, at a frequency of 5234.5Hz. The effective mass in the vertical direction is $m_{eff} = 18.03mg$, corresponding to a disc of Hytrel material $0.5mm$ in thickness and with a $3.1mm$ radius. The dome is nominally $0.5mm$ in thickness and the shock tube is $3mm$ in radius. A value of $3.1mm$ radius for the moving mass is used to calculate the equivalent surface area on which the shock wave input pressure is acting, as $A_{eq} = 31.09mm^2$.

The volume swept by the dome is represented in the simple model by the volume swept in the vertical movement of the disc of area A_{eq}. The pressure-volume relationship developed in Section 5.2.2 is converted back to an equivalent force - displacement relationship from

$$F_{eq} = PA_{eq} \qquad u = \frac{V}{A_{eq}} \tag{5.10}$$

where P is the pressure and V is the volume. The force-displacement relationship is shown in Fig. 5.21.

If we wish to use this relationship in order to provide us with a spring stiffness for the inverting dome during high-speed inversion, we cannot account for the loop, since it would require the equivalent mass to move backwards and forwards during the inversion.

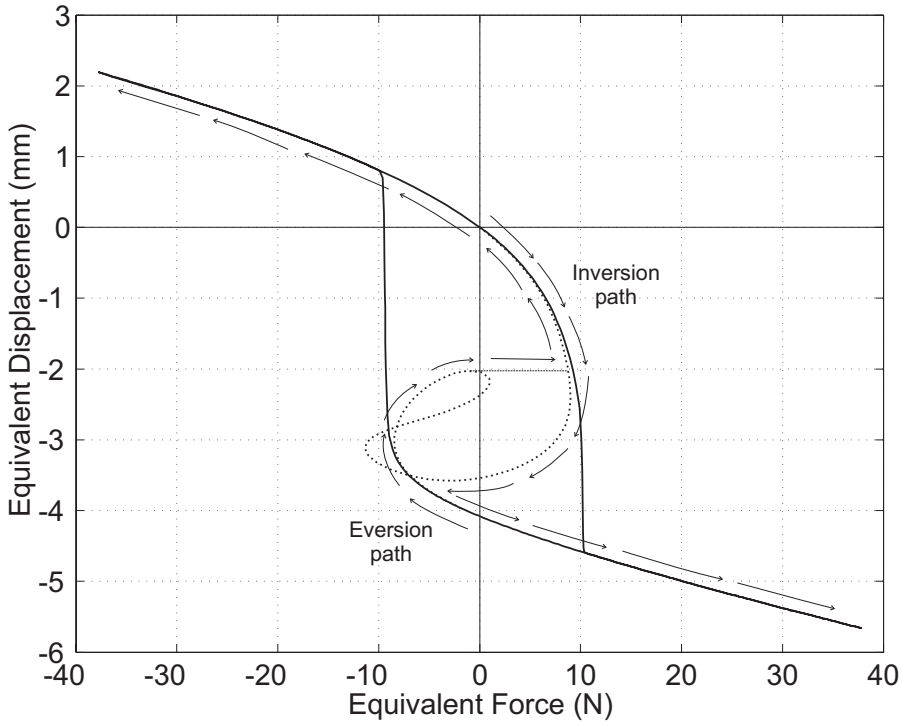

Fig. 5.21: Equivalent force-displacement relationship obtained for a cross-sectional area $A_{eq} = 31.09mm^2$.

We will hence assume that the dome can only continue to travel in the same direction, and that the loop is missed out completely during the inversion. Real dynamic dome behaviour will probably exhibit this jump since the dome never becomes stable *during* the snap-through inversion process. During high-speed inversion the dome does not take all the configurations found in the post-buckling analysis due to the presence of mechanical inertia. The paths used for *inversion* and *eversion* are also shown in Fig. 5.21.

There is an additional computational reason for which we are required to remove the loops. Since the numerical integration requires a value of F_D for a specific displacement, we require F_D to be a monotonic function of displacement for *inversion* and *eversion*.

Fig. 5.22 shows the equivalent mean force history obtained by multiplying the mean pressure history from Section 4.2 by the effective area. Also shown are upper and lower bounds in force, using the standard deviation measurements.

Due to the pressure history starting at a time of $-7\mu s$, in practice the numerical

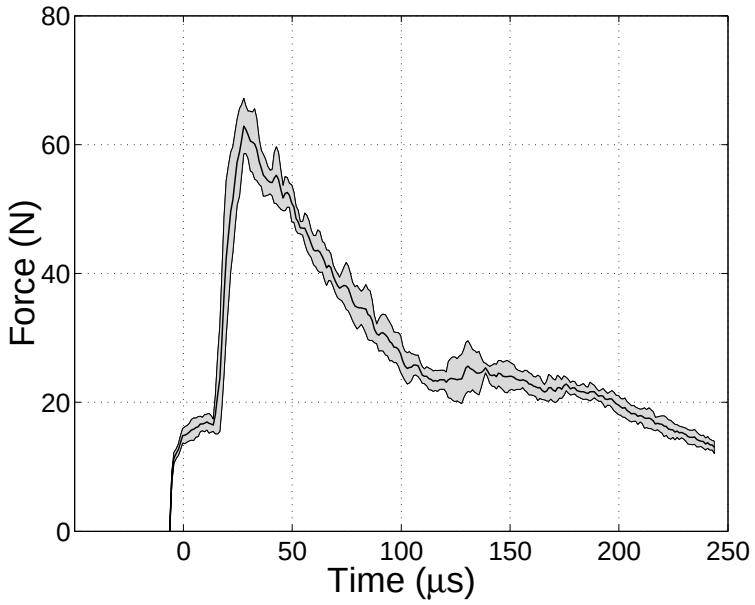

Fig. 5.22: Mean equivalent force acting on the area of the shock tube, with ±1 standard deviation upper and lower bounds shaded.

integration also begins at $-7\mu s$. Time $t = 0$ is considered to be the time at which the shock wave reaches the dome.

5.4.4 Results

The simple model is used with the mean input pressure data ± 1 standard deviation on both the *inversion* and the *eversion* process. The forces acting on the mass, the displacement, velocity and acceleration, and the kinetic and potential energies are shown for *inversion* in Fig. 5.23 and for *eversion* in Fig. 5.24.

The simple model predicts a peak velocity of 156.8m/s in *inversion* and 168.9m/s in *eversion* . These velocities are smaller than the peak velocities measured using particle velocimetry since they represent a mean velocity for a dome treated as a point mass.

The simple model predicts particle release at the maximum velocity, and since this velocity is constant for the whole mass, the time of release coincides with the time of maximum kinetic energy. The predicted time of release is $72 - 74\mu s$ in *inversion* and $75 - 77\mu s$ in *eversion*. A range is given since the pressure ± 1 standard deviation calculations have also been carried out. In both *inversion* and *eversion* the potential energy at release is relatively small compared to the kinetic energy. In addition, this potential energy remains relatively small until after the particles have been released. Hence, the dome is behaving mostly as a travelling membrane, the first case described in Section 5.3.7.

Clearly this simple model is limited in its scope, lacking the ability to track the movement of individual portions of the inverting dome. It does, however, have a number of advantages, being very quick to run and giving simple insight into the inversion of the dome as a whole.

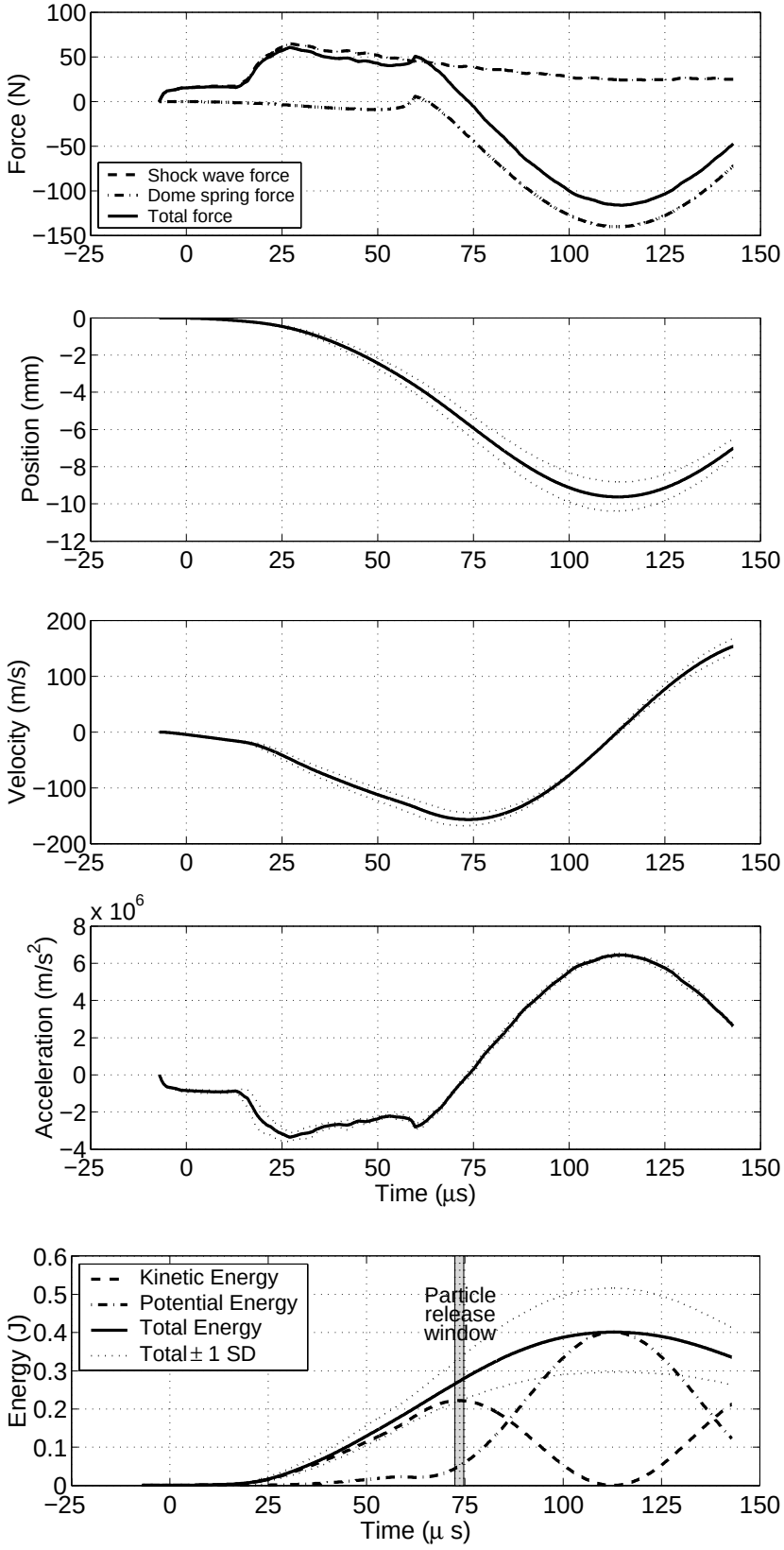

Fig. 5.23: Simple dynamic model results for the *inversion* process.

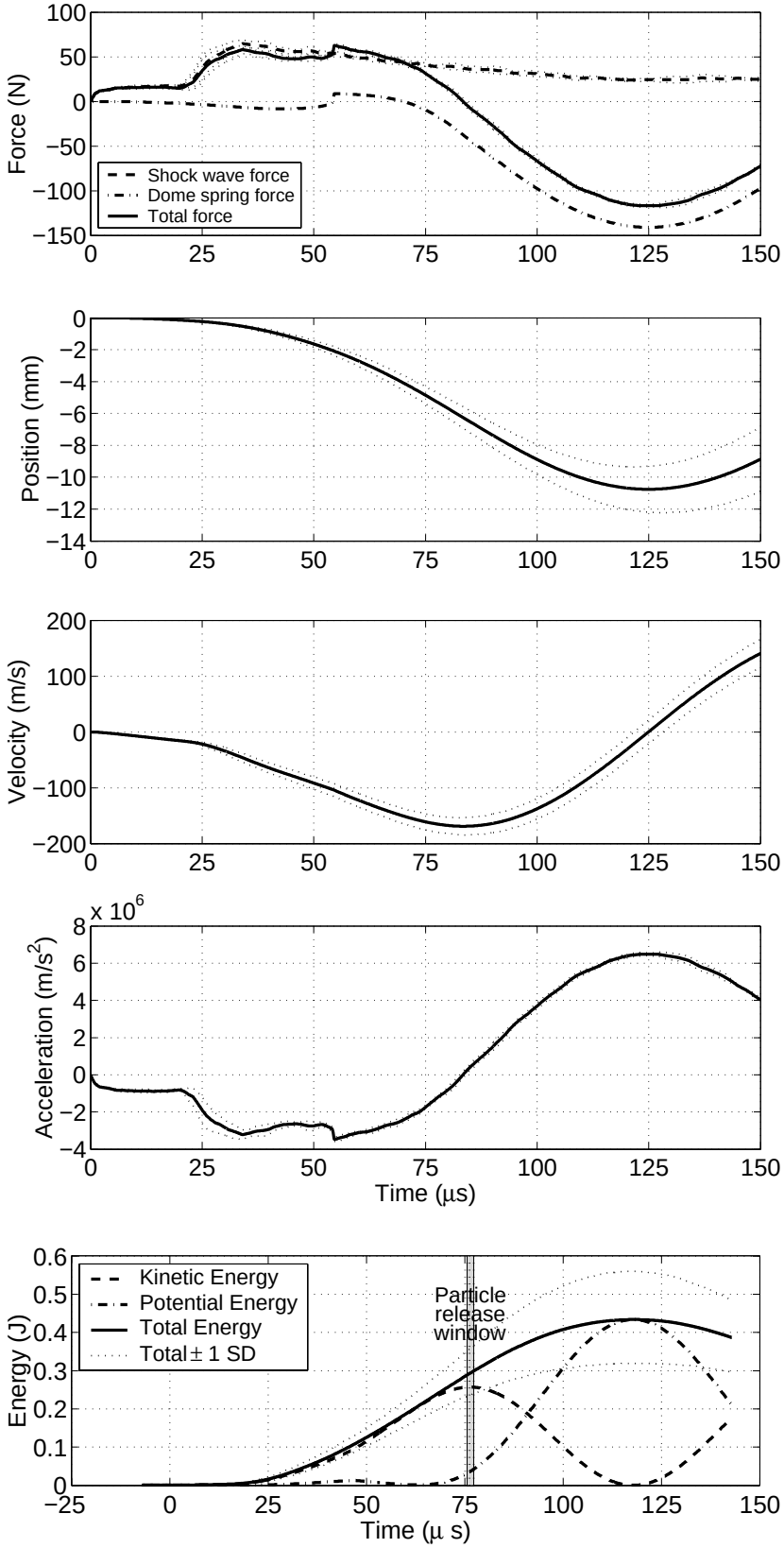

Fig. 5.24: Simple dynamic model results for the *eversion* process.

5.5 Moulding imperfection sensitivity

Section 4.1.1 has shown that manufactured domes can have a significantly different geometry from the nominal dome shown in Fig. 5.25(a). This section aims to introduce a number of model imperfections to the geometry of the dome and to investigate the effect of these on the peak velocities of an inverting dome. Imperfections are characterised by misalignment of the top injection-moulding plate with respect to the bottom plate. Three types of plate misalignment are investigated here: a horizontal shift, shown in Fig. 5.25(b), such as might be produced by residual material in the plate alignment pins; a vertical shift, shown in Fig. 5.25(c), produced by dust or residual plastic between the plates; and a rotational shift about a point on the axis of symmetry $0.25mm$ from the surface of the dome, shown in Fig. 5.25(d), due to asymmetrically positioned dust or residue. A fourth set of analyses is performed where the thickness of the dome is varied uniformly, shown in Fig. 5.25(e). The dynamic analyses are carried out on 24×2 meshes.

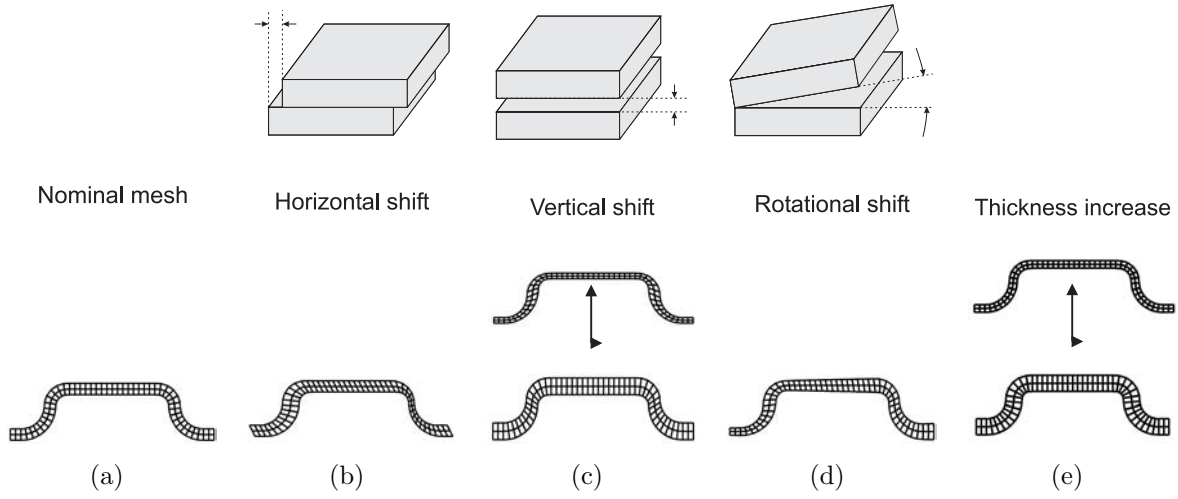

Fig. 5.25: (a) Nominal dome mesh, and (b) horizontal, (c) vertical and (d) rotational imperfections in the moulding process; (e) uniform change in thickness.

5.5.1 Horizontal shift

A horizontal shift of $0 - 250\mu m$ is introduced between the top and bottom plate, as shown in Fig. 5.25(b), which has the effect of thinning one side of the dome side wall and thickening the opposite side. The peak velocity of the apex of the dome, and the peak velocities of a number of points on a diameter are shown in Figure 5.26.

The peak velocity at the apex appears to drop significantly with increasing horizontal plate shift. However, if we examine the peak velocity across a diameter it is evident that the overall peak velocity varies less significantly, and that it occurs at a different place on the dome, away from the apex. The position of the peak velocity for a shift of $250\mu m$ is approximately $1mm$ away from the apex. In summary, the magnitude of the peak velocity does not appear to be highly sensitive to horizontal errors in moulding, although it may occur away from the apex of the dome.

This movement away from the centre has significant implications in the measurement of powder velocity using the particle velocimetry method described in Section 4.5. Fig. 5.27 shows velocity maps of inverting domes with and without plate shift at $t = 90\mu s$

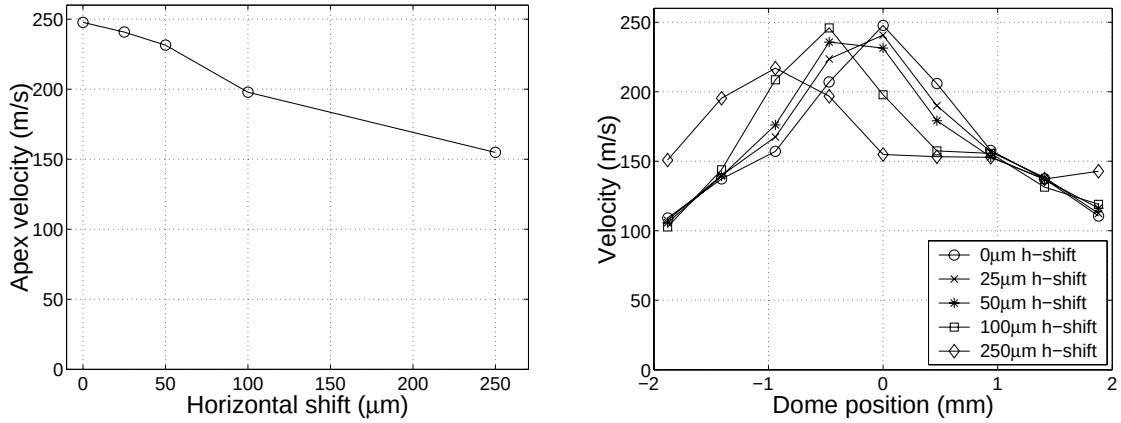

(a) (b)

Fig. 5.26: Effect of a horizontal shift in the moulding plates on (a) peak *inversion* velocity at the apex, and (b) peak *inversion* velocities along a diameter of the inverting dome.

after inversion. If the plate shift is significant, the peak velocity no longer occurs at the centre of the dome. In particle velocimetry the light beams will measure velocity across a diameter, and if the peak velocity does not occur on this diameter it will not be captured.

Fig. 5.28 illustrates the dynamic *inversion* of a normal dome and a dome with $250\mu m$ of horizontal plate shift at $10\mu s$ intervals during inversion. The Von Mises stress is shown in colour. The *inversion* of the dome with the horizontal shift is highly asymmetric, and not dissimilar to the images of asymmetric inversion shown in Fig. 4.14. There is no obvious significant increase in the maximum Von Mises stress due to the horizontal imperfection. This indicates that a significant weakening of the domes due to this sort of imperfection is not expected, although the behaviour after the *inversion* has taken place may differ more significantly. The paths of particles are also expected to differ, but a full analysis has not been carried out.

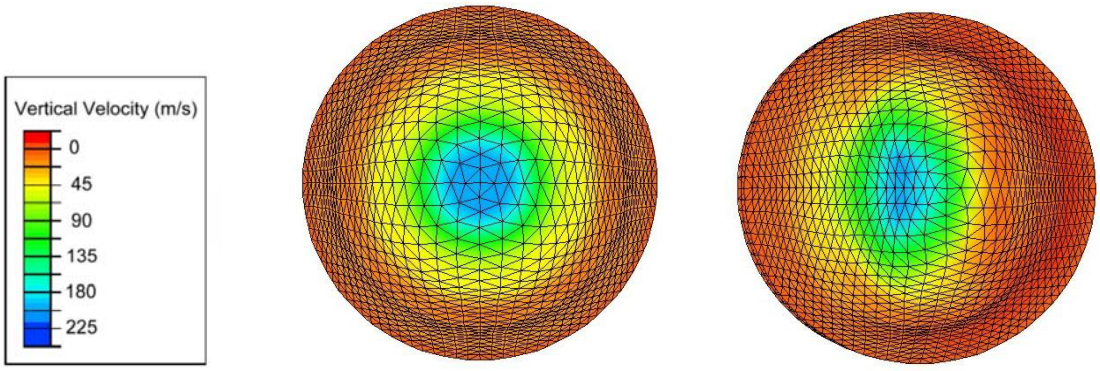

(a) (b)

Fig. 5.27: Vertical component of velocity for (a) a nominal dome and (b) a dome with $250\mu m$ horizontal plate shift in *inversion* seen from below at $t = 90\mu s$.

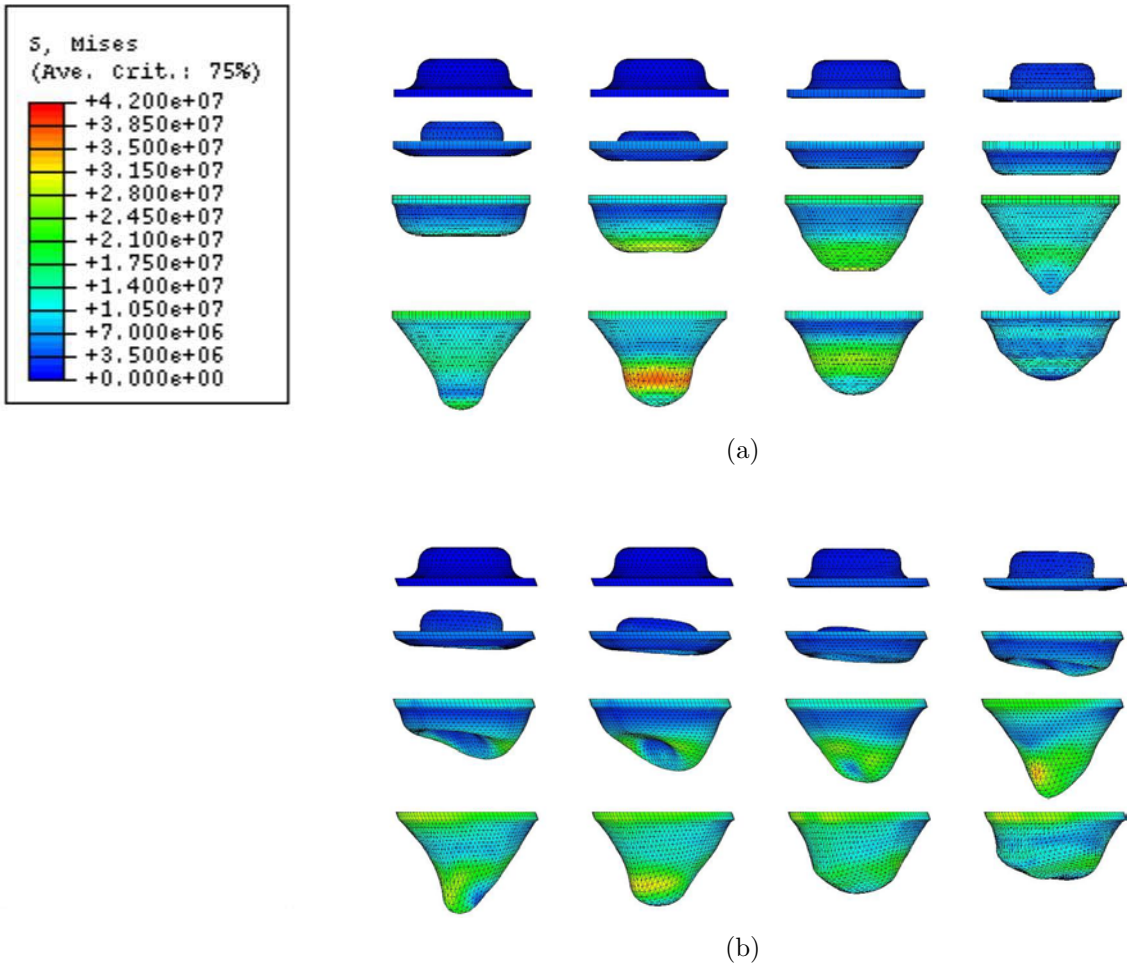

Fig. 5.28: Images of dome *inversion* produced at $10\mu s$ intervals for (a) a nominal dome and (b) a dome with $250\mu m$ horizontal plate shift.

5.5.2 Vertical shift

A vertical shift between $-250\mu m$ to $+250\mu m$ is introduced between the top and bottom plate, as shown in Fig. 5.25(c). The vertical shift does not affect the side walls of the dome, but alters the thickness of the central disc and of the edge, with positive values increasing the thickness. The peak velocity of the apex of the dome, and the peak velocities of a number of points on a diameter are shown in Figure 5.29.

Vertical shift appears to have a complicated effect on the dome. Intuitively, one would expect the peak velocity to rise with decreasing thickness, and therefore mass,

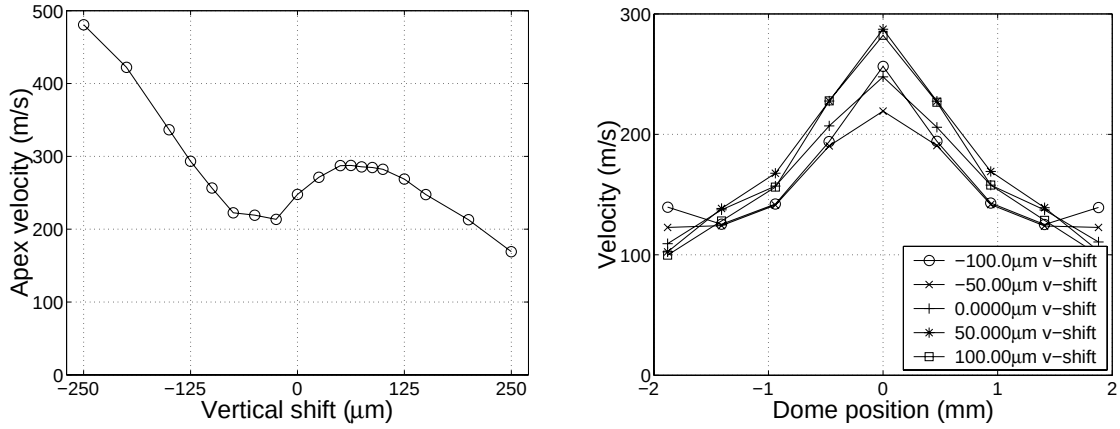

(a) (b)

Fig. 5.29: Effect of a vertical shift in the moulding plates on (a) peak *inversion* velocity at the apex, and (b) peak *inversion* velocities along a diameter of the inverting dome.

and vice versa. At large vertical shift this effect is evident, but for small vertical shift the effect is reversed. There is a local maximum in peak velocity at around $+60\mu m$, and a local minimum at around $-30\mu m$ of vertical shift.

If we wish to design a dome with peak velocity just under $300m/s$, the plateau located at a vertical shift of around $+60\mu m$ provides a design which is less sensitive to manufacturing imperfections of this sort. However, if we wish to increase the velocity to beyond $300m/s$ by vertical shift, we would need to move beyond $-125\mu m$ and the velocity would then be much more sensitive to vertical shift moulding errors.

5.5.3 Rotational shift

A rotational shift of $0 - 2.5°$ is introduced between the top and bottom plate about a point on the axis of symmetry $0.25mm$ from the surface of the dome, as shown in Fig. 5.25(d). The rotational shift affects the thickness of the outer edges of the dome most significantly. The peak velocity of the apex of the dome, and the peak velocities of a number of points on a diameter are shown in figure 5.30.

Rotational shift produces a change in peak velocity similar to a horizontal shift.

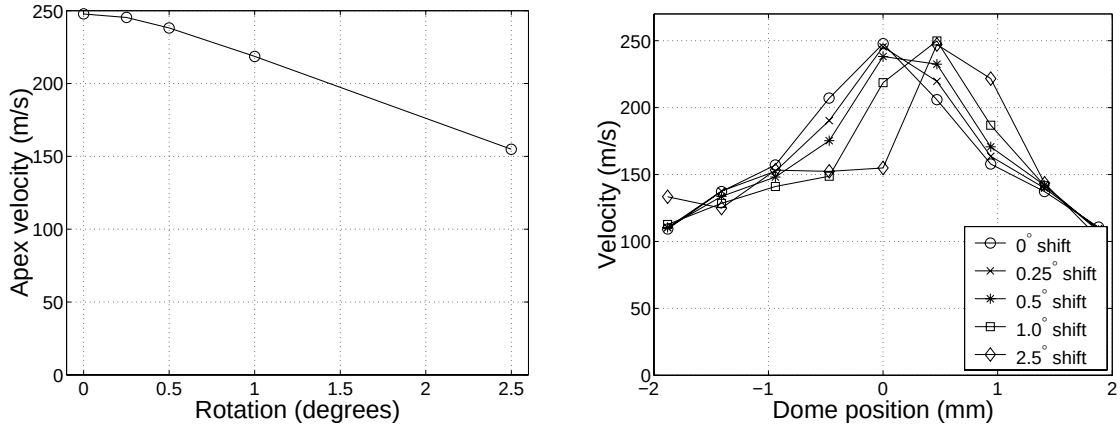

(a) (b)

Fig. 5.30: Effect of a rotational shift in the moulding plates on (a) peak *inversion* velocity at the apex, and (b) peak *inversion* velocities along a diameter of the inverting dome.

Although the peak velocity of the apex appears to drop significantly, in practice the peak velocity is not significantly affected and occurs away from the apex. Again, as with the horizontal shift, the peak velocity of the domes does not appear to be highly sensitive to a rotational shift.

5.5.4 Change in thickness

An overall thickness change to between $300\mu m$ and $700\mu m$ is introduced to the dome geometry, as shown in Fig. 5.25(e). The peak velocity of the apex of the dome, and the peak velocity of a number of points on a diameter are shown in Fig. 5.31. In addition, data from domes from two separate batches tested in Section 4.5.5 is included, with the mean thickness measurement used to plot the points.

The effect of a change in thickness is similar to that of a vertical shift in the moulding plates. The curve exhibits a local minimum and maximum at approximately $475\mu m$ and $525\mu m$ respectively. If we wanted to restrict the peak velocity to between $230m/s$ and $260m/s$ an allowable range in thickness of $450\mu m - 600\mu m$ would apply. In order to increase the velocity to beyond $300m/s$ the thickness must be decreased to less than

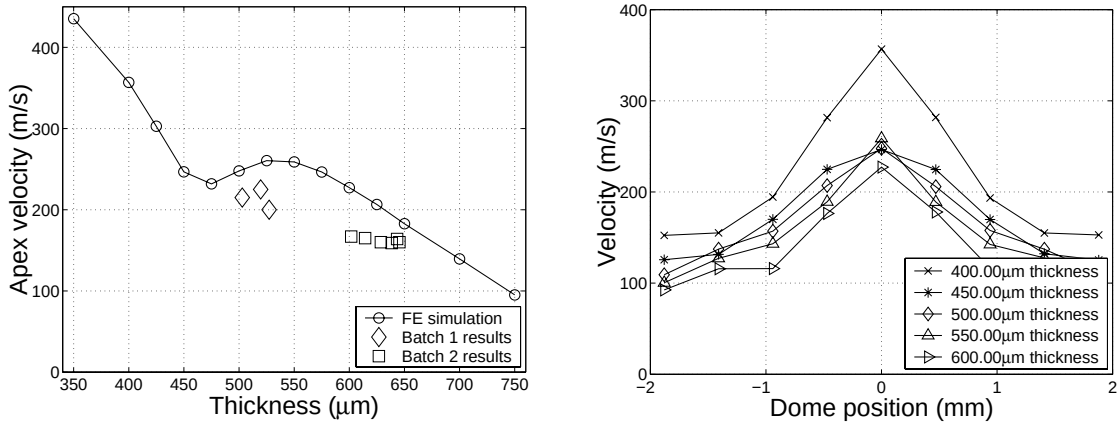

(a) (b)

Fig. 5.31: Effect of a change in dome thickness on (a) peak *inversion* velocity at the apex, and (b) peak *inversion* velocities along a diameter of the inverting dome.

$425\mu m$, in an area much more sensitive to variations in thickness.

The experimental values represent domes with complicated 3-d geometries and the mean thickness is used to plot the points; overall they appear a little lower than the FE prediction. This is likely to be explained by possible additional horizontal and rotational shifts of the mould, which move the peak velocity away from the apex. The velocity shown has been measured using particle velocimetry, and hence may not be the overall peak dome velocity.

5.6 Summary and conclusions

Section 5.1 has given the parameters used in the FE modelling of inverting domes. The construction of a material model from the tests of Chapter 3 has been presented. A method for meshing the geometry of the inverting domes has been devised which is adequate for similar dome geometries. The microtome slicing data has been used in the construction of a full 3-d dome mesh representing *actual* domes from a specific batch and mould set.

Section 5.2 has investigated the quasi-static behaviour of inverting domes. A simple

inflation has been used as a benchmark for mesh refinement, and 36×3 axisymmetric and 24×2 full 3-d meshes are used in most of the analyses. The stability curve of the dome has been explored using numerically stabilised and post-buckling analyses.

The dynamic behaviour of domes has been explored in Section 5.3. First an optimisation procedure is run to find a suitable level of Rayleigh damping for inverting domes at very high strain rates. This has been done by matching dynamic FE simulations on real domes to experimental data. A value of 7% of critical damping is found to fit the data best. Simulations have been run on nominal specifications domes in both *inversion* and *eversion*, and a procedure for determining the eventual path and trajectory of particles on the domes has been developed.

Section 5.4 has concerned itself with the development of a simple dynamic model consisting of a mass on a non-linear spring accelerated by a time-varying force as a simplified representation of the behaviour of the inverting dome. The simple model predicts a peak velocity of 156.8m/s in *inversion* and 168.9m/s in *eversion*, lower than the FE calculations since they represent a mean velocity for a dome treated as a point mass.

The issue of model imperfections as a result of moulding has been explored in Section 5.5. It was found that horizontal and rotational imperfections move the peak velocity away from the apex but do not significantly affect its magnitude. The peak velocity is not highly sensitive to vertical imperfections or to limited changes in thickness for the nominal specifications dome, although if larger vertical imperfections or thickness changes are imposed the sensitivity increases substantially.

Chapter 6

Design of improved injection-moulded domes

This chapter is concerned with improving the performance of injection-moulded inverting domes. Two basic approaches are presented here: the application of heat and pressure treatments, and a small variation in the dome's geometry. Section 6.1 investigates the effect of the application of pressure for a specified time at a specified temperature, resulting in small amounts of creep deformation in the domes. The performance of these domes is investigated using the stability curve, particle velocimetry and quasi-static burst tests.

Section 6.2 is concerned with the effect of lengthening the side wall of the dome. Moulds are manufactured to produce such a dome and particle velocimetry tests are performed on the domes with the new geometry. The possibility of combining the heat and pressure treatments with the new geometry is also explored.

6.1 Heat and pressure treatments

A range of combined heat and pressure treatments are applied to a batch of domes. The aim of the treatments is to deform the dome by means of pressure, and to allow stresses to relax by means of temperature, thus inducing permanent deformation and a state of self-stress in the domes. The treatments consist of applying a pressure to a

batch of inverting domes clamped to a holder, as shown in Fig. 6.1, and placing the holder in a pre-heated oven at a set temperature for a period of time. The pressure is applied either by means of a connection to a gas cylinder or through a screw-actuated piston. The pressure is applied either to the concave face (inflation) or to the convex face (inversion) of the domes. The holding device is sealed during the heat treatment.

6.1.1 The application of heat and pressure treatments

During the heat treatments, the pressure outside the device, within the oven, stays constant at atmospheric. There may be a small loss in pressure due to leaks within the device and due to the permeability of the domes during the heat-treatment, although neither is expected to be significant. Assuming ideal gas behaviour, the pressure p_{heat} applied at temperature T_{heat} is found from

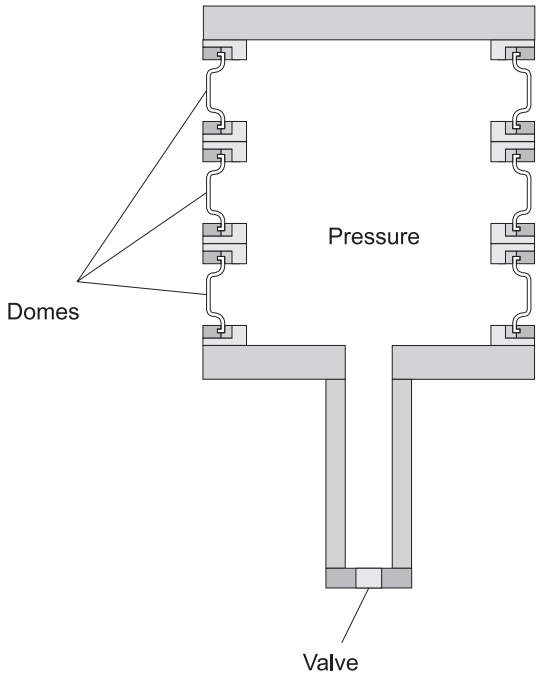

Fig. 6.1: A batch of inverting domes clamped to a holder to which pressure is applied. For inflation treatment domes are clamped as in the diagram; for inversion treatment domes are reversed.

$$p_{heat} = p_{atm}\left(\frac{T_{heat}}{T_{amb}}\right) \tag{6.1}$$

where p_{atm} is atmospheric pressure, T_{heat} is the temperature of the heat treatment, and T_{amb} is the ambient temperature at which the pressure is applied prior to heating. The three heat-treatments applied to the domes are shown in Fig. 6.2. The corresponding pressure at the treatment temperature is given in Table 6.1. Negative pressure indicates that the pressure is applied from the opposite side by mounting the dome in reverse.

The heat and pressure treatments permanently deform the domes by inducing small amounts of creep deformation in the stressed areas. The domes are visibly deformed after the treatments although no attempt has been made to accurately measure the extent of the deformation. The domes treated in *inversion* exhibit greater visible deformation than the domes treated in *eversion*. This is likely to be due to the greater stresses in the inverted domes compared to the inflated domes.

The creep deformation induced in the domes is expected to have three significant effects. The first is that the dome's geometry is altered by the deformation. In both the inversion and the inflation treatment the amount of travel between the two stable configurations is expected to increase. This increase in travel lengthens the time for which the dome is accelerated during high-speed inversion, and hence the peak velocity reached by the dome.

The second effect is a shift in the force-displacement stability curve. This effect is

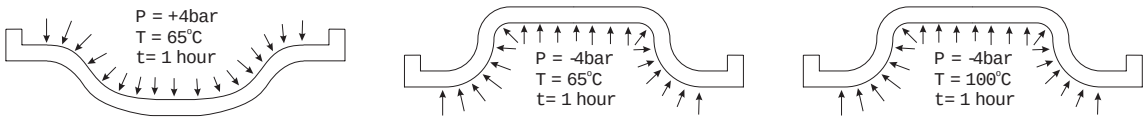

Fig. 6.2: Combined heat-pressure treatments (a) HT1, (b) HT2, (c) HT3 applied to injection-moulded inverting domes.

Table 6.1: Heat and pressure treatments applied to inverting domes.

Label	Direction of heat treatment	Pressure at T_{amb}	Temperature of treatment	Pressure at T_{heat}	Time of treatment
HT1	Inversion	+4bar	$65°C$	+4.61bar	1 hour
HT2	Inflation	-4bar	$65°C$	-4.61bar	1 hour
HT3	Inflation	-4bar	$100°C$	-5.09bar	1 hour

greatest during inversion treatment. Normally the dome is unstressed in the undeformed position, and stressed in a stable inverted position. The dome has no strain energy in the undeformed position and a finite quantity of stored strain energy state in the inverted position. During inversion treatment the creep deformation induces the greatest deformation in the areas that are more highly stressed in the inverted position. This deformation relaxes the inverted position by some degree. This will result in an easier *inversion* and less stored strain energy in the inverted position once the pressure is removed. The uninverted position will no longer be strain-free, and the stored strain energy increases. The *inversion* and *eversion* snap-through pressures are also affected by the treatment.

The third effect concerns the physical structure of the polymer. The induced deformation will largely be taken up by a rearrangement of the crystal matrix. To some degree the material will be permanently deformed and will no longer be isotropic , with the crystal $\overline{c}$ axes becoming oriented in the direction of the applied stress. The deformation may result in a strengthening of the polymer due to the reorientation of the crystal matrix, and a weakening of the polymer due to a thinning out of the material. It may also result in a different stress-strain behaviour due to the anisotropy. There

may also be a small increase in crystallisation as with annealing. The change in the physical structure of the polymer due to stretching will be investigated in more detail for isotropic material in Chapter 7.

6.1.2 Quasi-static behaviour

The quasi-static inversion process of a number of domes with treatment HT1 is investigated using the clear perspex fittings described in Section 4.3.3. A total of three domes are tested in *inversion* and three in *eversion*, and a typical *inversion* -*eversion* sequence is shown in Fig. 6.3. The permanent deformation induced by the treatment is visible in the undeformed images.

The apex displacement vs. pressure is shown in Fig. 6.4. The dome travel, measured in the same way as in Section 4.3.3, is around $7mm$, compared with around $5.5mm$ in the standard domes. The *inversion* pressure is $2.04 \pm 0.31bar$, smaller than the $3.45bar$ measured in the standard domes. The *eversion* pressure is $-4.76 \pm 0.07bar$, larger than the $-2.38bar$ measured in the standard domes.

This data indicates that the heat treatment has successfully increased the travel of the apex of the dome by around 25%, which should increase velocity during high-speed

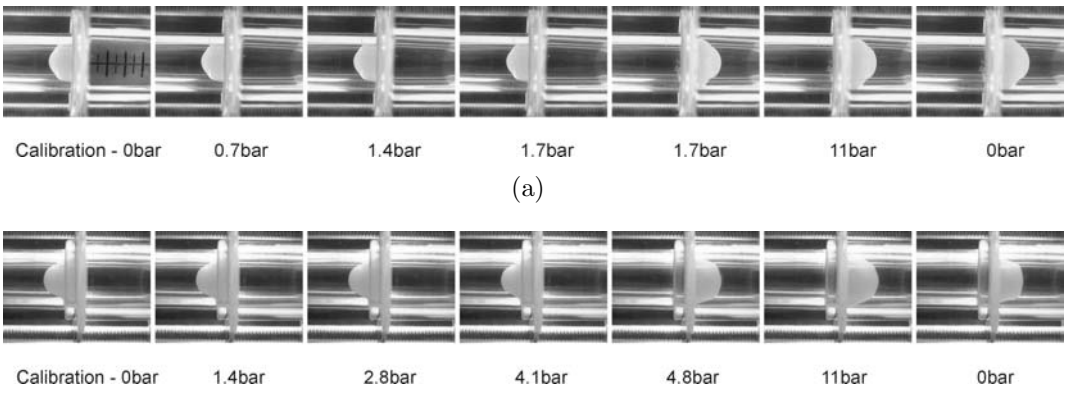

Fig. 6.3: Typical (a) *inversion* and (b) *eversion* experiments for a heat-treated dome.

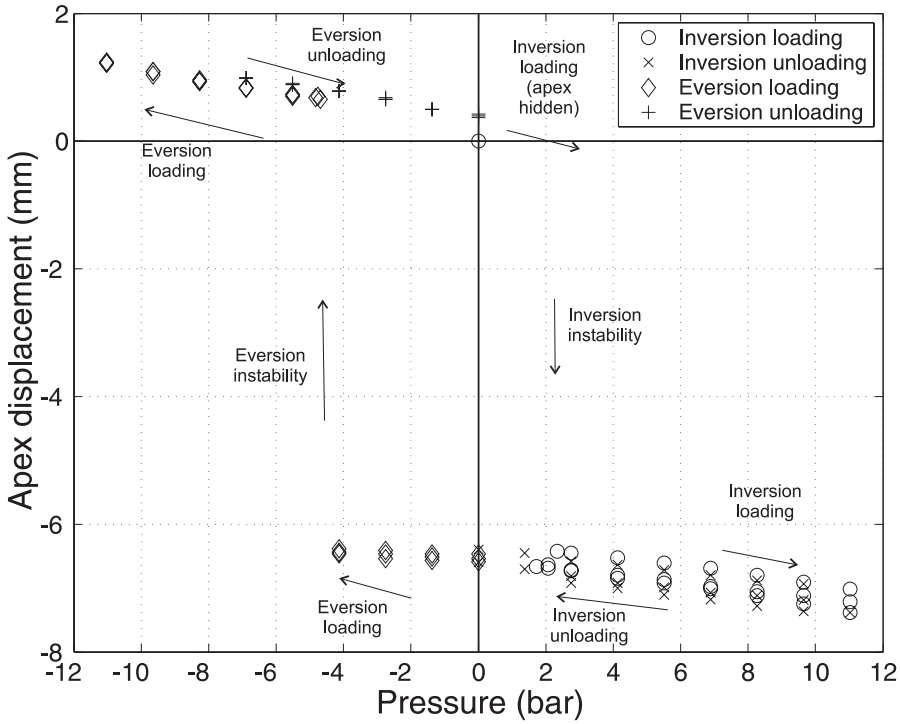

Fig. 6.4: *Inversion* and *eversion* displacements of the apex of a heat treated dome as a function of pressure. Zero displacement corresponds to zero for a non-heat treated dome.

inversion. Also, the treatment has affected the stability curve of the dome, by shifting the snap-through pressure to the left. Although the post-buckling part of the curve is not known, it is likely that less energy will be released upon *inversion* and more upon *eversion* when compared with the standard domes. This should make the energy released by the dome once it reaches instability during *inversion* smaller, and conversely the energy released during *eversion* greater. However, if we consider the path as a whole, it is now easier to invert a dome and harder to evert one, since there is a lower stiffness for *inversion* and a greater one for *eversion*. This effect could favor the *inversion* over the *eversion* for higher velocities.

6.1.3 FE analysis of quasi-static behaviour

Although no thorough treatment of the creep involved in the heat and pressure treatments is attempted, a simplified analysis is used to investigate the changes induced in the domes. It is assumed that during the heat treatment there will be a relaxation of the stresses induced in the domes by the deformation. The stress components in the deformed state during treatments are artificially reduced by a factor $(1 - f)$ where f is a stress relaxation factor. $f = 0$ means no reduction in stress, and $f = 1$ means full relaxation and zero stress. The dome is then allowed to relax to a new stable configuration. The *inversion* and *eversion* pressures of this new configuration are then found from stabilised *inversion* and *eversion* analyses. Fig. 6.5 shows the experimental values of *inversion* and *eversion* snap-through pressures and the FE calculated values for a range of values of f.

The simple relaxation model shows a decrease in the *inversion* pressure and an

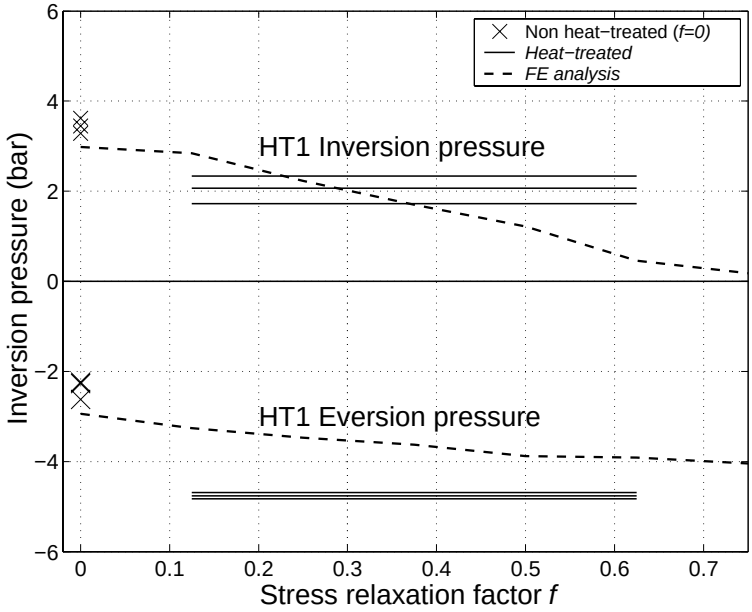

Fig. 6.5: *Inversion* and *eversion* snap-through pressures calculated from the FE analyses using a relaxation of stresses during treatment HT1 and the experimental measured pressures.

increase in the *eversion* pressure, as indicated by the experiment. However, the increase in *eversion* pressure found by experiment is larger than that shown by the FE analysis. One reason for this significant discrepancy may be that nominal geometry domes have been used in the FE analysis. Real domes are thicker, resulting in larger *inversion* and *eversion* pressures. The difference between experimental and FE snap-through pressures is less significant in the analysis on non-heat treated domes. The relationship between apex displacement and pressure is shown in Fig. 6.6 for a value of $f = 0.35$, which best fits the reduction in *inversion* pressure.

It is clear that the simple model fails to capture the increase in dome travel, since the experimental displacements after *inversion* are around $1.5mm$ larger than the FE calculation. The model does capture the shift in the stability curve to the left, although to a smaller degree than the experimental data indicates. A more sophisticated material

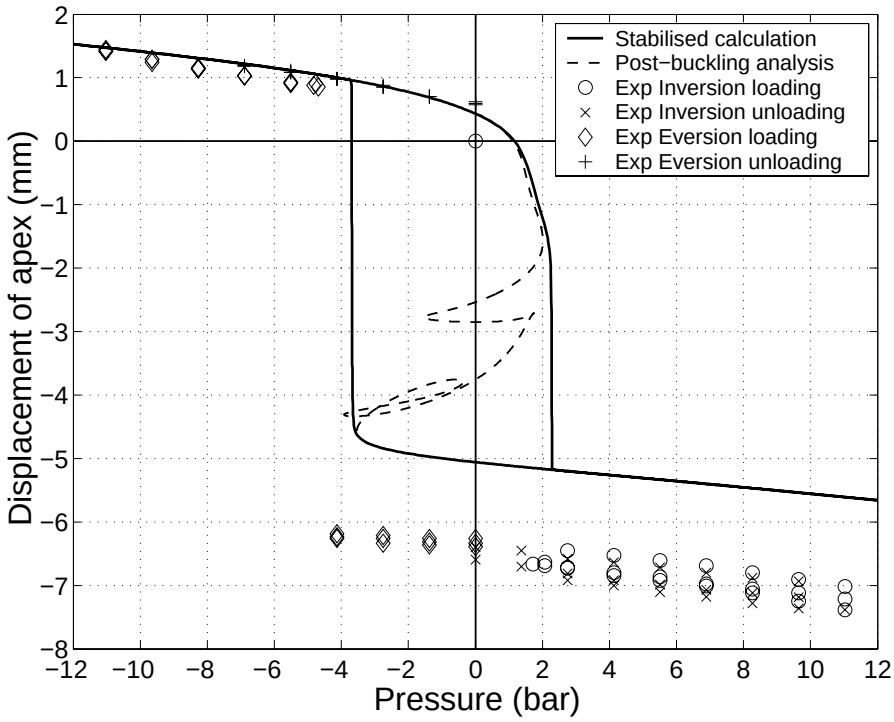

Fig. 6.6: Comparison between the FE stability curve for a treated dome with $f = 0.35$ and experimental data.

model of the processes involved during creep deformation together with accurate stress strain data at the treatment temperatures is likely to be required to improve the FE analysis of heat treated domes.

6.1.4 Particle velocimetry

Small batches of the domes produced using heat and pressure treatments HT1, HT2 and HT3 are tested in high-speed *inversion* and *eversion* using the particle velocimetry technique. The recorded velocities are compared with the results obtained from standard domes in Table 6.2.

The velocities produced on domes treated in HT1 show an improvement of about 50% in the *inversion* velocity and about 10% in the *eversion* velocity. It is likely that the increase in dome travel provides an overall increase in particle velocity. This will apply to both *inversion* and *eversion*. Additionally the shift of the stability curve is then likely to favour *inversion* over *eversion* by making the *inversion* path a lower energy barrier than the *eversion* path.

Table 6.2: Particle velocity measurements for high-speed *inversion* and *eversion* in treated domes. The number of domes tested for each condition is shown as n.

Heat and Pressure Treatment	Testing Condition	Mean particle velocity (m/s)	SD particle velocity (m/s)
none	Inversion (n=12)	162.2	5.2
none	Eversion (n=13)	206.9	9.6
HT1	Inversion (n=5)	243.0	16.8
HT1	Eversion (n=5)	224.6	5.9
HT2	Eversion (n=5)	257.8	5.2
HT3	Eversion (n=5)	263.2	9.2

Treatments HT2 and HT3 have only been tested in *eversion* since the deformation induced by the treatment was smaller than in HT1. In both cases there is an improvement of about 25% in the *eversion* velocity. Here we expect a small increase in the dome travel combined with a shift in the stability curve to the right. The actual stability curve has not been investigated experimentally for HT2 and HT3.

6.1.5 Quasi-static dome burst

The burst pressure of treated domes is measured using the method described in Section 4.6. The results are shown in Table 6.3.

Although the number of domes tested is small, it appears that HT1, the inverted treatment, has increased the burst pressure upon *inversion* and decreased the burst pressure on *eversion*. Conversely, HT3 has increased the *inversion* burst pressure and decreased the *eversion* pressure. One possible explanation for this result is that the microstructure changes in a way that attempts to resist the deformation applied during

Table 6.3: Dome burst pressure in quasi-static *inversion* and *eversion*, and the equivalent expected burst pressure for injection-moulded sheet.

Heat and Pressure treatment	Testing Condition	Mean burst pressure (bar)	SD burst pressure (bar)
none	Inversion (n=8)	14.5	0.5
none	Eversion (n=8)	14.9	0.4
none	Equivalent inj-m disc ($t = 640\mu m$)	15.6	
HT1	Inversion (n=4)	14.0	0.8
HT1	Eversion (n=4)	15.8	1.0
HT3	Inversion (n=3)	15.0	1.0
HT3	Eversion (n=3)	14.0	1.0

the treatment. The crystal $\overline{c}$ axes orient in the direction of the applied stress during the treatment. If they are subsequently tested at quasi-static burst in this same direction, they appear stronger. If they are tested in the reverse direction, the crystal $\overline{c}$ axes are no longer more favorably aligned, and the burst pressure decreases. Overall, however, the changes in burst pressure induced by the treatments are small and within the bounds of experimental error.

6.1.6 Conclusions

Heat and pressure treatments provide a simple way in which to induce small permanent deformations and changes in microstructure on injection-moulded domes. The treatments consist in the application of heat and pressure for a specified time to each dome. The treated domes show an increase in particle velocity of up to 50% over the untreated domes when tested using small quantities of drug powder, reaching mean velocities of up to $263.2 m/s$, as a result of an increase in the available dome travel, and a shift in the stability curve. The increase in dome travel favours both the high-speed *inversion* and the *eversion* process, although the shift in the stability curve will favour one path over the other. There are very small changes in the burst pressure that may be due to changes in microstructure.

6.2 Changes in dome geometry

Section 5.5 has shown that misalignment of the moulds will cause geometrical variations of domes which can alter the peak velocities. We now apply geometrical changes directly to the nominal dome and examine the effects.

6.2.1 Domes with a longer side wall

A change in the basic dome geometry is introduced by lengthening the vertical side wall between the two curved sections in the inverting dome. The cross-section of a dome with a longer side wall is shown in Fig. 6.7. Apart from the shaded region, the dome is identical to the specifications of Figure 2.4.

A number of meshes are created with varying lengths of side wall, and each model is analysed for high-speed *inversion*. The peak velocity reached by a range of nodes on the surface is recorded. The apex velocity and the velocity of other points on the dome are shown in Fig. 6.8. Although the FE calculation predicts a significant increase in the apex velocity, the increase in velocity of the rest of the dome is much more limited.

6.2.2 Particle velocimetry

A mould is manufactured to produce domes with a $0.5mm$ longer side wall. Initially some difficulties are encountered using the new moulds with the melt struggling to fill the mould. Two exit spurs are then added to aid the flow of the melt though the mould and adequate filling is achieved. The accuracy of the moulds has not been assessed. A number of the domes with the lengthened side wall are treated using treatment HT4,

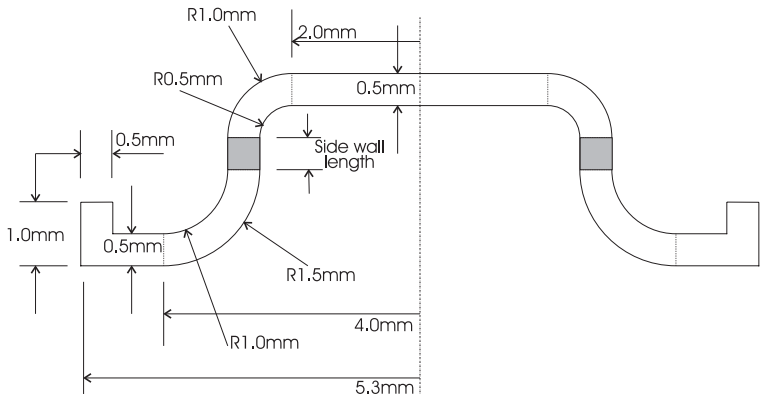

Fig. 6.7: Cross-section of a modified dome with a longer side-wall.

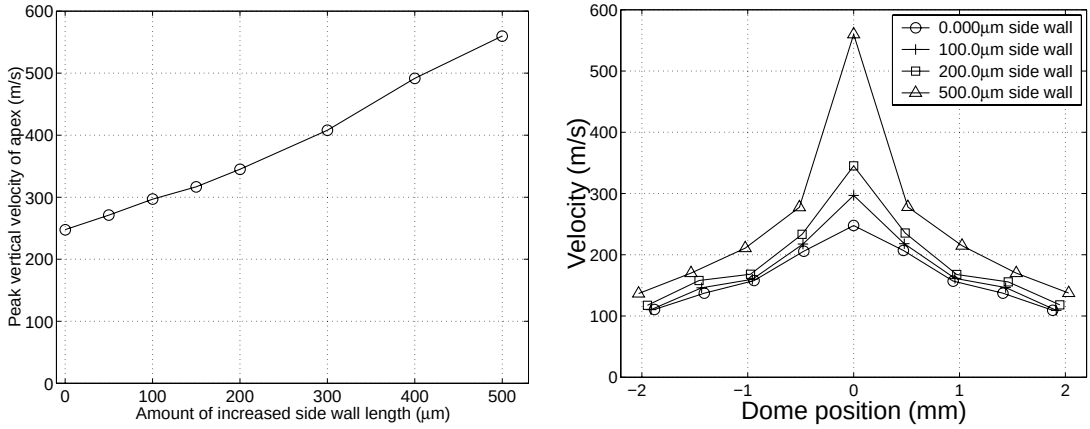

(a) (b)

Fig. 6.8: FE prediction of the effect of increasing the length of the dome side wall. (a) The peak velocity of the apex, and (b) the peak velocity of a range of points on the dome surface vs. side wall length.

reported in Table 6.4. The domes are then tested using the particle velocimetry, and the results are given in Table 6.5.

The new domes with the 0.5mm side wall invert with a much slower peak velocity than is predicted by the FE calculations. The *inversion* velocity is even slower than the original domes. There could be a variety of reasons for this discrepancy. Firstly, the accuracy of the mould has not been verified using the microtome slicing technique, and there is the possibility that the wall thickness of the dome is greater than specified. The new geometry may be more sensitive to manufacturing imperfections than the original

Table 6.4: Heat and pressure treatment applied to inverting domes with a lengthened side wall.

Label	Direction of heat treatment	Pressure at T_{amb}	Temperature of treatment	Pressure at T_{heat}	Time of treatment
HT4	Inversion	+4bar	100°C	+5.09bar	2 hours

Table 6.5: Particle velocity measurements for high-speed *inversion* and *eversion* in domes with a lengthened side wall. The number of domes tested for each condition is shown as n.

Dome type	Heat and Pressure Treatment	Testing Condition	Mean particle velocity (m/s)	SD particle velocity (m/s)
normal	*none*	*Inversion (n=12)*	*162.2*	*5.2*
normal	*none*	*Eversion (n=13)*	*206.9*	*9.6*
0.5mm SW	none	Inversion (n=5)	146.4	16.6
0.5mm SW	none	Eversion (n=5)	258.0	11.5
0.5mm SW	HT4	Inversion (n=5)	299.8	21.0

one. Secondly, the longer side wall results in the dome extending further up the shock tube. There is the possibility that if the dome is not located perfectly in the housing, it may rub along the shock tube on inversion. This friction could dissipate sufficient energy to slow the domes down. In high-speed *eversion*, however, the new domes perform better than the original domes, reaching an average peak velocity of $258 m/s$.

Domes treated using method HT4 reach an average peak velocity of $299.8 m/s$ on high-speed *inversion*. The improvement is likely to come from an increased dome travel and a shift in the stability curve, as indicated for previous heat-treatments. Any contact with the shock tube wall may also be removed by the deformation induced by treatment HT4.

6.2.3 Repeat testing and pre-inversion

The domes with the longer side wall appear to be harder to invert than the standard domes the first time they are inverted. A small number of tests have been performed on domes with a 0.5mm side wall repeating the test on the same dome a number of times,

and also pre-inverting the dome 5 times prior to testing. The results are given in Table 6.6.

There are a number of observations that can be made from these experiments. The velocity of the domes appears to increase with the number of re-tests in both *inversion* and *eversion*. This is not the case with the domes that have been heat-treated. Domes that have been heat-treated in the inverted position are subjected to a deformation similar to that of high-speed *inversion*. This deformation is likely to be greater than that resulting from a single high-speed *inversion* since it is due to the combination of time and temperature. Applying HT4 on the domes has the effect of making the *inversion* faster. This effect comes from an increase in the dome travel due to the

Table 6.6: Particle velocity measurements for high-speed *inversion* and *eversion* in domes with a longer side wall, with repeat tests and pre-inversion.

Dome type	Number of pre-inversions	Heat/pressure treatment	Testing Condition	Particle velocity (m/s)
0.5mm SW	none	none	1st *inversion*	168
0.5mm SW	1	none	2nd *inversion*	207
0.5mm SW	2	none	3rd *inversion*	215
0.5mm SW	none	none	1st *eversion*	256
0.5mm SW	1	none	2nd *eversion*	282
0.5mm SW	2	none	3rd *eversion*	276
0.5mm SW	5 manual	none	Inversion	203
0.5mm SW	inversions	none	Eversion	267
0.5mm SW	none	HT4	1st *inversion*	320
0.5mm SW	none	HT4	2nd *inversion*	310
0.5mm SW	none	HT4	3rd *inversion*	308

permanent deformation, and a change in the stability curve. This improvement can be achieved also by manual inversion of the domes, although in both the repeat tests and the pre-inversions the effect is less significant than with the heat and pressure treatments. Repeat testing of domes that have been heat-treated does not shown any improvement, probably because the permanent deformation induced by the treatment is much larger than that induced by the repeat testing. It is also possible that if there was any contact friction between the domes and the side wall of the shock tube, that the deformation due to the repeat testing and manual inversions ensures its removal.

6.2.4 Conclusions

FE modelling has been used to suggest design improvements to the geometry of the inverting domes. A dome with a longer side wall is designed in order to increase the dome travel. New moulds are manufactured to produce domes with a side wall of 0.5mm. The domes are subsequently tested using the particle velocimetry technique, and appear to be slower than the original domes in *inversion* but faster in *eversion*. Heat-treatment of the domes significantly improves the *inversion* velocity to $299.8 m/s$.

Repeat testing of the domes combined with manual pre-inversion prior to firing has been performed. Domes invert faster if they are re-used, and if they are pre-inverted. Domes that have been heat and pressure treated do not show this improvement. This indicates that the process of repeat-testing or pre-inversion achieves a similar result to heat and pressure treatment but to a lesser extent. The effect on the domes is to lengthen the dome travel and to shift the stability curve to a more favorable position.

6.3 Summary and conclusions

The main aim of this chapter has been to develop ways in which to improve the inversion velocity of injection-moulded inverting domes. The effects of inducing permanent deformation in domes using time, temperature and pressure treatments have been examined. The effect of one such treatment is analysed in detail using quasi-static pressure and imaging to reconstruct the stability curve. The curve has shown that the treated domes have a longer travel, and that the treatment shifts the stability curve in such a way as to favour *inversion* over *eversion* or vice versa. The highest mean velocity is obtained in *eversion* using an inflation treatment of $4bar$ for 1 hour at $100°C$, and is $263.2m/s$, or about 50% greater than in the untreated domes. Small changes in burst pressure are also recorded, and may be due to changes in microstructure.

We have also made use of FE methods to design an improved geometry for the inverting dome. A simple change is introduced, a lengthening of the side wall of the dome by $0.5mm$. Domes manufactured to these new specifications do not perform in the way indicated by the FE modelling. The discrepancy may be due to moulding inaccuracies and a greater imperfection sensitivity, as well as a possible contact between the dome and the shock tube wall during inversion. When used in *eversion*, the new domes out-perform the original domes and invert at $258m/s$, or about 25% faster.

A heat and pressure treatment is then applied to the domes with the new geometry. The *inversion* speed improved substantially over the untreated domes, reaching an average of $299.8m/s$. A small number of tests consisting of repeat high-speed *inversion* of the same domes, or the manual pre-inversion of domes prior to testing, has indicated that the velocity can be improved on untreated domes by mechanical means also, although not as much as with the heat and pressure treatments.

Chapter 7

Design and production of compression-formed domes

Injection-moulding discussed in the previous chapters has numerous advantages since it is a cheap and simple manufacturing technique that is suitable for mass production. This chapter will investigate an alternative manufacturing method, compression-forming. The procedure consists of stamping domes from sheet material by inducing strains from a shaped stamp. Its main advantage is that since the stamping procedure does not take place at temperatures above the melting point of Hytrel, the microstructure of the solid material can be significantly altered prior to stamping, with limited microstructure change due to the stamping process itself.

Firstly the process of compression-forming will be examined on plain compression-moulded Hytrel sheets. A number of adjustable parameters such as plunger shape, depth and forming temperature are addressed. The formed domes are then tested using the methods described in Chapter 4 for particle velocity and for quasi-static burst.

The effects of pre-stretching Hytrel sheet and the expected effects on the mechanical properties are then addressed. The pre-stretching operation is described in terms of deformation matrices. The actual procedure of pre-stretching the sheet in two perpendicular directions is then described. The sheet is then tested in uniaxial tension tests

and in quasi-static burst tests to observe the changes in properties due to the stretching operation.

Domes are then compression-formed from pre-stretched Hytrel sheet. The domes produced using this method are then tested for particle velocity and for quasi-static burst to assess the improvements in performance.

7.1 Compression-forming domes from sheet material

The compression-forming process consists of an upper and a lower stamp that are shaped similarly to the moulds used in the injection-moulding process. The stamps and the retaining equipment are shown in Fig. 7.1(a). The stamps are fixed onto retaining blocks that hold the stamps parallel and enable movement to take place up and down, to stamp the domes and subsequently to remove them. The vertical alignment is ensured by two guide rods, and the removal is assisted by springs.

The upper stamp is made up of an adjustable plunger whose shape consists of a $5mm$ diameter cylindrical rod with a $0.5mm$ radius on the top. The height of the plunger can be adjusted by means of a thread which is used to fix it to the stamp. The surrounding part of the stamp is simply a flat plate. The lower part of the stamp is made up of a $6mm$ diameter cylindrical hole with a $1mm$ radius on the edge, surrounded by a flat plate, shown in Fig. 7.1(b). When the stamps are brought together, a pair of spacers enable the stamps to be held at a specified distance apart, shown in Fig. 7.1(c). This distance is intended to be the thickness of the sheet material.

The forming process is performed in a `Moore` hydraulic press with a capacity of 50 tons. The press platens can be heated by means of built-in heating elements. The press and forming stamps are allowed to reach the desired temperature prior to forming. Dur-

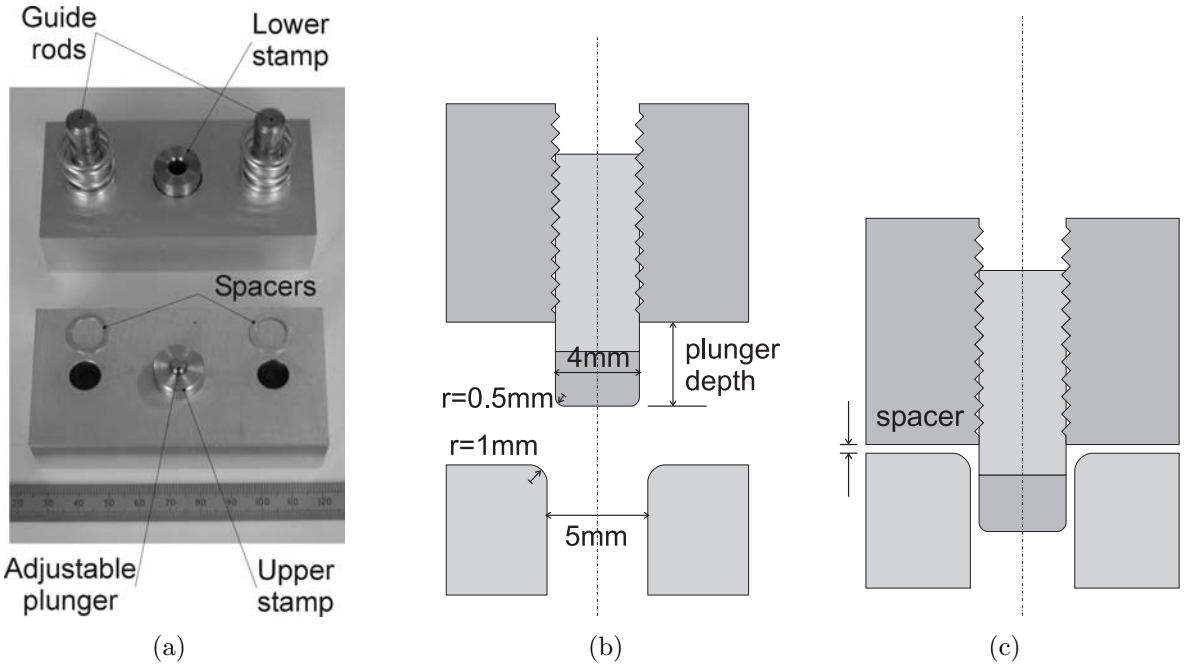

Fig. 7.1: (a) Equipment used for compression-forming domes from Hytrel sheet, and (b) the compression-forming stamps before forming and (c) during forming, with an adjustable threaded plunger and adjustable spacers.

ing the forming process, the sheet material is introduced between the heated separated formers and the formers are brought gently together over approximately 2 minutes to allow for the material to warm up to the temperature of the formers. The formers are then held at the separation dictated by the spacers for a further 2 minutes, after which the formers are separated and the material is removed. The material is then allowed to cool to room temperature. A strip of typical domes produced with this technique is shown in Fig. 7.2.

In order to produce a noticeable dome shape, the plunger depth must be larger than the equivalent in the injection moulds because the domes are under a state of stress during the forming process, and some spring-back occurs once the stress is relieved. After pressing, the domes are cut out from the sheet material using a custom-made punch which aligns the dome with the apex of the punch. This procedure is prone to

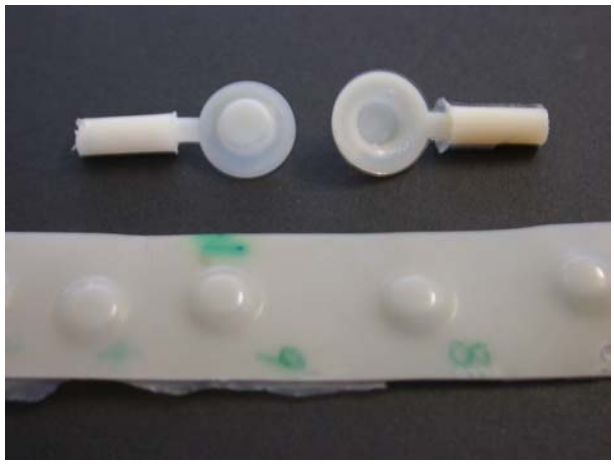

Fig. 7.2: Typical strip of compression-formed domes. Also shown are injection-moulded domes for comparison.

error, although industrially better methods could easily be employed.

7.2 Tests on isotropic compression-formed domes

A range of domes are compression-formed from isotropic Hytrel sheet produced with the technique described in Section 3.1.2. One batch of domes is produced at a temperature of $120°C$ with a range of plunger depths of $3-5mm$. Although the compression-moulded sheet is nominally $0.5mm$ thick, there are recorded variations in the thickness before forming, with a measurement range of 0.513 to $0.567mm$. The thickness of the material prior to forming is recorded using a micrometer. The measurement of the thickness of the domes after forming has not been attempted.

7.2.1 Particle velocimetry

A selection of these domes is tested using the particle velocimetry technique. The mean recorded velocities during *inversion* and *eversion* and the percentage of domes that burst during testing are shown for a range of plunger depths in Table 7.1.

At a plunger depth of $3mm$ the domes are not bistable, and it is not possible to

Table 7.1: Particle velocity measurements in *inversion* and *eversion* for domes formed from compression-moulded isotropic sheet for a range of plunger depths at $120°C$.

	Inversion		*Eversion*	
Plunger depth (mm)	Particle vel. (m/s)	Domes burst during test	Particle vel. (m/s)	Domes burst during test
3.0 ($n = 4$)	210.3	0%	unstable	
4.0 ($n = 4$)	254.8	0%	242.3	0%
5.0 ($n = 4$)	342.3	25%	313.5	25%

test them in *eversion*. There is a general trend of increasing velocity with increased plunger depth; varying the depth from 3 to $5mm$ increases the average particle velocity on *inversion* from 210 to $342m/s$. These velocities are already substantially higher than those achieved with the standard injection-moulded domes. However, 25% of domes made with a plunger depth of $5mm$ burst during testing.

Domes pressed with longer plunger depths result in a bigger, more well-defined domed shape. Hence, during *inversion* (and *eversion*) they will be able to travel for a longer distance before being drawn back by the stretched material. These experiments indicate that in order to achieve faster powder velocities it is desirable to use greater plunger depths. However, it appears that the strength of the domes is being reduced by the forming process — this is likely to be due to two factors. The first is that the forming process itself is making the domes thinner, and therefore weaker; the second is that since the domes are able to invert faster, they stretch more as a result of the momentum that is gained during the inversion. One way to separate the effects is to inflate domes to burst under quasi-static pressure, as will done in the next section.

A second batch of domes is produced at room temperature. Experimentation with a

range of plunger depths has indicated that the minimum useable depth at this temperature is $6mm$ - pressing at shorter plunger depths results in very small dome deformations and dome shapes very similar to the flat disc. Although particle velocities with these domes in *inversion* averaged $287m/s$, all of the domes burst during the inversion.

The more limited deformation of domes pressed at room temperature indicates that the permanent deformation is affected by the temperature - the residual strain increases with increasing temperature. The burst of these domes indicates that significant damage has been caused to the microstructure by the cold forming process.

7.2.2 Quasi-static dome burst

The batch of domes formed with plunger depths of $3-5mm$ at $120°C$ is tested for burst pressure in experiments as described in Section 4.6. The burst pressure P_{meas} is recorded from the experiments. It is not possible to attempt a calculation of the stress at burst since the thickness of the dome after pressing is not known. Instead, an expected burst pressure P_{calc} is calculated from unpressed sheet material of equivalent thickness, from the burst stress measured in Section 3.4.2. The ratio between the experimental burst pressure and the calculated burst pressure $\frac{P_{meas}}{P_{calc}}$ is an indication of the weakening effect of the dome forming process, and is shown in Table 7.2. This is done in order to account for the variations in thickness across the different domes.

The data shows that there is little measurable difference in the quasi-static burst pressure as a result of pressing. All of the compression-formed domes have approximately 80% of the strength of the original material, and this is likely to be a geometric effect due to the permanent deformation induced by the formers on the sheet material. This data would back the theory that $5mm$ and $6mm$ plunger domes are bursting as a result of the increased momentum they gain during inversion.

Table 7.2: Ratio of experimental to calculated burst pressure after forming.

Plunger depth (mm)	Inversion Mean ratio $\frac{P_{meas}}{P_{calc}}$	Eversion Mean ratio $\frac{P_{meas}}{P_{calc}}$
3.0 ($n = 4$)	82%	83%
4.0 ($n = 4$)	81%	82%
5.0 ($n = 4$)	79%	80%

7.2.3 Conclusions

Compression forming domes from sheet material is a viable technique, having produced indications of reliable powder velocities in *inversions* and *eversions* of around $250m/s$ without burst by pressing at $120°C$ with a plunger depth of $4mm$. Increasing the plunger depth beyond this value does produce faster powder velocities, but a percentage of domes burst during the process. The remainder of this chapter investigates the possibility of increasing the strength of the material, so that domes can be produced using this technique that invert fast and do not burst.

7.3 Pre-stretching Hytrel sheet

Chapter 3 has presented the microstructure of Hytrel as being made up of continuous and interpenetrating crystalline and amorphous domains. Stretching of the polymer results in permanent deformation of the crystalline domains, and stretching of the amorphous domains. The polymer does not fully recover since the crystalline domains deform plastically. If it is possible to pre-deform the polymer in a uniform way in the direction in which the stress will be applied, the polymer will appear stronger purely due to the geometric effect of reloading from a pre-strained state. Weakening may take place as a

result of the disruption of the crystal domains that will occur during the deformation. This can be prevented if the domains are allowed to recrystallise in their new, deformed state. The objective of this section is to describe a way in which Hytrel sheet may be pre-stretched prior to dome forming. A series of experiments has been performed to demonstrate the viability of this approach.

7.3.1 Planning the pre-stretching operation

The strength that is required in the inverting domes is in a direction perpendicular to the dome thickness. Little strength is required in the thickness direction since the deformation and the applied loads result in small stresses across the thickness of the dome. The dome acts as a membrane, required to resist stresses in the plane rather than in the thickness. Hence, an equibiaxial stretching of the Hytrel sheet should produce the required strength in the plane of the sheet, and in the domes.

The temperature at which the stretching takes place should be close to, but not above the crystallisation temperature of the hard blocks, given in DuPont's literature as $112°C$ [17]. The stretching process should not take place above the crystallisation temperature of the hard blocks, otherwise the deformation would result in a totally new crystalline structure, and the effects of orientation due to the stretching would be lost.

In addition, the procedure should take place at a temperature around the glass-transition temperature of the hard blocks, to facilitate crystallisation of the non-crystallised hard blocks as well as general polymer mobility. The T_g^{hard} has been measured in Hytrel 4056 as $80°C$ [28]. In Hytrel 4068 experiments from Section 3.3.8 have indicated that it is likely to be between 100 and $120°C$.

Li and White [32] performed a series of experiments on biaxially oriented Hytrel films, and used a stretching temperature of $90°C$ to produce the films for a range of

grades of Hytrel. Stretching at this temperature they were able to observe significant orientation in terms of film birefringence and wide-angle X-ray scattering. A stretching temperature of $90°C$ is therefore selected for the process.

The residual strain after uniaxial stretching at room temperature has been found in Section 3.3.7. Blundred [6] performed similar uniaxial load-unload experiments at $90°C$ and found that the residual strain is unaffected by the temperature for strains up to 200%, and that beyond 200% it is approximately half of the value at room temperature. The residual strain at higher temperatures is likely to be highly dependant upon the cooling rate of the material, and whether recovery is allowed to take place at the same temperature as the stretching. Blundred's experiments observed residual strain in samples unloaded at the same temperature as they are stretched, and hence the recovery is greater, and the residual strain smaller.

No residual strain data is available from biaxial strain experiments, although it is expected that these will not differ much from the superimposed residual strains resulting from two perpendicular constant-width operations. In order to aim for a residual strain of approximately 100% in each direction, the sheet is stretched to a maximum strain of 350% in each direction.

Due to the lack of an available biaxial stretcher during the course of this study, the stretching process is performed in two stages. The sequence of events involved in the stretching operation is shown diagrammatically in Fig. 7.3. Sheet material is clamped in wide grips to perform constant-width plane strain stretching (Fig. 7.3(a)). The material is stretched in the environmental chamber and subsequently cooled using a freeze spray (Fig. 7.3(b)). The load is then released, and residual strain is present in the sheet (Fig. 7.3(c)). The sheet is then unclamped and the central part is cut to a rectangular shape for stretching in the perpendicular direction (Fig. 7.3(d)). Finally, the stretching in the

perpendicular direction takes place in the same way (Fig. 7.3(e)).

Design of the grips prevents the samples from narrowing near the grips, although at large strains the samples narrow noticeably near the centre. It is therefore not reasonable to assume that samples have been stretched at constant-width. The resulting sheets show evidence of a range of residual strains at different positions. Stretching in a biaxial testing machine would enable the production of uniform strain in the sheet.

7.3.2 Stretching operations as deformation matrices

We denote the plastic (residual strain) components of the first stretching operation as deformation matrix Λ_1, the second as deformation matrix Λ_2, and the combined deformation matrix as Λ_C, and directions 1 and 2 as the axes of the first and second constant-width stretching operations, and direction 3 as the axis through the thickness of the sheet where burst occurs. Assuming incompressibility, the deformations imposed by the two-stage constant width stretching operation can be expressed in matrix form

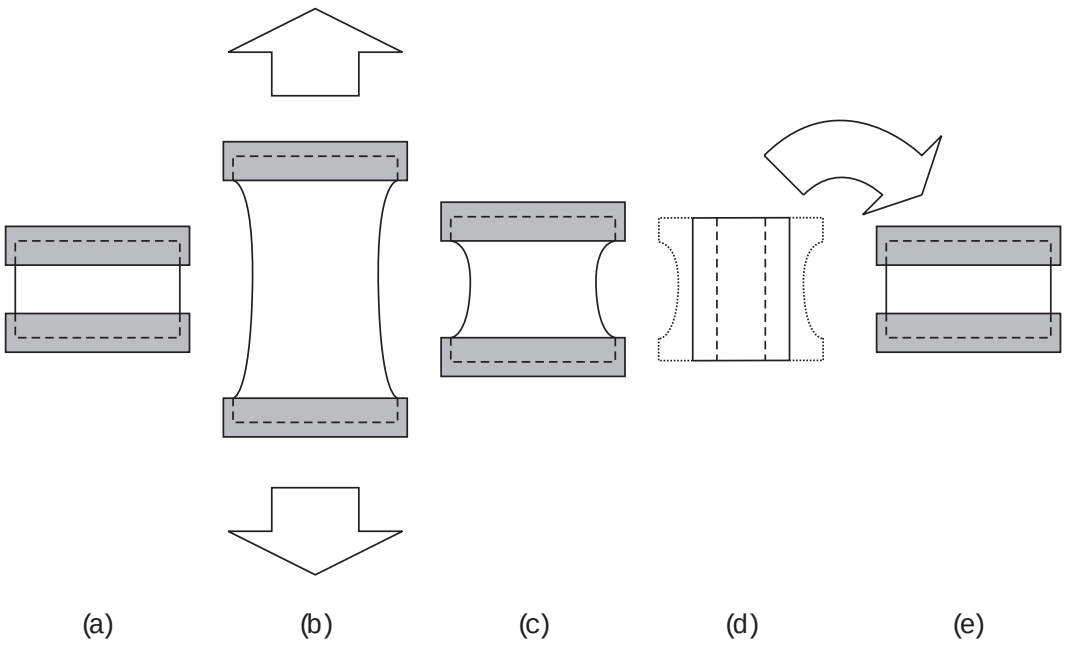

Fig. 7.3: Sequence of events involved in the two-stage biaxial stretching of Hytrel sheet.

as

$$\Lambda_1 \Lambda_2 = \Lambda_C \tag{7.1}$$

or, in full as

$$\begin{bmatrix} \lambda_1 & 0 & 0 \\ 0 & 1 & 0 \\ 0 & 0 & \frac{1}{\lambda_1} \end{bmatrix} \begin{bmatrix} 1 & 0 & 0 \\ 0 & \lambda_2 & 0 \\ 0 & 0 & \frac{1}{\lambda_2} \end{bmatrix} = \begin{bmatrix} \lambda_1 & 0 & 0 \\ 0 & \lambda_2 & 0 \\ 0 & 0 & \frac{1}{\lambda_1 \lambda_2} \end{bmatrix} \tag{7.2}$$

where λ_1 and λ_2 are the residual stretches in directions 1 and 2 for the first and second stretching operations respectively. Stretch is related to strain by $\lambda_i = 1 + \epsilon_i$. From the matrix deformations it is clear that for volume to be conserved, a stretch in direction 1 and constant width in direction 2 must result in a reduction in thickness in direction 3 by the inverse of the stretch in direction 1. Algebraically, for any individual deformation (or combination of individual deformations) the product of the principal stretches $\lambda_1^P, \lambda_2^P, \lambda_3^P \equiv 1$ for incompressible materials. Hence the stretch in direction 3, the thickness direction, that results after two perpendicular constant-width deformations is $\frac{1}{\lambda_1 \lambda_2}$.

The two-stage deformation process can also be expressed in terms of two different operations: an equibiaxial stretch in the plane of the sheet Λ_{EB}, with an associated reduction in thickness, and a planar deformation at constant volume and constant thickness Λ_{PD}. The equibiaxial deformation consists in a stretch of λ_{EB} in both directions in the plane, and a resulting stretch in the thickness direction of $\frac{1}{\lambda_{EB}^2}$. The planar deformation consists of a stretch in direction 1 of λ_{PD} and an inverse stretch of $\frac{1}{\lambda_{PD}}$ in direction 2, but no deformation in direction 3. This is expressed in matrix form as

$$\Lambda_{EB} \Lambda_{PD} = \Lambda_C \tag{7.3}$$

or in full as

$$\begin{bmatrix} \lambda_{EB} & 0 & 0 \\ 0 & \lambda_{EB} & 0 \\ 0 & 0 & \frac{1}{\lambda_{EB}^2} \end{bmatrix} \begin{bmatrix} \lambda_{PD} & 0 & 0 \\ 0 & \frac{1}{\lambda_{PD}} & 0 \\ 0 & 0 & 1 \end{bmatrix} = \begin{bmatrix} \lambda_{EB}\lambda_{PD} & 0 & 0 \\ 0 & \frac{\lambda_{EB}}{\lambda_{PD}} & 0 \\ 0 & 0 & \frac{1}{\lambda_{EB}^2} \end{bmatrix} \tag{7.4}$$

For the two series of deformations (7.1) and (7.3) to be identical we require the following relationships between the stretches

$$\lambda_{EB} = \sqrt{\lambda_1 \lambda_2} \qquad \lambda_{PD} = \sqrt{\frac{\lambda_1}{\lambda_2}} \tag{7.5}$$

7.3.3 Experimental pre-stretching operation

Sheet material $100mm$ long by $150mm$ wide is clamped in custom-made grips, leaving a section $50mm \times 150mm$ between the grips. The sheet is marked with a $5mm$ grid used to evaluate the residual strain at different points. Sheet material nominally $1mm$ thick is used for the stretching operation.

The sheet is loaded in the grips and the environmental chamber is set to $90°C$ [1]. The temperature is monitored by means of a thermocouple in contact with a region of the sample. Once the sample is up to temperature, the stretching process can begin. The sheet is stretched at a strain rate of $50mm/min$ to a maximum strain of 350%. During the tests there is often noticeable slip out of the grips; this is difficult to avoid since the large custom-made mechanical grips are not able to adjust for the changing thickness of the sample due to the stretching. Additional clamps are used to reduce this slip where possible. Hence, although the nominal maximum strain is 350%, in practice this will be somewhat less.

Once the maximum strain has been reached, the temperature is rapidly lowered by the use of a freezer spray, `Freez-it`, applied manually as evenly as possible on the

[1] The experimental pre-stretching operation is performed in collaboration with Michael Blundred of the Oxford University Engineering Department.

sheet. This brings the temperature of the sheet to around $-50°C$ rapidly, and reduces the amount of relaxation that takes place once the load is removed. Also, it helps to prevent any recrystallisation of the material in the new, stretched configuration. If crystallisation were to take place in this strain state, it would decrease the strength of the material due to the relaxation that has yet to take place. The process is shown in Fig. 7.4.

The load is then removed from the sheet, and significant relaxation takes place, bringing the sheet back to around 100% strain. The sheet is then removed from the clamps, and can be cut to a suitable size for the stretching operation in the perpendicular direction.

Fig. 7.5 shows a sheet when it is unstretched, stretched first in direction 1, and then in direction 2. It is clear from the grid that has been marked on the sheet that there is a wide range of residual strains present in the sheet. These are due to the non-uniform stresses that result from the stretching process.

It is noted that the stretching process is not always successful, with a number of sheets failing during the stretching operation. Two such failures are shown in Fig. 7.6.

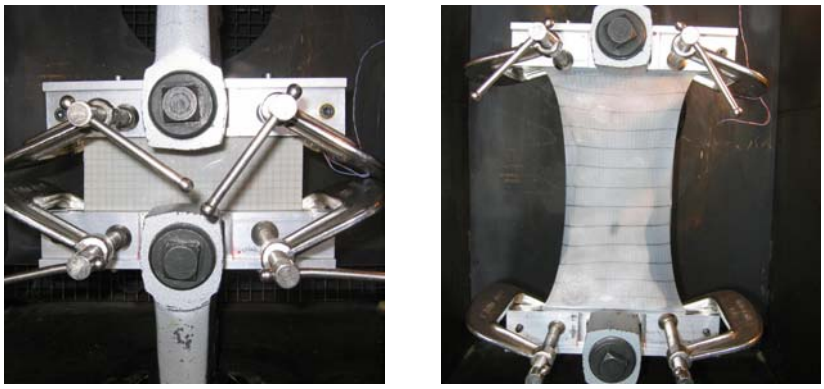

(a) (b)

Fig. 7.4: (a) Hytrel sheet ready for stretching in the environmental chamber, and (b) after stretching and freezing with the coolant spray.

(a) (b) (c)

Fig. 7.5: A Hytrel sheet (a) before stretching, (b) after stretching in the vertical direction, and (c) after subsequent stretching in the horizontal direction.

7.4 Properties of pre-stretched Hytrel sheet

7.4.1 Stress-strain response

Two specimens are cut from pre-stretched sheet extended by 350% stain in one direction only and are tested parallel and perpendicular to the direction of stretch. Another specimen is also cut from a sheet extended by 350% strain in both directions, parallel to the second stretch direction. Tensile tests are performed with the same equipment and procedures used in Section 3.3.5 at a strain rate of $0.002s^{-1}$. The accuracy of these reloading tests is limited due to the non-uniform residual strains, and hence non-uniform thickness of the test samples cut from the stretched sheets.

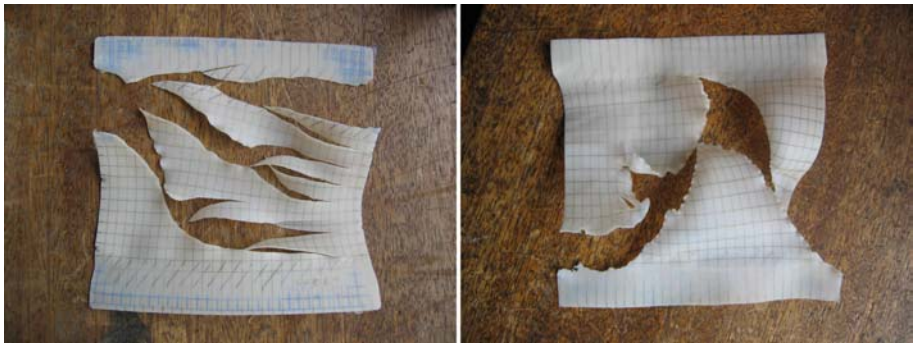

Fig. 7.6: Two Hytrel sheets that have failed during stretching.

The nominal stress nominal strain curves, shown in Fig. 7.7(a), show behaviour that could almost be attributed to different materials. If the data is shown in true stress true strain form, Fig. 7.7(b), and appropriate shifts in true strain are applied, the curves differ at the start, but all rejoin the virgin material's curve at higher strains.

Fig. 7.7(a) shows that the apparent behaviour of 350% biaxially stretched sheet is initially less stiff than that of virgin material. Beyond around 40% nominal strain the stress-strain curves for stretched sheet cross those of virgin material; the virgin sheet is then less stiff than the pre-stretched sheet. This is likely to be beneficial to the inverting dome, where most of the material does not stretch beyond 40% nominal strain in any given direction.

In real terms of material behaviour, however, the response is similar to the loading, unloading and reloading cycles seen in Section 3.3.5. The shifts in strain that have been applied on Fig. 7.7(b) correspond to the approximate residual strains in the direction of the re-test that occurred as a result of the first stretch of the material. No accurate measurements of this residual strain are possible since residual strain varies along the test

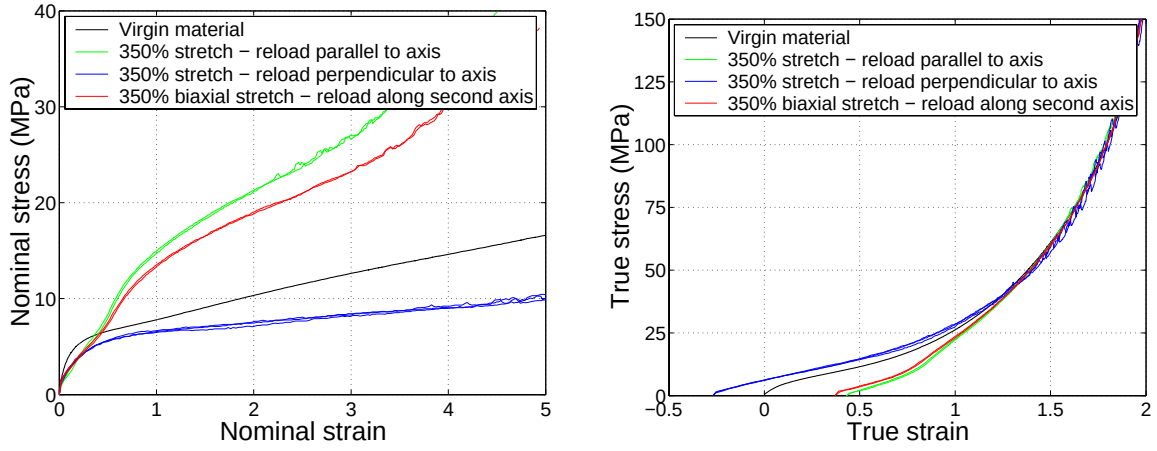

(a) (b)

Fig. 7.7: (a) Nominal stress and strain and (b) true stress and strain with appropriate strain shifts for re-testing of pre-stretched sheets.

specimens. This indicates that to a reasonable approximation the material's behaviour in each of the two stretching directions depends only on the residual strain in that direction, and that it behaves as if it was loaded, unloaded and reloaded in that direction. Deformation in one direction, however, can result in residual strain in the perpendicular direction due to Poisson's ratio effects.

7.4.2 Theoretical discussion of burst strength

Cella [10] stated that the failure in Hytrel results from the failure of the soft polymer segments, although tests of Section 3.4 have indicated that the hard segment crystallinity may also contribute. When the polymer is deformed, the hard segment crystal matrix deforms, and pulls with it the soft segments, whose ends are embedded in the crystal matrix. If we assume that the deformation of both phases is affine, both the soft segment chains and the crystal matrix will be rotated and stretched as a result of deformation.

For burst to occur, a number of soft segment chains must be taken to breaking strain. The failure creates a hole through the thickness of the sheet, and hence failure occurs in segments that were previously spanning across the hole. The components of the soft chains which contribute to resisting burst are the ones in the plane of the sheet, perpendicular to the burst direction. Assuming that the deformation does not alter the topology of the crystal matrix, the number of chains per unit length along the thickness direction will only be affected by deformation in this direction. This concept is best illustrated by means of a diagram, shown in Fig. 7.8.

Fig. 7.8(a) shows an isotropic piece of material, with randomly distributed soft segment chains. The chains are embedded in the crystal matrix (which is not shown in the diagram) and as such they will deform with the bulk polymer. Now, the grey line indicates the point at which we measure the number of chains per unit length; this is the

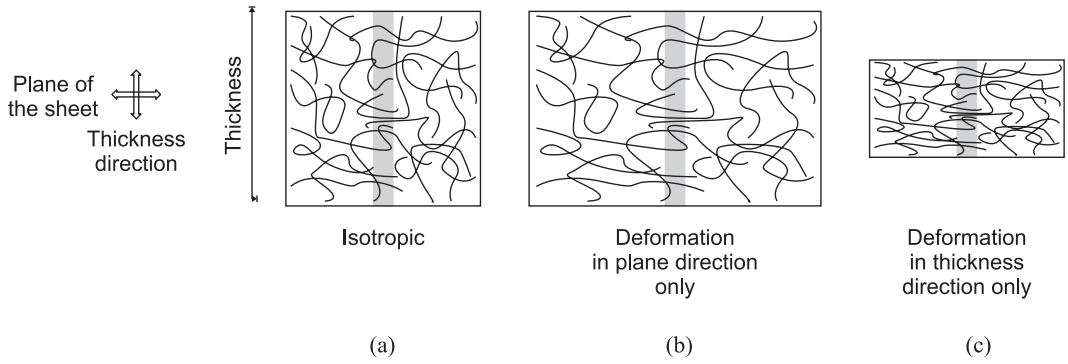

Fig. 7.8: Number of segments per unit length along the thickness direction in (a) isotropic sheet, (b) sheet deformed in the plane direction, and (c) sheet deformed in the thickness direction.

thickness direction, and chains crossing this line will have to fail in order for the sheet to burst. Fig. 7.8(b) shows the same piece of material that has experienced a deformation only in the plane of the sheet. No deformation has taken place in the direction of the thickness. The number of chains per unit length (measured along the grey line) which would have to break in order for burst to occur has not changed. Fig. 7.8(c) shows the piece of material that has experienced a deformation in the thickness direction. In this case the thickness has been reduced, and although the total number of chains in the thickness direction is unchanged, the reduction in thickness leads to an increase in the number of chains per unit length along this direction.

In practice, it is rather complicated to impose such deformations on a material, principally because it is almost incompressible. The deformations are easier to understand in the context of chains per unit length if we use the equivalent deformation matrices developed in Section 7.3.2, since these forms are equivalent to changes in thickness and changes in the plane of the sheet.

The equibiaxial component of the deformation Λ_{EB} is the part that affects the thickness of the sheet, and hence the number of soft segment chains per unit length along the thickness. If the number of chains per unit length in the thickness direction of isotropic

material is C, then the number of chains per unit length in deformed material will be $C(\frac{t_0}{t})$. Hence the breaking stress will increase by a factor of $\frac{t_0}{t}$, or from (7.4) by λ_{EB}^2 due to the deformation alone.

However, the stretch at burst must decrease since the material is already stretched. In isotropic material, the breaking stretch in equibiaxial burst tests was found to be $\lambda_{break} \simeq 2.35$ from the experiments of Section 3.4.2. If we assume that the overall stretch at burst remains constant at 2.35, in material equibiaxially pre-stretched to λ_{EB}, the stretch to burst will be $\frac{2.35}{\lambda_{EB}}$. In terms of the stretch seen by the pre-stretched material, the stretch to burst of the pre-stretched sheet $\lambda_{break}^{pre-stretched}$ will be

$$\lambda_{break}^{pre-stretched} = \frac{\lambda_{break}}{\lambda_{EB}} \tag{7.6}$$

so the material will reach the breaking stretch earlier if it has been pre-stretched. In material that has been pre-stretched in a non-symmetric manner, where $\lambda_{PD} \neq 0$, it is not so clear when burst will occur. Burst could occur when the first stretch reaches the breaking stretch, or when the second stretch reaches it, or in some combination of the two. Since the pre-stretch imposed on the material during the stretching process is mostly equibiaxial, we would expect (7.6) to be valid. Since the breaking stress depends on the thickness of the sheet at break, from (3.20), we would expect a decrease in breaking stress by a factor of

$$\left(\frac{\lambda_{break}^{pre-stretched}}{\lambda_{break}} \right)^2 = \frac{1}{\lambda_{EB}^2} \tag{7.7}$$

and therefore the effects of increased chains per unit thickness and residual stretch and reduced stretch to break will effectively cancel out.

The radius of curvature at burst may also change due to the change in mechanical

response and to the change in stretch to break. There will be a complex relationship between the actual radius of curvature at burst and the amount of pre-stretch, since each pre-stretch has an associated reloading stress-strain curve. The apparent response of pre-stretched material is initially less stiff than isotropic and at larger strains is more stiff than isotropic, as shown in Fig. 7.7(a). The radius of curvature is likely to increase compared with isotropic material due to the response at high strain being dominant at break. From (3.20), the radius of curvature and the burst stress are directly proportional to one another.

7.4.3 Experimental evaluation of burst strength

The testing of burst strength requires much smaller samples than tensile testing, and more accurate local measurements of the sheet strength can be made. The non-uniform stretching of the sheet provides a range of residual stretches and thicknesses, which, although undesirable for dome fabrication, is useful for comparison with the burst stress theory presented. Prior to testing, the residual stretch in the sheet is recorded from the deformed grid in the 1 and 2 directions, as shown in Fig. 7.9.

The residual stretches in the 1 and 2 directions are found from

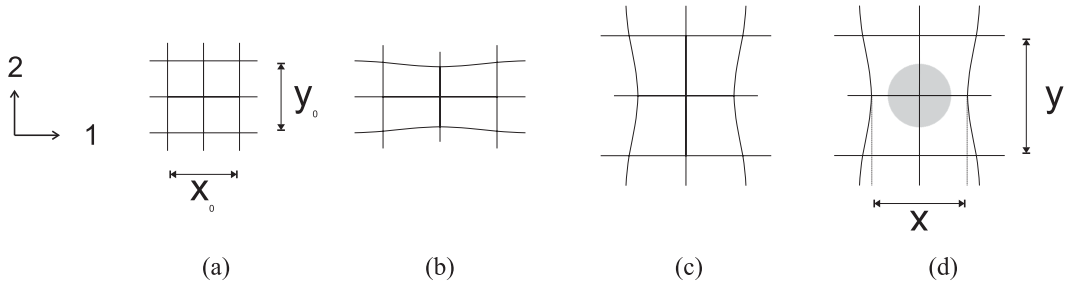

Fig. 7.9: (a) Initial state, (b) after stretch in direction 1, (c) after stretch in direction 2, (d) measurement of the residual stretch in the sheet.

$$\lambda_1 = \frac{x}{x_0} \qquad \lambda_2 = \frac{y}{y_0} \tag{7.8}$$

where x_0 and y_0 are the initial grid dimensions and x and y are the final dimensions after stretching. The component of equibiaxial stretch is calculated using (7.5). The errors involved in the grid measurements are of the order of $\pm 5\%$. The residual stretch has been calculated from the deformation of the grid rather than from thickness measurements since the thickness of the sheet prior to stretching can vary significantly from the nominal value of $1mm$, and was not recorded for each point on the sheet prior to stretching.

The thickness of the sheet is recorded after stretching, prior to burst testing, as t_0 using a micrometer. Small portions of the sheets are tested for burst strength with the procedure described in Section 3.4.2 in the context of isotropic material, and the pressure at burst is recorded [2]. The strain at burst and the radius of curvature have not been measured for each sample, and hence the effective burst stress could not be calculated.

Fig. 7.10 shows the burst pressure P_b normalised with respect to t_0 for a wide range of samples on the stretched sheet as a function of λ_{EB}. If the pre-stretched material behaved identically to isotropic material, then $\frac{P_b}{t_0}$ would show no pre-stretch dependance.

The experiments clearly show an increase in the normalised burst pressure with increasing equibiaxial component of stretch. This implies either an increase in the burst stress, or a decrease in the radius of curvature at burst. Now, from Fig. 7.7(a) one would expect a stiffer response, and an increase in the radius of curvature at burst. This indicates that it is the burst stress that is increasing with λ_{EB}. Since the effects of the deformation and of the pre-stretch cancel out, the increase must be coming from

[2] This series of tests is performed in collaboration with Michael Blundred of the Oxford University Engineering Department.

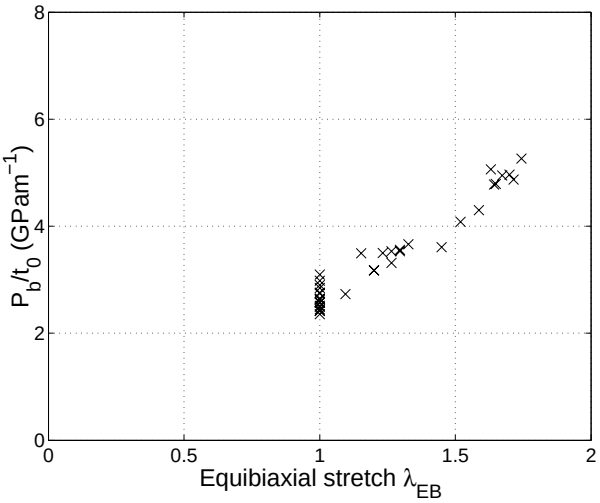

Fig. 7.10: Burst pressure normalised with respect to thickness in Hytrel 4068 as a function of the equibiaxial component of residual stretch.

something else. One possibility is that since the pre-stretching is being performed at a temperature close to the crystallisation temperature of the hard blocks, new crystallisation is being induced in a direction that resists failure. The morphology of the new crystal structures would be anisotropic and aligned in the directions of pre-stretch. The crystals may be highly elongated and ellipsoidal in shape. Electron microscopy could give some indication as to the change in microstructure.

It is possible that there may be an additional increase in burst strength due to increased crystallisation of the hard segments in the material taking place during the stretching process acting as an annealing effect. Tests on annealed and slow-cooled sheets in Section 3.4.2 indicate that this effect is small, accounting for less than 10% of the extra burst stress present in slow-cooled samples.

Fig. 7.11 shows a range of disc specimens that have been tested to burst using this experiment. The shape of the burst hole varies from circular in isotropic and equibiaxial discs to elliptical in discs showing a higher degree of planar deformation λ_{PD}. There does not appear to be any relationship between the normalised burst pressure and the

planar deformation component of stretch λ_{PD}.

7.5 Compression-forming domes from biaxially pre-stretched sheet material

The compression-forming of domes from biaxially pre-stretched Hytrel sheet is performed using the same technique as has been presented in Section 7.1. We have seen in the forming of domes from isotropic material that the operation at low temperature is more likely to damage the material's microstructure and results in less permanent deformation. Forming at a higher temperature results in greater deformation and less damage. The stresses observed by the material at higher temperatures are lower, as shown in Section 3.3.3, and permanent deformation is favoured due to the drop in yield stress, as shown in Section 3.3.8. Hence it would appear to be beneficial to form at higher temperatures. However, we also expect that higher temperatures will encourage recovery, and hence loss of the biaxial pre-stretch. A careful balance must be achieved between achieving sufficient deformation to produce a dome shape, limiting damage and reduction to burst strength, and retention of pre-stretch and the associated increase in

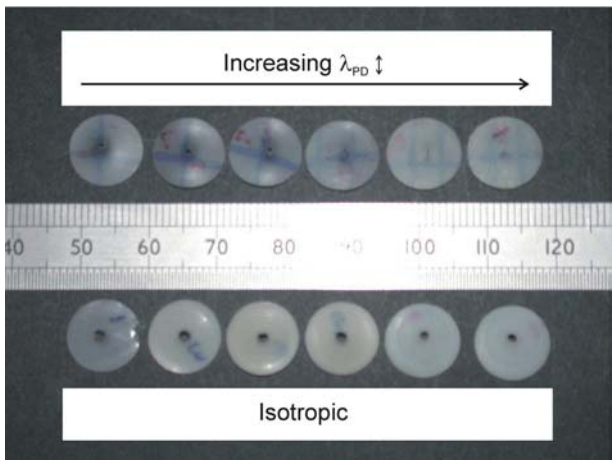

Fig. 7.11: Burst disc specimens, showing an increasingly elliptical failure hole as the component of the planar deformation increases.

burst strength.

A range of domes are produced from biaxially pre-stretched material with a range of residual stretch at temperatures of $50, 70$ and $90°C$. Domes are also formed at $120°C$ to show the extent of the recovery. Since the material is only in contact with the heated moulds for a maximum of 4 minutes, and exposed to room-temperature air in the vicinity, not all of the material may reach the temperature of the moulds. Domes are stretched using a plunger depth of $5mm$ and appropriate spacers.

Prior to forming, the thickness and the residual stretch of the sheet material at each dome forming point are recorded. After forming, the domes are cut out using a punch of diameter $10.6mm$ and are carefully weighed. The mass of a disc of material $10.6mm$ in diameter with the recorded thickness is evaluated from the density. The mass recovery is expressed in terms of the ratio of the mass difference seen in domes after forming to the calculated mass prior to forming divided by the mass difference of a $1mm$ disc of the same diameter (the nominal thickness of the sheet prior to pre-stretching) and the calculated mass prior to forming. Full recovery of 100% would require the sheet to return to an original thickness of $1mm$. The data is shown for a range of temperatures in Table 7.3. From the mass measurements after forming we can evaluate an equivalent sheet thickness that would produce this mass for a disc $10.6mm$ in diameter. The evaluated thickness after forming is an indication of the extent of equibiaxial orientation left after the forming process.

A range of biaxial pre-stretch has been used for each temperature. In general, the recovery is largest at the highest forming temperature of $120°C$, although even at this temperature only $35 - 55\%$ recovery is seen. At temperatures of $50 - 70°C$ the recovery is small, typically only $10 - 20\%$. There may be an effect of material being drawn into the forms due to the strain being imposed, although similar tests on domes made from

Table 7.3: Basic properties of domes pressed from biaxially pre-stretched Hytrel sheet.

Forming temp ($^\circ C$)	Dome number	Biaxial pre-stretch	Mass before forming (mg)	Mass after forming (mg)	Mass recovery (%)
50	1	1.50	34.6	40.5	9
	2	1.50	40.3	45.2	9
	3	1.50	39.5	46.0	11
	4	1.49	36.4	44.0	12
	5	1.49	37.8	43.7	10
	6	1.45	45.8	51.9	12
	7	1.45	38.6	43.9	9
	8	1.34	52.5	56.2	8
70	9	1.61	35.1	42.4	12
	10	1.51	34.0	42.9	14
	11	1.48	44.0	50.8	13
	12	1.43	45.6	56.0	20
	13	1.41	43.9	55.9	22
	14	1.34	59.8	64.9	13
	15	1.20	61.3	67.8	18
90	16	1.61	32.4	48.2	24
	17	1.55	38.1	54.2	27
	18	1.55	37.7	51.4	23
	19	1.34	57.1	70.0	32
	20	1.34	54.0	58.3	10
120	21	1.75	27.2	58.0	44
	22	1.73	29.3	57.0	40
	23	1.65	30.8	61.5	46
	24	1.63	29.7	56.9	40
	25	1.61	33.4	60.8	42
	26	1.61	30.8	58.3	41
	27	1.61	37.5	58.3	34
	28	1.53	41.2	69.4	50
	29	1.51	39.6	65.3	44
	30	1.48	37.3	64.3	45
	31	1.38	43.6	66.2	42
	32	1.34	51.1	76.8	55
	33	1.34	54.7	74.8	47

isotropic non-stretched sheet did not show evidence of this effect.

The material pre-stretching operation has been performed at a temperature of $90°C$ and quenching is achieved with the use of a freeze-spray in the stretched configuration. This is likely to result in an increase in the sheet's self-stress compared with hot unloading. When the quenched material is subsequently brought back to $90°C$, recovery towards the original state takes place. The mechanism by which this self-stress is affected by the temperature is governed by the hard segment structure. At $90°C$ the hard segment is near its T_g, and hence more mobile. The hard segments are being pulled backwards by the soft segment matrix, and if the resistance to the recovery is low (unloading at higher temperatures), then more recovery will take place, and less residual strain and self-stress is imposed. Since the samples are quenched before being unloaded, the hard segment is well below T_g, and far less mobile. The soft segments remain stretched, and only when the resistance of the hard segment matrix is lowered by reheating does the material subsequently recover. Only quenched sheets have been used for dome manufacture since hot cooling results in less residual strain, and less orientation.

The amount of recovery at a specific temperature appears to be related to the initial amount of pre-stretch. Higher pre-stretch results in greater recovery at a given temperature. This is an effect that is explained by considering that the restoring force exerted by the rubbery soft segment on the crystal matrix is larger in material that has been stretched further. Therefore, following an Eyring approach, a lower temperature will be required to cause yield (and loss of pre-stretch) since the stress is higher.

Recovery is to be avoided as it results in an apparent drop in burst stress and a thickening of the material, both of which are negative in terms of achieving strong, light-weight domes.

7.6 Performance of biaxially pre-stretched compression-formed domes

Domes produced using the pre-stretching technique are tested using both particle velocimetry to assess their performance in an inverting dome device, and burst strength tests, in order to assess whether domes could be used at higher pressures, or if even thinner domes with equivalent biaxial pre-stretch can be employed.

Due to the significant variations in thickness in biaxially-prestretched domes, as indicated by the variations in mass post-forming shown in Table 7.3, results are expressed as a function of dome mass. Although in most cases the domes are lighter than their equivalent injection-moulded counterparts, in some cases where the biaxial pre-stretch is low they can be heavier. In an industrial context, larger numbers of domes with identical well-defined biaxial pre-stretch could be easily produced and tested.

7.6.1 Particle velocimetry

A selection of the domes produced with the biaxial pre-stretch and forming technique are tested in a device, and the powder velocity is measured using particle velocimetry. The domes are tested in *inversion* only, and the results are shown as a function of dome mass for the range of forming temperatures in Fig. 7.12.

There is significant scatter in the data, expected due to the large number of variables that are not accounted for in the figure, such as the pre-stretch in individual domes, and the effect that non-symmetric pre-stretch may have on dome shape. Nevertheless, all of the domes invert without burst and accelerate powders to velocities far in excess of those seen in any injection-moulded domes. Although domes produced at 120° exhibit significant recovery, and are therefore heavier, they are still able to accelerate powder velocities between 200 and $400 m/s$. Domes produced at lower temperatures between 50

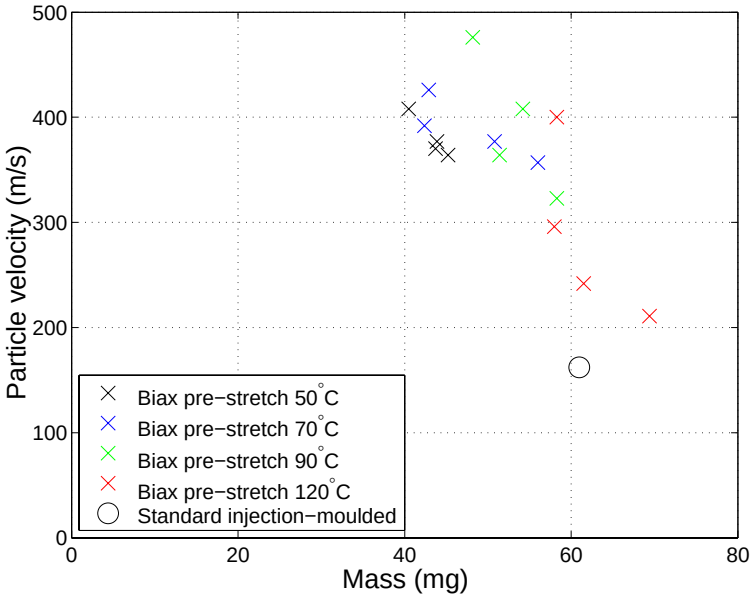

Fig. 7.12: Particle velocimetry data for the biaxially pre-stretched domes vs. dome mass. Also shown is the average value for a standard injection-moulded dome.

and $70°C$ are more consistent and lighter in weight, and are able to accelerate powder to velocities ranging between 350 and $425m/s$. In general, there is a trend between mass and powder velocity for heavier domes, although it appears that reducing the mass below around $55mg$ is not having a significant effect on powder velocity.

7.6.2 Quasi-static dome burst

A selection of the domes produced with the biaxial pre-stretch and forming technique are tested for burst pressure in *inversion* under quasi-static conditions. The domes experience some recovery during the forming process, and some of the strength gained as a result of the biaxial pre-stretch is lost during forming. The amount of equibiaxial pre-stretch remaining after forming will vary in different parts of the dome since some parts are stretched by the forms. Since the mass of the domes is known, an equivalent thickness t_{dome} can be evaluated that corresponds to a disc of $10.6mm$ diameter of equivalent mass. As an approximate measure of residual pre-stretch, we ignore the

dome-forming process strains and consider only the recovery. For the pre-stretched sheet material to recover to this thickness, it must undergo an equibiaxial deformation in reverse to that experienced during stretching, of the same form as matrix Λ_{EB}, but with

$$\frac{1}{\lambda_{EB}^{recovery}} = \frac{t_0^{sheet}}{t^{dome}} \tag{7.9}$$

where t_0^{sheet} is the thickness of the sheet prior to forming, and t^{dome} is the thickness corresponding to a disc of equivalent mass as the dome. Hence, the effective equibiaxial pre-stretch of the dome material λ_{EB}^{dome} will be the result of the initial sheet pre-stretch λ_{EB}^{sheet} and the recovery stretch $\lambda_{EB}^{recovery}$, and is given by

$$\lambda_{EB}^{dome} = \frac{\lambda_{EB}^{sheet}}{\lambda_{EB}^{recovery}} \tag{7.10}$$

The burst pressure is measured for a number of domes produced from pre-stretched sheet, and is normalised by the effective thickness t_{dome}. The results are shown in Fig. 7.13 for domes formed at a range of temperatures.

It is apparent from these results that domes produced at higher temperatures experience the largest loss of strength compared with the sheet material from which they are made. These domes have larger amounts of recovery and the normalised burst pressure is lower than that which would be expected from a simple decrease in equibiaxial stretch. Domes formed at lower temperatures of 50 to $70°C$ instead show little to no drop in the normalised burst pressure when compared to the oriented sheet material. Domes formed at $50°C$ have normalised burst pressures $30-40\%$ higher than the isotropic sheet, even though there are added strains due to the dome forming process. This means that thinner material can be used to manufacture domes without resulting in a lower burst

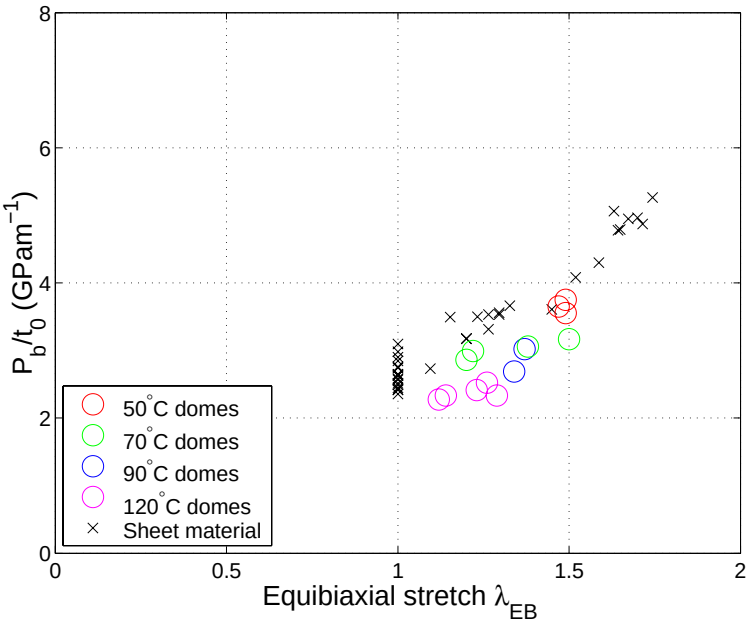

Fig. 7.13: Burst pressure normalised with respect to thickness for domes produced from pre-stretched sheet material. Also shown are the results from pre-stretched sheet material.

pressure.

7.7 Summary and conclusions

This chapter has examined the possibility of producing inverting domes using a different technique to injection-moulding: compression-forming, or stamping. Here the domes are produced from sheet material by inducing permanent deformation by means of shaped stamps. The procedure works best at higher temperatures.

In Section 7.1 we have described the moulds used to compression-form the domes, and have shown that by varying the temperature and shape of the moulds different domes can be produced. Domes produced from plain compression-moulded sheet are tested for particle velocity and for quasi-static burst. In general it was found that the larger the depth of the plunger in the moulds, the faster the particle velocity. However, when the plunger depth reached $5mm$, the deformation was such that some domes

were bursting on inversion. The quasi-static burst strength of domes produced with this technique is 20% lower than the strength of the sheet material from which they are made. No significant variation in quasi-static burst strength for different plunger depths was recorded. This indicates that the domes produced with the deeper plunger are experiencing larger stresses upon dynamic inversion due to their shape, since they are travelling faster. This is in contrast to injection-moulded domes that can burst due to the subsequent rise in pressure if the device is not vented, rather than the inversion process itself.

In Section 7.3 we investigated the possibility of inducing residual strain in Hytrel sheet so as to change the mechanical properties. A pre-stretching operation is performed in two perpendicular directions, and the process has been described by means of residual deformation matrices. The stretching procedure is carried out in a testing machine at a temperature of $90°C$. The mechanical properties of the pre-stretched sheet are then investigated. The stress-strain response is similar to that observed in the load-unload-reload cycles of Section 3.3.5, and the burst strength increases substantially with the degree of equibiaxial pre-stretch. It is not immediately obvious where the increase in strength is coming from, although it is likely that an anisotropic crystal structure is developed in the material as a result of the pre-stretching operation, and that this new structure contributes to strength.

Domes are then formed from the pre-stretched Hytrel sheet using the same plunger and moulds. We investigated the optimal temperature at which to perform the forming operation. There is loss of pre-stretch when the operation is carried out at a too high temperature, and if the temperature is too low, little deformation is produced. A good temperature range for the deformation is 50 to $70°C$.

The domes produced from pre-stretched sheet are then tested for particle velocity and

quasi-static burst. The particle velocities produced by these domes are mostly between 350 and $425 m/s$, substantially faster than the injection-moulded domes. The burst strength of the domes compares well to the burst strength of the pre-stretched sheet from which they are made, provided that the dome forming operation is not performed at a temperature greater than $70°C$.

The domes produced from pre-stretched sheet offer a substantial improvement in particle velocity over the traditional injection-moulded domes. The technology used to produce them is different, but not out of the reach of a suitably designed industrial process. These domes have achieved a significant objective: a lower mass, possible by the use of a smaller thickness with an increased burst strength, enabling significantly higher inversion velocities.

Chapter 8

Conclusions and further work

8.1 Conclusions

This thesis has investigated the behaviour of inverting domes within the PowderJect needle-less injection device, with the aim to increase the inverting velocity. The early device was limited by low powder injection velocities compared with other devices. Although extensive tests were carried out including gas dynamics within the device and particle penetration tests, there was limited understanding of mechanism by which the domes invert and accelerate powder. The thermoplastic elastomer from which domes are made, Hytrel, had been previously researched by a number of authors, but this information had not been used in the design process of inverting domes. Hence, both the mechanism of dome inversion and particle acceleration, and the way in which the properties of the material affect the design required further study.

We started by investigating the mechanical properties of Hytrel subjected to different thermal histories and have shown that slow cooling rates result in a stiffer material exhibiting significantly higher stresses at large strains. In addition, there is a small increase in the biaxial burst strength in slow-cooled samples compared with fast-cooled ones, indicating that the hard segment microstructure can contribute to the ultimate strength of the material. The effect of strain rate over 4 orders of magnitude has been

shown not to be as significant. The effect of process-induced orientation in thin discs of material injection-moulded from the edge has indicated that the anisotropy can be significant, especially at high strains. Tests at different temperatures have identified the glass-transition temperature of the hard blocks in Hytrel to be between 100 and 120°C.

A dome slicing technique has been developed, and using it we have shown that injection-moulded domes can be up to 40% thicker than intended in the nominal specifications. The snap-through behaviour of domes under quasi-static pressure has revealed that the buckling pressure is greater in *inversion*, the forward snap-through, than in *eversion*, the reverse, and that the inversion can be asymmetric. At high-speed, the dome displacement has been explored using high-speed imaging, and the drug powder with a particle velocimetry technique. *Eversion* of domes gave powder velocities of $206.9 \pm 9.6 m/s$ compared with $162.2 \pm 5.2 m/s$ in *inversion*. No significant difference in the quasi-static burst strength has been found. In dynamic conditions the vent-hole ensures that burst does not take place by relieving the pressure within the device.

Finite element modelling of both nominal domes and *actual* domes, with a geometry reconstructed from the slicing experiments has been performed for both quasi-static and dynamic conditions. Rayleigh damping is introduced to simulate the larger stress response at very high strain rates. There are large differences in inversion velocities between nominal and *actual* domes. The position of points on the dome is post-processed to project particle release velocities, and indicates that in *inversion* there will be a higher concentration of powder at the centre and edges of the target, and the reverse in *eversion*. Also, eversion has a larger range of peak velocities than inversion across a dome diameter and produces a larger target. A simple mechanical model of the dome has also indicated that *eversion* should yield faster velocities than *inversion*. Analysis of manufacturing imperfections indicates that the current design is not highly sensitive to

imperfections, although modifications can increase this sensitivity. Imperfections such as a small horizontal or rotational misalignment of the moulding plates simply result in a horizontal shift in position of the peak vertical velocity, but virtually no change in magnitude.

The application of heat and pressure treatments have been shown to significantly increase peak powder velocities in inverting domes. The mechanism by which this happens consists of a shift in the stability curve and an increase in the dome travel. A 50% increase in *inversion* velocities, and a 25% increase in *eversion* velocities have been achieved with this method. A dome with a lengthened side wall has been manufactured, and has produced an increase of 85% in inversion velocities over the original dome, reaching $299.8 m/s$.

Finally, we proposed a new method of dome production, compression-forming. This consists of stamping a dome shape onto sheet material, and can be performed on material that has been pre-stretched and can be stronger and thinner. Velocities of up to $250 m/s$ have been reached on stamped isotropic sheet without dome burst. The pre-stretching operation has been performed in two perpendicular stages at $90°C$. The stamping on pre-stretched sheet has to be performed at a lower temperature to avoid the loss of pre-stretch, and thus of strength. An optimal temperature of 50 to $70°C$ has been found, and domes repeatedly inverted with peak velocities of 350 to $425 m/s$, a substantial improvement over injection-moulded domes.

8.2 Recommendations for further work

A number of aspects of this research lend themselves to further study. The material model used in the FE simulations has not been able to capture a number of properties that would be desirable, such as the permanent deformation and the process-induced

anisotropy. A number of more sophisticated models exist, such as Ogden's [45] recent model simulating damage and the Mullins effect, but none have been applied to Hytrel. With a more sophisticated model, more accurate predictions could be made both of heat and pressure treatments and of the forming process and performance of biaxially pre-stretched compression formed domes.

The research on pre-stretched biaxially oriented domes is in its infancy, and a suitable mass-production method has not been thoroughly investigated. Research in this area would have to address the issue of drug particle retention since it would not be possible to injection-mould drug retaining fibres directly. If a suitable material model is pursued, it should be used to predict the dome shape that results from a particular plunger shape, and its effect on inversion.

Appendix A

Reconstruction of stress-strain data from grip displacements in non-uniform samples

This appendix is concerned with a method developed to process grip force-displacement data from a tensile test and a sample of non-uniform dimensions into stress-strain data. This method is useful for tests where a direct measurement of strain is not possible, or not available, and it is able to reconstruct non-linear elastic stress-strain curves. It is no substitute for direct measurement of strain since it makes use of a number of assumptions that may introduce errors into the final stress-strain curve.

Assumptions

1. During the test, the force carried through the specimen at any point in the test is constant with respect to the test direction.

2. The sample is under a purely uniaxial stress state.

3. Stress concentrations at the grips are small enough to be ignored.

4. The taper in the specimens is small enough such that the strain rate at any point in the specimen is approximately constant.

5. The rate dependance of the material's constitutive response is small enough to be ignored.

The reconstruction procedure

In a tensile test we obtain a set of n data pairs of force and displacement measurements $[F_i\ d_i]$. Let us define as $A(y)$ the cross-sectional area at position y on the specimen, of original length l_0, shown in Fig. A.1. The force, F_i, carried through the specimen is constant with respect to y for each data point, and hence the stress at height y, $\sigma_i(y)$, is always given by

$$\sigma_i(y) = \frac{F_i}{A(y)} \tag{A.1}$$

For a linear elastic material with elastic modulus E, the strain at height y, $\epsilon_i(y)$, is easily obtained by dividing by the modulus of elasticity E,

$$\epsilon_i(y) = \frac{\sigma(y)}{E} = \frac{F_i}{EA(y)} \tag{A.2}$$

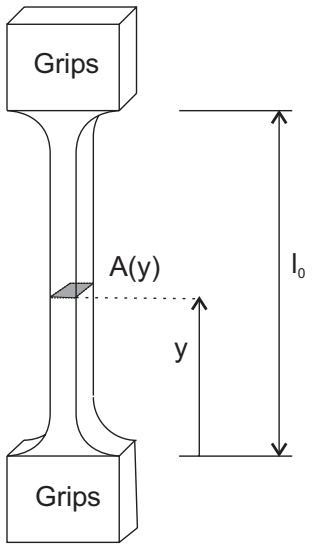

Fig. A.1: Specimen with variable cross-section $A(y)$ at position y.

When the material is not linear elastic, the strain needs to be found from a known stress-strain relationship. Integration of the strain with respect to y, the position along the specimen, gives the total displacement of the sample. l_i is defined as the displaced length of the sample, given simply by $l_i = d_i + l_0$.

$$\int_0^{l_0} \epsilon_i(y)dy = l_i - l_0 = d_i \tag{A.3}$$

For a linear elastic material it is usual to evaluate an effective length, l_e which, for an arbitrary effective cross-sectional area A_e, gives equivalent strain to that of the specimen with varying cross-section. A_e is usually taken to be the long and thinner part of the specimen of constant cross-section.

$$\int_0^{l_0} \epsilon_i(y)dy = d_i = \frac{F_i}{E}\int_0^{l_0} \frac{dy}{A(y)} = \frac{F_i l_e}{EA_e} \tag{A.4}$$

Dividing by the effective length l_e returns the strain

$$\frac{d_i}{l_e} = \epsilon(y) = \frac{F}{EA_e} \tag{A.5}$$

The effective length l_e is hence evaluated from

$$l_e = A_e \int_0^{l_0} \frac{dy}{A(y)} \tag{A.6}$$

When the material is not linear elastic, an iterative procedure can be used to reconstruct the correct stress-strain behavior from the force-displacement data set. For n force-displacement data pairs we can reconstruct the correct stress-strain curve with n data pairs, and, provided that there are sufficient data points, we cannot do better than assume that, to within the accuracy allowed by experimental error, this is piecewise

linear. The early part of the curve is also expected to be linear, and this is helpful to the procedure.

Starting at the first data point after $[F_0 \quad d_0] = [0 \quad 0]$, and assuming linearity at low strains, the strain ϵ_1 is obtained from the linear procedure, from

$$\epsilon_1(y) = \frac{d_1}{A_e \int_0^{l_0} \frac{dy}{A(y)}} \tag{A.7}$$

For each of the remaining data points, an optimization procedure is used to find the next strain point ϵ_{i+1} (corresponding to the known stress σ_{i+1}) that will give, by the integration given in (A.3), a displacement d_{opt} corresponding to the measured displacement d_i. A tangent modulus E^t_{i+1} is given as a starting value, equal to the tangent modulus at the previous step, E^t_i, to give a new strain data point ϵ_{i+1}.

$$\epsilon_{i+1} = \epsilon_i + \frac{\sigma_{i+1} - \sigma_i}{E^t_{i+1}} \tag{A.8}$$

The specimen is discretized in the y direction in order to enable numerical integration. A discretized stress function along the specimen is obtained for the new data point at F_{i+1} from (A.1). A discretized strain function along the specimen, $\epsilon(y)$, is then obtained from linear interpolation of the stress-strain curve obtained up to this step, with the added $[\sigma_{i+1}\epsilon_{i+1}]$ data point. The strain function is then integrated along y to give the displacement of the specimen. If this displacement is too large, then the procedure is repeated with a larger tangent modulus, and vice versa. Once the difference between the obtained displacement and the measured displacement is smaller than the specified tolerance, the $[\sigma_{i+1}\epsilon_{i+1}]$ data point is fixed, and the procedure can carry on with the next force-displacement data point. The discretization of the stress strain curve, with the optimization procedure for the current point, is shown in Fig. A.2.

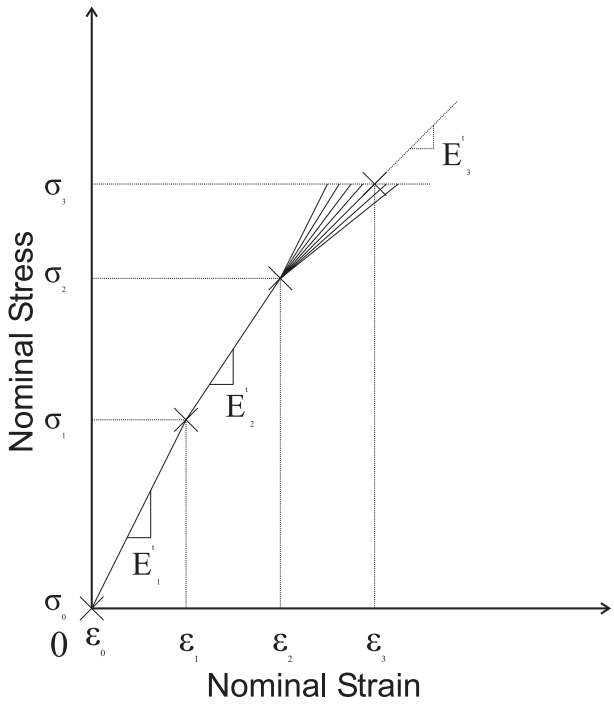

Fig. A.2: Discretized stress-strain curve, showing the optimization algorithm used to find the ith tangent modulus E_i^t that will give the $i+1$th strain value. The optimized value, when used to calculate the strain function along the specimen and integrated, will give a displacement equal to the measured displacement.

In practice, the discretization of the specimen needs to be finer if the variation in cross-sectional area with respect to position on the specimen is large. A value of 100 is taken for the data of the tests in Chapter 3. The Matlab [35] subroutine `fminbnd` is used to minimize the difference between d_{opt} and d_{i+1} to a tolerance of 0.01%.

Limitations

The procedure enables the reconstruction of stress-strain behavior from force-displacement measurements made at the grips in specimens of non-uniform cross-section and with non-linear material properties. However, using this method where the use of an extensometer in a uniform portion of specimens is not possible does still have some drawbacks. Firstly, there will be a stress concentration at the gripped region of the specimen - the grips need to apply a force on the specimen which will induce a stress through the thickness of the

specimen in the vicinity of the grips. Secondly, the stress state throughout the region close to the grips is unlikely to be uniaxial - the specimens have circular tapers at either end, and since the width of the specimens is constrained at the grips, a stress will be induced across the width of the specimen as a result of the thinning of the cross-section in the middle at large extensions. Hence, the stress state in the vicinity of the grips is certainly not uniaxial. An additional problem associated with this method is the fact that the strain rate will be different in different portions of the specimen; this is less of an issue with Hytrel since the material does not appear to be very sensitive to strain rate, as is shown in Section 3.3.6.

Bibliography

[1] Anderton G.E. and Treloar L.R.G. (1971). *Fracture and Tearing in Oriented Polyethylene*. Journal of Materials Science, **6**, pp. 562–571.

[2] Ashby M.F. and Jones D.R.H. (1992). *Engineering Materials 2 - An Introduction to Microstructures, Processing and Design*. Pergamon Press.

[3] Bellhouse B.J., Bell J., Greenford J.C. and Sarphie D.F. (1997). *Trans-Mucosal Particle Delivery*. US Patent 06010478.

[4] Bellhouse B.J., Sarphie D.F. and Greenford J.C. (1994). *Needleless Syringe Using Supersonic Gas Flow for Particle Delivery*. International Patent Wo4/24263.

[5] Bennett W.E. (1998). *Needle-Less Injection Through Mucosal Tissue*. MEng Thesis, Department of Engineering Science, University of Oxford.

[6] Blundred M.R. (2003). *Achievement of High Biaxial Strength in a Soft Polymer for a Medical Device*. MEng Thesis, Department of Engineering Science, University of Oxford.

[7] Briber R.M. and Thomas E.L. (1984). *Crystallisation Behaviour of Random Block Copolymers of Poly(butylene terephthalate) and Poly(tetramethylene ether glycol)*. Polymer, **26**, pp. 8–16.

[8] Buckley C.P. (2002). *Experimental Methods*, *CISM Course on Mechanics and Thermomechanics of Rubberlike Solids*, pp. 17–19. CISM, Udine, Italy.

[9] Cella R.J. (1973). *Morphology of Segmented Polyester Thermoplastic Elastomers*. Journal of Polymer Science, Symposium, (42), pp. 727–740.

[10] Cella R.J. (1977). *"Polyesters, Elastomeric"*, *Encyclopedia of Polymer Science and Technology - Plastics, Resins, Rubbers, Fibers*, pp. 485–510. Interscience Publishers, John Wiley & Sons, Inc., New York.

[11] Chen D., Weis K.F., Chu Q., Erickson C.A., Endres R., Lively C.R., Osorio J. and Payne L.G. (2001). *Epidermal Powder Immunisation induces both Cytotoxic t-Lymphocyte and Antibody Responses to Protein Antigens of Influenza and Hepatitis B Viruses*. Journal of Virology, **75** (23), pp. 11630–11640.

[12] Costigan C., Bellhouse B.J., Prasad K.V.R. and Carter F.V. (2000). *Development and Testing of the 6mm Oral PowderJect Device*. PJRC/GC/039/0800, PowderJect Internal Report.

[13] Costigan G., Liu Y., Brown G.L., Carter F.V. and Bellhouse B.J. (2003). *Evolution of the Design of Venturi Devices for the Delivery of Dry Particles to Skin or Mucosal Tissue*. In *24th International Symposium on Shock Waves*. Beiing, China.

[14] Douglas J.F., Gasiorek J.M. and J.A. Swaffield (2001). *Fluid Mechanics*. Pearson Education Limited.

[15] Duckworth G.M., Millward H.R., Potter C.D.O., Hewson G., Burkoth T.L. and Bellhouse B.J. (1998). *Oral PowderJect: A Novel System for Administering Local Anaesthetic to the Oral Mucosa*. British Dental Journal, **185** (10), pp. 536–539.

[16] E.I. Du Pont de Nemours & Co., Inc. (2003). *Hytrel Design Information*.
URL `http://www.dupont.com/enggpolymers/europe`

[17] E.I. Du Pont de Nemours & Co., Inc. (2003). *Hytrel Injection-moulding guide*.
URL `http://www.dupont.com/enggpolymers/europe`

[18] E.I. Du Pont de Nemours & Co., Inc. (2003). *Hytrel Product Guide and Porperties*.
URL `http://www.dupont.com/enggpolymers/europe`

[19] Glass I.I. and Patterson G.N. (1955). *A Theoretical and Experimental Study of Shock Tube Flows*. Journal of the Aeronautical Sciences, **22** (2), pp. 73–100.

[20] Greensmith H.W. and Thomas A.G. (1955). *Rupture of Rubber. III. Determination of Tear Properties*. Journal of Materials Science, **18**, pp. 189–200.

[21] Hassager O., Kristensen S. B., Larsen J. R. and Neergaard J. (1999). *Inflation and Instability of a Polymeric Membrane*. Journal of Non-Newtonian Fluid Mechanics, **88**, pp. 185–204.

[22] Henderson J.L. (1983). *Polyester Elastomer: The Designer's Link Between Rubber and Plastics*. Plastics Engineering, **6**, pp. 31–37.

[23] Hibbitt, Karlsson and Sorensen, Inc. (2001). *Abaqus/Standard User's Manual*. Version 6.2.7.

[24] Hoeschele G.K. (1974). *Über die Synthese von Polyätherester-Block Copolymeren*. Chimia, **28** (9), pp. 544–552.

[25] Hoeschele G.K. and Witsiepe W.K. (1972). *Polyätherester-Block-Copolymere — Eine Gruppe neuartiger thermoplasticher Elastomerer*. Die Angewalde Makromolekulare Chemie, **29/30** (354), pp. 267–289.

[26] Hofmann Werner (1989). *Rubber Technology Handbook*. Hanser.

[27] Hourston D.J. and Hughes I.D. (1977). *Polymeric Systems for Acoustic Damping. I. Poly(vinyl Chloride)-Segmented Polyether Ester Blends*. Journal of Applied Polymer Science, **21**, pp. 3099–3109.

[28] Hourston I.D. D.J. andd Hughes (1979). *Annealed Segmented Polyether Ester - Poly(vinyl chloride) Blends*. Polymer, **20**, pp. 823–826.

[29] Jelinski L.W., Schilling F.C. and Bovey F.A. (1981). *Carbon-13 Nuclear Magnetic Resonance Studies of Solid Segmented Copolymers. 1. Mobile Domains of a Polyester Thermoplastic Elastomer*. Macromolecules, **14**, pp. 581–586.

[30] Kendall M.A.F., Quinlan N.J., Thorpe S.J., Ainsworth R.W. and Bellhouse B.J. (1999). *The Gas-Particle Dynamics of a High-Speed Needle-Free Drug Delivery System*. In *22nd International Symposium on Shock Waves*. Imperial College, London.

[31] Kendall M.A.F., Wrighton Smith P.J. and Bellhouse B.J. (2000). *Transdermal Ballistic Delivery of Microparticles: Investigations Into Skin Penetration*. In *World Congress on Medical Physics and Biomedical Engineering*. Chicago, US.

[32] Li H. and White J.L. (2000). *Preparation and Characterization of Biaxially Oriented Films from Polybutylene Terephthalate Based Thermoplastic Elastomer Block Copolymers*. Polymer Engineering and Science, **40** (11), pp. 2299–2310.

[33] Li H. and White J.L. (2000). *Structure Development in Melt Spinning Filaments from Polybutylene Terephthalate Based Thermoplastic Elastomers*. Polymer Engineering and Science, **40** (4), pp. 917–928.

[34] Mark H.F. (1964). *Encyclopedia of Polymer Science and Technology - Plastics, Resins, Rubbers, Fibers*, p. 69. Interscience Publishers, John Wiley & Sons, Inc., New York.

[35] The MathWorks Inc. (2000). *Matlab V.6.00*.

[36] McCrum N.G., Buckley C.P. and Bucknall C.B. (1997). *Principles of Polymer Engineering*. Oxford University Press.

[37] Mitchell T.J. (2003). *The Ballistics of Microparticles Into the Mucosa and Skin*. DPhil Thesis, Department of Engineering Science, University of Oxford.

[38] Mitchell T.J., Kendall M.A.F. and Bellhouse B.J. (2001). *Micro-Particle Penetration to the Oral Mucosa*. In *Proceedings of the 2001 Bioengineering Conference*, pp. 763–764. Snowbird, Utah.

[39] Mullins L. (1947). *Effect of Stretching on the Properties of Rubber*. Journal of Rubber Research, **16**, pp. 275–289.

[40] Nabulsi S.M., H.R. Millward and B.J. Bellhouse (1999). *The Use of a Shock Tube for the Delivery of Powdered Drugs Into the Oral Mucosa*. In *22nd International Symposium on Shock Waves*. Imperial College, London, UK.

[41] Nishi T. and Kwei T.K. (1976). *Improvement of the Impact Strength of a Blend of Poly(vinyl Chloride) with Copolyester Thermoplastic Elastomer by Heat Treatment*. Journal of Applied Polymer Science, **20**, pp. 1331–1337.

[42] Nishi T., Kwei T.K. and Wang T.T. (1975). *Physical Properties of Poly(vinyl chloride)-Copolyester Thermoplastic Elastomer Mixtures*. Journal of Applied Physics, **46** (10), pp. 4157–4165.

[43] Ogden R.W. (1972). *Large deformation isotropic elasticity - on the correlation of theory and experiment for incompressible rubberlike solids*. Proceedings of the Royal Society A, **326**, p. 565.

[44] Ogden R.W. (2002). *Elasticity and inelasticity of rubber*, *CISM Course on Mechanics and Thermomechanics of Rubberlike Solids*. CISM, Udine, Italy.

[45] Ogden R.W. and Roxburgh D.G. (1999). *A Pseudo-Elastic Model for the Mullins Effect in Filled Rubber*. Proceedings of the Royal Society of London, Series A, **455**, pp. 2861–2877.

[46] Pesetskii S.S., Jurkowski B., Olkhov Y.A., Olkhova O.M., Storozhuk I.P. and Mozheiko U.M. (2001). *Molecular and Topological Structures in Polyester Block Copolymers*. European Polymer Journal, **37**, pp. 2187–2199.

[47] Quinlan N. (1999). *Gas and Particle Dynamics in Transdermal Powdered Drug Delivery*. DPhil Thesis, Engineering Science, University of Oxford.

[48] Richeson G.C. and Spruiell J.E. (1990). *Preparation, Structure and Properties of Copolyester-Ether Elastic Filaments*. Journal of Applied Polymer Science, **41**, pp. 845–875.

[49] Rivlin and Thomas (1953). *Rupture of Rubber I.*. Journal of Polymer Science, **10**, p. 291.

[50] Sanford J.C., Klein T.M., Wolf E.D. and N. Allen (1987). *Delivery of Substances Into Cells and Tissues Using a Particulate Bombardment Process*. Particulate Science and Technology, **5**, pp. 27–37.

[51] Sanford J.C., Wolf E.D. and Allen N.K. (1990). *Method for Transporting Substances Into Living Cells and Tissues and Apparatus Therefor*. US Patent 4945050.

[52] Sarphie D.F. (1992). *Gas Propulsion of Microparticles for the Transformation of Biological Cells*. DPhil Thesis, Engineering Science, University of Oxford.

[53] Shackelford J.F. (1992). *Introduction to Materials Science for Engineers*. Macmillan.

[54] Shen M., Mehra U., Niinomi M., Koberstein J.T. and Cooper S.L. (1974). *Morphological, Rheo-optical, and Dynamic Mechanical Studies of a Semicrystalline Block Copolymer*. Journal of Applied Physics, **45** (10), pp. 4182–4189.

[55] Thomas A.G. (1955). *Rupture of Rubber. II. The Strain Concentration at an Incision*. Journal of Polymer Science, **18**, pp. 177–188.

[56] Thomas S., Kuriakose B., Gupta B.R. and De S.K. (1986). *Scanning Electron Microscopy Studies on Tensile, Tear and Abrasion Failure of Plasticized Poly(vinyl chloride) and Copolyester Thermoplastic Elastomers*. Journal of Materials Science, **21**, pp. 711–716.

[57] Treloar L.R.G. (1975). *The Physics of Rubber Elasticity*. Clarendon Press, Oxford.

[58] Tsunoda K., Busfield J.J.C., Davies C.K.L. and Thomas A.G. (2000). *Effect of Materials Variables on the Tear Behaviour of a Non-Crystallising Elastomer*. Journal of Materials Science, **35**, pp. 5187–5198.

[59] Witsiepe W.K. (1972). *Segmented Thermoplastic Copolyester Elastomers*. US Patent no. 03651014.

[60] Wrighton Smith P.J. (2001). *Delivery of Particles by Powder Injection*. DPhil Thesis, Department of Engineering Science, University of Oxford.

[61] Young R.J. and Lovell P.A. (1991). *Introduction to Polymers*. Chapman and Hall, 2nd edition edition.

[62] Zhu L. and Wegner G. (1981). *The Morphology of Semicrystalline Segmented Poly(ether ester) Thermoplastic Elastomers*. Die Makromoleculare Chemie, **182**, pp. 3625–3638.

[63] Zhu L., Wegner G. and Bandara U. (1981). *The Crystallisation Behaviour and the Mechanical Properties of Segmented Poly(ether ester) Thermoplastic Elastomers*. Die Makromoleculare Chemie, **182**, pp. 3639–3651.